

**FIRST-PRINCIPLES STUDIES OF SUBSTRATE  
SUPPORTED METAL CLUSTERS: FROM  
FUNDAMENTALS TO APPLICATIONS**

*By*  
**AKANSHA SINGH**  
**PHYS08200904001**

**Harish-Chandra Research Institute, Allahabad**

*A thesis submitted to the  
Board of Studies in Physical Sciences  
In partial fulfillment of requirements  
for the Degree of*

**DOCTOR OF PHILOSOPHY**

*of*

**HOMI BHABHA NATIONAL INSTITUTE**



**October, 2015**



# Homi Bhabha National Institute<sup>1</sup>

## Recommendations of the Viva Voce Committee

As members of the Viva Voce Committee, we certify that we have read the dissertation prepared by Ms. Akansha Singh entitled "First-principles studies of substrate supported metal clusters – From fundamentals to application" and recommend that it may be accepted as fulfilling the thesis requirement for the award of Degree of Doctor of Philosophy.

---

Chairman – Prof. Sumathi Rao

**Date:**

---

Guide / Convener – Prof. Prasenjit Sen

**Date:**

*Prasenjit Sen*

*2/5/16*

---

Co-guide - -

**Date:**

---

Examiner – Prof. Abhishek Kumar Singh

**Date:**

*Abhishek Kumar Singh*

*2-5-2016*

---

Member 1- Prof. Pinaki Majumdar

**Date:**

*Pinaki Majumdar*

*2/5/16.*

---

Member 2- Dr. Aditi Sen De

**Date:**

*Aditi Sen De*

*02.05.16*

---

Final approval and acceptance of this thesis is contingent upon the candidate's submission of the final copies of the thesis to HBNI.

I/We hereby certify that I/we have read this thesis prepared under my/our direction and recommend that it may be accepted as fulfilling the thesis requirement.

**Date:** *2/5/16*

**Place:** *HRI*

*Prasenjit Sen*

**Prof. Prasenjit Sen**

**Guide**

---

<sup>1</sup> This page is to be included only for final submission after successful completion of viva voce.



## STATEMENT BY AUTHOR

This dissertation has been submitted in partial fulfillment of requirements for an advanced degree at Homi Bhabha National Institute (HBNI) and is deposited in the Library to be made available to borrowers under rules of the HBNI.

Brief quotations from this dissertation are allowable without special permission, provided that accurate acknowledgement of source is made. Requests for permission for extended quotation from or reproduction of this manuscript in whole or in part may be granted by the Competent Authority of HBNI when in his or her judgment the proposed use of the material is in the interests of scholarship. In all other instances, however, permission must be obtained from the author.

*Akansha Singh*  
Akansha Singh

02-05-2016



## DECLARATION

I, hereby declare that the investigation presented in the thesis has been carried out by me. The work is original and has not been submitted earlier as a whole or in part for a degree / diploma at this or any other Institution / University.

*Akansha Singh*  
Akansha Singh  
02-05-2015



## List of Publications arising from the thesis

### Journal

1. "Do  $Ag_n$  (up to  $n = 8$ ) clusters retain their identity on graphite? Insights from first-principles calculations including dispersion interactions", Akansha Singh, Chiranjib Majumder and Prasenjit Sen, *J. Chem. Phys.*, **2014**, *140*, 164705-164713.
2. "Density functional study of silver clusters on a stepped graphite surface: Formation of self-assembled nano-wires", Akansha Singh and Prasenjit Sen, *Phys. Chem. Chem. Phys.*, **2015**, *17*, 12708-12716.
3. "Finding the right support for magnetic superatom assembly", Akansha Singh and Prasenjit Sen, *Phys. Rev. B*, **2015**, *91*, 035438-035449.
4. "A comparative studies of Silver cluster supported over graphite surface using van der Waals interactions", Akansha Singh and Prasenjit Sen, *in preparation*.
5. "CO-oxidation by  $\alpha(0001)$ - $Al_2O_3$  supported  $Ag_nAu_m$  ( $n+m=2-4$ ) clusters", Akansha Singh, Chiranjib Majumder and Prasenjit Sen, *in preparation*.

### List of publication not related to the thesis

1. "Structural, electronic and magnetic properties of binary transition metal aluminum clusters: absence of electronic shell structure", Vikas Chauhan, Akansha Singh, Chiranjib Majumder and Prasenjit Sen, *J. Phys. Cond. Matt.*, **2014**, *26*, 035438-035449.
2. "Antiferromagnetic spin structure and negative thermal expansion of  $Li_2Ni(WO_4)_2$ ", Sunil K. Karna, C. W. Wang, R. Sankar, M. Avdeev, Akansha Singh, I. Panneer Muthuselvam, V. N. Singh, G. Y. Guo, and F. C. Chou, *Phys. Rev. B*, **2015**, *92*, 014413-014420.
3. "Tellurium-bridged two-leg spin ladder in  $Ba_2CuTeO_6$ ", G. Narsinga Rao, R. Shankar, Akansha Singh, I. Panneer Muthuselvam, Viveka Nand Singh, Guang-Yu Guo and F. C. Chou, *Phys. Rev. B*, **2016**, *93*, 10440-104411.

4. "Peierls transition and edge reconstruction in phosphorene nanoribbons", Ajanta Maity, Akansha Singh and Prasenjit Sen, *in preparation*.

*Akansha Singh*  
Akansha Singh

02-05-2016

## **DEDICATIONS**

To my father...



## ACKNOWLEDGEMENTS

First and foremost, I would like to express my special thanks to my supervisor Prof. Prasenjit Sen for his sincere guidance, care, patience, and continuous support during my Ph.D. work. I have been fortunate to have such an advisor who gave me the freedom to explore on my own, and at the same time the guidance to recover when my steps faltered. I would also like to thank Dr. Chiranjib Majumder, who has been always there to listen and give advice. I would like to thank Prof. G. V. Pai, who have been so helpful throughout my Ph.D. that no words can express my gratitude. He did not only help in reshaping my research skills, but also helped in the every good and bad phases of life. I would also like to thank Prof. Pinaki Majumdar, Prof. Sumathi Rao, and Prof. T. P. Pareek for their continuous encouragement. Next, I would like to thank Dr. Vikas Chauhan, Dr. Pooja Shrivastava, Dr. Rajarshi Tiwari, Dr. Sabyasachi Tarat, Dr. Madhuparana Karmakar, Nyayabanta, and Ajanta. I really enjoyed many beneficial discussions with them. I would like to thank the entire condensed matter group at Harish-Chandra Research Institute (HRI), they were very supportive and I would also like to acknowledge many useful discussions with them. I would like to acknowledge the use of the High Performance Scientific Computing facility at HRI and Amit Kulve for his constant technical support.

Many friends have helped me stay calm through these difficult years. Their support and care helped me overcome my setbacks and stay focused on my graduate study. I would like to express my gratitude to Madhuparana, Nyayabanta, Anushree, Saurabh, Shrobona, Avijit and Swapno.

None of this would have been possible without the love and patience of my family.

I would thank my mother, in-laws and my brothers (Chi and Shanki), sister Neha, and rest of my family, without their love, support, and faith, this venture could not have been successful. I specially want to remember my father, who was the first and best teacher I ever had. I wish he could see that I am doing fine and getting the highest degree of the subject he taught me since childhood. Last but not the least, I would like to thank my husband Vivek, for always cheering me up and stood by me. He has been a constant source of love, concern, and support all these years. Thank you for accompanying me in this wonderful journey.



# Contents

<b>Synopsis</b>	<b>v</b>
<b>List of Figures</b>	<b>xi</b>
<b>List of Tables</b>	<b>xviii</b>
<b>1 Introduction</b>	<b>1</b>
1.1 Atomic clusters . . . . .	1
1.2 Metal clusters . . . . .	2
1.2.1 The Shell Models . . . . .	3
1.3 Superatoms . . . . .	5
1.3.1 Magnetic superatoms . . . . .	6
1.3.2 Cluster assembled materials . . . . .	9
1.4 Surface supported clusters . . . . .	10
1.4.1 Characterization of the surface supported clusters . . . . .	11
1.4.2 Production of substrate supported clusters by atomic vapor de- position . . . . .	13
1.4.3 Deposition of preformed clusters . . . . .	14
1.4.4 Softlanding . . . . .	17
1.4.5 Cluster assembled films . . . . .	19
1.5 Heterogeneous catalysis . . . . .	19
1.6 Purpose and structure of the thesis . . . . .	23
<b>2 Theoretical methods</b>	<b>25</b>

2.1	Introduction . . . . .	25
2.2	The many body problem and Born-Oppenheimer approximation . . . . .	26
2.3	The Density functional theory . . . . .	28
2.3.1	The Hohenberg-Kohn (HK) theorems . . . . .	28
2.3.2	The Kohn-Sham (KS) equations . . . . .	29
2.4	The exchange-correlation functional . . . . .	32
2.5	The Plane wave basis set . . . . .	34
2.6	The pseudopotential theory . . . . .	36
2.6.1	Projector Augmented Wave method (PAW) . . . . .	38
2.7	Geometry optimization . . . . .	40
2.8	Molecular dynamics simulations . . . . .	44
2.8.1	Molecular dynamics at constant temperature . . . . .	46
2.9	Nudged elastic band method . . . . .	47
2.10	Bader charges . . . . .	50
2.11	van der Waals corrections . . . . .	53
<b>3</b>	<b>Adsorption of small <math>\text{Ag}_n</math> clusters over clean graphite substrate</b>	<b>57</b>
3.1	Motivation . . . . .	57
3.1.1	Experimental motivation . . . . .	57
3.1.2	Theoretical motivation . . . . .	60
3.2	Computational methods . . . . .	64
3.3	Clean graphite surface . . . . .	66
3.4	Structure of gas phase silver clusters . . . . .	67
3.5	Structure of deposited silver clusters . . . . .	69
3.6	A comparison between different methods . . . . .	78
3.7	Conclusions . . . . .	85
<b>4</b>	<b>Adsorption and diffusion of small silver clusters (<math>n = 1 - 8</math>) on a stepped graphite surface</b>	<b>87</b>
4.1	Introduction . . . . .	87
4.2	Computational methods . . . . .	91
4.3	Band structure of a relaxed arm-chair step edge . . . . .	94
4.4	Zero temperature adsorption of clusters . . . . .	94

4.5	Finite temperature results . . . . .	101
4.6	Band structure of 1D monoatomic chain along step edge . . . . .	104
4.7	Conclusions . . . . .	105
<b>5</b>	<b>Finding the right support for deposition and self assembly of magnetic superatoms</b>	<b>107</b>
5.1	Introduction . . . . .	107
5.2	Method . . . . .	109
5.3	Isolated FeCa <sub>8</sub> superatom . . . . .	110
5.4	FeCa <sub>8</sub> adsorbed on substrates . . . . .	112
5.4.1	Alumina substrate . . . . .	114
5.4.2	Ca substrate . . . . .	114
5.4.3	h-BN substrate . . . . .	115
5.4.4	Graphene substrate . . . . .	119
5.4.5	Two FeCa <sub>8</sub> units on h-BN and graphene . . . . .	124
5.5	LSDA results . . . . .	127
5.6	Conclusions . . . . .	130
<b>6</b>	<b>CO oxidation on Al<sub>2</sub>O<sub>3</sub> supported Ag<sub>n</sub>Au<sub>m</sub> model catalysts</b>	<b>131</b>
6.1	Introduction . . . . .	131
6.2	Computational method . . . . .	135
6.3	Gas phase structure of Ag <sub>n</sub> Au <sub>m</sub> clusters . . . . .	136
6.3.1	Adsorption and coadsorption of O <sub>2</sub> and CO molecules . . . . .	137
6.4	Structure of Ag <sub>n</sub> Au <sub>m</sub> clusters supported over alumina . . . . .	144
6.4.1	Absorption of O <sub>2</sub> molecule on supported Ag <sub>n</sub> Au <sub>m</sub> clusters . . . . .	148
6.4.2	Adsorption of CO molecule on supported Ag <sub>n</sub> Au <sub>m</sub> clusters . . . . .	150
6.4.3	Coadsorption of CO and O <sub>2</sub> molecule over supported Ag <sub>n</sub> Au <sub>m</sub> clusters . . . . .	151
6.5	Conclusions . . . . .	153
<b>7</b>	<b>Future prospects</b>	<b>155</b>
7.1	Introduction . . . . .	155
7.2	High energy deposition of silver clusters on a clean graphite surface . . . . .	155
7.3	Silver clusters over a bent graphite substrate . . . . .	156

7.4	Real space studies of FeCa <sub>8</sub> on graphite . . . . .	157
7.5	Catalytic studies of water gas shift reaction . . . . .	157
<b>APPENDIX</b>		<b>159</b>
<b>A</b>	<b>Adsorption of small Ag<sub>n</sub> clusters over clean graphite substrate</b>	<b>159</b>
<b>B</b>	<b>Study of small Ag<sub>n</sub> clusters on stepped graphite surface</b>	<b>162</b>
<b>C</b>	<b>Finding the right support for deposition and self assembly of magnetic superatoms</b>	<b>163</b>
<b>D</b>	<b>CO oxidation on Al<sub>2</sub>O<sub>3</sub> supported Ag<sub>n</sub>Au<sub>m</sub> model catalysts</b>	<b>166</b>
	<b>Bibliography</b>	<b>167</b>

## SYNOPSIS

Atomic clusters are aggregates of atoms consisting of a few to a few hundred atoms. They exhibit extreme size dependence of properties, which are distinct from those of an atom and the corresponding bulk. Properties of a cluster can be tuned by changing its size, composition, and even the number of electrons. Due to this freedom, clusters are considered as building blocks for designer new materials. By assembling such clusters, one can produce materials with novel functional and structural properties. These are called cluster assembled materials (CAM) [1]. Rapid progress in nanoscience and nanotechnology makes CAM's potentially useful in many applications, *e.g.*, miniaturization of electronic devices, development of highly selective sensors, fabrication of selective and efficient catalysts *etc.*

Great interest in the area of cluster science arose in 1984 [2] when Knight *et al.*, observed sharp peaks at sizes 8, 20, 40, 58 and 92 in the mass abundance spectrum of gas phase  $\text{Na}_N$  clusters. These peaks indicated higher stability at these sizes with respect to their neighbors. In order to explain the enhanced stability of metal clusters of certain sizes, various theoretical models have been proposed, which can be collectively called “shell models” [3]. These models assume that the valence electrons of all the atoms are confined within the finite volume of the cluster. Assuming the confining potential of the cluster to be spherically symmetric, one obtains the following sequence of one-electron orbitals arranged in the order of increasing energy:  $1\text{S}^2$ ,  $1\text{P}^6$ ,  $(1\text{D}^{10}$ ,  $2\text{S}^2)$ ,  $(1\text{F}^{14}$   $2\text{P}^6)$ , . . . . This leads to completely filled orbitals at certain electron counts, explaining the observed enhanced stability of metal clusters at specific sizes. The most exciting consequence of this electronic shell structure is the idea of “superatom” [4]. Existence of electronic shells in simple metal clusters and their dominating role in governing stability ensures that clusters exhibit electronic and chemical features similar to elemental atoms. Such atomic clusters that mimic properties of elemental atoms, and retain their identity in assemblies, are termed superatoms. Recently, the idea of superatoms has been extended to “magnetic superatoms”. For a cluster to qualify as magnetic superatom, it has to retain its structural identity and magnetic moment, or a part thereof, in dimers or assemblies. Known examples of magnetic superatoms include  $\text{VCs}_8$ ,  $\text{MnAu}_{24}$  [5],  $\text{FeCa}_8$  [6],  $\text{FeMg}_8$  [7],  $\text{CrSr}_9$  and  $\text{MnSr}_{10}$  [8].

For these clusters and superatoms to be useful in practical applications, it is essential to support them on some substrate. For example, cluster arrays and cluster assembled films fabricated over substrates can have applications in electronics and magnetic stor-

age devices. Substrate supported clusters can be fabricated either by depositing atoms which leads to the formation of clusters at various nucleation sites, or by depositing pre-formed size-selected clusters. Systems fabricated by these two methods can have completely different structures and properties. We are interested in deposition of pre-formed size selected clusters. After deposition, cluster-substrate interaction can alter the properties of the gas phase clusters, and can lead to unexpected electronic and geometric properties. An understanding of these interesting aspects for different cluster sizes is essential for bottom-up design of materials.

Depending on the nature of bonding between cluster and substrate, adsorption of clusters over substrate can be broadly classified into two categories. (1) Physisorption: when cluster-substrate interactions are weak van der Waal's type, and most of the properties of the gas phase clusters are preserved after deposition, *e.g.*, xenon on graphite [9], coinage metal clusters on MgO substrate [10]. (2) Chemisorption: when cluster-substrate interactions are very strong and the structure and properties of the gas phase clusters are heavily modified after deposition. In this regime, new chemical bonds form between the clusters and the substrate, *e.g.*, Au and Pt clusters on TiO<sub>2</sub> substrate [11].

For past many years, various experimental and theoretical studies have been performed on different metal clusters deposited on various substrates. Among these, coinage metals, particularly silver clusters over graphite substrate have attracted a lot of experimental attention [12--14]. The clean (0001) surface of graphite is very inert as it does not have any dangling bonds, and is expected to have weak interactions with clusters. In one of the early studies, Ganz *et al.*, [12] performed scanning tunneling microscopy to understand the static and dynamic behavior of Ag (and also Au, Cu and Al) atoms and clusters over Highly Ordered Pyrolytic Graphite (HOPG) at room temperature. They could identify single adatoms, dimers, small clusters and two dimensional islands containing hundreds of atoms. Silver atoms were always found above  $\beta$  sites of a graphite sheet. A  $\beta$  site carbon atom does not have a neighbor directly below it in the second layer. Busolt *et al.*, [13] deposited size selected Ag clusters containing 2 to 9 atoms on graphite. Within this size range, the larger clusters were found to retain their identity after deposition. Ndlovu *et al.*, [14] found the formation of Ag clusters of an average size 1.2 nm after deposition of atoms. They also found isolated Ag atoms near  $\beta$  sites, and reported a charge transfer from the clusters to the substrate as indicated by the positions of the Ag core level peaks in the X-ray photoelectron spectra. In general,

all these experiments conclude that Ag atoms physisorb on the HOPG substrate, and they are quite mobile at room temperature.

Like all real surfaces, graphite surfaces have point defects and steps. A lot of experimental groups have studied the structure and diffusion of silver clusters near step edges of graphite. In one such study Francis *et al.*, [15] examined morphologies and diffusion of silver clusters (fabricated by the atomic deposition) near the step edges at different temperature. At room temperature, the clusters were seen only on the wide terraces and step edges. Near the step edges they found a region denuded of any clusters. Cluster density was found to be much higher at the steps than on the terraces. The clusters formed large irregular shapes on the terraces, whereas at the steps cluster sizes were smaller, varying between 1 to 10 nm. As the temperature was increased above 118 °C, no cluster was seen even on the wider terraces, and all of them were observed at the step edges. Some of the clusters at the step edges had dumbbell shapes. These observations imply that Ag adatoms and clusters diffuse easily on clean terraces even at room temperature. They may get trapped at point defects on the terraces. Once they reach the steps, they can diffuse only along the step edges. But their mobility along the steps is lower compared to that on the terraces. In order to understand the behavior of pre-formed clusters, Francis *et al.*, [16] deposited clusters of an average size of 160 atoms. Carroll *et al.*, [17] deposited Ag cluster anions containing 50, 100 and 400 atoms and Goldby *et al.*, [18] deposited Ag clusters containing 50-250 atoms. In a separate study, Carroll *et al.*, [19] deposited size-selected Ag<sub>400</sub> clusters. They found that the size of the particles (particles are aggregates of clusters) at the steps are smaller than those on the terraces. Also more clusters were found at the steps than on the terraces, which was explained by the presence of dangling bonds on the step edge carbon atoms. Clusters have reduced mobility along the step edge as they are strongly bonded to the dangling bonds of the step edge.

Given its fundamental and technological importance, Ag/HOPG system has also attracted some theoretical attention. Duffy and Blackman [20] studied adsorption of Ag adatoms and dimers on HOPG, Jalkanen *et al.*, [21] studied adsorption of Ag adatom, dimer, Ag<sub>6</sub> and Ag<sub>13</sub> clusters on a single layer of graphite (*i.e.*, graphene) using density functional theory (DFT). But there have been no systematic theoretical studies of deposition and adsorption of Ag clusters on HOPG substrate over a range of cluster sizes. Some details about the diffusion of these clusters on terraces and step edges are also not fully understood. Do step edges act as attractive sinks for adatoms and clusters?

How do the atoms and clusters get trapped? How do they diffuse along the step edges? We try to answer these questions from first principles calculations.

As stated above, it is important for the stable cluster unit to retain its structural identity and magnetic properties in assemblies for it to qualify as a magnetic superatom. In the original papers [5--8], such tests were performed by calculating properties of isolated dimers of the stable clusters. However, for these superatoms to be useful in building CAM, such assemblies have to be made in a form that can be made to rest, for example on some substrate. Deposition and self-assembly of magnetic superatoms can lead to production of magnetic thin films whose properties can be tuned by choosing the building blocks, i.e., the superatoms. In order to form useful assemblies of magnetic superatoms, proper substrates have to be identified. Some of the desired properties of a substrate are: (1) the superatom-substrate interaction should be weak, so that superatom retains its structural identity; (2) the superatom-substrate interaction should be such that a substantial part of the magnetic moment of the free superatom is maintained even after deposition; (3) assemblies of two or more superatoms should retain their structural and magnetic properties over the substrate. Clearly, this is a stringent set of requirements. It is possible that different substrates may be ideal for different superatoms. Till now, there have been no experimental or theoretical studies on assemblies of magnetic superatoms on substrates. Hence, we took FeCa<sub>8</sub> as a prototype example and explored its properties on different types of substrates. We chose alumina ( $\alpha$  - Al<sub>2</sub>O<sub>3</sub>), calcium, graphene and hexagonal-BN (h-BN) as possible substrates, and performed DFT calculations to understand the electronic and magnetic properties of isolated units and assemblies of FeCa<sub>8</sub>.

It has been discovered that small metal clusters deposited over oxide substrates show enhanced catalytic activities for a variety of reactions. In particular, oxide supported small gold clusters have high reactivity towards CO oxidation at low temperatures [22, 23]. A large number of experimental and theoretical studies demonstrated that the chemical reactivity of Au clusters is strongly size-dependent, and mostly clusters containing  $\sim 10$  Au atoms are the active participants in the CO-oxidation reaction [24]. Some experimental studies also suggest that chemical reactivity of bimetallic Au-Ag clusters is much higher than that of pure Au or Ag clusters. Recently CO-oxidation on Au-Ag catalysts supported over mesoporous aluminosilicate [25] demonstrated the synergetic effect of combining Au and Ag; Ag was found to activate O<sub>2</sub>, while Au was found to adsorb CO. The best performing Au-Ag catalyst was the one

with Au/Ag ratio of 3:1. A few theoretical studies on adsorption of O<sub>2</sub> [26] and CO [27] molecules over gas phase pure Ag and Au, and bimetallic Au<sub>n</sub>Ag<sub>m</sub> clusters ( $n + m = 2 - 3$ ,  $n = 0 - 3$ ,  $m = 0, 3$ ) have also been reported. But the coadsorption of O<sub>2</sub> and CO molecules, which is an important step for the CO-oxidation reaction, has not been studied in these works. Effects of the presence of an oxide or any other support on the reactivity of these bimetallic clusters have not been addressed. Motivated by these facts, we studied the electronic and chemical properties of small Ag<sub>n</sub>Au<sub>m</sub> ( $n + m = 2 - 4$ ) clusters over the  $\alpha$  - Al<sub>2</sub>O<sub>3</sub>(0001) substrate and compared them with the gas phase clusters.

In summary, my thesis is comprised of two themes: study of (1) ground state properties, and (2) possible applications of substrate supported metal clusters within the framework of DFT. Study of ground state structure and electronic properties of silver clusters over clean and stepped graphite substrate belongs to the first theme. Possible self-assembly of silver nano wires on a stepped graphite substrate, self-assemblies of magnetic superatoms over inert substrates, and catalytic activity of alumina supported Ag<sub>n</sub>Au<sub>m</sub> ( $n + m = 2 - 4$ ) for the CO-oxidation reaction belong to the second theme.

This thesis is organized as follows.

**Chapter 1** is an introduction to the topic of atomic clusters, superatoms and substrate supported clusters. The first few sections consist of description of gas phase metal clusters, their stabilities and the theory of magnetic superatoms. The effect of cluster impact energy on the cluster morphology and a few experimental techniques to study the properties of supported metal clusters, that are related to the thesis, are described in detail. In the end, I review the previous theoretical works for substrate supported metal clusters.

**Chapter 2** is devoted to the methods and techniques used to perform the calculations in this thesis. Techniques for solving the Kohn-Sham equations using plane-wave basis sets, and construction of PAW potentials are discussed. The second section contains an overview of *ab-initio* molecular dynamics simulations and climbing image nudged elastic band methods. The methods that incorporate the dispersion interactions within the DFT framework are also discussed.

**Chapter 3** presents our studies of pre-formed Ag<sub>n</sub> clusters ( $n = 1 - 8$ ) over clean graphite substrates using the vdW-DF2 method. A summary of the experimental and

previous theoretical results are discussed as motivation. We find that except for  $\text{Ag}_3$ , all clusters prefer to stay parallel to the surface over top sites of graphite. Our study reveals that the results obtained with vdW-DF2 method are in best agreement with the experimental observations. A comparison of these results with those from the widely used LSDA and DFT-D2 methods have also been presented.

**Chapter 4** describes the morphologies and diffusion of small silver clusters (up to 8 atom) at the arm-chair step edge of graphite. The chapter starts with the experimental motivations which indicate that clusters near step edges have reduced mobility in comparison to those on terraces. We present the ground state structures of silver clusters on step edge at zero temperature. Then diffusion of  $\text{Ag}_5$  and  $\text{Ag}_8$  clusters at 600 K, and their structures, after they are annealed below room temperature, have been discussed in detailed. Based on these, we propose a way of fabricating self-assembled atomically thin silver nano-wires at the step edges.

**Chapter 5** discusses the adsorption of the magnetic superatom  $\text{FeCa}_8$  on different types of substrates. Both  $\alpha\text{-Al}_2\text{O}_3(0001)$  and  $\text{Ca}(001)$  substrates are found to have a strong interactions with the superatom (chemisorption). On the other hand,  $\text{FeCa}_8$  has weak interactions with h-BN and graphene, and retains its structure after deposition (physisorption). While the magnetic interaction between two  $\text{FeCa}_8$  units deposited on h-BN involves only direct exchange, substrate mediated RKKY interaction also plays a role on graphene. We estimate the minimum cluster density necessary to fabricate cluster assembled films over h-BN.

**Chapter 6** describes the reactivity of  $\text{Ag}_n\text{Au}_m$  ( $n + m = 2 - 4$ ) clusters supported over the  $\alpha\text{-Al}_2\text{O}_3(0001)$  substrate towards oxidation of CO molecule. We find that coadsorption of CO and  $\text{O}_2$  is possible on the gas phase  $\text{Ag}_n\text{Au}_m$  clusters, but the barriers for the oxidation reaction are quite high. The ground state structures of supported  $\text{Ag}_n\text{Au}_m$  clusters and how alumina substrate plays a major role in the coadsorption of  $\text{O}_2$  and CO molecules, are described in detail. We find that the  $\text{AgAu}_2$ ,  $\text{Ag}_2\text{Au}$  and  $\text{AgAu}_3$  clusters supported over alumina substrate are promising catalysts for CO oxidation. Possible reaction mechanisms are also discussed.

# List of Figures

1.1	Mass abundance spectrum of $\text{Na}_N$ clusters [2]. . . . .	3
1.2	Molecular orbitals (MO) and energy states of $\text{FeCa}_8$ cluster [6]. . . . .	8
1.3	Molecular-dynamics simulations of the morphology of films obtained by deposition of $\text{Mo}_{1043}$ clusters with increasing incident kinetic energies per atom onto a $\text{Mo}(001)$ substrate [67]. . . . .	16
1.4	Possible elementary growth processes for two clusters meeting on a surface (a) aggregation (b) coalescence. For atomic deposition, only process (a) is possible [66]. Black circles represent atomic clusters. . . . .	17
1.5	A schematic diagram for Eley-Rideal mechanisms and Langmuir-Hinschelwood, reproduced from Ref. [83]. . . . .	20
1.6	A schematic diagram for CO-oxidation by L-H mechanism, reproduced from Ref. [91] . . . . .	22
2.1	(a) Schematic diagram of all-electron (solid lines) and pseudoelectron (dashed lines) potentials and their corresponding wave functions. The radius at which all-electron and pseudoelectron values match is designated $r_c$ (b) Oxygen $2p$ radial wave function (solid line) and corresponding norm-conserving [116] (dotted line) and ultrasoft [117] (dashed line) pseudo wave functions. The figure is reproduced from Ref. [117]	37
2.2	Schematic representation of the PAW transformation. The auxiliary wave function is constructed from the full wave function by subtracting the oscillatory part close to an atom and replacing it by a smooth function. . . . .	38

2.3	Schematic 1D energy profile showing minimum energy path (MEP) which connect two local minima A and B separated by a transition state $X^\dagger$ [137]. . . . .	47
2.4	DFT calculations of the MEP for $\text{CH}_4$ dissociative adsorption on the Ir(111) surface. A regular NEB calculation and a CI-NEB calculation are compared, both involving 8 movable images. The regular NEB results in a low resolution of images near the SP, and the interpolation gives an underestimate of the activation energy. The CI-NEB put one of the images at saddle point and gives accurate energy barriers [139].	49
2.5	Phase portraits. A pair of gradient paths terminates or originates respectively, at the CP for a 1D maximum or minimum. In 2D, all of the gradient paths in a plane terminates or originates, at the maximum or minimum (CP) respectively. At (2,0) CP, a pair of paths originates at the CP, (positive curvature), and another pair terminates at the CP (negative curvature). All other gradient paths avoid the CP. A 3D display of a (3, 1) CP shows the set of trajectories that terminate at the CP and define a surface and the unique pair that originates there and defines a line [141]. . . . .	51
3.1	(a) A $14 \text{ \AA} \times 16 \text{ \AA}$ constant current STM image showing an isolated Ag monomer on graphite. (b), (d) and (f) are computer-generated models showing the graphite lattice positions with the adatom and dimer shapes superimposed. (c) A $32 \text{ \AA} \times 32 \text{ \AA}$ constant current STM image of a Ag dimer. (e) A $20 \text{ \AA} \times 18 \text{ \AA}$ current image of a Ag trimer in a linear form [12]. . . . .	58
3.2	Position of the Fermi-level as a function of cluster size obtained from the two photon electron spectroscopy with femtosecond pump and probe lasers [13]. . . . .	59
3.3	The changes of the Ag $3d$ states as a function of particle size on sputtered HOPG. The sizes of the particles were determined using scanning tunneling microscopy (STM). . . . .	60
3.4	Ag $3d$ level spectra of Ag bulk, deposited $\text{Ag}_5$ and $\text{Ag}_{10}$ (spectrum with squares) clusters on sputter-damaged HOPG, and 1 nm-sized Ag islands prepared using thermal evaporation of Ag atoms on the same substrate are compared . . . . .	61

3.5	Structure, bond lengths, and energies (relative to the ground state isomers) of gas phase $\text{Ag}_n$ clusters in vdW-DF2. Magenta colored circles represent Ag atoms. . . . .	68
3.6	Spin density iso-surface plots for Ag adatom (a), and gas phase ground state isomers of $\text{Ag}_3$ (b), $\text{Ag}_5$ (c) and $\text{Ag}_7$ (d) clusters deposited on HOPG. Isosurface is plotted at an isovalue 45 electron/ $\text{\AA}^3$ . Yellow circles represent carbon atoms of graphite sheet. . . . .	71
3.7	The ground state structures of $\text{Ag}_n$ clusters deposited on a graphite substrate obtained using vdW-DF2. Here magenta colored circles represent Ag atoms, turquoise colored circles represent the top layer carbon atom of graphite and gray colored circles represent the bottom two carbon atoms of graphite. . . . .	72
3.8	Some higher energy structures of $\text{Ag}_n$ clusters deposited on a graphite substrate obtained using vdW-DF2. . . . .	73
3.9	Some low-energy structures of $\text{Ag}_n$ clusters deposited on a graphite substrate obtained using LSDA. . . . .	77
3.10	Some low-energy structures of $\text{Ag}_n$ clusters deposited on a graphite substrate using DFT-D2. . . . .	84
4.1	A SEM image showing Ag clusters on surface steps and terraces after deposition of Ag onto HOPG at (a) 20 °C and (b) 118 °C temperature [15].	89
4.2	Structure of the a relaxed graphite surface with an arm-chair step edge. Bottom two layers are periodic in $x$ and $y$ directions. The step edge is periodic only in the $y$ direction. Blue circle represent the carbon atoms of the top layer (step edge), while the green stick frame represent the lower graphite layers. Small red circles represent passivated hydrogen atoms. . . . .	91
4.3	Band structures of the (a) unreconstructed and (b) reconstructed arm-chair step of graphite. Dotted red line represent the Fermi level. . . .	92
4.4	The ground state structures of gas phase $\text{Ag}_n$ clusters ( $n = 2 - 8$ ) obtained using L(S)DA. Here large red colored circles represent Ag atoms. . . . .	93
4.5	Structure of a stepped graphite surface with single Ag adatom adsorbed at an active site. Top and bottom panels show top and side views. Color coding is same as in Fig. 4.2 and Fig. 4.4 . . . . .	95

4.6	Partial (band decomposed) charge density plot for a silver adatom deposited over a stepped graphite surface. Charge density isosurface is plotted at an isovalue of 0.1 electron/Å <sup>3</sup> . . . . .	96
4.7	Spin density plot for a silver adatom deposited over a stepped graphite surface. Isosurface is plotted at an isovalue of 100 e/Å <sup>3</sup> . . . . .	97
4.8	Lowest energy structures obtained after adsorption of Ag <sub>n</sub> (n = 2 – 8) clusters on a stepped graphite surface. Relevant bond lengths are indicated (in Å). . . . .	99
4.9	Spin density isosurface plot for the Ag <sub>5</sub> cluster bonded at the armchair step edge of graphite. . . . .	100
4.10	Top panels: Snapshots from the MD simulation of an Ag <sub>5</sub> cluster on a stepped graphite surface at T= 600 K at specified times. Bottom panels: Snapshots after 6 ps of MD simulation at each temperature. . .	101
4.11	Top panels: Snapshots from the MD simulation of an Ag <sub>8</sub> cluster on a stepped graphite surface at T= 600 K at specified times. Bottom panels: Snapshots after 6 ps of MD simulation at each temperature. . .	103
4.12	Band structures of an ordered nanowire with one silver atom at each active site. . . . .	104
4.13	Band structures of system annealed to 200K for (a) Ag <sub>5</sub> and (b) Ag <sub>8</sub> cluster. . . . .	105
5.1	The lowest energy structure of FeCa <sub>8</sub> using (a)vdW-DF2 and (b)LSDA.	111
5.2	The MO's, and corresponding charge densities of FeCa <sub>8</sub> using (a) vdW-DF2 and (b) LSDA. Degeneracy of the MO's are also indicated. . . .	112
5.3	The lowest energy structure of FeCa <sub>8</sub> supported over alumina (a) and calcium (b) substrates. In panel (b) the substrate Ca atoms are shown with a darker (blue) color to distinguish them from the Ca atoms of the superatom. . . . .	113
5.4	Density of states of FeCa <sub>8</sub> deposited over alumina surface. . . . .	115
5.5	Density of states of FeCa <sub>8</sub> deposited over calcium surface. . . . .	116
5.6	The lowest energy structure of FeCa <sub>8</sub> supported over h-BN sheet (a) and Graphene (b) using vdW-DF2. First column: top view; second column: side view . . . . .	117
5.7	Some high energy isomers of FeCa <sub>8</sub> deposited over BN-sheet obtained using vdW-DF2. . . . .	118

5.8	Total density of states, and atom projected partial density of states of h-BN supported FeCa <sub>8</sub> . . . . .	119
5.9	Spin density isosurface of FeCa <sub>8</sub> deposited over h-BN using vdW-DF2 (plotted at isovalue 115 a.u.) . . . . .	120
5.10	Scatter plot of adsorption energy and magnetic moment for various structures of FeCa <sub>8</sub> on h-BN. The two structures with moment 4 $\mu_B$ are the lowest energy one and the one shown in Fig. 5.7(a). The one with a moment of 2 $\mu_B$ is the one in Fig. 5.7(b). The structure having no magnetic moment is a still higher energy one with large distortion of the anti-prism cage. . . . .	121
5.11	Difference in the adsorption energies (circle) of FeCa <sub>8</sub> having magnetic moment of 4 $\mu_B$ (fixed-moment) and no magnetic moment (non-magnetic) on a graphene sheet represented by supercells of various sizes; and the moment (square) obtained through self-consistent calculations (M). . . . .	122
5.12	Dimer of FeCa <sub>8</sub> deposited over h-BN sheet using vdW-DF2 . . . . .	124
5.13	Lowest energy structure of FeCa <sub>8</sub> supported over h-BN sheet (a) and Graphene (b) using LSDA method. First column- top view; second column- side view . . . . .	127
5.14	DOS of FeCa <sub>8</sub> deposited over BN-sheet using LSDA . . . . .	128
5.15	DOS of FeCa <sub>8</sub> deposited over graphene using LSDA . . . . .	129
6.1	The ground state structures of gas phase Ag <sub>n</sub> Au <sub>m</sub> clusters. The golden colored circles represent Au atoms, while green colored circles represent Ag atoms. . . . .	137
6.2	A schematic diagram for MO's for Ag <sub>2</sub> , AgAu and Au <sub>2</sub> (from left) clusters respectively. The black colored lines denote the occupied MO's, while the brown colored lines denote the MO's. The labels s and d correspond to MO's which have majority contributions from the s and d states of the atoms. . . . .	138
6.3	A schematic diagram for MO's for Ag <sub>3</sub> , Ag <sub>2</sub> Au, AgAu <sub>2</sub> and Au <sub>3</sub> (from left) clusters respectively. The color scheme and labeling is same as in Fig. 6.2. The up and down arrows represent the majority and minority spin channels. . . . .	139

6.4	Adsorption of O <sub>2</sub> molecule on gas phase Ag <sub>n</sub> Au <sub>m</sub> clusters. The red circles denote O atom. Rest of the color scheme is same as in Fig. 6.1.	140
6.5	Adsorption of CO molecule on gas phase Ag <sub>n</sub> Au <sub>m</sub> clusters. The yellow colored circles denote C atoms. Rest of the color scheme is same as in Fig. 6.4.	141
6.6	Coadsorption of CO and O <sub>2</sub> molecule on gas phase Ag <sub>n</sub> Au <sub>m</sub> clusters.	142
6.7	The MEP for the CO-oxidation by L-H mechanism on Ag <sub>2</sub> Au <sub>2</sub> cluster. The blue circles represent the energy of each image on the elastic band. The plot has been fitted by the spline interpolation.	143
6.8	The MEP for the CO-oxidation by L-H mechanism on Ag <sub>3</sub> Au cluster. The other descriptions of figure are same as in Fig. 6.7.	144
6.9	The ground state structures of Ag <sub>n</sub> Au <sub>m</sub> clusters supported over Al <sub>2</sub> O <sub>3</sub> surface.	145
6.10	The charge density difference plot for Ag <sub>n</sub> Au <sub>m</sub> supported over Al <sub>2</sub> O <sub>3</sub> surface. The red colored isosurface represent the excess of electronic charge while the blue colored isosurfaces represent the lack of electronic charge density.	146
6.11	Adsorption of O <sub>2</sub> molecule on Ag <sub>n</sub> Au <sub>m</sub> clusters supported over Al <sub>2</sub> O <sub>3</sub> surface.	149
6.12	Adsorption of CO molecule on Ag <sub>n</sub> Au <sub>m</sub> clusters supported over Al <sub>2</sub> O <sub>3</sub> surface.	150
6.13	Coadsorption of CO and O <sub>2</sub> molecule on Ag <sub>n</sub> Au <sub>m</sub> clusters supported over Al <sub>2</sub> O <sub>3</sub> surface.	151
7.1	Schematic view of a three-faced pleat. The faces are terminated by sharp bends. The two outer borders of the pleat are concave and two inner borders between the faces are convex.	156
A.1	Structure, bond lengths, and energies (relative to the ground state isomers) of gas phase Ag <sub>n</sub> clusters as found in our global search methods using L(S)DA.	159
A.2	Structure, bond lengths, and energies (relative to the ground state isomers) of gas phase Ag <sub>n</sub> clusters in DFT-D2.	160
A.3	Structure, bond lengths, and energies (relative to the ground state isomers) of gas phase Ag <sub>n</sub> clusters in DFT-D2.	161

B.1	Energy barrier for the diffusion of a silver adatom along the step edge of graphite. . . . .	162
C.1	Adsorption sites of Alumina and Calcium surface. Top panel: alumina surface (top and side views). Lower panel: calcium surface (top and side views). Different layers are represented with different colors. . .	163
C.2	Partial charge density of 2D states of h-BN supported FeCa <sub>8</sub> cluster. .	164
C.3	Considering the two FeCa <sub>8</sub> units are in the ground state over substrate and diffusing towards each other, we can guess two possible structures of a dimer, (a) each atom of triangular face is connected to only one atom of the other triangular face, and (b) one atom of each triangular face is connected to two atoms of the other triangular face . . . . .	164
C.4	Dimer of FeCa <sub>8</sub> deposited over h-BN sheet using vdW-DF2 deposited at a distance of 8.5 Å. . . . .	165
D.1	A schematic diagram for the energy eigen states for Ag <sub>4</sub> , Ag <sub>3</sub> Au, Ag <sub>2</sub> Au <sub>2</sub> , AgAu <sub>3</sub> , and Au <sub>4</sub> (from left) clusters respectively. The color scheme and labeling is same as in Fig. 6.2. . . . .	166

# List of Tables

3.1	A summary of the absorption energies obtained in various theoretical works [20, 168] for an Ag adatom and dimer at different sites of a graphite surface. . . . .	61
3.2	Properties of graphite as reproduced by different exchange-correlation functionals. $a_0$ is the intra-layer lattice constant and $c_0$ is the inter-layer separation. $E_c$ and $E_B$ are the cohesive energy and the interlayer binding energy respectively. . . . .	66
3.3	Adsorption energy ( $E_a$ ) and magnetic moment (M) of a silver adatom at various points on a graphite substrate obtained using vdW-DF2 method. . . . .	70
3.4	Details of silver clusters on graphite from vdW-DF2 studies. $E_a$ and $E_c$ are the adsorption energy and cohesive energy respectively; $M$ is the magnetic moment and $q$ is the charge transfer from the cluster to surface in terms of electronic charge. $Z_r$ denotes the maximum relaxation of the C atoms on the top layer and $\Delta Z_c$ represents the maximum deviation of a top layer C atom from their average position. . . . .	74
3.5	Adsorption energy $E_a$ and magnetic moment silver adatom at various points on a graphite substrate obtained using LSDA. . . . .	76
3.6	Properties of silver clusters deposited on a graphite substrate obtained with LSDA method. All notations are defined in Table 3.4. . . . .	78
3.7	Properties of a silver adatom at various points on a graphite substrate obtained using DFT-D2. $E_a$ is the adsorption energy, $E_{\text{disp}}^{\text{Ag-C}}$ is the Ag-C dispersion contribution, and $M$ is the magnetic moment in the system. . . . .	81

3.8	Properties of silver clusters deposited on a graphite substrate obtained with DFT-D2 method. All notations are defined in Table 3.4 and Table 3.7. . . . .	85
4.1	Adsorption energies, magnetic moments and charge transfer from the cluster to the graphite substrate in the lowest energy structures of Ag clusters adsorbed on an armchair step edge of graphite. . . . .	98



# Introduction

## 1.1 Atomic clusters

Physical properties of macroscopic materials are largely independent of their shape and size because of small surface to volume ratios. However as one goes to the small size limit and manipulate matter at the atomic, molecular, and supermolecular scales, systems show striking properties that depend on their shapes and sizes. One of the most prominent examples are atomic clusters. Atomic clusters are aggregates of a few to a few thousand atoms. They constitute a new “phase” of matter with a wide range of possible sizes, compositions and charge states. Their properties are very distinct from that of individual atoms, molecules or the corresponding bulk. Clusters are different from their corresponding bulk mainly because of two reasons: first, the arrangement of atoms in a cluster is very different from the bulk, and second, unlike bulk, the number of atoms on the surface of a cluster is a substantial fraction of the total number of atoms. We distinguish clusters from molecules in the following sense. Molecules exist in nature under ambient pressure and temperature, while clusters are metastable and can only be produced in labs under special experimental conditions. Bonding in molecules is either covalent or ionic in nature, while bonding within clusters can be metallic, covalent, van der Waals or ionic.

The most striking feature of atomic clusters is that they exhibit extreme size-dependence of electronic, magnetic, chemical, and optical properties. Their properties change non-monotonically as the size varies from the atomic to the bulk limit. Addition or removal of even a single atom or electron can induce dramatic changes in properties of

clusters [3]. This exciting feature gives us the freedom to tune properties of cluster according to the desired need. Due to this reason, clusters are considered as the ideal candidates to serve as a building blocks for designer new materials.

Based on the type of constituent atoms and the nature of bonding, atomic clusters can be broadly classified as rare gas clusters ( $\text{Ar}_N, \text{Xe}_N$ ), semiconductor clusters ( $\text{Ge}_N, \text{Si}_N$ ), metal clusters ( $\text{Na}_N, \text{Ag}_N$ ) and ionic clusters ( $(\text{NaCl})_N, (\text{NaF})_N$ ). In this thesis our focus is on certain types of metal clusters.

## 1.2 Metal clusters

Bulk metallic systems have finite density of states at the Fermi energy and hence have a gapless spectra. However, one cannot define metal clusters in the same way as they always have discrete electronic spectra due to the finite size. In cluster science, clusters formed out of atoms that are metallic in the bulk are termed metal clusters. Metal clusters can be of simple metals, noble metals, transition metals (TM), and also of more than one species, called alloy clusters.

Clusters in which bonding between the atoms is mostly through the outermost delocalized  $s$  and  $p$  electrons, are known as simple metal clusters. Thus clusters composed of group-IA (alkali), group-IIA, and group-IIIA metal elements form simple metal clusters. These clusters having certain specific number of valence electrons are more stable with respect to their neighboring sizes [2, 3]. The origin of their stability can be understood in terms of quantum mechanical models, best known as “shell models”, which are described in the next section.

Like alkali elements, group-IB noble metal elements (Cu, Au, Ag) are also monovalent and have one electron in their outermost  $ns$  orbital. However, these elements also have filled  $(n - 1)d^{10}$  orbitals. Depending on the energy gap between the outermost  $ns^1$  and  $(n - 1)d^{10}$  orbitals, the  $d$  states may also contribute to bonding. We will discuss this issue again in chapter 6 in more detail. Noble metal clusters have many similarities with alkali clusters [28]. However, due to the presence of  $(n - 1)d^{10}$  electrons, structural evolution some of these clusters is found to be very different from that of alkali clusters. For example, structure of Au clusters containing as many as 13 atoms is planar [29] (two dimensional (2D) to three dimensional (3D) transition for Au clusters strongly depends on the method used [30--32]).  $\text{Cu}_N$  clusters having more

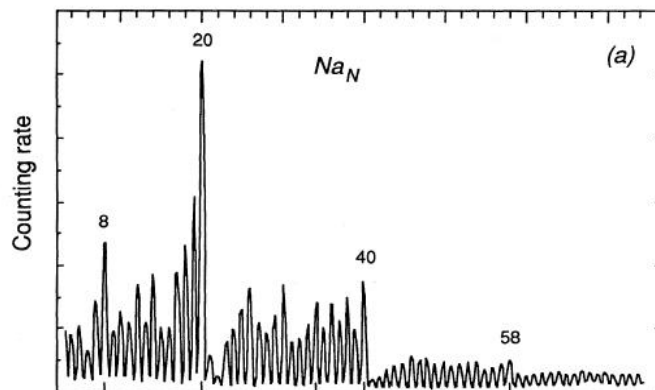


Figure 1.1: Mass abundance spectrum of  $Na_N$  clusters [2].

than 3 atoms assume 3D structures, while simple metal clusters transform to the 3D structures when they have more than 6 atoms [33, 34]. The properties of TM clusters are very different from those of the simple metal clusters, and their stability cannot be explained using shell models. In this thesis, we will only focus on some simple and noble metal clusters.

### 1.2.1 The Shell Models

In 1984, Knight and co-workers [2] observed a non-monotonic behavior in the mass spectra of small gas phase sodium clusters. They found that the mass spectra of  $Na_N$  clusters exhibit a pattern of intense peaks (Figure 1.1) at sizes  $N = 2, 8, 20, 40, 58, \dots$ , where  $N$  denotes the number of atoms in a cluster. These were called magic clusters as these peaks indicate enhanced stability at these sizes compared to their neighbors.

The origin of this enhanced stability for certain sizes can be understood in terms of quantum mechanical models. One can assume that the valence electrons of all the metal atoms in these clusters are free to move within the volume of the cluster. This quantum confinement produces discrete electronic energy levels with certain degeneracies, where the degree of degeneracy depends on the symmetry of the confining potential. The simplest possible choice one can take is that the confining potential is

spherically symmetric. In particular the confining potential  $V(r)$  is defined as

$$\begin{aligned} V(r) &= 0 ; r < R_0 \\ &= \infty ; r \geq R_0 \end{aligned} \quad (1.0)$$

where  $R_0 = xN^{1/3}r_s$ ;  $r_s$  is the Wigner-Seitz radius in the corresponding bulk, and  $x$  is the valency of the metal atom. By solving the Schrödinger equation for this potential, one can obtain the one-electron energy levels  $E_{nl}$ .

$$E_{nl} = \frac{\hbar^2 \beta_{nl}^2}{2mR_0^2}, \quad (1.1)$$

where  $\beta_{nl}$  is the  $n^{\text{th}}$  zero of  $l^{\text{th}}$  spherical Bessel function. And the energy eigenfunctions have the form

$$\Psi_{nlm}(r, \theta, \phi) = A_{nl} j_l(\beta_{nl}r/R_0) Y_l^m(\theta, \phi), \quad (1.2)$$

where  $A_{nl}$  are determined through normalization,  $j_l(\beta_{nl}r/R_0)$  are spherical Bessel functions and  $Y_l^m(\theta, \phi)$  are spherical harmonics. Due to the spherical symmetry, the energy eigenstates of the cluster depend on the principle quantum number  $n$  and orbital angular momentum  $l$ , but they are degenerate in the magnetic quantum number  $m$ . Thus energy states have  $2(2l + 1)$  fold degeneracies. These energy states form the electronic shells ( $nl$ ), which are arranged in increasing energy as  $1S^2 1P^6 1D^{10} 2S^2 1F^{14} 2P^6 1G^{18} \dots$ . These electronic shells will be completely filled when there are 2, 8, 18, 20, 34, 40, 58,  $\dots$  electrons in the cluster. As filled electronic shells lead to greater stability in atoms (*e.g.*, rare gas atoms), the completely filled shells are expected to lead enhanced stability in clusters. In fact, the molecular orbitals (MO) of a cluster for a given angular momentum look very similar to those of an atom. The only difference is that in case of atoms the atomic orbitals are localized on the atom, while in case of clusters the MO's are delocalized over the entire cluster. Since sodium is a monovalent atom, stability of  $\text{Na}_N$  clusters at  $n = 8, 20, 40, 58, \dots$ , can be easily understood in terms of the shell model. However, spherical shell model also predicts stability at size  $N=18, 34$ , and 68 which were not observed with high intensity in the mass spectrum (Figure 1.1).

One may also choose other confining potentials *e.g.*, spherical harmonic potential or Woods-Saxon potential [3], which give the shell filling at electron count 2, 8, 20, 40, 70, 112 ... and 2, 8, 18, 20, 34, 40, 58, 68, 70, 92 ... respectively. The other realistic model is spherical jellium model, which also include the electron-electron interactions. In this model, one assumes that the positive charge of all the ions in the cluster is distributed uniformly over the spherical volume of the cluster. The effective one electron energy levels for such a charge distribution are also arranged in the order  $1S^2 1P^6 1D^{10} 2S^2 1F^{14} 2P^6 \dots$

Although these models discussed above are quite successful in explaining the relative stability of magic clusters, however they cannot capture the fine structure of the mass abundance spectrum. To explain this fine spectra, one has to include the spheroidal deformations in the confining potential based on the ideas of Nilsson model. More information about the method can be found in Ref. [3, 35--37].

### 1.3 Superatoms

One of the most exciting developments in the field of cluster science has been the idea of superatoms [7, 38--45]. The idea of superatom was first proposed by Jena and Khanna in 1990 based on the observation that electronic structure of some simple metal (alkali [5, 46], alkaline earth [6, 8], noble metal [43]) clusters obey the shell models. The existence of the electronic shells in simple metal clusters and their dominating role in governing stability indicate that some clusters may exhibit electronic and chemical features similar to the elemental atoms. Such atomic clusters that mimic properties of elemental atoms are termed as superatoms. Recently, Castleman and Khanna [4] gave an updated definition of a superatom according to which atomic clusters that retain their identity in assemblies, and mimic properties of elemental atoms are termed superatoms.

Superatom behavior of atomic clusters has been established through experimental demonstrations and first principles electronic structure calculations. In one of the experiments, Leuchtner *et al.*, [47] found size dependent reactivity of aluminum cluster anions towards oxygen molecule. They found that clusters containing 13, 23, and 37 atoms were not reactive to oxygen. Since each aluminum atom has three valence electrons, the total number of valence electrons in an anion cluster will be  $3N + 1$ . Non-reactive behavior of anions of size 13, 23, and 37 can be accounted for by shell

closings at 40, 70, and 112 electrons. Thus stability of these sizes can be explained using shell models. The electronic shell structure of the cluster not only explains the mass abundance spectrum, but also has a direct impact on chemical properties. Similar non-reactive behavior is well known for inert gas atoms due to their closed electronic configuration. Therefore these Al cluster anions can be regarded as analogues of the inert gas atoms. This conjecture has been supported by the theoretical calculations of Khanna and Jena [38, 39].

In a similar manner,  $\text{Al}_{13}$ , which is one electron short of a closed electronic shell, has been found to behave as a halogen atom and has been termed a superhalogen. Theoretical calculations performed by Khanna *et al.*, [38] showed that electron affinity of  $\text{Al}_{13}$  is 3.7 eV, which is comparable to that of a Cl atom (3.6 eV). Later experimental studies by Li *et al.*, [48] confirmed the theoretical findings. Similarly,  $\text{Al}_{14}$  with 42 valence electrons has been found to mimic the properties of the alkaline earth atoms [41]. Another experimental study combined with the theoretical calculations [42] revealed that  $\text{Al}_7^-$  behaves as a multiple valence superatom.  $\text{Al}_7^-$  is a 22 electron system with an electronic configuration  $1\text{S}^2 1\text{P}^6 1\text{D}^{10} 2\text{S}^2 1\text{F}^2$ . It likes to bind strongly to atoms that need 2 or 4 electrons to fill their shells because then  $\text{Al}_7^-$  cluster can achieve a shell closure with 18 or 20 electrons. Apart from aluminum clusters, ligated  $\text{Au}_N$  cluster with thiolate and other ligands are also considered as superatoms. The ligands surround the metallic core and withdraw electrons. The clusters are stable when electron count leads to a filled electronic configuration [44].

### 1.3.1 Magnetic superatoms

Although electronic shell orbitals for a given angular momentum resemble those in atoms, the filling of the electronic states in simple metal clusters do not follow Hund's rule. Clusters can also undergo Jahn-Teller distortions absent in atoms. Typically, the energy gain in Jahn-Teller distortion is much larger than the exchange splitting. Hence these clusters usually have low spin ground states. Small metal clusters with odd number of electrons are doublet, while clusters having even number of electrons are singlet. Superatoms which gain stability through closed shell configuration are non-magnetic as magnetism requires spin unpaired electrons.

A breakthrough in the direction of producing magnetic superatoms came in 2009

when Reveles *et al.*, [5] proposed a way to induce spin dependent splitting in the electronic states of the cluster. They proposed binary clusters involving TM atoms which have both localized and delocalized electronic states. Two things can happen in such systems [49]:

- Magnetic moment arises from the localized orbitals of the TM atom, while stability is achieved through shell filling of the delocalized electrons. For example in  $\text{VCs}_8$  [5], each Cs atom contributes one delocalized electron, while the V atom contributes three  $d$  electrons and two  $s$  electrons. Hence the cluster has 13 valence electrons. Eight of these electrons fill the  $1S^2$  and  $1P^6$  shell orbitals, while the remaining five electrons occupy the V atomic  $3d$  states. The D-states of the cluster has majority contribution from the atomic  $d$  state of the V. Thus the cluster has five unpaired electrons which give a magnetic moment of  $5 \mu_B$ .
- The localized  $d$ -states of the TM can hybridize with cluster D-states and induce an exchange splitting, which can stabilize magnetism in a superatom. For example, in  $\text{FeMg}_8$  and  $\text{FeCa}_8$  both having 24 valence electrons, the atomic  $d$  orbitals of Fe induce exchange splitting in the cluster D-orbitals. Both the clusters have electronic configuration  $1S^2 1P^6 1D^{10} 2S^2 2D^4$ . All four 2D electrons are in the majority spin channel. Thus four unpaired spins in 2D orbitals leads to a magnetic moment of  $4 \mu_B$ .

One of the qualifying criteria used to decide whether a stable magnetic cluster is a superatom or not is to try and form dimers of it. This is the first test whether it would be stable in assemblies and whether it would retain (at least part of) its magnetic moment. For example, although both  $\text{VNa}_8$  and  $\text{VCs}_8$  turn out to be stable clusters within the respective  $\text{VA}_N$  series ( $A=\text{Na}, \text{Cs}$ ), when two  $\text{VNa}_8$  clusters put together, they merged completely to form a  $\text{V}_2$  dimer surrounded by sixteen Na atoms, and lost their magnetic moments. Therefore, by the modern definition,  $\text{VNa}_8$  does not qualify as a magnetic superatom.  $\text{VCs}_8$ , on the other hand, retains its identity and form stable dimers and trimers with distinct magnetic properties. Similarly, dimers of  $\text{FeMg}_8$  [7],  $\text{FeCa}_8$  [6],  $\text{CrSr}_9$ , and  $\text{MnSr}_{10}$  [8] were found to be stable in which individual cluster units retain their identity. Therefore, these stable clusters qualify as magnetic superatoms.

As already mentioned,  $\text{FeCa}_8$  [6] has 24 valence electrons as each Ca atom contributes two valence electrons and Fe contributes six  $d$  electrons and two  $s$  electrons.

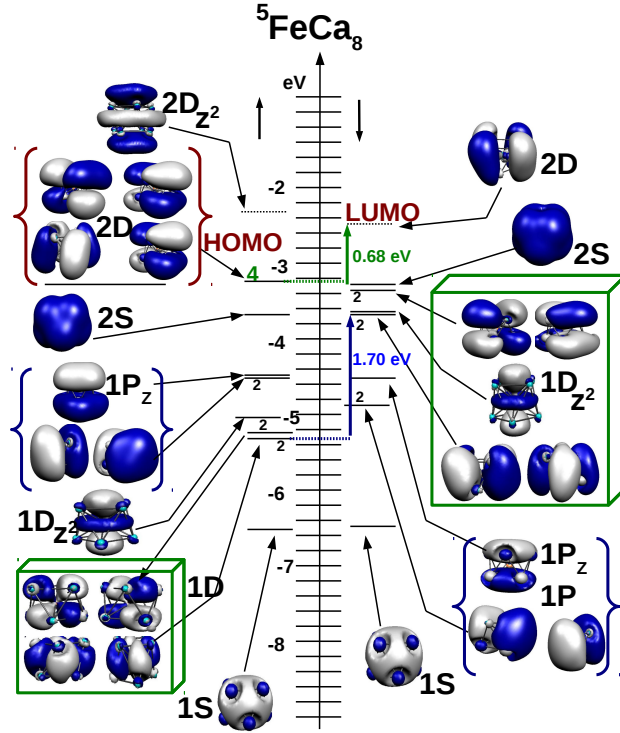


Figure 1.2: Molecular orbitals (MO) and energy states of  $\text{FeCa}_8$  cluster [6].

It has a large gap ( 0.68 eV) between the highest occupied and lowest unoccupied molecular orbitals (HOMO-LUMO gap). A large HOMO-LUMO gap is the signature of stability of the clusters as clusters will resist in both donation and acceptance of electrons. The  $1S^2 1P^6 1D^{10} 2S^2 2D_\alpha^4$  electronic configuration of  $\text{FeCa}_8$ , where  $\alpha$  ( $\beta$ ) denotes the majority (minority) spin channel, is shown in a molecular orbital (MO) diagram in Fig.1.2. The  $\text{FeCa}_8$  cluster has an oblate shape, which lifts the degeneracies of the P and D shell orbitals. Thus 2D-states of the cluster split into a group of 4 ( $2D_{xy}$ ,  $2D_{x^2-y^2}$ ,  $2D_{xz}$  and  $2D_{yz}$ ) and the  $2D_{z^2}$  state. Further, the hybridization of the atomic 3d states of Fe induce exchange splitting in the cluster D-states. Thus 20 electrons give filled  $1S^2 1P^6 1D^{10} 2S^2$  orbitals. The remaining four unpaired electrons occupy the four 2D-states in the majority channel, leading to a magnetic moment of 4  $\mu_B$ . They also calculated the dimer structure of the  $\text{FeCa}_8$ . In the dimer structure, two

units of  $\text{FeCa}_8$  retain their identities and couple ferromagnetically. Thus a dimer possess a magnetic moment of  $8 \mu_B$ . The antiferromagnetic state of the dimer was found to 0.021 eV higher than the ferromagnetic state. Hence,  $\text{FeCa}_8$  qualifies as a magnetic superatom.

### 1.3.2 Cluster assembled materials

Since clusters and superatoms exhibit interesting size and shape dependent properties, they are considered as building blocks for designer new materials [1, 4]. By assembling clusters, one can produce materials with novel functional and structural properties. These are called cluster assembled materials (CAM). Properties of CAM's can be tuned by choosing appropriate building blocks.

A well known example of CAM are fullerene based materials [50]. Fullerene ( $\text{C}_{60}$ ) can be combined to form a face-centered cubic (FCC) solid in which structural identities of  $\text{C}_{60}$  cluster are retained. Such crystals are called fulleride which have very different properties than diamond or graphite. Alkali-doped fullerides [51]  $\text{A}_3\text{C}_{60}$  ( $\text{A} = \text{K}, \text{Rb}, \text{Cs}$ ) are also capable of forming high crystalline solids with striking properties. These doped fullerides show superconductivity which can be tuned by changing the interfullerene spacing. Al clusters may form another class of CAM. Liu *et al.*, [52] found that an  $\text{Al}_{13}\text{K}$  cluster is an ionically bonded superatom complex, very much like a  $\text{KCl}$  molecule. This led to the idea that such motifs can also be used for cluster assemblies. They found that  $\text{Al}_{13}\text{K}$  may form a BCC structure with a lattice constant of 6.52 Å. The small size of K relative to  $\text{Al}_{13}$  causes strong interaction between the  $\text{Al}_{13}$  units and  $\text{Al}_{13}$  becomes cuboctahedral in the solid phase. The system is metallic and stable against lattice distortions. Later the ionic nature of  $\text{Al}_{13}\text{K}$  cluster has also been confirmed in the experiments by Zheng *et al.*, [53]. In a combined experimental and theoretical studies [41], an  $\text{Al}_{13}\text{I}_x^-$  cluster was also found to be an ionically bonded superatom complex. They showed that the extra electron was held by the aluminum motif, which indicates that its electron affinity is higher than that of iodine.

The theoretical work by Reber *et al.*, [54] showed that the  $\text{A}_3\text{O}$  species act as superalkali ( $\text{A} = \text{alkali atoms}$ ). They showed that the binding energy of  $\text{Al}_{13}\text{K}_3\text{O}$  is 5.53 eV, which is much larger than that for  $\text{Al}_{13}\text{K}$  (2.51 eV). Thus an  $\text{Al}_{13}\text{K}_3\text{O}$  is a strongly bound molecule. It can be assembled into stable superatom assemblies  $(\text{Al}_{13}\text{K}_3\text{O})_N$

with  $\text{Al}_{13}$  and  $\text{K}_3\text{O}$  as the superatom building blocks. The larger alkali motifs ( $\text{K}_3\text{O}$ ) reduces the interactions between  $\text{Al}_{13}$  units in the assembled materials allowing the  $\text{Al}_{13}$  units to maintain their discrete superatomic character.

In another studies by Castleman *et al.*, [55], the mass abundance spectra of  $\text{As}_N\text{K}_M^+$  clusters showed the existence of prominent peaks at  $\text{As}_6\text{K}_3^+$  and  $\text{As}_7\text{K}_3^+$ , indicating their greater stability. From the experimental as well as theoretical studies, they found that both these clusters are very stable and can be used as building blocks for CAM's.

## 1.4 Surface supported clusters

Surface supported clusters brought a revolution in the field of nanoscience and heterogeneous catalysis. It is one of the most active fields of research in material science. One of the obvious reasons for this is the industrial demand for miniaturization of electronic devices [56]. Secondly, supported metal clusters are very good catalysts and play a vital role in the chemical industries. Surface supported clusters provide a way for bottom-up approach to synthesis of materials through self-assembly. The self-assembly is a phenomenon where clusters assemble themselves spontaneously to form larger units or films. Two different methods can be employed to fabricate supported clusters [57]: (i) deposition of atomic vapor, (ii) deposition of preformed clusters from a cluster source, either size-selected or otherwise. Both of these techniques are discussed in the later sections.

The deposition of clusters over surfaces often changes its properties compared to that of the free clusters by the cluster-substrate interaction (due to hybridization, changes in the geometry, diffusion, alloy formation *etc.*,) and cluster-cluster interaction (in case of high coverages). Depending on the nature of bonding between the cluster and substrate, adsorption of clusters over substrates can be broadly classified into two categories. (1) Physisorption: when cluster-substrate interactions are weak van der Waal's type, and most of the properties of the gas phase clusters are preserved after deposition. For example, deposition of xenon on graphite [9], adsorption of noble metal clusters on MgO substrate [10]. (2) Chemisorption: when cluster-substrate interactions are strong and the structure and properties of the gas phase clusters are heavily modified after deposition. In this regime, new chemical bonds form between the clusters and the substrate, *e.g.*, Au and Pt clusters on  $\text{TiO}_2$  substrate [11], Au clusters on

CeO<sub>2</sub> substrate [58].

### 1.4.1 Characterization of the surface supported clusters

Many experimental techniques [59] have been used to measure and understand properties of surface supported clusters. These include X-ray photoelectron spectroscopy (XPS), scanning tunneling microscopy (STM), scanning electron microscopy (SEM), atomic force microscopy (AFM), transmission electron microscopy (TEM/HRTEM), Raman spectroscopy *etc.* Brief discussions of some of these techniques relevant to this thesis are given below.

#### X-ray photoelectron spectroscopy (XPS)

This technique is used to understand changes in the electronic structure of a cluster due to the presence of a substrate. Electronic properties of gas phase clusters are very sensitive to the number of atoms. Presence of a surface may significantly influence the electronic structure of the cluster. When these two are brought in contact, depending on the strength of cluster-surface interaction, the highest occupied level in cluster will adjust to the Fermi level of the substrate. This may also induce a charge accumulation at the cluster-surface interface [57]. The other cluster levels (valence as well as core) may also change compared to those in the gas phase. The shift in core-level binding energy in comparison to the bulk value is known as core-level shift. Since core-level shift depends on the bonding environment, using this one can obtain information about the nature of the cluster-surface interaction.

In XPS, a material is irradiated with a beam of X-rays. In this process, a photon is absorbed by an atom in the material, leading to the emission of a core electron. The kinetic energy distribution of thus emitted photoelectrons is measured. Since the energy of an incident X-ray ( $h\nu$ ) is known, one can calculate binding energy (BE) of the emitted electron as

$$E_b = h\nu - E_{kinetic} - \Phi, \quad (1.3)$$

where  $E_b$  is the binding energy (BE) of the emitted electron,  $E_{kinetic}$  is the kinetic energy of the emitted electron and  $\Phi$  is the work function which has to be overcome by

the electron reaching the vacuum.

The binding energy of an electron is equal to the energy difference between the initial (with  $n$  electrons) and final states (with  $(n - 1)$  electrons) of the atom.

$$E_b = E_f(n - 1) - E_i(n), \quad (1.4)$$

where  $E_f(n-1)$  is the energy of the final state and  $E_i(n)$  is the energy of the initial state. The final state is one in which  $(n - 1)$  electrons have “relaxed” after the emission of the core electron. In absence of relaxation of these electrons, the binding energy would be exactly equal to the negative of the orbital energy ( $\epsilon_k$ ) from which the photoelectron is emitted. This approximation is known as Koopmans' theorem.

$$E_b = -\epsilon_k. \quad (1.5)$$

However in absence of relaxation of the  $(n - 1)$  electronic states the atom is not in its ground state. The removal of a photoelectron creates a hole in the atom. The remaining electrons can relax to screen the hole, and thereby lower the energy of the final state. Hence binding energy of an electron depends on both the initial and final state effects. The initial state effects are caused by chemical bonding, which influences the electronic configuration in and around the atom. On the other hand, the relaxation processes (final state effects) are similar in magnitude in all the cases and does not depend on chemical environment. Thus core-level shifts are usually thought of initial state effects. However, this is true only up to an approximation. In general core-level shift depends on both initial and final state effects.

The core-level energy shifts are closely related to the charge transfer in the outermost electronic orbitals of the atoms. The charge redistribution of the valence electrons induces shifts in the binding energies of the core-electrons. Thus the information about the valence (oxidation state) of the atoms can be obtained through the core-level shifts. The loss of electrons in the valance orbitals causes an increase in binding energies of the core electrons, which leads to a positive shift in the core-levels. On the other hand, an excess of electron charge in the valance orbitals causes a decrease in the binding energies of core electrons and leads to the negative core level shifts.

### **Scanning tunneling microscopy (STM)**

Scanning tunneling microscopy is a technique for producing surface images with atomic scale resolution. In this method a fine probe tip scans the surface with clusters, measuring the tunneling current at constant voltage (constant voltage imaging mode) as a function of its position. The principle of STM is based on the phenomenon of quantum tunneling. When a conducting tip is brought very near to a metallic or semi-conducting surface, a bias between the two can allow electrons to tunnel through the vacuum between them. The STM images represent the convolution of the density of the occupied surface and unoccupied tip states, or the other way round, depending on the bias direction. Since the density of states is correlated with the positions of the nuclei, the STM images are correlated with the position of the atoms. More details about the technique can be found in Ref. [59].

### **Scanning electron microscopy (SEM)**

The scanning electron microscope is a technique that images the sample surface supporting clusters by scanning it with a focused beam of electrons. In this method, electrons interact with atoms of the sample and produce various signals in the form of secondary electrons, back scattered electrons and characteristic X-rays. These signals contain information about the sample's surface topography, composition, etc. More details about this method can be found in Ref. [59].

## **1.4.2 Production of substrate supported clusters by atomic vapor deposition**

In this method, the material, whose clusters are to be produced, is vaporized by thermal evaporation. The atomic vapor is deposited onto the substrate with thermal energy ( $\sim 0.1$  eV) and flux under Ultra High Vacuum (UHV) condition. The flux is expressed in units of monolayer (ML) per second, where 1 ML is defined as a single continuous layer or film that is one unit cell in thickness. The deposited flux of atoms undergoes elementary growth processes before condensing into the stable clusters. The elementary growth processes includes nucleation, diffusion, aggregation, and evaporation of the atoms.

The terrace of a substrate has periodic lattice sites (adsorption wells), separated by energy barriers. It can also have some defects such as vacancy, step edge or dislocation. The adatoms can arrive on the terrace at different random positions. Some adatoms can bind to the surface defect sites, some can evaporate from the surface, and rest can diffuse on the terrace, of the substrate. Among all the elementary growth processes, the diffusion of adatoms is most fundamental. The diffusion processes are thermally activated jumps mostly in form of straight adatom movements between adjacent lattice sites. However, concerted movements of several atoms may also be involved. Transition state theory (TST), assumes that the adatom stay in their adsorption wells large enough to thermally equilibrate. When they have sufficient thermal energy to overcome the energy barriers between the neighboring lattice sites, they perform the thermally activated jumps. This assumption is justified if the energy barrier between the lattice sites satisfies  $E \ll k_B T$ . Diffusion along the terrace ends when the adatoms collide with other adatoms or get trapped at the defect sites. During collisions adatoms may also undergo aggregation and form bonds to aggregate as clusters. Aggregation is the process in which diffusing adatoms assemble together to form clusters. Depending on the bond energy and the number of neighbors, thus formed clusters can remain stable or decay again as adatoms. This process gives rise to another process known as nucleation. If the formed cluster is large enough to grow more rapidly than it decays on the time-scale of deposition, the process is known as nucleation. Thus nucleation is the series of atomic processes in which the adatoms condense as stable clusters. This is the first irreversible step towards the formation of new phase (cluster) on the terrace.

A stable cluster is also known as the nucleus for the growth processes. The attachment of one adatom to the critical size above which cluster remains stable, results into a stable nucleus. The critical cluster size can be defined as  $(i_c - 1)$ , where  $i_c$  is the number of atoms in the smallest stable cluster. More details about the methods and different elementary processes can be found in the Ref. [57].

### 1.4.3 Deposition of preformed clusters

A major limitation with atomic deposition is that one does not have any control over the size and shape of the clusters. A more controlled way of fabricating substrate supported clusters is to deposit preformed clusters on a substrate. Hence by selecting the

size of the incident clusters, one can change the growth mechanisms [60, 61] and characteristics of the materials. For example, it has been shown that by changing the mean size of incident carbon clusters, one can modify the properties of carbon film, from graphitic to diamondlike [62].

By depositing preformed clusters on a substrate, one can build nanostructures of two types: (1) Separated clusters or islands in submonolayer range. (2) Thin films or cluster-assembled materials (CAM) (few monolayers). One would like to grow organized arrays of low coordinated clusters with specific electronic and catalytic properties as they can have potential use in many applications. The second subfield is that of nanostructured materials as thin or thick films, which show mechanical, catalytic, and magnetic properties different from their crystalline counterparts [63--65].

The morphology of the deposited clusters depends on a number of factors including the cluster and substrate materials, temperature, size of the cluster, cohesive energies, and kinetic energies of the cluster. All these factors strongly influence the outcome of the complex cluster-substrate collision process [57, 66]. Broadly, collision process can be classified in to three regimes based on the impact energy of the incident clusters.

- *Low energy depositions:* An interaction is considered to be low energy when the kinetic energy per atom ( $E_{at}$ ) of the incoming cluster is smaller than the binding energy per atom ( $E_{coh}$ ). Typical limits for this deposition are around  $E_{at} \approx 0.1$  eV. In this case, deposited clusters retain the memory of the gas-phase properties and cluster deformations induced by collisions are elastic.
- *Medium energy depositions:* If  $E_{at}$  is comparable to  $E_{coh}$ , clusters may undergo plastic deformations. Generally, in this regime  $E_{at}$  can have the values between 1-10 eV. The deposition of clusters may also induce defects in the surface.
- *High energy depositions:* If  $E_{at}$  is higher than  $E_{coh}$ , the impact is considered to be high energy. Typically, in this regime  $E_{at}$  has a lower bound of 10 eV. At such high energies, the incoming cluster decomposes upon impact. Part of the cluster is implanted in the surface resulting in an intermixing of the cluster and the surface.

The films made by clusters in different energy regimes can be easily identified. Low-energy deposition produces an amorphous and easily removable film. At medium

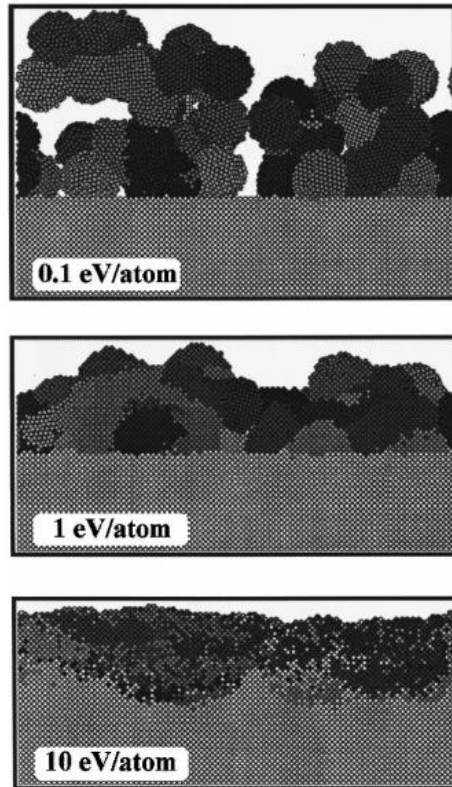


Figure 1.3: Molecular-dynamics simulations of the morphology of films obtained by deposition of Mo<sub>1043</sub> clusters with increasing incident kinetic energies per atom onto a Mo(001) substrate [67].

energies, the film adheres more strongly to the substrate, while high-energy deposition gives a hard shiny metallic coating. These processes have been studied theoretically using molecular dynamics (MD) simulations by Haberland *et al.*, [67]. Mo<sub>1043</sub> clusters were deposited on the Mo(001) surface at different impact energies. The resulting film morphologies are reproduced from Ref. [67] in Fig. 1.3. At low impact energies, clusters may suffer little distortion, but overall they retain their gas phase properties. There is no damage to the surface. Clusters tend to pile up on the substrate, which leave large cavities in the film. Thus film consists a highly porous arrays of randomly stacked particles. At medium energies, individual clusters can be identified but they are deformed from their gas phase structures. This deposition will also induced some defects on the terrace. At high impact energies, clusters are completely fragmented and lose their identity. The film is smooth due to the flattening of the cluster. A fraction of

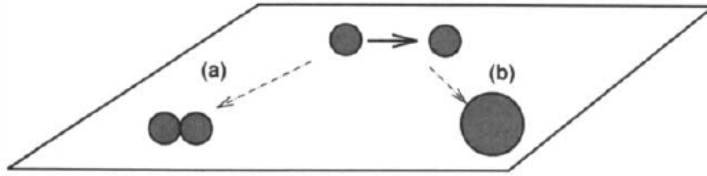


Figure 1.4: Possible elementary growth processes for two clusters meeting on a surface (a) aggregation (b) coalescence. For atomic deposition, only process (a) is possible [66]. Black circles represent atomic clusters.

the cluster intermix with surface layers and this implantation runs several layers deep.

Clusters also undergo various elementary growth processes after deposition over the surface. Similar to the atomic deposition, they may nucleate, diffuse, aggregate and evaporate on the terrace of the substrate. In addition, clusters can also merge to form another larger cluster during the diffusion, which was not possible in the atomic deposition. This process is known as coalescence of the clusters. A schematic diagram of aggregation and coalescence is shown in Fig. 1.4. So when two clusters meet at the surface by diffusion, they may either aggregate or coalesce. The choice between two type of interaction depends on several factors such as cluster size, temperature, cluster and substrate materials *etc.* One can also define a critical size  $N_c$  such that if two clusters of size  $N > N_c$  collide with each other, they will not merge to form a larger clusters and aggregate with each other. On the other hand if size of one of the cluster is smaller than  $N_c$ , they will coalesce into a single cluster. The critical size depends on the bonding strength of the cluster atoms. For more details we refer to Ref. [66, 68].

#### 1.4.4 Softlanding

The field of softlanding is driven by the idea to preserve the unique properties of pre-formed size-selected clusters and stabilize them on the surface. A straightforward criterion for softlanding would be that the cluster should be adsorbed on the surface without any collision-induced deformations and implantation. The process strongly depends on cluster size and material, as well as the substrate properties like surface energy, hardness, corrugation, polarizability, and temperature [69]. Softlanding of the small clusters on the surfaces which have large cluster-substrate interactions, is not possible. When a cluster arrives at the surface, it gets accelerated due to the attractive cluster-

substrate interaction. Its translational energy is transformed into internal energy and both the surface and the cluster get heated. In case of small clusters, this internal energy leads to atomic rearrangement and implantation. For example, MD simulations of  $\text{Ag}_7$  and  $\text{Ag}_{19}$  clusters, which were deposited on Pd (100) and Pd (111) surface with almost zero impact energy [70], reveal partial implantation and atom exchange. Hence softlanding does not necessarily preserve the properties of the small gas phase clusters on those surfaces which have large cluster-substrate interactions. However for larger clusters with several hundreds of atoms, the structural deformation and implantation become less important. For large clusters (at low energy depositions) the energy available to each atom is small. Thus it is impossible for the cluster to undergo the atom exchanges required for the implantation. A pronounced atomic rearrangement but no significant atom exchange has been found for  $\text{Cu}_N$  and  $\text{Au}_N$  up to  $N = 55$ , deposited on Pd(100) at negligible kinetic energy [71].

Softlanding is much more simple in case of inert surfaces. Due to the smaller cluster-surface interaction, small clusters do not gain translational energy. Hence, when deposited at low impact energies, small as well as larger clusters retain their gas phase identity after deposition. Honea *et al.*, [72] compared the Raman spectra of the mass selected small silicon clusters (size 4, 6 and 7) deposited over solid  $\text{N}_2$  with those with gas phase case. Raman spectroscopy gives the information about the geometry of the cluster. They find that geometry of the deposited clusters is same as in the gas phase. In other studies, Busolt *et al.*, [13, 73] measured the spectra of small silver clusters deposited over graphite for the two photon photoelectron processes. They found a strong dependence of the spectra on cluster size which indicates that their gas phase identities are retained and the deposition is achieved without fragmentation.

Another way to achieve softlanding of clusters is to dissipate the impact energy in a controlled manner prior to deposition over the substrate. This can be achieved by using a buffer layer consisting films of rare gases above the substrate. This method extends the kinetic energy range for the softlanding process. For example MD simulations have shown that small  $(\text{NaCl})_N$  can be softlanded on the substrate using a rare-gas (Ne, Ar) buffer layer at a kinetic energy of 2.72 eV per atom [74]. Also  $\text{Ag}_7$  clusters do not suffer any fragmentation when deposited on Pt (111) surface covered with a thick layer of Argon at a kinetic energy of 2.9 eV per atom [75]. Instead of rare-gases one may also use other inert molecules such as  $\text{C}_{60}$  as the buffer layer [76].

### 1.4.5 Cluster assembled films

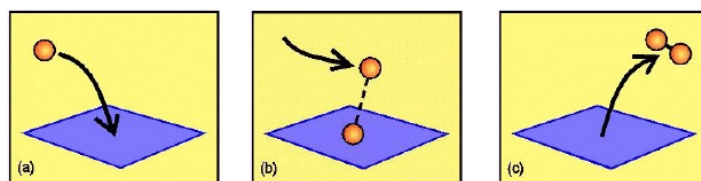
By depositing clusters using the softlanding or low energy cluster beam deposition (LECBD) technique, one can obtain the cluster assembled films. The morphologies of the cluster assembled films will be determined by the strength of the cluster-substrate interactions [77]. If the cluster-substrate interactions are large, the diffusion of the clusters will be limited and the growth will be organized as random paving of the individual clusters. If the cluster-substrate interaction is weak, the diffusion will be large and cluster will prefer to form large ramified islands on the surface. Depending on the deposition conditions (cluster and substrate material, cluster size, flux, temperature *etc.*), the diffusion and coalescence of the supported clusters leads to growth of granular thin film. The grain size for the coalescence of the clusters is limited by a critical size ( $N_c$ ).

One can also form the cluster assembled films by depositing the TM clusters ( $\text{Fe}_N$ ,  $\text{Ni}_N$ ,  $\text{Co}_N$  *etc.*) using LECBD technique [78--80]. It has been found that for TM clusters, only the random paving type of growth is possible. This is true for a wide range of substrates including graphite, organic materials and various other metals. Hence it is reasonable to assume that cluster assembled magnetic films produced by depositing TM clusters always grow from random paving of individual clusters. At finite thickness of the film, TM clusters will undergo various growth process (diffusion, coalescence, *etc.*) and organize as highly porous and granular thin film. The characteristic magnetic behavior of these films are determined by the competition between the grain anisotropy and the exchange interactions between grains. For the deposition of cluster of average size  $\text{Fe}_{150}$ ,  $\text{Co}_{300}$ ,  $\text{Ni}_{300}$  at 300K [78, 80], the mean size of the supported grains are found to be 5 nm, 3 nm, and 4 nm respectively. It has been found that for Fe clusters, the grains crystallize in a BCC structure, while for Co and Ni, grains crystallize in the FCC structures. Such magnetic films have enormous applications in the high density memory devices and spintornics.

## 1.5 Heterogeneous catalysis

Catalysis by small clusters is one of the most active fields of chemical sciences. The presence of a large number of low-coordination sites such as corners and edges in the

(1) Eley-Rideal Mechanism



(2) Langmuir-Hinshelwood Mechanism

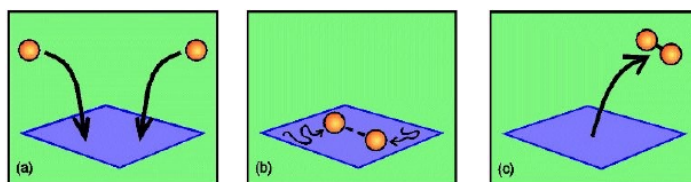


Figure 1.5: A schematic diagram for Eley-Rideal mechanisms and Langmuir-Hinshelwood, reproduced from Ref. [83].

clusters make them highly reactive and efficient catalysts. In particular, substrate supported metal clusters play a very important role in heterogeneous catalysis and chemical industries. The role of any catalyst is to lower the activation energy barrier of the rate limiting step to carry out a chemical reaction. This accelerates the process and enables the reaction to proceed at lower temperatures. The choice and preparation of substrate must be tailored to the type of the reactants and the desired reaction. Substrate may itself be directly involved in the catalytic process. Migration of reactants from the substrate to the cluster may also favor the formation of a desired compound with novel properties. These materials have wide applications in battery technology, ultra-capacitors, fuel cells, and environmental chemistry. Due to this reason a lot of effort is devoted to the understanding of this phenomena and creating tailor-made catalysts with high efficiency and desired selectivity [81].

The reactivity of these catalysts depends upon various factors, some of which are discussed below.

- **Size:** The catalytic reactivity of the clusters strongly depends on the number of atoms in the cluster. In the nonmonotonic regimes, where cluster size are small, each atom is important for the catalytic behavior of the cluster. The chemical and physical properties of the clusters often change dramatically by the addition

or removal of a single atom. For example, the reactivity of  $\text{Fe}_N$  clusters with  $\text{H}_2$  shows a dramatic dependence on cluster size [82]. The reactivity of  $\text{H}_2$  is negligible for Fe cluster of size  $N < 5$ . It increases and stabilizes between size  $5 < N < 15$ , shows a drop between  $15 < N < 23$  and reaches maximum for  $\text{Fe}_{23}$ . Above  $\text{Fe}_{23}$  there are no further large variations in reactivity. Thus the reactivity of  $\text{H}_2$  for Fe clusters is maximum for size 23.

- **Charge state:** The charge state of the clusters can considerably influence their catalytic reactivity [84--87]. For example, it has been found that  $\text{Au}_N^-$  clusters can readily adsorb the  $\text{O}_2$  molecule and activate the O-O bond for further oxidation reaction [84, 85]. On the other hand, positively charged  $\text{Au}_N^+$  clusters have strong binding with the CO molecule [86] and other hydrocarbons [88], but not with  $\text{O}_2$ .
- **Composition:** The catalytic reactivity of a cluster can also be modified by changing its composition. By changing constituents of a cluster atom by atom, the activity, selectivity and stability of the catalyst can be tuned to a maximum for a specific reaction. For example, in the production of hydrogen, water react with methane at high temperature to produce  $\text{CO}_2$  and  $\text{H}_2$  in the presence of Ni catalyst [89]. However, under the desired reaction conditions, a graphitic carbon may also form, which can block the Ni catalysts and decrease its efficiency. It has been found that addition of slight amounts of gold to the catalyst increases its resistance toward carbon formation. The gold segregates at the surface of the catalyst mainly on the weakly coordinated sites, and reduces the formation of graphitic carbon which is responsible for deactivation of the catalyst [90].
- **Cluster-substrate interaction:** The cluster-substrate interaction can influence the electronic and structural properties of the supported clusters which can modify their catalytic reactivity. An epitaxial stress at the cluster-substrate interface may change the structure of the clusters and they can acquire different equilibrium shapes compare to those in the gas phase. The strength of cluster-substrate interaction will depend on the cluster and substrate materials. Depending on this strength, there can be a charge transfer to or from the substrate. Hence clusters can either have an excess or a deficit of electrons, which will decrease their tendency to accept or donate electrons, respectively [87]. These effects will be more prominent for small clusters.

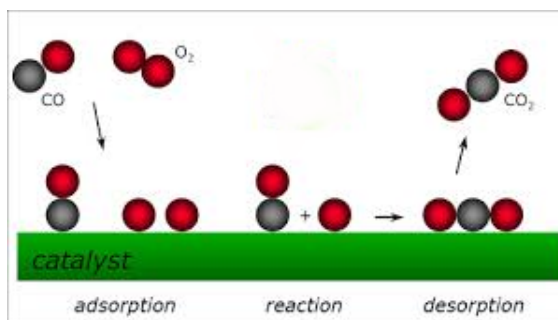
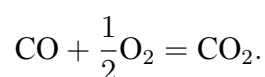


Figure 1.6: A schematic diagram for CO-oxidation by L-H mechanism, reproduced from Ref. [91]

There are many types of catalytic reactions and various reaction mechanisms. For bimolecular reactions, there can be two ways in which a reaction can proceed, which are schematically shown in Fig. 1.5. (1) Eley-Rideal (E-R) mechanism, in which only one of the reactants adsorbed on the catalyst and other molecule reacts directly from the gas phase. (2) Langmuir-Hinshelwood (L-H) mechanism, in which both the reactants are chemisorbed on the catalyst and the reaction takes place through the adsorbed species. This is the most common mechanism. For best possible conditions, the reactants must be adsorbed strongly enough to be activated, but not too strongly, because then they would be too stable to react with each other. Desorption of the product would be easier if the product is weakly bonded to the surface.

Let us consider the example of oxidation of carbon monoxide through L-H mechanism,



This is the very important reaction for eliminating CO from the environment. It is extremely exothermic and catalyzed by transition metals such as Rh, Pd, and Pt, but also by Au in the form of nanoparticles supported on certain oxides. Oxidation of carbon monoxide requires coadsorption of both the reactants on the catalyst. A schematic diagram is shown in Fig. 1.6. The CO molecule undergoes associative chemisorption, while O<sub>2</sub> molecule undergoes activated (with elongated O-O bond) or dissociative (bond breaking) chemisorption. These adsorbates diffuse on the catalyst towards each other until they meet and react to form CO<sub>2</sub>. Then the CO<sub>2</sub> molecule desorb from the catalyst surface and complete the reaction cycle.

The main aim of catalysis community is to find a catalyst for CO-oxidation which can activate O<sub>2</sub> molecule by elongating O-O bond length. The metals such as Pt, Pd, Rh, and Au are good catalysts but are very expensive. Many groups are trying to minimize the cost by replacing or alloying them with other metals and trying to understand the underlying mechanisms to lower the reaction barriers.

## 1.6 Purpose and structure of the thesis

Motivated by the interesting concepts and enormous applications of supported clusters, the major part of my thesis is devoted to determine and understand the morphologies of the substrate supported clusters. Particularly we are interested in the small metal clusters deposited over inert surfaces. As discussed above clusters can be easily soft-landed on the inert surface. For comparisons, we also used relatively reactive surfaces such as alumina surface to understand the change in behavior of the supported clusters. In this thesis we will determine the electronic and structural changes in the clusters after deposition on the surfaces. We will analyze the electronic, magnetic, and catalytic properties of the substrate supported clusters and discuss their potential use in various applications. The plan of my thesis is as follows.

**Chapter 2** is devoted to the methods and techniques used to perform the simulations in this thesis. The basic theoretical framework is DFT, which allows to solve the many-particle problem through independent electron approximation. Next we have discussed the techniques for solving the Kohn-Sham equations using plane-wave basis sets, and construction of PAW potentials. An overview of *ab-initio* molecular dynamics simulations, Bader charge analysis, and climbing image nudged elastic band methods are also discussed. A brief summary of the optimization of gas phase clusters and surface supported clusters are also discussed. In the end, we have discussed the methods that incorporate the dispersion interactions within the DFT framework.

**Chapter 3** includes our results on preformed Ag<sub>n</sub> clusters ( $n = 1 - 8$ ) deposited over clean graphite substrates using the vdW-DF2 method. We begin with the experimental motivations and discuss the previous theoretical efforts. In our simulations, we find that except for Ag<sub>3</sub>, all clusters prefer to stay parallel to the surface over top sites of graphite. For adatoms our results agrees with the experimental observations. Since experiments are performed at finite temperature, few high energy isomers may

also compete in the energetics and structures of the deposited clusters. Hence, few high energy isomers and their structures has also been discussed. Our study reveals that the results obtained with the vdW-DF2 method are in the best agreement with the experimental observations. In the end we present a comparison of these results with those from the widely used LSDA and DFT-D2 methods.

**Chapter 4** describes the morphologies and diffusion of small  $\text{Ag}_n$  ( $n = 1, 8$ ) clusters at the arm-chair step edge of graphite. In the beginning, we discuss the experimental motivations which indicate that clusters near step edges have reduced mobility in comparison to those on terraces. Then we present the ground state structures of silver clusters on step edge at zero temperature obtained in our simulations. We also discuss the diffusion of  $\text{Ag}_5$  and  $\text{Ag}_8$  clusters at 600 K, and their structures, after they are annealed below room temperature. In the end, we draw our conclusions and propose a way of fabricating self-assembled atomically thin silver nano-wires at the step edges.

**Chapter 5** discusses the substrate supported magnetic superatom using DFT calculations. The results for adsorption of the magnetic superatom  $\text{FeCa}_8$  on different types of substrates are discussed in detail. We find that both  $\alpha\text{-Al}_2\text{O}_3(0001)$  and  $\text{Ca}(001)$  substrates have a strong interaction with the superatom (chemisorption). On the other hand,  $\text{FeCa}_8$  has a weak interaction with h-BN and graphene, and retains its structure after deposition (physisorption). Towards the end, we describe the behavior of two  $\text{FeCa}_8$  units over h-BN and graphene sheet and discuss the exchange interactions between them. We have also estimated the minimum cluster density necessary to fabricate cluster assembled films over h-BN.

**Chapter 6** discusses the reactivity of  $\text{Ag}_n\text{Au}_m$  ( $n + m = 2 - 4$ ) clusters supported over the  $\alpha\text{-Al}_2\text{O}_3(0001)$  substrate towards CO-oxidation. We start with the experimental and theoretical motivations and discuss why the bimetallic AgAu clusters are considered as better candidates for CO-oxidation in comparison to pure Au clusters. Then we describe the ground state structures for gas phase  $\text{Ag}_n\text{Au}_m$  ( $n + m = 2 - 4$ ) clusters and discuss the results for adsorption and coadsorption of CO and  $\text{O}_2$  molecules on these clusters. Next we discuss the role of the alumina surface in the CO-oxidations on these clusters. For that we first determine the ground state structures of supported  $\text{Ag}_n\text{Au}_m$  clusters and perform the adsorption and coadsorption of CO and  $\text{O}_2$  molecule over the supported clusters. We end the chapter with our conclusions.

# Theoretical methods

## 2.1 Introduction

Materials are made of atoms, which in turn are made of electrons and nuclei. Nuclei are massive compared to the electrons, and can be described using classical mechanics (except for hydrogen and helium), while the motion of electrons is governed by quantum mechanics. Therefore, all the electronic, magnetic and chemical properties of the materials can be understood in terms of the complex behavior of the electrons. The study of behavior of electrons in materials started in the early 19<sup>th</sup> century, when Drude (1900) and Lorentz (1909) attempted to understand the conduction of electrons in metals. They assumed that metals contain free electrons that move in a uniform positive background provided by the ions and explained the electrical conductivity in metals. Unfortunately, their theory could not explain the other properties of the metallic systems. There was no big progress until the establishment of quantum mechanics in the 1920s. In the 1930s, band theory for independent electrons was formed, which classified the materials into insulators, semiconductors, and metals. Later several other methods were proposed for the treatment of electron-electron interaction such as Hartree-Fock method [92--94], Møller-Plesset perturbation theory, [95] and coupled cluster theory [96]. Rapid developments in electronic structure calculations were made after the formulation of density functional theory (DFT) in 1960s. Since then, the electronic structure calculations based on DFT have become more and more popular in condensed matter physics, quantum chemistry, and materials science. DFT is by far the most widely used approach for electronic structure calculations. It is usually called first principle method

because it allows one to calculate many properties of a system without any adjustable parameter. It has become a useful tool to understand the characteristic properties of materials and to make specific predictions of experimentally observable phenomena for real materials and to design new materials.

## 2.2 The many body problem and Born-Oppenheimer approximation

The description of a system with a set of atomic nuclei and electrons interacting via Coulombic electrostatic forces can be given in terms of many-body interacting Hamiltonian<sup>1</sup>:

$$\begin{aligned} \hat{H} = & - \sum_{I=1}^P \frac{1}{2M_I} \nabla_I^2 - \sum_{i=1}^N \frac{1}{2} \nabla_i^2 + \frac{1}{2} \sum_{I=1}^P \sum_{J \neq I}^P \frac{Z_I Z_J}{|\mathbf{R}_I - \mathbf{R}_J|} \\ & + \frac{1}{2} \sum_{i=1}^N \sum_{j \neq i}^N \frac{1}{|\mathbf{r}_i - \mathbf{r}_j|} - \sum_{I=1}^P \sum_{i=1}^N \frac{Z_I}{|\mathbf{R}_I - \mathbf{r}_i|}. \end{aligned} \quad (2.1)$$

Here  $\mathbf{R} = \{\mathbf{R}_I, I = 1, \dots, P\}$  is a set of  $P$  nuclear coordinates, and  $\mathbf{r} = \{\mathbf{r}_i, i = 1, \dots, N\}$  is a set of  $N$  electronic coordinates.  $Z_I$  and  $M_I$  are the nuclear charges and masses, respectively. The first and second terms represent the kinetic energy operators ( $\hat{T}_n$  and  $\hat{T}_e$ ) of the nuclei and electrons, the third and fourth terms represent the repulsive interactions ( $\hat{V}_{nn}$  and  $\hat{V}_{ee}$ ) of the nuclei and electrons respectively. The last term represents the attractive potential ( $\hat{V}_{ne}$ ) between the nuclei and electrons. In principle, the total energy of the system can be obtained by solving the Schrödinger equation.

$$\hat{H}\xi(\mathbf{R}, \mathbf{r}) = E_{tot}\xi(\mathbf{R}, \mathbf{r}), \quad (2.2)$$

where  $E_{tot}$  is the total energy and  $\xi(\mathbf{R}, \mathbf{r})$  is the many-body wave function of the electron-nuclei system. In principle Eq. (2.2) is the way to calculate energy of the system. However it is impossible to solve it exactly due to the presence of nucleus-nucleus and electron-electron interactions. One has to make approximations in order to progress. The first important approximation is the so-called Born-Oppenheimer ap-

---

<sup>1</sup>In atomic units:  $\hbar = m_e = e = 1$

proximation [97]. This assumes that the electronic motion and the nuclear motion in many-body systems can be separated. This idea arises from the fact that nuclei are  $10^2 - 10^5$  times heavier than the electrons (since  $M_I \gg m_e$ , where  $m_e$  is the mass of electron) and move much slower than the electrons. Hence electrons can be considered in their ground state with respect to the momentary positions of the nuclei at all the times. Thus the full Hamiltonian ( $\hat{H}$ ) in Eq. (2.1) can be split into two parts: a nuclear subsystem ( $\hat{H}_n$ ) and an electronic subsystem ( $\hat{H}_e$ ).

$$\hat{H}_n = \hat{T}_n + \hat{V}_{nn} \quad (2.3)$$

$$\hat{H}_e = \hat{T}_e + \hat{V}_{ne} + \hat{V}_{ee}. \quad (2.4)$$

The many body wave function  $\xi(\mathbf{R}, \mathbf{r})$  can be written as

$$\xi(\mathbf{R}, \mathbf{r}) = \sum_n \Theta_n(\mathbf{R}) \Psi_n(\{\mathbf{R}\}, \mathbf{r}), \quad (2.5)$$

where  $\Theta_n(\mathbf{R})$  are the nuclear wave functions and  $\Psi_n(\{\mathbf{R}\}, \mathbf{r})$  are the electronic wave functions that parametrically depend on the positions of the nuclei. Then the total energy of the system is equal to the sum of the nuclear energy ( $E_N$ ) and electronic energy ( $E$ ),  $E_{tot} = E_N + E$ . The electronic energy for a fixed nuclear configuration can be determined by solving the electronic Schrödinger equation,

$$\hat{H}_e \Psi(\mathbf{R}, \mathbf{r}) = E \Psi(\{\mathbf{R}\}, \mathbf{r}). \quad (2.6)$$

An exact solution of Eq. (2.6) is still impossible due to the many body nature of the electron-electron interactions, and requires further approximations. One fundamental approach to solve the electronic Schrödinger equation (Eq. (2.6)) is the Hartree-Fock approximation, which reduces the many-electron problem into one electron problem. It is a mean-field theory in which an electron moves in an average field generated by the other electrons. In this the  $N$ -electron wave function  $\Psi(\{\mathbf{R}\}, \mathbf{r})$  is approximated by a Slater-determinant of single particle wave functions, which ensures the antisymmetry of the many-body wave function upon particle exchange, and thereby includes the exchange effect in an exact manner. However, it ignores Coulomb correlations. In order to improve upon the Hartree-Fock approximation, other methods have been

proposed that account for correlation effects. These include the second or fourth order perturbation theory by Møller and Plesset (MP2 or MP4) [95], configuration interaction (CI), multiconfiguration self-consistent field (MCSCF), and coupled cluster approaches (CC) [97, 98]. These methods are quite accurate, but are computationally very expensive. DFT is an alternative to these wave function based methods, which replaces the complicated  $N$ -electron wave function and the associated Schrödinger equation by a formulation based on the electron density  $\rho(\mathbf{r})$  alone.

## 2.3 The Density functional theory

### 2.3.1 The Hohenberg-Kohn (HK) theorems

In 1964 Hohenberg and Kohn [99] developed an exact formal variational principle to determine the ground state energy of a many-electron system, where the electron density is chosen to be the basic variable. They gave two theorems that laid the foundation of the DFT.

**Theorem I:** *The external potential  $v(\mathbf{r})$  is uniquely determined by the ground state electron density  $\rho(\mathbf{r})$  within a trivial additive constant.* Thus the ground state density determines the full Hamiltonian, except for a constant shift of the energy. Hence all properties of the many-body electronic system such as its total energy, kinetic energy, and potential energy are also functionals of the ground state electron density  $\rho(\mathbf{r})$ .

**Theorem II:** *For a trial density  $\tilde{\rho}(\mathbf{r})$ , such that  $\tilde{\rho}(\mathbf{r}) \geq 0$  and  $\int \tilde{\rho}(\mathbf{r})d\mathbf{r} = N$ , the total energy functional  $E[\tilde{\rho}]$  has a lower bound equal to the ground state energy  $E[\rho(\mathbf{r})]$  of the system:*

$$E[\rho(\mathbf{r})] \leq E[\tilde{\rho}(\mathbf{r})], \quad (2.7)$$

where  $\rho(\mathbf{r})$  is the ground state electron density of the system.

Using the first theorem, the total energy functional for an electronic system at a certain external potential  $v(\mathbf{r})$  can be written as,

$$E_v[\rho] = T_e[\rho] + V_{ne}[\rho] + V_{ee}[\rho] = F_{HK}[\rho] + \int \rho(\mathbf{r})v(\mathbf{r})d\mathbf{r}, \quad (2.8)$$

where

$$F_{HK}[\rho] = T_e[\rho] + V_{ee}[\rho], \quad (2.9)$$

$F_{HK}$  is called the Hohenberg-Kohn functional. It is a universal functional of  $\rho(\mathbf{r})$  due to its independence on the external potential. It includes kinetic energy of the electrons  $T_e[\rho]$  and the interaction energy between the electrons  $V_{ee}[\rho]$ .

The second KS theorem provides a variational principle for  $E_v[\rho(\mathbf{r})]$  with  $\rho(\mathbf{r})$  as the basic variable. The minimization of the total energy functional  $E_v[\tilde{\rho}(\mathbf{r})]$  with respect to trial density  $\tilde{\rho}(\mathbf{r})$ , gives the ground state density  $\rho(\mathbf{r})$ , which in turn determines the ground state energy  $E[\rho(\mathbf{r})]$  of the system. Hence ground state density  $\rho(\mathbf{r})$  which minimizes  $E[\rho(\mathbf{r})]$  can be obtained via the stationary principle

$$\delta\{E_v[\rho] - \mu[\int \rho(\mathbf{r})d\mathbf{r} - N]\} = 0, \quad (2.10)$$

where  $\mu$  is the Lagrange multiplier for the constraint  $\int \rho(\mathbf{r})d\mathbf{r} = N$ . Eq. (2.10) gives the Euler-Lagrange equation,

$$\mu = \frac{\delta E_v[\rho]}{\delta \rho(\mathbf{r})} = v(\mathbf{r}) + \frac{\delta F_{HK}[\rho]}{\delta \rho(\mathbf{r})}, \quad (2.11)$$

where  $\mu$  is the chemical potential of the  $N$ -electron system.

### 2.3.2 The Kohn-Sham (KS) equations

In principle, if we knew the exact functional  $F_{HK}$ , Eq. (2.11) would provide an exact solution for the ground-state energy. Unfortunately, the exact form of  $F_{HK}$  is unknown, leaving the Hohenberg-Kohn theorems without much of practical relevance. In 1965, Kohn and Sham [100] gave an ansatz which state that the exact ground state density of an interacting system can be identified with the ground state density of a reference system of noninteracting particles. This maps the problem of the system of interacting electrons onto a reference system of non-interacting electrons and introduces a set of single particle equations known as Kohn-Sham equations. The ground state density

$\rho(\mathbf{r})$  of a non-interacting system can be written as

$$\rho(\mathbf{r}) = \sum_i^N |\psi_i(\mathbf{r})|^2, \quad (2.12)$$

where  $\psi_i(\mathbf{r})$  are one-electron orbitals known as Kohn-Sham orbitals. The Hamiltonian for non-interacting reference system with the same ground state density  $\rho(\mathbf{r})$  can be written as

$$\hat{H}_R = \sum_i^N \left[ -\frac{1}{2} \nabla_i^2 + v_{eff}(\mathbf{r}_i) \right]. \quad (2.13)$$

Here the effective potential  $v_{eff}(\mathbf{r})$  is such that the ground state density of  $\hat{H}_R$  is same as  $\rho(\mathbf{r})$ . Since  $\hat{H}_R$  is non-interacting, the ground state wave function  $\Psi_s(\mathbf{r})$  is a Slater determinant of the  $N$  lowest-energy eigenfunctions.

The kinetic energy  $T_s[\rho]$  of the reference system can be written as

$$T_s[\rho] = \langle \Psi_s | -\frac{1}{2} \sum_i^N \nabla_i^2 | \Psi_s \rangle = -\frac{1}{2} \sum_i^N \langle \psi_i | \nabla^2 | \psi_i \rangle. \quad (2.14)$$

The one-electron orbitals  $\psi_i(\mathbf{r})$  can be obtained by solving the one-electron Schrödinger equation

$$\left[ -\frac{1}{2} \nabla^2 + v_{eff}(\mathbf{r}) \right] \psi_i(\mathbf{r}) = \hat{H}_{KS} \psi_i(\mathbf{r}) = \epsilon_i \psi_i(\mathbf{r}), \quad (2.15)$$

where  $\hat{H}_{KS}$  is the one-electron Hamiltonian and  $\epsilon_i$  are the Kohn-Sham orbital energies. Hence an interacting system is transformed to a noninteracting system, where electrons move in an effective potential  $v_{eff}(\mathbf{r})$ . Using Eq. (2.14) and Eq. (2.9), the universal functional  $F_{HK}$  can be written as

$$F_{HK}[\rho] = T_s[\rho] + J[\rho] + E_{xc}[\rho], \quad (2.16)$$

where  $J[\rho]$  is classical Coulomb energy term, defined as,

$$J[\rho] = \frac{1}{2} \iint \frac{\rho(\mathbf{r})\rho(\mathbf{r}')}{|\mathbf{r} - \mathbf{r}'|} d\mathbf{r} d\mathbf{r}'. \quad (2.17)$$

$E_{xc}[\rho]$  is exchange-correlation energy, defined as,

$$E_{xc}[\rho] = (T_e[\rho] - T_s[\rho]) + (V_{ee}[\rho] - J[\rho]). \quad (2.18)$$

The exchange-correlation energy contains the kinetic correlations which are ignored in  $T_s[\rho]$ , and the non-classical part of the electron-electron interaction energy. By substituting Eq. (2.16) in the total energy functional (Eq. (2.8)), the Kohn-Sham energy functional is obtained as

$$E_{KS}[\rho] = \int \rho(\mathbf{r})v(\mathbf{r})d\mathbf{r} + T_s[\rho] + J[\rho] + E_{xc}[\rho]. \quad (2.19)$$

Now minimizing the Kohn-Sham energy functional  $E_{KS}[\rho]$  with respect to density  $\rho(\mathbf{r})$ , under the constraint  $\int \rho(\mathbf{r})d\mathbf{r} = N$ , we get the Euler-Lagrange equation as

$$\mu = v(\mathbf{r}) + \frac{\delta T_s[\rho]}{\delta \rho(\mathbf{r})} + \frac{\delta J[\rho]}{\delta \rho(\mathbf{r})} + \frac{\delta E_{xc}[\rho]}{\delta \rho(\mathbf{r})}. \quad (2.20)$$

Here  $\mu$  is the chemical potential of the reference system, which should coincide with the the chemical potential of the interacting system. Using equations (2.11) and (2.20), the KS effective potential can be defined as

$$\begin{aligned} v_{eff}(\mathbf{r}) &= v(\mathbf{r}) + \frac{\delta J[\rho]}{\delta \rho(\mathbf{r})} + \frac{\delta E_{xc}[\rho]}{\delta \rho(\mathbf{r})}, \\ &= v(\mathbf{r}) + \int \frac{\rho(\mathbf{r}')}{|\mathbf{r} - \mathbf{r}'|} d\mathbf{r}' + v_{xc}(\mathbf{r}), \end{aligned} \quad (2.21)$$

where the exchange-correlation potential  $v_{xc}(\mathbf{r})$  is defined as

$$v_{xc}(\mathbf{r}) = \frac{\delta E_{xc}[\rho]}{\delta \rho(\mathbf{r})}. \quad (2.22)$$

In the Kohn-sham formalism electrons move in an effective potential  $v_{eff}(\mathbf{r})$ , which depends on the classical Coulomb potential, exchange-correlation potential, and the external potential  $V_{ext}(\mathbf{r})$ . Since  $v_{eff}(\mathbf{r})$  depends on the density  $\rho(\mathbf{r})$  through the classical Coulomb potential and exchange-correlation potential  $v_{xc}(\mathbf{r})$ , which in turn depend on the  $\psi_i(\mathbf{r})$ , the solution of Eq. (2.15) and Eq. (2.12) can only be achieved by

self-consistency. To solve these equations, for a given nuclear configuration, we start with some trial charge density and calculate  $v_{eff}(\mathbf{r})$ . Then the Kohn-Sham equations are solved to get  $\psi_i$ 's, and the new charge density  $\rho(\mathbf{r})$  is obtained. The same process is repeated iteratively till the old and new charge densities are same or the change in energies obtained in two consecutive iterations is below a given tolerance.

If the exact forms of  $E_{xc}[\rho]$  were known, the Kohn-Sham solutions would lead to the exact ground state energy. The Kohn-Sham approach is thus in principle exact. The approximation only enters when we have to decide on an explicit form for the unknown functional for the exchange-correlation energy  $E_{xc}$ . The central goal of modern density-functional theory is therefore to find better and better approximations to the exchange-correlation energy.

## 2.4 The exchange-correlation functional

The simplest approximation for  $E_{xc}$  was introduced by Kohn and Sham and is known as the local density approximation (LDA) [100]. The basic idea of this approximation is to consider an electronic system having an inhomogeneous electron density to be composed of locally homogeneous regions, and express the exchange-correlation energy as

$$E_{xc}^{LDA}[\rho] = \int \rho(\mathbf{r}) \varepsilon_{xc}(\rho(\mathbf{r})) d\mathbf{r}, \quad (2.23)$$

where  $\varepsilon_{xc}(\rho(\mathbf{r}))$  denotes the exchange-correlation energy per particle of a homogeneous electron gas of density  $\rho(\mathbf{r})$ . The corresponding exchange-correlation potential becomes,

$$v_{xc}^{LDA}(\rho(\mathbf{r})) = \frac{\delta E_{xc}^{LDA}[\rho]}{\delta \rho(\mathbf{r})} = \varepsilon_{xc}[\rho(\mathbf{r})] + \rho(\mathbf{r}) \frac{\partial \varepsilon_{xc}^{LDA}[\rho]}{\partial \rho}. \quad (2.24)$$

Further,  $\varepsilon_{xc}(\rho(\mathbf{r}))$  can be divided into exchange and correlation contributions

$$\varepsilon_{xc}(\rho) = \varepsilon_x(\rho) + \varepsilon_c(\rho). \quad (2.25)$$

The exchange part can be calculated by the Hartree-Fock approximation for a homogeneous electron gas as given in Ashcroft and Mermin [101].

$$\varepsilon_x(\rho) = -\frac{3}{4}\left(\frac{3}{\pi}\right)^{1/3}\rho(\mathbf{r})^{1/3}. \quad (2.26)$$

The correlation part  $\varepsilon_c(\rho)$  cannot be expressed in such an explicit functional form. Only numerical values are known from the highly accurate quantum Monte Carlo calculations of Ceperly and Alder [102]. This has been fitted to analytical forms by Vosko, Wilk and Nusair [103] and Perdew and Zunger [104], which are used in most of the current electronic structure calculations.

The extension of LDA for spin-polarized systems with charge densities  $\rho_\uparrow(\mathbf{r})$  and  $\rho_\downarrow(\mathbf{r})$ , (for up and down spin electrons respectively) can be written as.

$$E_{xc}^{LSDA} = -\frac{3}{2}\left(\frac{3}{4\pi}\right)^{1/3} \int [\rho_\uparrow(\mathbf{r})^{4/3} + \rho_\downarrow(\mathbf{r})^{4/3}] d\mathbf{r} + \int \rho(\mathbf{r})\varepsilon_c(\rho_\uparrow(\mathbf{r}), \rho_\downarrow(\mathbf{r})) d\mathbf{r}. \quad (2.27)$$

This is called local spin density approximation (LSDA). Here  $\varepsilon_c(\rho_\uparrow(\mathbf{r}), \rho_\downarrow(\mathbf{r}))$  is the correlation energy per electron in a homogeneous electron gas.

From the above discussion, it seems that LDA should be a good approximation if the electron density  $\rho(\mathbf{r})$  is slowly varying. It works well for the metals. It produces good geometries for covalent, ionic, or metallic. However, it underestimates the band gaps in semiconductors and insulators. Also it fails to reproduce the properties of strongly correlated systems, particularly Mott insulators. Intense efforts have been devoted to improve upon LDA. A straightforward correction to the LDA is to construct an exchange-correlation functional based on electron density as well as its gradient. This approximation is known as generalized gradient approximation (GGA) [105, 106].

$$E_{xc}^{GGA}[\rho_\uparrow, \rho_\downarrow] = \int d\mathbf{r} \rho(\mathbf{r})\varepsilon_{xc}(\rho(\mathbf{r}))F_{xc}(\rho_\uparrow, \rho_\downarrow, |\nabla\rho_\uparrow|, |\nabla\rho_\downarrow|, \dots), \quad (2.28)$$

where  $F_{xc}$  is dimensionless and chosen by a pre-defined set of criteria. There are a large number of distinct GGA functionals depending on the form of the function  $F_{xc}$ . Two of the most widely used functionals in the literature are the Perdew-Wang functional (PW91) [107] and the Perdew-Burke-Ernzerhof functional (PBE) [108].

## 2.5 The Plane wave basis set

In practical applications, the KS orbitals are expanded in terms of some basis functions. For periodic systems, the widely used basis is a set of plane wave. The plane wave expansion of the Kohn-Sham orbitals can be written as follows [109]

$$\psi_i(\mathbf{r}) = \frac{1}{\sqrt{\Omega}} \sum_{\mathbf{q}} c_{i,\mathbf{q}} e^{i(\mathbf{q}\cdot\mathbf{r})}, \quad (2.29)$$

where  $\Omega$  is the volume of the crystal composed of  $N_{cell}$  primitive cells each of volume  $\Omega_{cell}$ . The  $c_{i,\mathbf{q}}$  are the expansion coefficients of the wave function in the basis of orthonormal plane wave, denoted by  $\phi_{\mathbf{q}}(\mathbf{r})$ , where  $\phi_{\mathbf{q}}(\mathbf{r}) = \langle \mathbf{r} | \mathbf{q} \rangle$  satisfy  $\langle \mathbf{q}' | \mathbf{q} \rangle = \delta_{\mathbf{q},\mathbf{q}'}$ . Now inserting this in Eq. (2.15), and taking inner product with  $|\mathbf{q}'\rangle$ ,

$$\sum_{\mathbf{q}} \langle \mathbf{q}' | \hat{H}_{eff} | \mathbf{q} \rangle c_{i,\mathbf{q}} = \epsilon_i \sum_{\mathbf{q}} \langle \mathbf{q}' | \mathbf{q} \rangle c_{i,\mathbf{q}} = \epsilon_i c_{i,\mathbf{q}'}. \quad (2.30)$$

The matrix element of the kinetic energy operator can be written as

$$\langle \mathbf{q}' | -\frac{1}{2} \nabla^2 | \mathbf{q} \rangle = \frac{1}{2} |\mathbf{q}'|^2 \delta_{\mathbf{q},\mathbf{q}'}. \quad (2.31)$$

The effective potential  $V_{eff}$  has the periodicity of the lattice and therefore can be expressed as a sum of the Fourier components.

$$V_{eff}(\mathbf{r}) = \sum_m V_{eff}(\mathbf{G}_m) \exp(i\mathbf{G}_m \cdot \mathbf{r}), \quad (2.32)$$

where  $\mathbf{G}_m$  are the reciprocal lattice vectors and  $V_{eff}(\mathbf{G}_m)$  are the Fourier components of  $V_{eff}(\mathbf{r})$ .

$$V_{eff}(\mathbf{G}) = \frac{1}{\Omega_{cell}} \int_{\Omega_{cell}} V_{eff}(\mathbf{r}) \exp(-i\mathbf{G} \cdot \mathbf{r}) d\mathbf{r}. \quad (2.33)$$

Thus the matrix element of the potential can be written as

$$\langle \mathbf{q}' | V_{eff} | \mathbf{q} \rangle = \sum_m V_{eff}(\mathbf{G}_m) \delta_{\mathbf{q}'-\mathbf{q},\mathbf{G}_m}. \quad (2.34)$$

The matrix elements of the  $V_{eff}$  are nonzero only if  $\mathbf{q}$  and  $\mathbf{q}'$  differ by a reciprocal lattice vector  $\mathbf{G}_m$ . Assuming  $\mathbf{q} = \mathbf{k} + \mathbf{G}_m$  and  $\mathbf{q}' = \mathbf{k} + \mathbf{G}_{m'}$  for any given  $\mathbf{k}$ , the Schrödinger-like equation is given by

$$\sum_m \langle \mathbf{k} + \mathbf{G}_{m'} | \hat{H}_{eff} | \mathbf{k} + \mathbf{G}_m \rangle c_{i,m}(\mathbf{k}) = \epsilon_i c_{i,m'}(\mathbf{k}), \quad (2.35)$$

$$\sum_m \left[ |\mathbf{k} + \mathbf{G}_m|^2 \delta_{m,m'} + V_{eff}(\mathbf{G}_m - \mathbf{G}_{m'}) \right] c_{i,m}(\mathbf{k}) = \epsilon_i(\mathbf{k}) c_{i,m'}(\mathbf{k}). \quad (2.36)$$

The above equation is the basic Schrödinger-like equation of a periodic crystal with a plane wave basis set. Eigenfunctions of the Eq. (2.35), for a given  $\mathbf{k}$  are given by Eq. (2.29), with the sum over  $\mathbf{q}$  restricted to  $\mathbf{q} = \mathbf{k} + \mathbf{G}_m$ . Hence

$$\begin{aligned} \psi_{i,\mathbf{k}}(\mathbf{r}) &= \frac{1}{\sqrt{\Omega}} \sum_m c_{i,m} \exp(i(\mathbf{k} + \mathbf{G}_m) \cdot \mathbf{r}), \\ &= \exp(i\mathbf{k} \cdot \mathbf{r}) \frac{1}{\sqrt{N_{cell}}} u_{i,\mathbf{k}}(\mathbf{r}), \end{aligned} \quad (2.37)$$

where

$$u_{i,\mathbf{k}}(\mathbf{r}) = \frac{1}{\sqrt{\Omega_{cell}}} \sum_m c_{i,m} \exp(i\mathbf{G}_m \cdot \mathbf{r}); \quad \Omega = N_{cell} \Omega_{cell}.$$

This is the Bloch's theorem, where  $u_{i,\mathbf{k}}(\mathbf{r})$  carries the periodicity of the crystal. Here for each  $\mathbf{k}$ , the allowed reciprocal vectors  $\mathbf{G}$  are infinite. Hence, in principle infinite number of plane waves are required to represent the wave functions with infinite accuracy. However, the coefficient  $c_{i,m}(\mathbf{k})$  for the plane waves with small kinetic energy are typically more important than those with large kinetic energy. Thus the plane wave basis set can be truncated to include only plane waves that have kinetic energies less than a particular energy cutoff  $E_{cut}$ ,

$$\frac{1}{2} |\mathbf{k} + \mathbf{G}|^2 \leq E_{cut}. \quad (2.38)$$

Employing a finite basis set may introduce some inaccuracies. Therefore, appropriate convergence tests have to be performed in order to find  $E_{cut}$  that is sufficiently large to compute the property of interest with required accuracy.

## 2.6 The pseudopotential theory

Most physical and chemical properties of crystals depend to a very good approximation only on the distribution of the valence electrons. The core electrons do not participate in chemical bonds and they are strongly localized around the nuclei. On the other hand, the deeply bound core electrons require a huge number of plane wave basis functions for their description which increases the computational cost. The pseudopotential approximation [110--112] allows the electronic wave functions to be expanded using a much smaller number of plane waves, by replacing the strong ionic potential with a weaker and screened pseudopotential. In this approach only the chemically active valence electrons are considered explicitly, while the inert core electrons are eliminated within the “frozen-core approximation”. All the electrostatic and quantum-mechanical interactions of the valence electrons with the cores, such as the nuclear Coulomb attraction screened by the core electrons, Pauli repulsion, and exchange and correlation between core and valence electrons, are accounted for by an angular momentum-dependent pseudopotential.

The concept of pseudopotentials is illustrated in Fig. 2.1(a), where true valence wave function  $\Psi$  is peaked far away from the nucleus (dashed curve). It has strong oscillations near the nucleus which ensure its orthogonality to the core states. The description of these nodes by plane wave demands high energy cutoffs. Since the true valence wave function  $\Psi$  within the core region does not contribute significantly to the bonding properties, it can be approximated by a smooth and nodeless “pseudo-wave function”  $\Psi_{ps}$ . The core region is defined by a cut-off radius  $r_c$  which includes all the nodes of the all-electron valence wave functions. Thus  $\Psi_{ps}$  is constructed in such a way that it matches with the true valence wave function outside the core radius and smoothens the strong oscillations inside the core radius.

The effective potential corresponding to this pseudo wave function  $\Psi_{ps}$  within the core region is called the pseudopotential  $V_{ps}$ . There are many schemes for construction of pseudopotentials proposed by various authors such as Troullier and Martins [113, 114], Kerker [115], Hamann, Schlüter, and Chiang [116], Vanderbilt [117], Goedecker-Teter-Hutter [118]. In general, pseudopotentials can be constructed in the following manner. (1) The eigenvalues of the pseudo-wave functions and true wave functions should be identical for a chosen electronic configuration of the atom. (2) Both

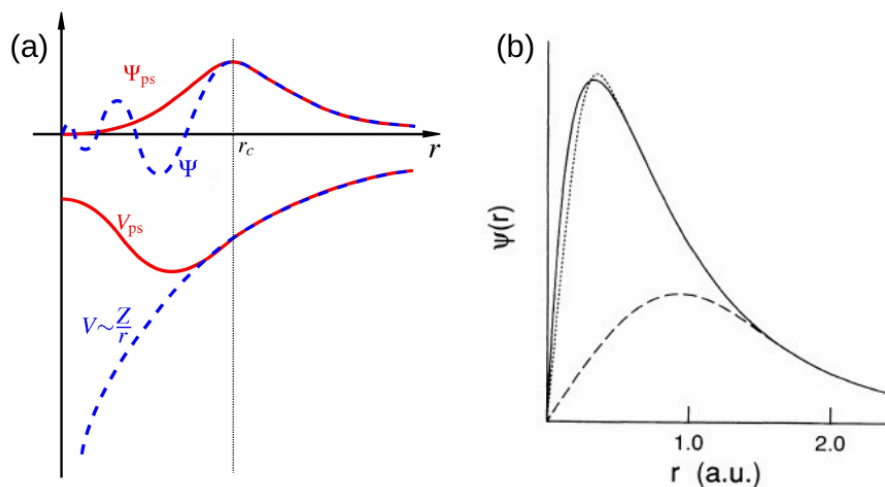


Figure 2.1: (a) Schematic diagram of all-electron (solid lines) and pseudoelectron (dashed lines) potentials and their corresponding wave functions. The radius at which all-electron and pseudoelectron values match is designated  $r_c$  (b) Oxygen  $2p$  radial wave function (solid line) and corresponding norm-conserving [116] (dotted line) and ultrasoft [117] (dashed line) pseudo wave functions. The figure is reproduced from Ref. [117]

wave functions should be identical outside a cutoff radius  $r_c$ . (3) The pseudo-wave function should be nodeless. (4) The logarithmic derivative of both the wave functions should agree at  $r_c$ . If the norm of the pseudo-wave function is equal to the norm of the all electron wave function within the core region, such pseudopotentials are called “norm-conserving” pseudopotentials. These are more accurate and have good transferability properties, *i.e.*, the pseudopotential constructed in one environment (usually the atom) can faithfully describe the valence properties in different chemical environments.

The main constraint with the norm-conserving pseudopotentials is that good transferability requires the core radius  $r_c$  to be just larger than the position of the outermost maximum of the true wave function, because only then the charge distribution of the true wave function is well reproduced by the pseudo wave function. For example,  $r_c$  is smaller for the  $2p$  state in comparison to the  $3p$  state, because for  $2p$  state there is no state of the same angular momentum to which it has to be orthogonal. Hence the pseudo wave function for  $2p$  state is similar to the all-electron wave function (Fig. 2.1(b)) as it has to match the charge of the the all-electron wave function inside the core radius. A  $2p$

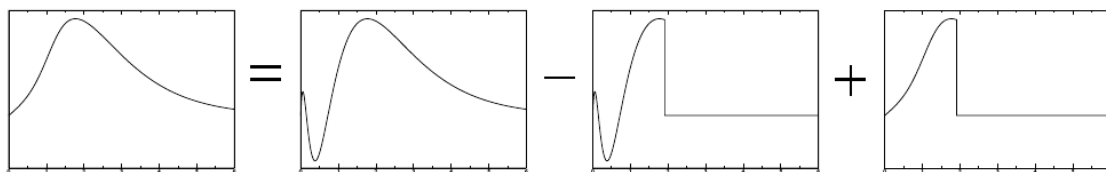


Figure 2.2: Schematic representation of the PAW transformation. The auxiliary wave function is constructed from the full wave function by subtracting the oscillatory part close to an atom and replacing it by a smooth function.

state is more strongly peaked near the core in comparison to the  $3p$  state. Consequently, the sharp peak of  $2p$  state requires a large number of plane waves to be represented accurately in comparison to the  $3p$  state. Same is true for  $d$  states of the second-row transition metals. Therefore, for elements with strongly localized orbitals such as transition metals and rare-earth elements, the resulting norm-conserving pseudopotentials have smaller value of the cut-off radius  $r_c$  and thus require large plane wave basis sets. This increases the required computational time and efforts. Vanderbilt [117, 119] showed that this problem can be solved by relaxing the norm-conservation condition. This greatly reduced the energy cutoff because a large value of cut-off radius  $r_c$  could be used. The pseudo wave function  $\Psi_{ps}$  can be made much softer within the core region. However this results in a charge deficit in the core region. To compensate for this deficit, augmentation charges which are defined as the charge density difference between true and pseudo-wave functions, are introduced in the core region. The core radius  $r_c$  can now be chosen quite large independently of the position of the maximum of the true wave function. Only for the augmentation charges, a small cutoff radius must be used to restore the charge distribution of the true wave function accurately. These pseudopotentials are called ultra-soft pseudopotentials.

### 2.6.1 Projector Augmented Wave method (PAW)

A major drawback of the pseudopotential method is that all information on the full wave function close to the nuclei is lost. This can influence the calculation of certain properties, such as hyperfine parameters, and electric field gradients at atomic nuclei produced by the charge outside the nucleus in a chemical environment.

In 1994 Blöchl [120] developed the PAW method, which in principle is a frozen-core all electron method. It combines the advantage and accuracy of all-electron methods with computationally less expensive pseudopotential methods. Its close connection to the ultra-soft pseudopotential was derived by Kresse and Joubert in 1999 [121]. The PAW method is based on the division of the whole space  $\Omega_w$  into distinct regions: a collection of non-overlapping spherical regions (the augmentation spheres) around each atom  $\Omega_a$  and the remainder, the interstitial region  $\Omega_1$ .

$$\Omega_w = \Omega_1 + \bigcup_a \Omega_a. \quad (2.39)$$

The plane wave basis sets, which are ideal for the interstitial region  $\Omega_1$ , are difficult to use for the description of wave function in the augmentation spheres. This problem can be circumvented by introducing auxiliary smooth wave functions  $\tilde{\Psi}_i(\mathbf{r})$  which can be obtained from the all-electron wave function  $\Psi_i(\mathbf{r})$  via an invertible linear transformation  $\mathcal{T}$ .

$$|\Psi_i\rangle = \mathcal{T} |\tilde{\Psi}_i\rangle, \quad (2.40)$$

where  $i$  is composite index for band,  $\mathbf{k}$ , and spin. This yields the transformed KS equations,

$$\hat{H}_{KS} |\Psi_i\rangle = \epsilon_i |\Psi_i\rangle \Rightarrow \hat{H}_{KS} \mathcal{T} |\tilde{\Psi}_i\rangle = \epsilon_i \mathcal{T} |\tilde{\Psi}_i\rangle. \quad (2.41)$$

$$\mathcal{T}^\dagger \hat{H}_{KS} \mathcal{T} |\tilde{\Psi}_i\rangle = \mathcal{T}^\dagger \mathcal{T} \epsilon_i |\tilde{\Psi}_i\rangle. \quad (2.42)$$

Auxiliary wave functions are obtained by solving Eq. (2.42) and then transforming them back to true wave function using Eq. (2.40). The operator  $\mathcal{T}$  modifies the smooth auxiliary wave function in each atomic region, so that the resulting all-electron wave functions have the correct nodal structures. The operator  $\mathcal{T}$  can be written as,

$$\mathcal{T} = 1 + \sum_a \mathcal{T}^a, \quad (2.43)$$

where  $\mathcal{T}^a$  is the transformation centered on atom  $a$  and has no effect outside a certain

atom specific augmentation region defined by  $|\mathbf{r} - \mathbf{R}^a| < r_c^a$ . Here  $\mathbf{R}^a$  specifies the position of atom  $a$ . Hence the auxiliary and all-electron wave functions are identical outside the augmentation spheres. The cutoff region of radius  $r_c^a$  should be chosen such that there are no overlaps between the augmentation spheres. Inside the augmentation spheres, the true wave function  $\Psi_{AE}^n$  can be expanded in terms of partial waves  $\phi_l^a$ . For each of these partial waves, we can define a corresponding auxiliary smooth partial wave  $\tilde{\phi}_l^a$ , and write,

$$|\phi_l^a\rangle = (1 + \mathcal{T}^a) |\tilde{\phi}_l^a\rangle. \quad (2.44)$$

$$\mathcal{T}^a |\tilde{\phi}_l^a\rangle = |\phi_l^a\rangle - |\tilde{\phi}_l^a\rangle. \quad (2.45)$$

Hence for every atom, the local operator  $\mathcal{T}^a$  adds the difference between the true and auxiliary partial wave functions. This is schematically shown in Fig. 2.2. Any physical quantity can be evaluated by calculating the expectation value of the operator in terms of either the true or auxiliary wave function.

$$\langle A \rangle = \sum_n f_n \langle \Psi_i | A | \Psi_i \rangle = \sum_n f_n \langle \tilde{\Psi}_i | \mathcal{T}^\dagger A \mathcal{T} | \tilde{\Psi}_i \rangle, \quad (2.46)$$

where  $f_n$  are the occupation number of the valence states.

Thus the PAW method is an all-electron method and not a traditional pseudopotential method. It uses information of full density and potential. The converged results of the PAW method do not depend on a reference system such as an isolated atom. There are no transferability errors and the high spin atoms can be described efficiently.

## 2.7 Geometry optimization

The main purpose of geometry optimization is to find the lowest energy structure of a system from an arbitrary starting geometry. Within Born-Oppenheimer approximation, the motion of the nuclei and the electrons can be separated, hence a geometry optimization is a two step process. (1) The electronic self consistent calculation for a given geometry, (2) the ionic relaxation of the nuclei according to the Hellmann-

Feynman theorem [122].

The Hellmann-Feynman force acting on the  $I^{th}$  atom can be written as

$$\mathbf{F}_I = -\frac{\partial E_{total}}{\partial \mathbf{R}_I} = -\left[\frac{\partial E_N}{\partial \mathbf{R}_I} + \frac{\partial E}{\partial \mathbf{R}_I}\right]. \quad (2.47)$$

$\mathbf{R}_I$ 's is the position of the  $I^{th}$  atom. The forces due the electrons  $\mathbf{F}_I^e$  on the  $I^{th}$  nuclei can be written as

$$\begin{aligned} \mathbf{F}_I^e &= -\frac{\partial}{\partial \mathbf{R}_I} \langle \Psi_s | \hat{H}_e | \Psi_s \rangle \\ &= -\left\langle \Psi_s \left| \frac{\partial \hat{H}_e}{\partial \mathbf{R}_I} \right| \Psi_s \right\rangle - \left\langle \frac{\partial \Psi_s}{\partial \mathbf{R}_I} \left| \hat{H}_e \right| \Psi_s \right\rangle - \left\langle \Psi_s \left| \hat{H}_e \right| \frac{\partial \Psi_s}{\partial \mathbf{R}_I} \right\rangle. \end{aligned} \quad (2.48)$$

Since  $\Psi_s$  is an eigenfunction of  $\hat{H}_e$ ,

$$\begin{aligned} \mathbf{F}_I^e &= -\left\langle \Psi_s \left| \frac{\partial \hat{H}_e}{\partial \mathbf{R}_I} \right| \Psi_s \right\rangle - E \left\langle \frac{\partial \Psi_s}{\partial \mathbf{R}_I} \left| \Psi_s \right\rangle - E \left\langle \Psi_s \left| \frac{\partial \Psi_s}{\partial \mathbf{R}_I} \right\rangle, \\ &= -\left\langle \Psi_s \left| \frac{\partial \hat{H}_e}{\partial \mathbf{R}_I} \right| \Psi_s \right\rangle - E \frac{\partial}{\partial \mathbf{R}_I} \langle \Psi_s | \Psi_s \rangle. \end{aligned} \quad (2.49)$$

However  $\Psi_s$  are normalized  $\langle \Psi_s | \Psi_s \rangle = 1$  and last term in the above Eq. (2.49) vanishes. Then total force on the  $I^{th}$  atom can be written as

$$\mathbf{F}_I = -\frac{\partial E_N}{\partial \mathbf{R}_I} - \left\langle \Psi_s \left| \frac{\partial \hat{H}_e}{\partial \mathbf{R}_I} \right| \Psi_s \right\rangle. \quad (2.50)$$

Hence the forces on the nuclei can be calculated using Eq. (2.50). Once the forces are known, one can use optimization techniques such as the steepest descent (SD) or conjugate gradient (CG) method to move the nuclei towards the local minimum. This will generate a new nuclear configuration and the same process (electronic self-consistent cycle) will be repeated to calculate the forces in the new nuclear configuration using Eq. (2.50). Based on the new forces, again the nuclei are moved to new positions. The process continues till the force on each atom is below a given threshold value. At the end of this process, the nuclei reach an equilibrium configuration which is a local minimum of their potential energy surface (PES)<sup>2</sup>.

<sup>2</sup>A potential energy surface describe the energy of system as a function of all nuclei configuration in a  $3P - 6$  dimensional space.

## Global minimization of gas phase clusters

An optimization technique described above gives only the nearest local minimum of the potential energy surface (PES). In order to obtain the global minimum of the PES one has to scan the whole PES and compare the energies of all the minima. However the task is non-trivial as the number of local minima increases exponentially with the number of atoms in the cluster. Hence one has to use a systematic search scheme to reduce unnecessary scan of higher energy local minima (poor sampling regions). One such technique is the evolutionary algorithm or genetic algorithm implemented in USPEX [123--126]. The fundamental idea of the algorithm is to start with a set of initial structures and evolve them using heredity and mutation operators. To have good initial guesses, usually the initial structures are generated by applying possible point group symmetries for a given size  $P$  of the cluster to randomly produced atomic coordinates. Later, these initial structures are relaxed to their nearest local minima using a local optimization technique (SD or CG) and energies of all the optimized structures are compared. Among the relaxed structures, a certain number worst (having high energy) structures are rejected. The remaining structures serve as parents in the creation of the next generation. The new generation is produced by applying the heredity, atomic permutation, soft-mutation, and mutation operators [124, 125]. Using heredity, new structures are produced by matching slices (chosen in random direction and with random positions) of the parent structures. A certain fraction of the new generation is created with mutation by randomly changing the positions of some atoms. In soft-mutation operator, atoms are moved along the eigenvectors of the softest normal mode of vibrations. These low frequency modes are associated with the low curvature of PES. The structures obtained by these variational operations are then optimized to their nearest local minima. Consequently, new structures are obtained which were separated by barriers on the PES. Certain number of best optimized structures of this generation serve as parents for the next generation. This cycle continues till the lowest energy structures of a pre-defined number of generations turn out to be the same. At the end of these cycles, the best structure we obtain is our calculated global minimum of the cluster of size  $P$ .

### Structure optimization of supported clusters: A random rotation technique

As discussed in section 1.4.4, in LECBD experiments, the clusters can land on the substrate randomly at all possible positions and in all possible orientations. To mimic this process we consider the special symmetry points on a given surface as the bonding sites, and consider many orientations of the cluster at each site. We assume an incoming cluster as a rigid body and place its center of mass (COM) at some height ( $h$ ) above the special symmetry points of the surface. The height  $h$  is usually taken as the sum of the covalent radii of the two adjacent surface and cluster atoms. Different orientations of the cluster are generated by rotating it around its COM using Euler angles. In LECBD experiments, clusters have small impact energies. Since the kinetic energy of an incoming cluster is small enough that it does not dissociate on its impact with the substrate, we take the simplified view that the cluster is stationary and relax its structure on the substrate. As the impact energy is small we assume that cluster land without any kinetic energy.

Let us suppose  $\mathbf{R}_I$  are the coordinates of the cluster atoms. The new rotated coordinates  $\mathbf{R}'_I$  can be achieved by,

$$\mathbf{R}'_I = \mathbf{A}\mathbf{R}_I \quad (2.51)$$

$$\mathbf{A} = \begin{bmatrix} \cos(\psi)\cos(\phi) - \cos(\theta)\sin(\phi)\sin(\psi) & \cos(\psi)\sin(\phi) + \cos(\theta)\cos(\phi)\sin(\psi) & \sin(\psi)\sin(\theta) \\ -\sin(\psi)\cos(\phi) - \cos(\theta)\sin(\phi)\cos(\psi) & -\sin(\psi)\sin(\phi) + \cos(\theta)\cos(\phi)\cos(\psi) & \cos(\psi)\sin(\theta) \\ \sin(\theta)\sin(\phi) & -\sin(\theta)\cos(\phi) & \cos(\theta) \end{bmatrix},$$

where  $\mathbf{A}$  is the matrix [127] which transforms the coordinates  $\mathbf{R}_I$  to new rotated coordinates  $\mathbf{R}'_I$ . The Euler angles  $(\phi, \theta, \psi)$  are the sequence of three elemental rotations about the axes of the coordinate system. First a cluster is rotated about the  $z$ -axis with an angle  $\phi$ , the second rotation is performed by an angle  $\theta$  about the intermediate  $x$ -axis (changed due to first rotation) and the last rotation is performed by an angle  $\psi$  about the new  $z$ -axis (changed due to last two rotation). The allowed values of  $\phi, \theta$  and  $\psi$  are  $[0, 2\pi]$ ,  $[0, \pi]$  and  $[0, 2\pi]$  respectively. We choose these angles from uniform random distributions between the allowed values. Each triplet  $(\phi, \theta, \psi)$  gives a particular orientation of the cluster. Each of these initial configurations is optimized to the nearest local minimum. By comparing the adsorption energies (defined later) of all the optimized configurations, we determine most preferred structure of the adsorbed cluster.

## 2.8 Molecular dynamics simulations

All the above methods are applicable to systems at zero temperature. But experiments are performed at finite temperatures where dynamics of nuclei play an important role in determining the properties of the system. Molecular dynamics (MD) simulations [128-131] allow us to study the dynamics and follow the trajectories of the nuclei at finite temperatures. In this method the equilibrium and dynamic properties of the nuclei are studied by integrating their classical equations of motion. The nuclei are assumed to be classical particles and their motions are described by the Newtonian mechanics. This is a very good approximation (except for the light elements) as atoms have large mass and their de Broglie wavelengths at room temperature ( $\lambda \sim 0.1 \text{ \AA}$ ) are much smaller than the interatomic separations (of the order of a few  $\text{\AA}$ ).

For a set of nuclei with an interaction energy  $E(\{\mathbf{R}_J\})$  the basic equations of motion are

$$M_I \ddot{\mathbf{R}}_I = -\frac{\partial E(\{\mathbf{R}_J\})}{\partial \mathbf{R}_I} = \mathbf{F}_I(\{\mathbf{R}_J\}). \quad (2.52)$$

These equations are integrated numerically using discrete time steps. By taking a small step in time and using approximate numerical methods one can predict the new nuclei positions and velocities at the end of the step. At the new positions, the atomic forces are recalculated and another step in time is made. This procedure is repeated many thousands of times in a typical simulation. We used Verlet algorithm, which is most widely used method in MD simulations. The Verlet algorithm uses no explicit velocities. To know, the position of every particle at time  $t_0 + \Delta t$ , it only requires force at time  $t_0$  and the positions at time  $t_0$  and  $t_0 + \Delta t$  respectively. Due to this reason it is very straightforward and its storage requirements are modest. The position  $\mathbf{R}_I(t_0 + \Delta t)$  can be expanded using the Taylor expansion

$$\mathbf{R}_I(t_0 + \Delta t) = \mathbf{R}_I(t_0) + \mathbf{U}_I(t_0)\Delta t + \frac{\mathbf{F}_I(t_0)}{2M}(\Delta t)^2 + \ddot{\mathbf{R}}_I(t_0)\frac{(\Delta t)^3}{6} + \mathcal{O}(\Delta t)^4.$$

Similarly,

$$\mathbf{R}_I(t_0 - \Delta t) = \mathbf{R}_I(t_0) - \mathbf{U}_I(t_0)\Delta t + \frac{\mathbf{F}_I(t_0)}{2M}(\Delta t)^2 - \ddot{\mathbf{R}}_I(t_0)\frac{(\Delta t)^3}{6} + \mathcal{O}(\Delta t)^4,$$

where  $\mathbf{U}_I(t_0)$  is the velocity of  $I^{th}$  particle at time  $t_0$ . Combining the above equations, we can write

$$\mathbf{R}_I(t_0 + \Delta t) = 2\mathbf{R}_I(t_0) - \mathbf{R}_I(t_0 - \Delta t) + \frac{\mathbf{F}_I(t_0)}{M} \Delta t^2. \quad (2.53)$$

In a similar manner one can calculate the velocities at time  $t_0$

$$\mathbf{U}_I(t_0) = \frac{\mathbf{R}_I(t_0 + \Delta t) - \mathbf{R}_I(t_0 - \Delta t)}{2\Delta t} + \mathcal{O}(\Delta t^4). \quad (2.54)$$

Once the positions at  $\mathbf{R}_I(t_0)$  and  $\mathbf{R}_I(t_0 - \Delta t)$  are known, one can find the positions at subsequent time intervals. In Verlet algorithm the error in the estimation of new positions is only  $\mathcal{O}(\Delta t^4)$ . Even though the equations are only approximate for any finite  $\Delta t$ , the total energy is conserved and the simulations remain stable for long runs.

The forces on the nuclei are determined by the nuclei-nuclei and electron-nuclei interactions. Within Born-Oppenheimer approximation, the electron stay in their instantaneous ground state as the nuclei move. Thus the forces on the nuclei can be calculated by the Hellmann-Feynman theorem (2.50). The total energy of the system of nuclei and electrons using the Kohn-sham formalism can be written as

$$E_{tot}^{KS}[\rho](\mathbf{R}) = \int \rho(\mathbf{r})v(\mathbf{r})d\mathbf{r} + T_s[\rho] + J[\rho] + E_{xc}[\rho] + V_{nn}(\mathbf{R}). \quad (2.55)$$

Now the forces can be determined as

$$\mathbf{F}_I = -\frac{\partial E_{tot}^{KS}[\rho](\mathbf{R})}{\partial \mathbf{R}_I} = -\int \rho(\mathbf{r}) \frac{\partial v(\mathbf{r})}{\partial \mathbf{R}_I} d\mathbf{r} - \frac{\partial V_{nn}(\mathbf{R})}{\partial \mathbf{R}_I}. \quad (2.56)$$

Hence at each time step of the MD simulation, one has to solve an electronic problem for a given nuclei configuration to determine the potential  $v(\mathbf{r})$ . Later total force on  $I^{th}$  atom is calculated using Eq. (2.56). This kind of approach is known as Born-Oppenheimer molecular dynamics (BOMD).

In this way, using Eq. (2.53) we can generate a number of time-correlated points in the phase-space which are trajectory of each particle. Using the equipartition theorem the average kinetic energy of the system can be written as

$$\frac{N_f}{2} k_B T = \left\langle \frac{1}{2} M_I \dot{\mathbf{R}}_I^2 \right\rangle, \quad (2.57)$$

where  $N_f$  ( $N_f = 3P - 3$  for a system with a fixed total momentum) is the degrees of freedom. The instantaneous temperature can be calculated using velocities of the atoms.

$$T(t) = \sum_{I=1}^P \frac{M_I \dot{\mathbf{R}}_I^2(t)}{k_B N_f}. \quad (2.58)$$

### 2.8.1 Molecular dynamics at constant temperature

In above case, the total energy of the system is conserved and thus the kinetic energy and so the instantaneous temperature of the system fluctuates around their average values. The MD simulations of this type generates a microcanonical (NVE) ensemble. However it would be more practical to perform the MD simulation at constant temperature to replicate the real experiments more faithfully. An approach to control the temperature is the extended system dynamics in which the physical system is attached to a fictitious thermostat known as Noé Hoover thermostat [132--136]. This adds an additional fictitious degree of freedom  $s$  (corresponding to the thermostat) to the physical system. Now the total energy of the physical system is allowed to fluctuate by a thermal contact with the thermostat. But the total energy of the extended system is still conserved. It has been shown [132] that this extended system produces a canonical ensemble in the physical system due to heat exchange between fictitious degree of freedom and the physical system. The coupling between the two systems is controlled by the fictitious mass  $Q$  associated with the degree of freedom  $s$ . The time step of the physical system  $\Delta t$  is not equal to the time step of the extended system  $\Delta t''$  and scaled according to  $\Delta t = \Delta t''/s$ . The temperature of the system is related to the average of the kinetic energy. A temperature control can be achieved by controlling the velocity. The velocity  $U_I$  of the physical system can be controlled by the variable length of the physical time step as  $U_I = d\mathbf{R}_I/dt = sd\mathbf{R}_I''/dt'' = sU_I''$ , where  $U_I''$  is velocity in the extended system.  $\mathbf{R}_I$  and  $\mathbf{R}_I''$  are the positions of the particles in physical and extended system respectively with  $\mathbf{R}_I = \mathbf{R}_I''$ . More details about the method can be obtained in Ref. [132, 133]

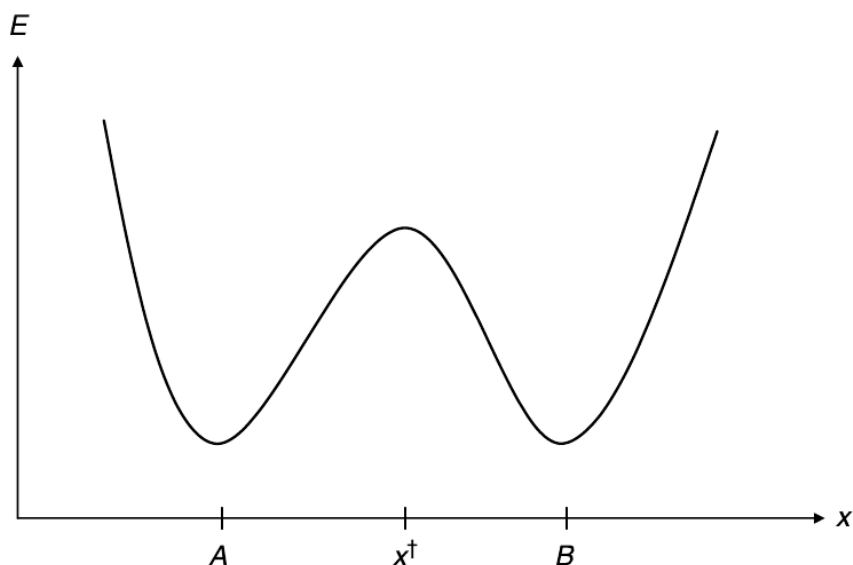


Figure 2.3: Schematic 1D energy profile showing minimum energy path (MEP) which connect two local minima A and B separated by a transition state  $X^\ddagger$  [137].

## 2.9 Nudged elastic band method

An important problem in theoretical chemistry and in condensed matter physics is to identify a minimum energy path (MEP) between two local minima of the PES. This has been schematically shown in Fig. 2.3, where energy of the system is plotted against the reaction pathway. In 1D, a MEP can roughly be defined as a line connecting two local minima (A and B) passing through a transition state ( $X^\ddagger$ ) of the PES, while in a multidimensional space MEP is the line connecting local minima passing through the saddle point (SP). The energy at the saddle point (SP) is the potential energy maximum along the MEP. It is the minimum energy required for the reaction to take place and called as activation energy. The method that is most widely used for finding MEP and the activation barrier in plane-wave DFT calculations is the nudged elastic band (NEB) method [138]. The MEP is found by generating a set of images (different configurations) of the system between the initial and final states. These images are connected through fictitious springs and mimic an elastic band. Optimization of this band involving minimization of the forces on the images gives a MEP between A and B.

Let us suppose an elastic band has  $M+1$  images which are denoted as  $[\mathbf{X}_0, \mathbf{X}_1, \mathbf{X}_2, \dots, \mathbf{X}_M]$ .

Successive images are connected through springs of force constant  $k_1, k_2, \dots, k_{M-1}$ . Each image describes a different atomic configuration,  $\mathbf{X}_m = \{\mathbf{R}_I^m, I = 1, \dots, P\}$ . The end points  $\mathbf{X}_0$  and  $\mathbf{X}_M$  are the initial and final states (correspond to the local minima A and B respectively) and are kept fixed during the optimization. Only the  $M - 1$  intermediate images are adjusted for the optimization of the elastic band. For each image, we use DFT to compute the force acting on the system (called as true force),

$$\mathbf{F}_m^t = -\nabla E_{tot}(\mathbf{X}_m). \quad (2.59)$$

The spring forces are calculated as

$$\mathbf{F}_m^s = k_{m+1}(\mathbf{X}_{m+1} - \mathbf{X}_m) - k_m(\mathbf{X}_m - \mathbf{X}_{m-1}). \quad (2.60)$$

A local tangent at an image  $m$  is a unit vector  $\hat{\boldsymbol{\tau}}_m = \boldsymbol{\tau}_m/|\boldsymbol{\tau}_m|$  pointing along the line defined by the two adjacent images  $\mathbf{X}_{m+1}$  and  $\mathbf{X}_{m-1}$ .  $\boldsymbol{\tau}_m$  can be calculated by the bisection of two unit vector as

$$\boldsymbol{\tau}_m = \frac{\mathbf{X}_m - \mathbf{X}_{m-1}}{|\mathbf{X}_m - \mathbf{X}_{m-1}|} + \frac{\mathbf{X}_{m+1} - \mathbf{X}_m}{|\mathbf{X}_{m+1} - \mathbf{X}_m|}. \quad (2.61)$$

In NEB, the optimization [139, 140] of the band is achieved through a force projection scheme in which the spring forces do not interfere with the convergence of the elastic band to the MEP. In this method, the total force acting on an image is the sum of the true force perpendicular to the local tangent and spring forces along the local tangent. Hence the total force acting on an image  $m$  is

$$\begin{aligned} \mathbf{F}_m &= \mathbf{F}_m^t|_{\perp} + \mathbf{F}_m^s|_{\parallel}, \\ &= -[\nabla E_{tot}(\mathbf{X}_m) - (\nabla E_{tot}(\mathbf{X}_m) \cdot \hat{\boldsymbol{\tau}}_m)\hat{\boldsymbol{\tau}}_m] + (\mathbf{F}_m^s \cdot \hat{\boldsymbol{\tau}}_m)\hat{\boldsymbol{\tau}}_m. \end{aligned} \quad (2.62)$$

In this projection scheme, the parallel spring force components control the spacings between the images along the band and perpendicular true force components direct the elastic band towards the MEP of the surface. The other components of the forces ( $\mathbf{F}_m^t|_{\parallel}$  and  $\mathbf{F}_m^s|_{\perp}$ ) are ignored. An optimization algorithm is then used to relax the  $M - 1$  images according to the forces in Eq.(2.62), and all the images are optimized simultaneously. Thus one obtain new position and new forces for the images. It is an iterative

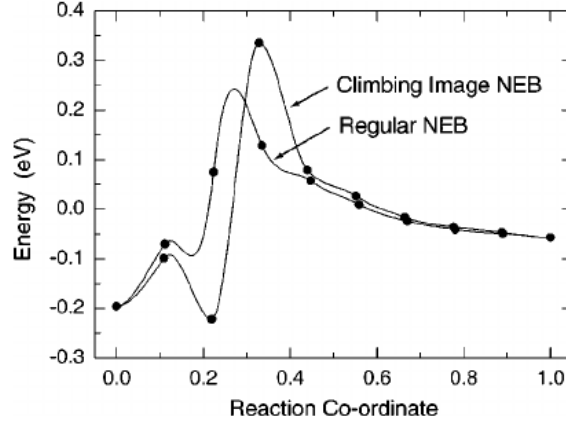


Figure 2.4: DFT calculations of the MEP for  $\text{CH}_4$  dissociative adsorption on the Ir(111) surface. A regular NEB calculation and a CI-NEB calculation are compared, both involving 8 movable images. The regular NEB results in a low resolution of images near the SP, and the interpolation gives an underestimate of the activation energy. The CI-NEB put one of the images at saddle point and gives accurate energy barriers [139].

scheme, hence the same cycle will be repeated until the perpendicular components of true force are zero (or below a given tolerance).

An elastic band is optimized to the MEP and the position of the SP is interpolated (shown in Fig. 2.4). The energy barrier can be calculated by comparing the energies of the SP and initial local minimum (A). However in many cases, resolution of MEP obtained by NEB method is poor near the SP, which gives inaccurate result for the energy barriers. This problem can be solved by a small modification known as climbing image nudged elastic band method (CI-NEB) [139]. In this method, after few iterations with the regular NEB, one identifies an image which has the highest energy ( $m_{max}$ ). This image is then made to move uphill in energy along the elastic band by removing the spring forces completely. Then the force on this image is calculated as

$$\mathbf{F}_{m_{max}} = -\nabla E_{tot}(\mathbf{X}_{m_{max}}) + 2(\nabla E_{tot}(\mathbf{X}_{m_{max}}) \cdot \hat{\boldsymbol{\tau}}_{m_{max}}) \hat{\boldsymbol{\tau}}_{m_{max}}. \quad (2.63)$$

The climbing image will have the perpendicular component of true force and negative of parallel component of true force, which will drag it uphill towards the saddle point. When the forces are converged, the climbing image converges to the SP. The CI-NEB brings one of the images right to the saddle point and gives accurate energy barrier.

The more details are given in Ref. [139, 140].

## 2.10 Bader charges

The properties of molecules and materials are often understood in terms of charge transfer between atoms. However all the DFT methods give the distribution of the electronic charge and one needs a special technique to determine the charge transfer between atoms. The Bader scheme [141] is solely based on the topology of the electronic charge density  $\rho(\mathbf{r})$ , which has a definite value at each point in space inside a molecule or a material. The topology of the charge density carries all the informations about the atoms, bonds and structure of the system. The critical points  $\rho(\mathbf{r}_c)$  (CP) of the charge density correspond to the maximum, minimum or the saddle point of the charge density distribution and satisfy

$$\nabla\rho(\mathbf{r}_c) = 0. \quad (2.64)$$

The behavior of the density  $\rho$  in the neighborhood of a CP is obtained via a Taylor expansion about  $\mathbf{r}_c$ . By ignoring the higher order terms, one can obtain a real and symmetric Hessian matrix of  $\rho$  and diagonalized it to obtain a set of eigenvalues and eigenvectors. The eigenvalues correspond to the principal curvature of  $\rho(\mathbf{r})$  at the CP and eigenvectors correspond to the associated axes. Each CP can be labeled by  $(\omega, \sigma)$ , where  $\omega$  (rank) is the number of non-zero curvatures and  $\sigma$  (signature) is the sum of signs of the curvatures. In 3D, for a stable CP,  $\omega = 3$ . There are four possible CP's of rank 3.

- $(3, -3)$ , when all curvatures of  $\rho(\mathbf{r})$  are negative, and  $\rho(\mathbf{r})$  has a local maximum at  $\mathbf{r}_c$ .
- $(3, -1)$ , when 2 curvatures are negative and  $\rho(\mathbf{r})$  is a maximum at  $\mathbf{r}_c$  in the plane defined by these two axes. The third axis has positive curvature and  $\rho(\mathbf{r})$  is minimum at  $\mathbf{r}_c$  along the axis perpendicular to the plane defined by other axes with positive curvature.
- $(3, -2)$ , 2 curvatures are positive and  $\rho(\mathbf{r})$  is a minimum at  $\mathbf{r}_c$  in the plane defined by these two axes. The third axis has negative curvature and  $\rho(\mathbf{r})$  is maximum

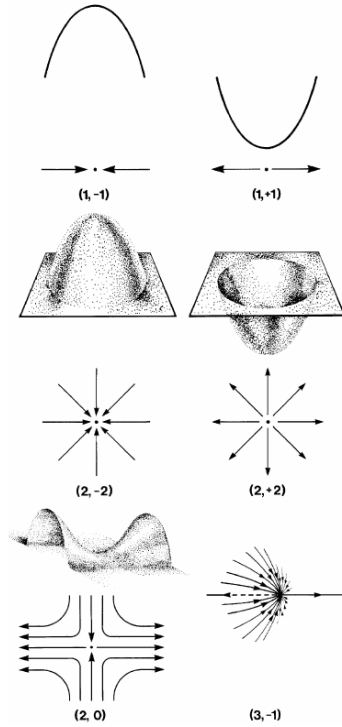


Figure 2.5: Phase portraits. A pair of gradient paths terminates or originates respectively, at the CP for a 1D maximum or minimum. In 2D, all of the gradient paths in a plane terminates or originates, at the maximum or minimum (CP) respectively. At (2,0) CP, a pair of paths originates at the CP, (positive curvature), and another pair terminates at the CP (negative curvature). All other gradient paths avoid the CP. A 3D display of a (3, 1) CP shows the set of trajectories that terminate at the CP and define a surface and the unique pair that originates there and defines a line [141].

at  $\mathbf{r}_c$  along the axis perpendicular to the plane defined by the other two axes.

- (3, +3), when all curvatures are positive and  $\rho(\mathbf{r})$  has a local minimum at  $\mathbf{r}_c$ .

One can calculate the trajectories of  $\nabla\rho$  which are also known as the gradient paths. It can be obtained by calculating the gradient vector of  $\rho$  at some arbitrary point  $\mathbf{r}_0$  and moving a distance  $\Delta\mathbf{r}$  in the direction of vector  $\nabla\rho(\mathbf{r}_0)$  and repeating the procedure until the path so generated terminates. In this way one can obtain all the trajectories of the  $\nabla\rho$ , which represent the gradient vector field of the charge density at a fixed nuclear configuration. Every trajectory originates or terminates at a CP where  $\nabla\rho = 0$ , which also applies to any point at infinity. A schematic phase portrait of trajectories in the neighborhood of a CP is illustrated in Fig. 2.5. In 1D,  $\rho$  has a maximum at the (1,-1)

CP and two gradient vectors terminate here. At a (1,+1) CP,  $\rho$  has a minimum and two gradient vectors originate at the CP. Similarly in 2D, at a (2,-2) CP, all trajectories of  $\nabla\rho$  terminate, while at a (2,+2) CP these trajectories originate. An interesting case is (2,0) CP, which has eigenvalues of opposite sign ( $\sigma = 0$ ) and  $\rho$  has the saddle point at the CP. In this case, the two trajectories associated with the axis of negative curvature terminate at the CP, while two trajectories associated positive curvature will originate at the CP. All other trajectories formed by the linear combination of the the associated eigenvectors avoid the CP. In 3D, a (3,-1) CP has two negative eigenvalues and one positive eigenvalue. Trajectories associated with the pair of negative eigenvalues as well as trajectories obtained from the linear combination of associated eigenvectors terminate at the CP and define a surface. Two trajectories associated with the positive curvature originate at the CP. The charge density has a maximum in the surface at the CP and has a minimum at the same point along the perpendicular axis.

Similarly, all trajectories terminate at the (3,-3) CP which corresponds to one of the nuclei of the system. The region of space traversed by all the trajectories that terminate at a particular nucleus is known as the basin of attraction of the nucleus (also known as Bader volumes). Since all (3,-3) CP's correspond to the position of the nuclei, space of any molecular charge distribution can be partitioned in to disjoint regions (basins). These basins are separated by the interatomic surfaces which terminate at the (3,-1) CP's. The interatomic surface  $S(\mathbf{r})$  define the boundary of basins of the nuclei and satisfies the following constraint

$$\nabla\rho(\mathbf{r}) \cdot \hat{n}(\mathbf{r}) = 0 \quad \text{for all the points on the surface } S(\mathbf{r}), \quad (2.65)$$

where  $\hat{n}(\mathbf{r})$  is the unit vector normal to the surface at each point  $\mathbf{r}$ . Hence the interatomic surface is also known as the zero-flux surface.

In summary, the idea is to divide the space of the molecular charge distribution in terms of Bader volumes. Each Bader volume contain a single charge density maximum which is mostly at a nucleus. These volumes are separated by a surface on which charge density is minimum normal to the surface. The charge enclosed within a Bader volume is approximated as the electronic charge of the enclosed atom. Hence by integrating the charge density within the Bader volume the electronic charge of an atom within the molecule or a material can be calculated. By subtracting this from the charge of the

isolated atom, one can calculate the charge transfer to/from that atom in the system. More details about the method can be found in Ref. [142--145].

## 2.11 van der Waals corrections

It is well known that most popular DFT functionals such as LDA or GGA do not describe the long-range electron correlation that are responsible for the van der Waals (vdW) interactions<sup>3</sup>. The dispersion interactions are viewed as non-local electron correlations, which cannot be captured by standard exchange-correlation functionals. An accurate and efficient estimation of vdW forces in conjunction with DFT functionals is non-trivial and is still a matter of discussion. One of the dispersion-corrected DFT approach was proposed by Grimme [146--148], known as DFT-D2 (or DFT-D) method. In this method, a semi-empirical attractive term is added to the DFT energy to account for medium and long-distance dispersive forces, so that total energy is now written as

$$E_{tot} = E_{\text{DFT}} + E_{\text{disp}}, \quad (2.66)$$

where  $E_{\text{DFT}}$  is the DFT total energy computed with a given exchange-correlation functional and  $E_{\text{disp}}$  is a semi-empirical pair-wise dispersion correction given by

$$E_{\text{disp}} = -s_6 \sum_{i=1}^{N_{at}-1} \sum_{j=i+1}^{N_{at}} \frac{C_6^{ij}}{R_{ij}^6} f_{\text{damp}}(R_{ij}, R_0^{ij}). \quad (2.67)$$

Here  $N_{at}$  is the number of atoms in the system,  $s_6$  is a global scaling factor and depends on the exchange-correlation functional,  $C_6^{ij}$ 's are the dispersion coefficients for the atom-pair  $ij$  and  $R_{ij}$  is the interatomic distance. For a pair of different elements, the value of  $C_6^{ij}$ 's is determined by the geometric mean of the coefficients of individual elements.  $f_{\text{damp}}$  is a damping function which avoids divergence of the  $R_{ij}^6$  term at small distances and double-counting effects of correlation at intermediate distance. It

---

<sup>3</sup>van der Waals forces is a general term which include the forces between (1) two permanent dipoles (Keesom force), (2) a permanent dipole and a corresponding induced dipole (Debye force) (3) two instantaneously induced dipoles (dispersion force). In this thesis we will use van der Waals forces and dispersion forces as synonyms.

determines the range of the dispersion correction.

$$f_{\text{damp}}(R_{ij}, R_0^{ij}) = \frac{1}{1 + \exp(-d(R_{ij}/s_{r,n}R_0^{ij} - 1))}, \quad (2.68)$$

where  $R_0^{ij}$  is cutoff radius for the atom pair which is taken as the average of the empirical atomic vdW radii.  $d$  is the global constant that determines the steepness of the damping function (the higher the value of  $d$ , the closer it is to a step function), and  $s_{r,n}$  is a scaling factor and determines the range of interaction covered by the given DFT exchange-correlation functional. While using the DFT-D2 method, we used the PBE exchange correlation functional in the DFT part and the value of  $s_6$  is taken as 0.75. For all our calculation, we considered pair interactions up to a radius of 8 Å and used the default values of other parameters given in VASP [149--151].

In another approach the dispersion forces are treated within the DFT formalism by means of a non-local correlation functional. Dispersion forces result due to interactions between multipole moments arising out of charge density fluctuations around the atoms. DFT-D2 method only includes dipole-dipole interaction through a semi-empirical approach. Higher order interactions are, however, neglected. Dion *et al.*, [152, 153] have proposed a method which calculates the dispersion energy solely based on the electron density. Within this approach the exchange-correlation energy  $E_{xc}$  is calculated as

$$E_{xc} = E_x^{\text{GGA}} + E_c^{\text{LDA}} + E_c^{\text{nl}}, \quad (2.69)$$

where  $E_x^{\text{GGA}}$  is the exchange energy in the revPBE approximation [154],  $E_c^{\text{LDA}}$  is the local correlation energy calculated within LDA, and  $E_c^{\text{nl}}$  represents the non-local term describing the dispersion energy and can be calculated as

$$E_c^{\text{nl}}[\rho] = \int d\mathbf{r}_1 d\mathbf{r}_2 \rho(\mathbf{r}_1) \phi(\mathbf{r}_1, \mathbf{r}_2) \rho(\mathbf{r}_2), \quad (2.70)$$

The kernel  $\phi(\mathbf{r}_1, \mathbf{r}_2)$  depends on the distance  $|\mathbf{r}_1 - \mathbf{r}_2|$ , charge density  $\rho$  and its gradient [153]. This method is called as van der Waals density functional (vdW-DF) method. It adds the description of dispersion interactions within the DFT formalism and calculate the correlation of all ranges self-consistently. The biggest advantage of vdW-DF

method over DFT-D2 method is that in this method dispersion effects are included naturally via the charge density and do not depend on the parameters.

The vdW-DF method greatly improves the bond lengths of the dispersion bonded systems in comparison to the GGA or LDA results. However for some materials (*e.g.*, graphene, systems with hydrogen bonds), vdW-DF overestimates the long range dispersion interactions and gives large bond lengths [155, 156] in comparison to experimental results. Although dispersion effects are purely correlational in nature, somehow the exchange part of revPBE produces repulsive interaction in the dispersion regime. Thus the exchange part of revPBE gives large intermolecular binding distances and inaccurate binding energies. To circumvent this problem, a second version of the van der Waals density functional was proposed by Lee *et al.* [157]. They incorporated a less repulsive exchange functional (rPW86 [158]). The method is known as the vdW-DF2 method. This method has been found to give good results for a broad class of materials. Later various other vdW functionals have also been proposed to improve the performance of the dispersion bonded systems such as optPBE-vdW, optB88-vdW, vdW-DFC09<sub>x</sub>, vdW-DF2C09<sub>x</sub> *etc.* Comparisons of these methods for a number of materials are given in Ref. [156, 159, 160].

All our calculations have been performed using VASP where these methods have been implemented by J. Klimes [155, 156] using the algorithms of Roman-Perez *et al.* [161] More details about the methods have been given in Ref. [152, 153, 157].



# Adsorption of small $\text{Ag}_n$ clusters over clean graphite substrate

## 3.1 Motivation

### 3.1.1 Experimental motivation

One of the early experiments to study deposition of silver atoms or clusters on highly oriented pyrolytic graphite (HOPG) (0001) was performed by Ganz *et al.*, [12] They used a STM technique to study the static and dynamic behavior of Ag (also Cu, Au, and Al) atoms and clusters deposited in situ on HOPG in an ultra-high vacuum chamber. They found isolated silver atoms, dimers, clusters of 3 or more atoms and large two and three dimensional islands after deposition of the atoms. Isolated silver atoms were always found above the  $\beta$  sites of a graphite sheet as shown in Fig. 3.1(a,b). A  $\beta$  site carbon atom does not have a neighbor directly below it in the second layer. None of their images showed isolated Ag atoms above hollow sites. This is very different from the physisorption of noble gas atoms, which prefer to get adsorbed above hollow sites of graphite [162]. Ag dimers were found to be parallel to the surface at or near  $\beta$ -sites, and had a bond length of  $2.5 \pm 0.2 \text{ \AA}$  (Fig. 3.1(c,d)). This is comparable to a free dimer bond length of  $2.5 \text{ \AA}$ . They also identified trimers in a linear form (Fig. 3.1(e,f)), in which the Ag atoms were seen above  $\beta$ -sites with bond lengths of roughly  $2.5 \text{ \AA}$ .

Other experiments also studied deposition of silver atoms and clusters on HOPG. Busolt *et al.*, [13, 73] studied the stability of size-selected  $\text{Ag}_n^+$  clusters ( $n = 2 -$

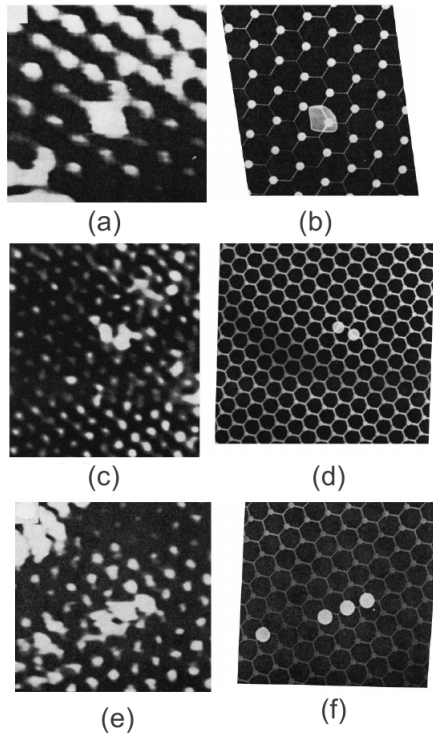


Figure 3.1: (a) A  $14 \text{ \AA} \times 16 \text{ \AA}$  constant current STM image showing an isolated Ag monomer on graphite. (b), (d) and (f) are computer-generated models showing the graphite lattice positions with the adatom and dimer shapes superimposed. (c) A  $32 \text{ \AA} \times 32 \text{ \AA}$  constant current STM image of a Ag dimer. (e) A  $20 \text{ \AA} \times 18 \text{ \AA}$  current image of a Ag trimer in a linear form [12].

9) deposited with an impact energy of  $1 - 2 \text{ eV}$  at low coverage on HOPG at  $77 \text{ K}$ . Their two photon photoemission spectra reveal a pronounced odd/even oscillation in the Fermi-level position of the supported clusters with an exception of  $\text{Ag}_3$  (shown in Fig. 3.2). This is similar to the odd-even oscillation of ionization potentials [163] and electron affinity [164] of gas phase silver clusters, which can be understood in terms of shell models. This similarity indicates that deposited clusters retain their size and identity on HOPG.

In another experiment, Goldby *et al.*, [18] investigated film growth via deposition of soft landed, size-selected silver clusters of sizes  $50 - 250$  atoms on a graphite substrate. They found that at room temperature deposited clusters are mobile and coalesce into three-dimensional particles with a “universal” diameter of  $14 \text{ nm}$ . This was assumed to be a consequence of lattice mismatch between the silver clusters and graphite. Ndlovu

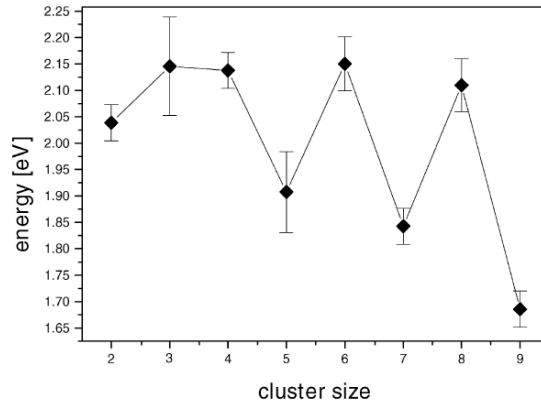


Figure 3.2: Position of the Fermi-level as a function of cluster size obtained from the two photon electron spectroscopy with femtosecond pump and probe lasers [13].

*et al.*, [14] in their experiments found formation of Ag clusters up to an average size of about 1.2 nm after deposition of atoms. But beyond this size there was no further coalescence of the clusters. They also found isolated Ag atoms only near  $\beta$  sites, and reported a charge transfer from the cluster to the substrate as indicated by the positions of the Ag 3d core levels in XPS. In general, all these experiments conclude that Ag atoms are weakly bound to the HOPG substrate, and they are quite mobile at least around room temperature.

Lopez-Salido *et al.*, [165] performed a combined STM and XPS studies on the Ag islands prepared by evaporating Ag atoms on a HOPG surface sputtered by Ar ions. They showed that the Ag 3d core level binding energy is very sensitive to the particle size. The shift (towards higher binding energy) in the Ag 3d level with respect to bulk Ag value, increases almost linearly with decreasing particle diameter (Fig. 3.3). In other words, Ag particle size can be estimated by measuring Ag 3d binding energy. For particles with a diameter of 1 nm (less than 30 atoms in a particle), the core level shift is 0.6 eV. The positive core level shift depends upon several facts including charge transfer, less efficient screening of the core-hole in smaller clusters, change in bond lengths in Ag clusters compared to bulk Ag, *etc.*

In another experiment [166], Lopez-Salido *et al.*, deposited size-selected Ag cluster anions consisting of 3 – 16 atoms on a HOPG surface sputtered by Ar ions using a LECBD technique at room temperature. Using XPS spectra and STM images, they found that below a coverage of  $4 \times 10^2 \text{ cm}^{-2}$ , Ag clusters retain their identity and exist

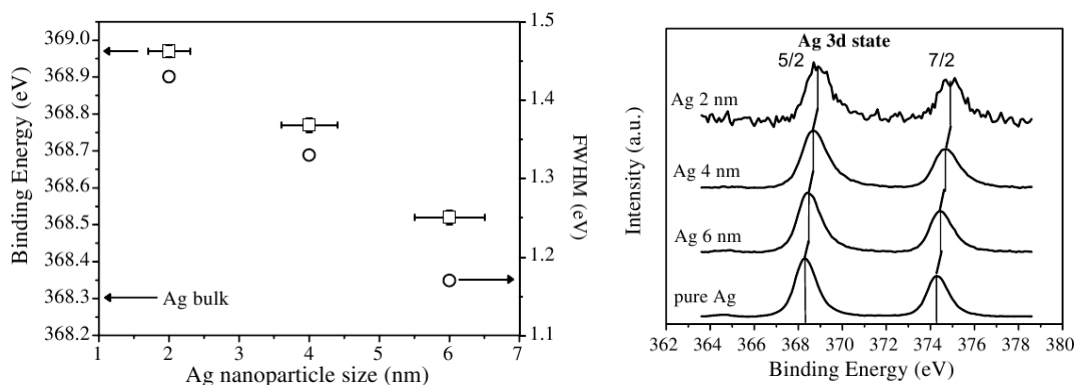


Figure 3.3: The changes of the Ag 3d states as a function of particle size on sputtered HOPG. The sizes of the particles were determined using scanning tunneling microscopy (STM).

as individual clusters. They also pointed out that structures of soft landed clusters are different from those of Ag “islands” grown by thermal evaporation of Ag atoms. XPS spectra of the Ag 3d levels for pre-formed Ag<sub>5</sub> and Ag<sub>10</sub> clusters are shown in Fig. 3.4. No size dependent shift in the Ag 3d binding energy was seen for these clusters. This is contrary to the Ag 3d spectra of thermally grown Ag islands, which show a linear shift in the core level position towards higher BE with decreasing particle size [165]. The large difference in the core level shifts of the deposited mass-selected clusters (core level shift of 0.2 eV) and similarly sized Ag islands (core level shift of 0.6 eV) indicates that Ag atoms in the two species are in different chemical environments. An absence of size-dependent core level shift in the spectrum of deposited size-selected Ag clusters also indicates an absence of charge transfer from the clusters to the surface. A core level shift and charge transfer was present for the clusters grown by the atomic thermal evaporation on the graphite surface.

### 3.1.2 Theoretical motivation

Given its fundamental and technological importance, Ag/HOPG system has also attracted theoretical attention. In an early work, Rafii-Tabar [167] studied the process of deposition of Ag adatoms on HOPG through classical MD simulations. The attempt was to explain the experimental observations of Ganz *et al.*, [12] Both pair-wise and many-body interatomic potentials were employed to describe the interactions within

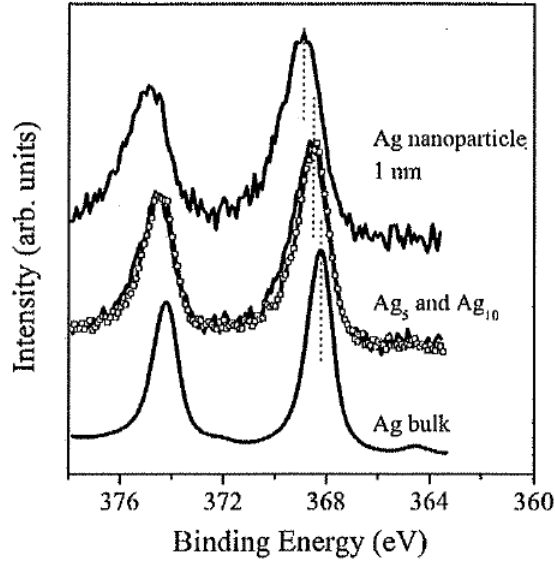


Figure 3.4: Ag 3d level spectra of Ag bulk, deposited Ag<sub>5</sub> and Ag<sub>10</sub> (spectrum with squares) clusters on sputter-damaged HOPG, and 1 nm-sized Ag islands prepared using thermal evaporation of Ag atoms on the same substrate are compared

Table 3.1: A summary of the absorption energies obtained in various theoretical works [20, 168] for an Ag adatom and dimer at different sites of a graphite surface.

Reference	Method	$E_a$ for an adatom				$E_a$ for a dimer			
		$\beta$	$\alpha$	hollow	bridge	$\beta$	$\alpha$	hollow	bridge
Ref. [20]	LDA	0.54	0.27	0.33	0.23	0.37	0.37	0.38	0.36
Ref. [168]	LDA	0.44	0.43	0.39	0.43	-	-	0.52	0.54

the Ag/HOPG system. The Ag-Ag interactions were described by a many-body potential of Finnis-Sinclair type. The C-C bonding in a basal plane was described by Tersoff's non-central potential, while the C-C bonding between the basal planes was described by a pair-wise Lennard-Jones potential. To describe the interaction between Ag and C interface, they constructed a pair-wise Morse-type potential. Using these potentials, they found that Ag atoms were very mobile on the terraces. Diffusing Ag atoms form small 2D and 3D clusters and islands. An adatom was seen above  $\beta$ -site, a dimer also resides at or near  $\beta$ -sites.

Subsequently, first principles approaches, particularly based on DFT, have been taken to address the problem. Duffy and Blackman [20] studied adsorption of Ag adatoms and dimers on graphite using the LDA. They used a cluster model (fragment)

for the graphite surface with 2 carbon layers in AB stacking. The dangling bonds on the outer C atoms were saturated with H atoms in order to maintain  $sp^2$  hybridization of all C atoms. Only the metal atoms were relaxed during structure optimization. All the C atoms were fixed to their bulk positions. For an Ag adatom, a  $\beta$  site was found to be the most favorable followed by the hollow,  $\alpha$ , and the bridge sites. The  $\alpha$ -site carbon atoms on the surface have a neighbor directly below them in the second layer. The bond between  $\alpha$  and  $\beta$ -site is a bridge site. For Ag dimers, the highest adsorption energy (defined later) was obtained for a parallel orientation at the  $\beta$ -site. The adsorption energies for an adatom and a dimer at all the sites obtained by them are listed in Table 3.1. The adsorption energies of a dimer at all sites are nearly equal. Based on this observation, they argued that an Ag dimer would be much more mobile than an isolated adatom.

The same problem was studied by Wang *et al.*, [168] again using LDA. They modeled the graphite surface by a  $3 \times 3$  unit cell with 4 layers in AB stacking. The metal atoms and top two layers of graphite were allowed to relax during the simulations. They also found that the  $\beta$ -sites are most favorable for Ag adatoms. The ordering of the various sites was, however, different from that in Duffy and Blackman's studies. The  $\beta$ -site was followed by the bridge,  $\alpha$ , and hollow (which was the least stable) sites. They also found a parallel orientation of Ag dimer to be most stable. However, it seems that in both these studies [20, 168], a perpendicular orientation of the dimer was not considered.

Jalkanen *et al.*, [21] studied adsorption of Ag adatom, dimer,  $Ag_6$ , and  $Ag_{13}$  clusters on a single layer of graphite (*i.e.*, graphene sheet) using the PW91 [107] (and PBE [108] in some cases) gradient corrected functional. The GGA functionals almost do not give any binding of the adatom to the sheet. For an  $Ag_2$  dimer, a perpendicular, atop orientation was 0.11 eV more stable than the parallel, atop orientation. But again, the adsorption energies are very small in both cases. They also found that the hollow site is the least stable for both the parallel and perpendicular orientations of the silver dimer. For the  $Ag_6$  cluster, a parallel, atop orientation was found to be the most stable.

Graphite is a layered material held together by van der Waals forces. The local and semi-local exchange-correlation functionals used in DFT are not capable of describing dispersion forces. The LDA does give a binding between successive layers in graphite, but reproduces the energetics rather poorly (Section 3.3). GGA function-

als behave poorly for both energetics and inter-layer separation. It has been argued that dispersion forces play a major role in the interaction between metal adatoms and clusters and the graphite surface [21, 169], and also between metal substrates and a graphene over-layer [170]. Therefore Ag/HOPG system presents a challenge for the DFT methods. Attempts have been made to incorporate dispersion forces within a DFT formalism, and such methods have been applied to the Ag/HOPG system as well. Jalkanen *et al.*, [21] used the semi-empirical corrections proposed by Elstner [171] and Grimme [146] for this purpose. These methods did produce binding between the Ag atoms, clusters and the graphene sheet. The on-top site was found to be most favorable for an adatom. Recently Amft *et al.*, [169] have explored the effects of dispersion forces in the binding of Cu, Ag, and Au adatoms on a graphene sheet. They used two different approaches for this. The first is Grimme's semi-empirical correction (DFT-D2), and the second is to use a non-local correlation functional [152, 157] in the energy. Grimme's approach produced the hollow site as the most favorable one for an adatom, but the vdW-DF method gave the top site to be the most favorable, just as in LDA. It should be pointed out, however, that in all the methods, the differences in adsorption energies of an adatom at various sites were rather small.

There have been no systematic theoretical studies of deposition and adsorption of Ag clusters on a HOPG substrate over a range of cluster sizes. Such studies have only focused on adatom, dimer, Ag<sub>6</sub>, and Ag<sub>13</sub> clusters. Thus there is a big gap in our understanding of the structure, energetics, and electronic properties of Ag atoms and clusters deposited on HOPG. Given the amount of experimental efforts that has been devoted to this system, it is important to develop this understanding. How far do Ag clusters retain their geometric and electronic identity after deposition on the HOPG substrate? What determines the energetics of various gas phase isomers after deposition? Also, there is a need for incorporation of dispersion interactions in the DFT formalism for a proper treatment of the Ag/HOPG system. However, the best way to incorporate these effects is still an open question that would require comparison of theoretical results with experiments for it to be settled. As we have discussed above, vdW-DF gives the correct binding site for an Ag adatom, which DFT-D2 does not. LSDA, on the other hand, produces a qualitatively correct result in that the atop site (on graphene) or the  $\beta$  site (graphite) is found to be the most favorable one for an Ag adatom. How do their behavior differ for larger clusters, is still not clear. In order to get insights into these issues,

we have studied adsorption of Ag adatom and clusters containing up to eight atoms on a clean HOPG substrate using three different approaches: vdW-DF2, LSDA, and DFT-D2. Primarily, we will describe the results obtained through vdW-DF2 method, which gives the best agreement with experiments. We will give a comparison of the results obtained by LSDA and DFT-D2 methods, which have been used for the studies of this system, and argue why these methods are not the best to describe the Ag/graphite bonding.

## 3.2 Computational methods

All our calculations are performed within the framework of DFT. Since we are interested in studying deposition of pre-formed size selected Ag clusters on graphite, it is important to find the structures of free Ag clusters in the gas phase. Structures of isolated gas phase  $\text{Ag}_n$  clusters were searched to locate the global minimum at each size except  $n = 2$ . The global structure search was performed using an evolutionary algorithm as implemented in the USPEX [123, 124] code. The initial population size was taken as 10 and the population size in each subsequent generation was kept at 10. Fitness criterion used for these calculations was the energy of the clusters. Energies were calculated within a plane wave DFT formalism using VASP. The population in a generation was produced by applying specially designed variational operators (heredity, mutation, and soft-mutation) [125] to the preceding generation, as discussed in chapter 1. Calculations were carried out up to a maximum of 25 generations with the halting criterion that if the energy of the best structure did not change for 10 generations the calculation would be stopped. Each generated structure was relaxed to its nearest local minimum using CG method as implemented in VASP. The clusters were placed inside a periodic box such that the closest distance between neighboring clusters in adjacent unit cells is 10 Å. Interactions between the valence electrons and the ion cores were represented by the PAW [120, 121] potentials. Brillouin zone (BZ) integrations were performed using the  $\Gamma$ -point only. For each structure, energy calculations in VASP were performed at four increasing levels of accuracy in terms of energy cutoff for the plane wave basis set. The cutoffs used were ENMAX of the POTCAR file, 300 eV, 350 eV, and 400 eV. The structures were considered converged when all the force components were smaller than 0.001 eV/Å. The global search for the structures

was performed at the L(S)DA level only. Spin polarized calculations were done only for the odd sized clusters and all of them exist in a doublet state. Simple metal clusters of even sizes generally have singlet ground states, which was also confirmed in our test calculations. A number of low energy L(S)DA structures at each size were taken and re-optimized using vdW-DF2 before depositing them on the graphite substrate. In all the sections the gas phase ground state structures are denoted as GPGS structures.

For the clusters supported over graphite surface, all the calculations have been performed using VASP with an energy cutoff of 400 eV. The graphite (0001) surface is represented in a repeated slab geometry. We consider three C layers in the slab with a vacuum layer of 15 Å separating two successive slabs. Top two layers were fully relaxed while the bottom layer was held fixed. Addition of more layers or relaxing all three layers did not change the adsorption energies of an adatom at different sites. The lateral dimensions of the slab are chosen according to the size of the cluster being deposited. The distances between the cluster in the simulation cell and its periodic images are always kept larger than 8 Å, to rule out possibility of any interactions between them. BZ integrations are performed with Monkhorst-Pack  $k$ -point meshes that ranged from  $(6 \times 6 \times 1)$  to  $(1 \times 1 \times 1)$  depending on the lateral size of the HOPG slab. The lateral size of the slabs ranged from  $9.76 \text{ Å} \times 8.46 \text{ Å}$  for an adatom to  $17.09 \text{ Å} \times 16.92 \text{ Å}$  for the  $\text{Ag}_8$  cluster. For the deposited clusters we performed spin-polarized calculations at all sizes.

The relative stability of the clusters deposited on a substrate has been measured in terms of cohesive energy  $E_c$  and adsorption energy  $E_a$ . For a cluster composed of  $n$  atoms, these two quantities are defined as:

$$E_c = nE_{\text{Ag}} + N_{\text{C}}E_{\text{C}} - E_T(\text{Ag}_n/\text{graphite}), \quad (3.1)$$

$$E_a = E_T(\text{Ag}_n) + E_T(\text{graphite}) - E_T(\text{Ag}_n/\text{graphite}), \quad (3.2)$$

where  $E_{\text{Ag}}$  and  $E_{\text{C}}$  are the energies of isolated Ag and C atoms respectively,  $E_T(\text{Ag}_n)$  is the total energy of the gas phase  $\text{Ag}_n$  isomer at its local minimum of structure,  $E_T(\text{graphite})$  is the total energy of the clean  $N_{\text{C}}$ -atom graphite slab,  $E_T(\text{Ag}_n/\text{graphite})$  is the total energy of  $N_{\text{C}}$ -atom graphite slab plus  $\text{Ag}_n$  cluster adsorbed on it. The cohesive energies can obviously be used to compare relative energetic stabilities of different isomers of a particular size deposited at different locations on the substrate. On the

Table 3.2: Properties of graphite as reproduced by different exchange-correlation functionals.  $a_0$  is the intra-layer lattice constant and  $c_0$  is the inter-layer separation.  $E_c$  and  $E_B$  are the cohesive energy and the interlayer binding energy respectively.

Functionals	$a_0$ (Å)	$c_0$ (Å)	$E_c$ (eV/atom)	$E_B$ (meV/Atom)
LDA	2.44	3.33	8.98	23.3
PBE-GGA	2.46	4.32	7.97	0.76
DFT-D2	2.46	3.22	8.07	50.3
vdW-DF	2.47	3.63	8.59	53.5
vdW-DF2	2.47	3.56	8.48	51.3
Experimental	2.46 [173]	3.35 [173]	7.37 [174]	$52 \pm 5$ [175]

other hand, the adsorption energy  $E_a$  is the energy gain in adsorbing a cluster on the HOPG substrate. This is also a measure of the energy that has to be supplied for the cluster to desorb from the substrate and go to its gas phase structure. Once the clusters are formed in the gas phase, a comparison of  $E_a$  will give a measure of relative ease of forming different adsorbed structures. Larger values of  $E_c$  and  $E_a$  imply greater stability of the deposited clusters. For a given size a lower total energy leads to higher  $E_c$  and  $E_a$ .

### 3.3 Clean graphite surface

As already mentioned in section 3.2, we used the vdW-DF2 [157] method for these calculations. However, to benchmark our calculations, and to show that this method works better for bulk graphite, we also used the LDA and the DFT-D2 methods for this system. Table 3.2 shows the in-plane lattice constant ( $a_0$ ), interlayer distance ( $c_0$ ),  $E_c$  and interlayer binding energy  $E_B$  of graphite for different exchange-correlation functionals. The interlayer binding energy  $E_B$  is defined as

$$E_B = 2E_T(\text{graphene}) - E_T(\text{graphite}), \quad (3.3)$$

where  $E_T(\text{graphene})$  is the total energy of a single layer of graphite (graphene) and  $E_T(\text{graphite})$  is the total energy of graphite having two layers in the unit cell. LDA gives a binding between successive carbon layers with an interlayer separation of 3.33 Å.

It gives  $E_B = 23.02$  meV/atom and  $E_c$  of bulk graphite to be 8.98 eV/atom. These results are in good agreement with other LDA calculations reported in the literature [172]. The experimental value for the interlayer lattice constant [173] is 3.35 Å, whereas cohesive energy [174] and interlayer binding energy [175] are 7.37 eV/atom and  $52 \pm 2$  meV/atom respectively. These results show that although LDA reproduces the interlayer separation rather well, it cannot reproduce the energetics well. This should not be a surprise, because LDA cannot treat dispersion forces responsible for binding between successive layers, but produces a finite binding because of its tendency to over-bind.

While PBE produces the intra-layer lattice constant quite accurately, it completely fails to describe the interlayer binding. DFT-D2 produces  $a_0$  accurately, but seriously underestimates  $c_0$ . It does well for  $E_c$  and does better than LDA and PBE for  $E_B$ . vdW-DF produces  $a_0$  in good agreement with experiments but overestimates  $c_0$  by nearly 10%. It also overestimates  $E_c$  and  $E_B$ . We used two exchange functionals for the vdW-DF method: revPBE [154] (vdW-DF) and rPW86 [157] (vdW-DF2). Both these functionals produce results in good agreement with experiments. However, the rPW86 exchange functional corrects the overestimation in  $c_0$ ,  $E_c$ , and  $E_b$  to a large extent obtained using the revPBE functional. Results using rPW86 is presented in Table 3.2 as vdW-DF2, and we use this functional for all calculations of Ag clusters on graphite.

### 3.4 Structure of gas phase silver clusters

The low energy gas phase structures of silver clusters containing up to eight atoms found using the vdW-DF2 method are shown in Fig. 3.5. For comparison, the low energy structures from L(S)DA are shown in Fig. A.1 in the Appendix. The Ag<sub>2</sub> dimer in Fig. 3.5 has a slightly longer bond length compared to the LDA value (Fig. A.1(a)). In fact, it has been reported in the literature that vdW-DF methods produce slightly longer bond lengths than LDA [156, 170]. We find this to be true for all the Ag<sub>n</sub> clusters we studied. Ag<sub>3</sub> turns out to be an isosceles triangle with one longer and two marginally shorter sides. Ag<sub>4</sub> is a rhombus in its lowest energy structure. In addition to the GPGS isomers, we have shown higher energy isomers up to  $\sim 0.7$  eV in Fig. 3.5, and have studied their deposition on graphite substrate. While it is expected that the GPGS isomers will be produced in greater abundance in a cluster beam, depending on

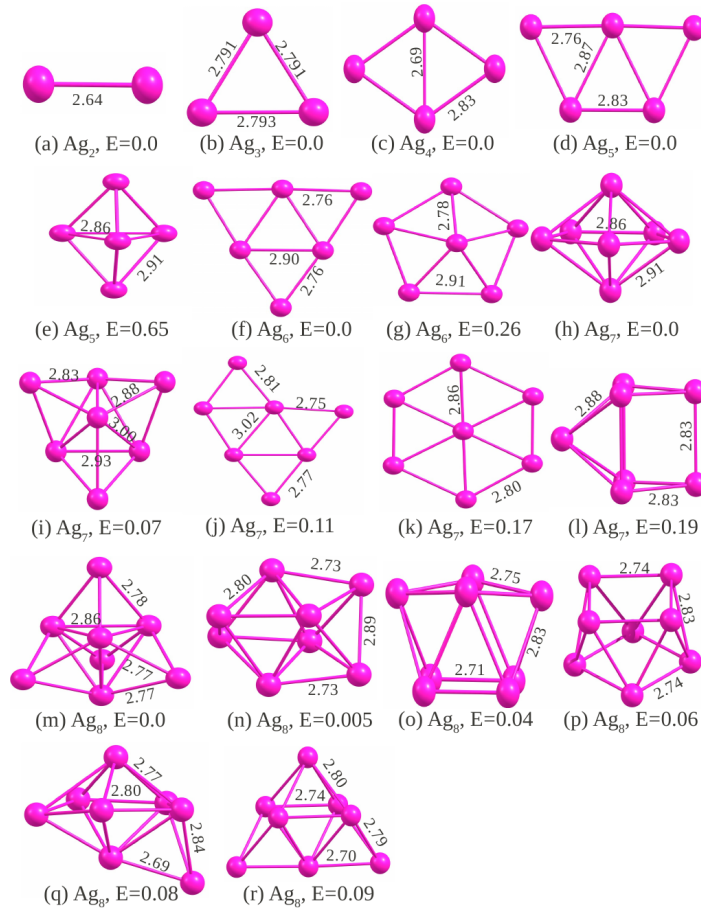


Figure 3.5: Structure, bond lengths, and energies (relative to the ground state isomers) of gas phase  $\text{Ag}_n$  clusters in vdW-DF2. Magenta colored circles represent Ag atoms.

the temperature of the clusters, and kinetics of the growth process, higher energy isomers may be present [176]. For  $\text{Ag}_5$ , therefore, we show two isomers in Fig. 3.5. The GPGS is a planar structure with two-fold symmetry. A triangular bi-pyramid is 0.65 eV higher. The GPGS of  $\text{Ag}_6$  is a planar structure with three-fold symmetry. A pentagonal pyramid is 0.26 eV higher. The GPGS structure of  $\text{Ag}_7$  is a pentagonal bi-pyramid followed by a tri-capped tetrahedron (Fig. 3.5(i)), and a planar structure obtained from the GPGS of  $\text{Ag}_6$  by capping one of the Ag-Ag bonds (Fig. 3.5(j)). The planar structure (Fig. 3.5(j)) is 0.96 eV higher than the GPGS structure in LSDA (Fig. A.1(l)), but is only 0.11 eV higher in vdW-DF2. This isomer has the lowest energy after deposition on HOPG as discussed below.  $\text{Ag}_7$  also have two more isomers, a centered hexagon planar structure (Fig. 3.5(k)), and a capped prism structure (Fig. 3.5(l)). These two are

0.17 eV and 0.19 eV higher than the GPGS respectively. We have shown six isomers for  $\text{Ag}_8$  which we have deposited on the substrate. The GPGS is a tri-capped triangular bi-pyramid (Fig. 3.5(m)). This is different from the LDA ground state, which is a bi-capped octahedron (Fig. A.1(m)). The tri-capped triangular bi-pyramid was 70 meV higher than the ground state in LDA (Fig. A.1(n)). The bi-capped octahedron in Fig. 3.5(n) (bco1) is nearly degenerate with the GPGS in vdW-DF2. These two are followed by two anti-prism structures (Fig. 3.5(o,p)), a capped pentagonal bi-pyramid (Fig. 3.5(q)), and another bi-capped octahedron (bco2, Fig. 3.5(r)) structure. We would like to point out that in bco1 two neighboring triangular faces sharing an edge are capped, while in bco2, two faces sharing a corner are capped. Our L(S)DA GPGS and low energy isomers are the same as those reported in Ref. [176].

### 3.5 Structure of deposited silver clusters

As stated in chapter 1 clusters can approach the substrate at any point, and in any random orientation. To mimic this process we used random rotation technique described in section 2.7. For each isomer we choose at least five different random sets of the Euler angles and four special symmetry points of the graphite surface: the top sites  $\alpha$  and  $\beta$ , the bridge site and the hollow sites. All these initial structures are then relaxed to their nearest local minima using the conjugate gradient method as implemented in VASP. Sometimes different initial structures relax to the same final geometry.

*Ag adatom:* Adsorption energies of an Ag adatom at different sites and the spin moments in the system are given in Table 3.3. For an Ag adatom, both on-top  $\beta$  and  $\alpha$  sites turn out to be the most favorable with the same adsorption energy of 0.22 eV. They are followed by the bridge and the hollow sites. At the  $\beta$  site, the Ag-C distance is 3.30 Å, which is much larger than the sum of their covalent radii  $R_c$  ( $R_c(\text{Ag}) = 1.45$  Å,  $R_c(\text{C}) = 0.76$  Å). This rules out any chemical bond between them. Note that the ordering of the adsorption energies and the Ag-C distance at the  $\beta$  site we find are exactly the same as those reported in Ref. [169], though the adsorption energy they found in vdW-DF was slightly lower. Because of the large Ag-C distance, adsorption of the Ag atom causes only a minor deformation of the graphite surface. Relaxation of the  $\beta$  site C atom, on which the Ag atom is adsorbed, is only 0.05 Å. Overall deformation within the top layer of the graphite slab is measured by the deviation of the individual C

Table 3.3: Adsorption energy ( $E_a$ ) and magnetic moment (M) of a silver adatom at various points on a graphite substrate obtained using vdW-DF2 method.

Site	$E_a$ (eV)	$M$ ( $\mu_B$ )
$\beta$	0.215	0.99
$\alpha$	0.215	0.99
bridge	0.214	0.99
hollow	0.209	0.99

atoms ( $\Delta z_C$ ) from their average  $z$  coordinate (perpendicular to the surface). Maximum  $\Delta z_C$  is only 0.01 Å.

An isolated Ag atom has one unpaired electron and graphite is non-magnetic. When the atom is placed on the graphite substrate the moment turns out to be  $0.99 \mu_B$ , *i.e.*, almost the entire moment of the atom is retained. This moment is localized almost entirely on the Ag atom as can be seen from the spin density iso-surface plot presented in Fig. 3.6(a). This implies that there is no charge transfer between the cluster and the substrate. To get a quantitative estimate of the charge transfer, we calculated Bader charges on all the atoms. We find a negligible charge transfer ( $0.01e$ ,  $e$ -electronic charge) from the Ag adatom to graphite. All these point towards a physisorption scenario. As we will see below, preference of an Ag adatom for the top sites plays a major role in determining the low energy structures of clusters.

*Ag<sub>2</sub> dimer:* An Ag<sub>2</sub> dimer has the lowest energy in a parallel orientation on graphite (Fig. 3.7(b)) with both the silver atoms near top sites. This structure has  $E_a = 0.32$  eV, and the silver atoms are at an average distance of 3.48 Å from the nearest carbon atoms. Interactions with the substrate do not alter the dimer bond length, it retains its gas phase value of 2.64 Å. Here we do not always distinguish between  $\alpha$  and  $\beta$  sites since the difference in  $E_a$  at these sites for an adatom is very small. Our results for Ag<sub>2</sub> are in agreement with Duffy *et al.*, [20] and Wang *et al.*, [168] but contrary to the results of Jalkanen *et al.*, [21] who found a perpendicular orientation of the dimer at the top and bridge sites to be most favorable. Our LDA results suggest that a perpendicular orientation of Ag dimer is more stable, which is similar to the behavior of Au<sub>2</sub> dimers on graphite [21, 177, 178]. In fact, Au clusters prefer perpendicular structures up to Au<sub>4</sub> within LSDA [179], which is argued to be because of Pauli repulsion effect [180]. We find a similar trend for Ag clusters in LSDA. We also found another parallel structure

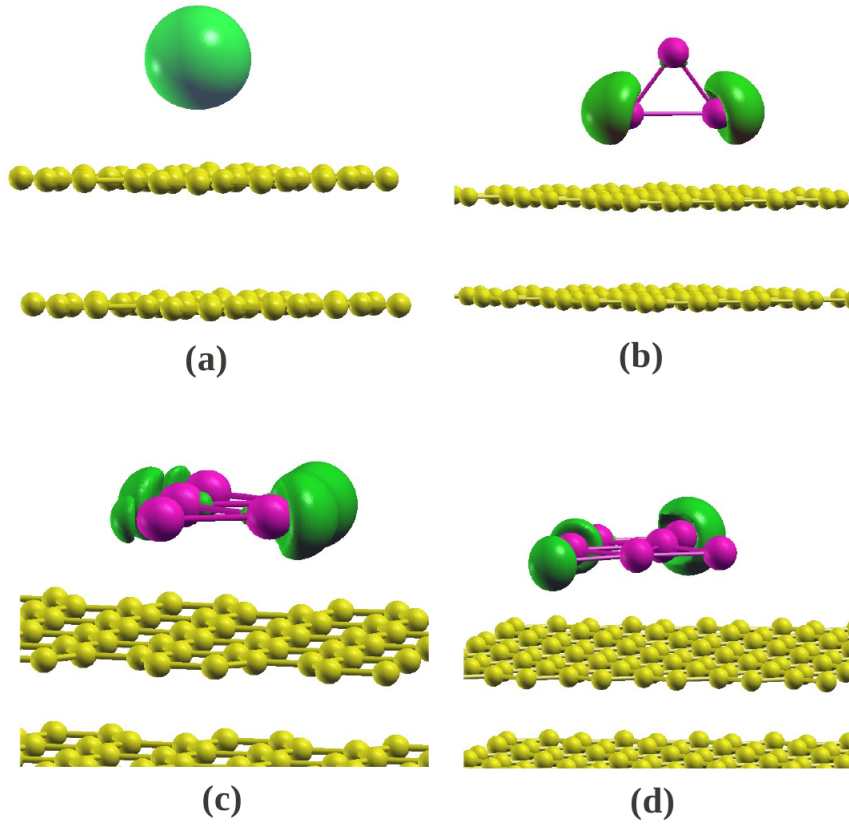


Figure 3.6: Spin density iso-surface plots for Ag adatom (a), and gas phase ground state isomers of  $\text{Ag}_3$  (b),  $\text{Ag}_5$  (c) and  $\text{Ag}_7$  (d) clusters deposited on HOPG. Iso-surface is plotted at an isovalue  $45 \text{ electron}/\text{\AA}^3$ . Yellow circles represent carbon atoms of graphite sheet.

for  $\text{Ag}_2$  with both silver atoms near hollow sites. This structure is only 3 meV higher. Perpendicular structures at top sites are 20 meV higher than the lowest energy structure. In the lowest energy structure we found a negligible charge transfer from the cluster to the substrate.

*Ag<sub>3</sub> cluster:*  $\text{Ag}_3$  turns out to be rather unusual among all the clusters we have studied here. The lowest energy structure for  $\text{Ag}_3$  is perpendicular to the surface (Fig. 3.7(c)). Of the clusters that have planar ground states in the gas phase,  $\text{Ag}_3$  is the only one that is perpendicular to the substrate in its lowest energy state after deposition.  $\text{Ag}_3$  is unusual in other ways also; there is a larger charge transfer from  $\text{Ag}_3$  to

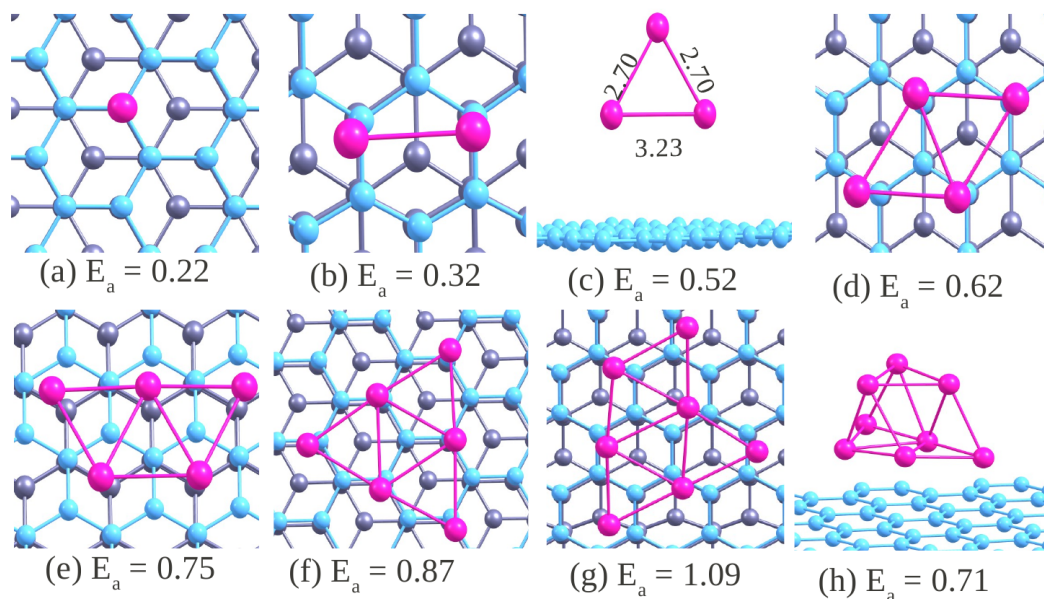


Figure 3.7: The ground state structures of  $\text{Ag}_n$  clusters deposited on a graphite substrate obtained using vdW-DF2. Here magenta colored circles represent Ag atoms, turquoise colored circles represent the top layer carbon atom of graphite and gray colored circles represent the bottom two carbon atoms of graphite.

the substrate than any other cluster. This leads to a greater reduction in the moment on the cluster (see Table 3.4). The remaining moment, however, is localized on the cluster as shown by the spin density iso-surface plot in Fig. 3.6(b). In the perpendicular structure, one of the Ag-Ag sides is parallel to the surface and the two Ag atoms are above top sites. This has an adsorption energy  $E_a = 0.52$  eV.  $\text{Ag}_3$  also undergoes a large structural deformation. The Ag-Ag bond parallel to the substrate is elongated by as much as  $\sim 0.44$  Å (Fig. 3.7(c)), while the other two bonds undergo slight contractions from their gas phase values. A parallel structure with all Ag atoms over top sites is, however, only 4 meV higher (Fig. 3.8(a)). Another parallel structure with all Ag atoms near hollow sites is 13 meV higher than the lowest energy structure. Details of all the Ag clusters deposited on graphite are given in Table 3.4.

*Ag<sub>4</sub> cluster:* For  $\text{Ag}_4$  cluster again we find a parallel structure to have the lowest energy with all four Ag atoms near top sites (Fig. 3.7(d)). This has an adsorption energy of 0.62 eV. The cluster retains its gas phase geometry on the substrate with no change in Ag-Ag bond lengths. A parallel structure with all silver atoms over hollow sites is 9

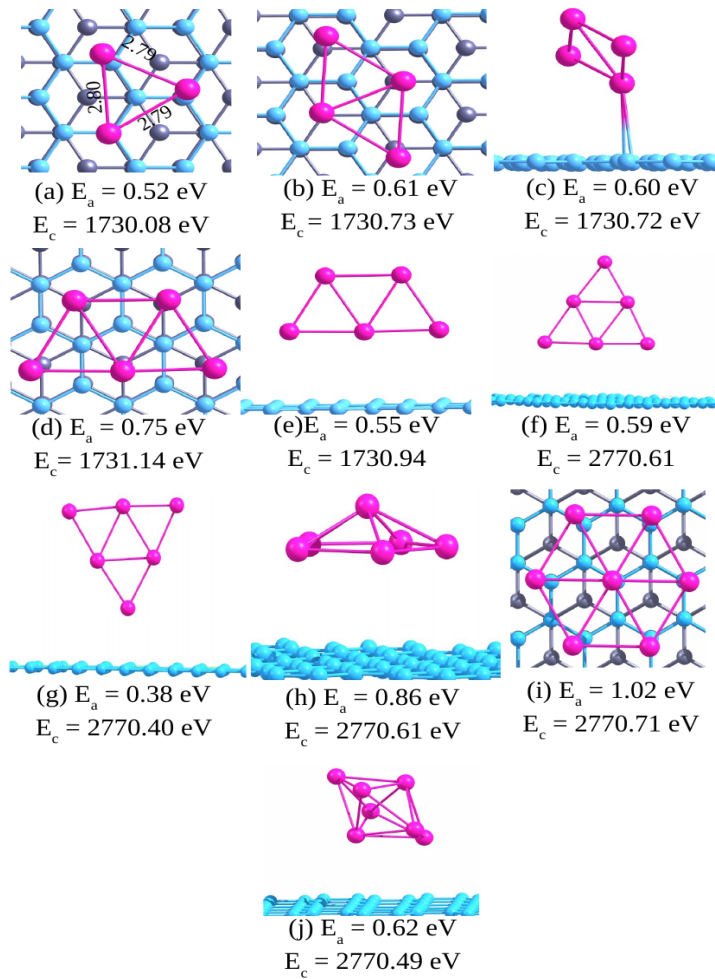


Figure 3.8: Some higher energy structures of Ag<sub>n</sub> clusters deposited on a graphite substrate obtained using vdW-DF2.

meV higher (Fig. 3.8(b)). A tilted structure (Fig. 3.8(c)) and a perpendicular structure with one of the Ag atoms above a top site are 18 meV and 27 meV higher than the lowest energy structure respectively. Gas phase Ag<sub>4</sub> cluster has four valence electrons and is a singlet. There was no spin moment after its deposition on the substrate either, neither was there any charge transfer between the cluster and the substrate.

*Ag<sub>5</sub> cluster:* For Ag<sub>5</sub> cluster, we deposited the GPGS structure (Fig. 3.5(d)) and the triangular bi-pyramid isomer (Fig. 3.5(e)). The planar GPGS isomer stays parallel to the surface with all the Ag atoms above or near top sites. It has the highest  $E_a = 0.75$  eV (Fig. 3.7(e)). This structure also has the highest  $E_c$  among all the structures

Table 3.4: Details of silver clusters on graphite from vdW-DF2 studies.  $E_a$  and  $E_c$  are the adsorption energy and cohesive energy respectively;  $M$  is the magnetic moment and  $q$  is the charge transfer from the cluster to surface in terms of electronic charge.  $Z_r$  denotes the maximum relaxation of the C atoms on the top layer and  $\Delta Z_c$  represents the maximum deviation of a top layer C atom from their average position.

Size	Fig. reference	$E_a$ (eV)	$E_c$ (eV)	$M$ ( $\mu_B$ )	$q$ (e)	$Z_r$ ( $\text{\AA}$ )	$\Delta Z_c$ ( $\text{\AA}$ )
1	3.7(a)	0.22	922.17	0.99	0.01	-0.05	-0.01
2	3.7(b)	0.32	922.76	0.00	0.02	-0.08	-0.03
3	3.7(c)	0.52	1730.08	0.80	0.16	-0.06	-0.02
4	3.7(d)	0.62	1730.74	0.00	0.04	-0.09	-0.03
5	3.7(e)	0.75	1731.15	0.96	0.05	-0.10	-0.04
6	3.7(f)	0.87	2770.89	0.00	0.06	-0.10	-0.05
7	3.7(g)	1.09	2770.78	0.95	0.07	-0.07	-0.03
8	3.7(h)	0.71	3232.32	0.00	0.04	-0.07	-0.05

for deposited  $\text{Ag}_5$  clusters. The average distance between C and Ag atoms is found to be quite large. In the present case it is 3.6  $\text{\AA}$ . There is little impact of the substrate on the Ag-Ag bond lengths in the cluster. They increase only by 0.01  $\text{\AA}$ . Two other structures are obtained from deposition of the GPGS isomer. A parallel structure with all silver atoms over hollow sites is only 7 meV higher (Fig. 3.8(d)) than the previous structure. A perpendicular structure with the Ag-Ag-Ag side parallel to the plane of graphite is nearly 0.2 eV higher (Fig. 3.8(e)). Interestingly, the triangular bi-pyramid isomer has an adsorption energy 1.4 eV in its lowest energy state on the surface, much larger than that of the ground state isomer. After deposition, this isomer loses its non-planar structure, and goes to the the same structure as the GPGS Fig. 3.7(e). Thus it is the interaction with the substrate that transforms the triangular bi-pyramid isomer to the planar isomer without any energy barrier. In the gas phase, they are obviously separated by a barrier. A higher energy in the gas phase leads to a higher  $E_a$  for the triangular bi-pyramid isomer.

An  $\text{Ag}_5$  cluster has one unpaired electron in the gas phase. The moment remains intact even after deposition on the substrate. The spin density iso-surface plot for the lowest energy adsorbed structure for the GPGS isomer shows that it is located entirely on the cluster (Fig. 3.6(c)). This is consistent with the fact that we do not find any charge transfer between the cluster and the substrate in our Bader charge analysis.

*Ag<sub>6</sub> cluster:* Ag<sub>6</sub> cluster follows the trend of preference for parallel structures and top sites. The GPGS isomer prefers to stay parallel to the surface with all silver atoms close to the top sites (Fig. 3.7(f)). This structure has the highest  $E_c$  and highest  $E_a = 0.87$  eV. In this case also, the average Ag-C distance is 3.6 Å, which indicates a weak interaction between the cluster and the substrate. All Ag-Ag bond lengths increase marginally by 0.01 Å from their gas phase values. A parallel structure with the Ag atoms above hollow sites is only 6 meV higher. We also found two perpendicular structures for the planar isomer. The structure with one of its sides parallel to substrate (Fig. 3.8(f)) is  $\sim 0.3$  eV higher than the lowest energy structure, while the one with an Ag vertex close to the surface (Fig. 3.8(g)) is  $\sim 0.5$  eV higher. Ag<sub>6</sub> cluster has no magnetic moment in the gas phase. A weak interaction with the substrate ensures that there is no moment after deposition also. The pentagonal pyramid isomer (Fig. 3.5(g)), in its lowest energy structure after deposition, has an adoption energy 0.86 eV, only 9 meV lower than the lowest energy structure. This structure retains its gas phase geometry over the substrate (Fig. 3.8(h)).

*Ag<sub>7</sub> cluster:* We deposited five gas phase isomers of Ag<sub>7</sub> (Fig. 3.5(h-l)). Interestingly, in its lowest energy structure, the centered hexagon (Fig. 3.5(k)) deformed to the low symmetry planar isomer (Fig. 3.5(j)) after deposition as shown in Fig. 3.7(g). This structure has the highest adsorption energy ( $E_a = 1.09$  eV) as also the highest cohesive energy among all the deposited Ag<sub>7</sub> structures we have found. We also found one more structure from the centered hexagon where it retained its gas phase geometry (Fig. 3.8(i)) and had a slightly lower  $E_a$  (1.02 eV). Deposition of the pentagonal bi-pyramid, the GPGS isomer, gives a lower adsorption energy of 0.62 eV. It undergoes a minor distortion after adsorption (Fig. 3.8(j)) with the Ag-Ag bond lengths now varying between 2.87 to 2.92 Å. The other two gas phase isomers, tri-capped tetrahedron (Fig. 3.5(i)) and the capped prism (Fig. 3.5(k)) have  $E_a$ 's of 0.71 eV and 0.83 eV respectively. The first of these largely retains its gas phase structure. Interestingly, the second one transforms to a pentagonal bi-pyramid after deposition. A higher gas phase energy leads to a higher  $E_a$  for the capped prism compared to the gas phase pentagonal bi-pyramid.

Ag<sub>7</sub> cluster has one unpaired electron in the gas phase which is retained after deposition. In the lowest energy structure obtained from the gas phase ground state, the moment turns out to be 0.95  $\mu_B$ . Spin density iso-surface plot in Fig 3.6(d) again shows

Table 3.5: Adsorption energy  $E_a$  and magnetic moment silver adatom at various points on a graphite substrate obtained using LSDA.

Site	$E_a$ (eV)	$M$ ( $\mu_B$ )
$\beta$	0.379	0.82
$\alpha$	0.376	0.85
bridge	0.370	0.82
hollow	0.307	0.90

that the moment is entirely localized on the cluster.

*Ag<sub>8</sub> cluster:* We deposited six gas phase isomers of Ag<sub>8</sub> shown in Fig. 3.5, each with a number of random orientations. We obtained a large number of stable structures from these, and present some of the low energy structures in detail. After deposition the bco2 (Fig. 3.5(r)) turned out to have the highest adsorption energy  $E_a = 0.71$  eV (Fig. 3.7(h)). It prefers an orientation in which five of the Ag atoms are close to the substrate without any significant distortion of its structure. In fact, this structure turns out to have the highest  $E_c$  among all deposited Ag<sub>8</sub> structures we have found. A low total energy after deposition and a high gas phase energy leads to a large  $E_a$ . The GPGS isomer (Fig. 3.5(m)) also retains its structure after deposition (Fig. A.3(a)). However, since only three Ag atoms can get close to the surface, it has an  $E_c$  that is 12 meV smaller than the previous structure (Fig. 3.7(h)). Because of a lower gas phase energy, its  $E_a$  is also smaller, and is 0.61 eV. Structures, adsorption energies and cohesive energies for the other isomers in their lowest energy structures after deposition are given in Fig. A.3 in the Appendix. The bco1 (Fig. 3.5(n)) cluster changes to an anti-prism structure (Fig. A.3(b)) after deposition with adsorption energies of 0.57 eV. The gas phase anti-prism isomers (Fig. 3.5(o,p)) are adsorbed with adsorption energies of 0.61 and 0.70 eV respectively (Fig. A.3(c,d)). The capped pentagonal bi-pyramid isomer (Fig. 3.5(q)) is adsorbed with an adsorption energy 0.64 eV. Ag<sub>8</sub> being an even electron cluster does not have any moment, and no moment was found after deposition either.

In all these structures, we observed that for a particular size, except for Ag<sub>3</sub> cluster, the isomer which have large Ag-C interactions after deposition, have high cohesive energies. For example, among the two high energy isomers of deposited Ag<sub>5</sub> cluster (shown in Fig. 3.8(d,e)), a parallel structure with larger number of Ag-C bonds has higher cohesive energy in comparison to the the perpendicular structure. Secondly,

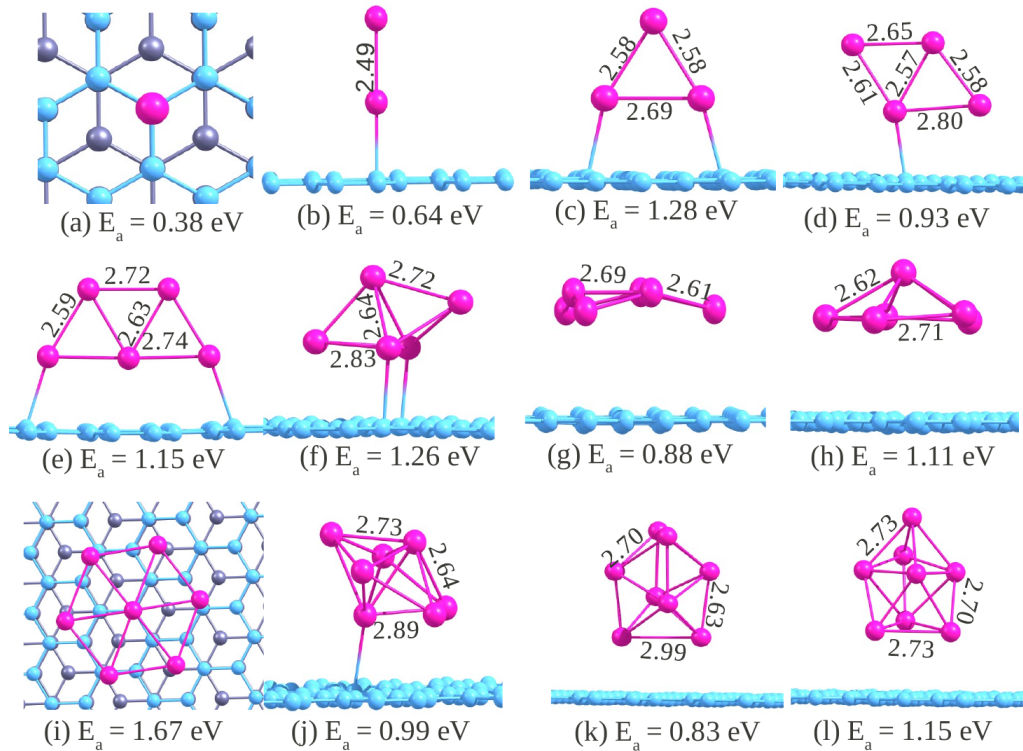


Figure 3.9: Some low-energy structures of  $\text{Ag}_n$  clusters deposited on a graphite substrate obtained using LSDA.

for a particular size a higher energy gas phase isomer having an  $E_c$  comparable to or higher than the GPGS isomer gives higher adsorption energy. In case of  $\text{Ag}_5$ , the GPGS structure gives the highest  $E_c$  after deposition as it has a large number of Ag-C bonds (all five Ag atoms above top sites). On the other hand, the triangular bi-pyramid, has the highest  $E_a$  as it has high gas phase energy than the GPGS structure. Interestingly, to gain the maximum benefits from the Ag-C bonding, it transforms to a planar structure after deposition.

For  $\text{Ag}_6$ , the deposited GPGS has all six Ag atoms close to the surface and consequently it has the highest  $E_c$ . On the other hand, the pentagonal pyramid isomer has high gas phase energy and that is why it has the highest  $E_a$ . An interesting point to note here is that unlike the pentagonal bi-pyramid isomer of  $\text{Ag}_5$ , it does not transform to a planar structure after deposition. The case of  $\text{Ag}_7$  is special in the sense that the isomer that has high energy in gas phase has the highest  $E_c$  and  $E_a$  after deposition.

Table 3.6: Properties of silver clusters deposited on a graphite substrate obtained with LSDA method. All notations are defined in Table 3.4.

Size	Fig. reference	$E_a$ (eV)	$E_c$ (eV)	M ( $\mu_B$ )	$q$ (e)	$Z_r$ ( $\text{\AA}$ )	$\Delta Z_c$ ( $\text{\AA}$ )
1	3.9(a)	0.38	968.96	0.83	0.05	0.06	0.07
2	3.9(b)	0.64	971.65	0.00	0.04	0.03	0.04
3	3.9(c)	1.28	1821.18	0.00	0.27	0.10	0.06
4	3.9(d)	0.93	1823.61	0.00	0.08	0.08	0.09
5	3.9(e)	1.15	1826.17	0.02	0.43	0.12	0.12
5	3.9(f)	1.26	1825.89	0.35	0.38	0.13	0.07
6	3.9(g)	0.88	2918.63	0.00	0.01	0.11	0.08
6	3.9(h)	1.11	2918.73	0.00	0.01	0.10	0.08
7	3.9(j)	0.99	2921.56	0.00	0.33	0.13	0.09
7	3.9(i)	1.67	2921.43	0.00	0.56	0.31	0.27
8	3.9(k)	0.83	3408.47	0.00	0.06	0.15	0.04
8	3.9(l)	1.15	3408.46	0.00	0.03	0.17	0.06

The 3D GPGS retains its structure after deposition and does not transform to a planar structure. For  $\text{Ag}_8$ , the bco2 isomer which has the largest number of Ag-C neighbors has the highest  $E_c$ . In this case also all the isomers retain their 3D structures after deposition. From this discussion it seems that only  $\text{Ag}_5$ , which has smaller number of Ag-Ag bonds, undergoes a transformation to a planar structure. For other sizes ( $n > 5$ ) where Ag-Ag interactions are large, clusters retain their structure after deposition. An exception to this is the capped prism isomer of  $\text{Ag}_7$  cluster, which transforms to the pentagonal bi-pyramid after deposition. All these facts indicate that a competition between maximizing Ag-Ag and Ag-C interactions determines the energetics of the deposited clusters.

### 3.6 A comparison between different methods

In this section, we compare the results obtained in vdW-DF2 method with those obtained using LSDA and DFT-D2 methods. The lowest energy structures of deposited silver clusters obtained using LSDA and DFT-D2 methods are given in Fig. 3.9 and Fig. 3.10 respectively.

**LSDA results:** An Ag adatom prefers the  $\beta$ -site (Fig. 3.9(a)) followed by the  $\alpha$ , bridge and hollow sites (Table 3.5.). This is very similar to what we obtained in vdW-

DF2 method except that the adsorption energies in LSDA are larger (which is usually the case [156]). For all other sizes we generated a number of structures using our random rotation technique and optimized them to the nearest local minima. In LSDA a dimer prefers to stay perpendicular to the surface with a preference for the  $\beta$ -site in a complete contrast to vdW-DF2. It has an adsorption energy 0.64 eV. Adsorption over graphite also does not bring about any structural change in the  $\text{Ag}_2$  dimer. The gas phase dimer has a bond length of 2.49 Å (in LDA) which essentially remains unchanged (2.5 Å) after adsorption. We did not find any dimer parallel to the surface. We deliberately constructed initial structures with the dimer perfectly parallel to the surface. But the dimer became perpendicular to the surface after optimization. At the bridge site the adsorption energy of dimer is marginally lower, 0.63 eV. There were no dimers close to the hollow sites. We did not find any charge transfer between cluster and surface. Similarly, for an  $\text{Ag}_3$  cluster, we only found structures with its triangular plane perpendicular to the substrate. In the lowest energy structure an Ag-Ag side stays parallel to the surface (Fig 3.9(c)).  $\text{Ag}_3$  is an isosceles triangle in the gas phase with two sides equal to 2.60 Å, and the third one being 2.61 Å. After adsorption the side close to the surface elongates to 2.69 Å and the other two sides of the triangle are compressed to 2.58 Å. This structure has an adsorption energy 1.28 eV. There is a jump in  $E_a$  for  $\text{Ag}_3$  from those of the adatom and the dimer, though  $E_a$  per atom remains of the same order. For a comparison we list the adsorption energies for all the sizes in Table 3.6. In the lowest energy structure the  $\text{Ag}_3$  cluster on graphite loses its moment. Bader analysis shows a charge transfer of  $0.27e$  from the  $\text{Ag}_3$  cluster to the graphite substrate. In case of  $\text{Ag}_4$  also, we only find structures with the plane of  $\text{Ag}_4$  perpendicular to the substrate. A structure having an Ag-Ag side parallel to the substrate with one Ag atom close to an  $\alpha$  site and another close to a  $\beta$  site has the largest  $E_a$  of 0.93 eV (Fig 3.9(d)). Thus, there is a marked decrease in  $E_a$ , and more so in  $E_a$  per atom compared to  $\text{Ag}_3$ .

Up to  $\text{Ag}_4$  all the stable structures after deposition had the plane of the clusters perpendicular to the substrate.  $\text{Ag}_5$  is the smallest size at which we got stable structures with the cluster plane tilts away from a perfectly perpendicular orientation. However, the lowest energy structure still has the cluster plane perpendicular to the substrate (Figure 3.9(e)). The parallel structure is 0.3 eV less stable than the perpendicular structure. This is opposite to what we found in vdW-DF2 methods, where a perpendicular structure is 0.2 eV less stable than the parallel structure. The adsorption energy of the  $\text{Ag}_5$

cluster in its lowest energy configuration (perpendicular orientation) is 1.15 eV. There is a marked increase in  $E_a$  from  $\text{Ag}_4$  to  $\text{Ag}_5$ . Bader analysis for the lowest energy structure revealed a charge transfer of  $0.43e$  from the cluster to the substrate. As a result the moment of the gas phase cluster is essentially lost (moment after deposition is  $0.02 \mu_B$ ). For GPGS structure of  $\text{Ag}_6$ , a parallel configuration is 78 meV lower in energy than the perpendicular structure. This is the smallest size at which the lowest energy structure is parallel. This structure has an adsorption energy of 0.88 eV (Figure 3.9(g)). In this case also, we did not find any charge transfer from cluster to surface.

Table 3.6 lists data for two different isomers each of size 5, 6, 7, and 8 obtained within LSDA. For  $\text{Ag}_5$ , the triangular bi-pyramid (Fig. A.1(e)), which is 0.38 eV higher than the GPGS structure (Fig. A.1(d)), has high adsorption energy ( $\sim 1.26$  eV) after deposition. The GPGS structure of  $\text{Ag}_5$  has the highest  $E_c$  (Table 3.6) due to large number of Ag-C bonds. Unlike vdW-DF2 method, the triangular bi-pyramid isomer retains its structure after deposition Fig. 3.9(f). Similarly, for  $\text{Ag}_6$ , the pentagonal pyramid (Fig. A.1(g)), which is 0.12 eV higher than the GPGS structure (Fig. A.1(f)), has the highest adsorption energy after deposition (Fig. 3.9(g,h)). On the other hand, the deposited GPGS structure, which is parallel and has large Ag-C bonds has the highest cohesive energy.

For  $\text{Ag}_7$ , a planar centered hexagon (Fig. A.1(k)), which is 0.81 eV higher than the GPGS pentagonal bi-pyramid, has the highest adsorption energy ( $E_a = 1.67$  eV) (Fig. 3.9(i)). Interestingly, the same structure also has the largest cohesive energy  $E_c$  after deposition as it has a larger number of Ag-C bonds in comparison to the non-planar pentagonal bi-pyramid structure. The deposition of GPGS structure (pentagonal bi-pyramid) (Fig. A.1(i)) has a smaller adsorption energy ( $E_a = 0.10$  eV) and retains its structure. This is similar to what we found in the vdW-DF2 method. Interestingly, after deposition of the centered hexagon, the spin on the  $\text{Ag}_7$  cluster is lost. This is due to an appreciable charge transfer from the cluster to the substrate. For  $\text{Ag}_8$ , the highest adsorption energy is obtained for the anti-prism structure (Fig. 3.9(l)), which is 0.33 eV higher than the  $E_a$  of the GPGS bco1 structure. After deposition this structure converts to the bco1 isomer (Figure 3.9(l)) with one of the faces parallel to the plane of graphite. The highest  $E_c$  is obtained from deposition of GPGS bco1 structure.

All odd sized clusters, except for the adatom, transfer their charges to the graphite substrate. This causes a stronger bonding between the cluster and the surface (Ta-

Table 3.7: Properties of a silver adatom at various points on a graphite substrate obtained using DFT-D2.  $E_a$  is the adsorption energy,  $E_{\text{disp}}^{\text{Ag-C}}$  is the Ag-C dispersion contribution, and  $M$  is the magnetic moment in the system.

Site	$E_a$ (eV)	$E_{\text{disp}}^{\text{Ag-C}}$ (eV)	$M$ ( $\mu_B$ )
hollow	0.496	-0.290	0.99
$\alpha$	0.486	-0.273	0.99
$\beta$	0.487	-0.280	0.98
bridge	0.484	-0.297	0.98

ble 3.6). We see an even-odd oscillation in adsorption energy with size. Clusters up to  $\text{Ag}_5$  stay perpendicular to the surface.  $\text{Ag}_6$  onwards, clusters prefer to stay parallel to the surface. Clearly there is a transition from perpendicular to parallel structures with size. Similar behavior has been seen for gold clusters supported over graphite [169, 179], where transformation from perpendicular to parallel structures occurred for a four-atom cluster. This behavior has been explained in terms of Pauli-repulsion interaction [180]. When a cluster is deposited over the surface, apart from the attractive interactions, repulsive interactions arise due to the occupied orbitals of the adsorbate and the substrate. At smaller sizes, attraction due Ag-C bonding is small in comparison to the Pauli-repulsion term, and clusters try to stay perpendicular to the substrate in order to minimize their energy. As the size increases, number of Ag-C bonds increases. The attraction dominates over the repulsion term, and the clusters prefer parallel configurations.

**DFT-D2 results:** In DFT-D2 method, the hollow site turns out to be most favorable for an Ag adatom. This is in agreement with the calculations of Amft *et al.*, [169] but is contrary to the experimental observations of Ref. [12, 14]. Clearly, this preference for the hollow site is an effect of the semi-classical dispersion correction term. This term over-emphasizes the pair-wise interactions between the C and Ag atoms. At the hollow site an Ag atom can benefit from its interactions with six neighboring C atoms, while at the top site it can benefit from only one C atom. We list the adsorption energy  $E_a$  and dispersion energy  $E_{\text{disp}}^{\text{Ag-C}}$  at all four sites in Table 3.7. Although  $E_{\text{disp}}^{\text{Ag-C}}$  is marginally higher at the bridge site (in magnitude) than at the hollow site, its contribution at the hollow site is 10 meV higher than that at the  $\beta$ -site. This pair-wise interaction seems to dominate the energetics of other Ag clusters also. A dimer prefers to stay parallel

to the substrate with both silver atoms over hollow sites with an adsorption energy  $E_a = 0.52$  eV (Figure 3.10(b)). This parallel structure is 35 meV more stable than a perpendicular dimer at the  $\beta$  site. The dimer elongated marginally to 2.59 Å after deposition from a gas phase bond-length of 2.58 Å (in DFT-D2). We do not find any charge transfer from the dimer to the graphite surface.

In case of  $\text{Ag}_3$ , the lowest energy structure is exactly what was found in LSDA and vdW-DF2: the  $\text{Ag}_3$  plane perpendicular to the substrate, and two Ag atoms close to  $\alpha$  and  $\beta$  sites (Figure 3.10(c)). After deposition, the Ag-Ag side close to the substrate is elongated by 0.02 Å and the other two sides are compressed by 0.12 Å. This has an adsorption energy of 1.13 eV. Again, there is a sharp increase in  $E_a$  compared to  $\text{Ag}_2$ , just as we found in LDA. Bader analysis shows a transfer of  $0.51e$  from the cluster to the substrate. A parallel structure with all three Ag atoms over hollow sites is 11 meV higher in energy.

For the  $\text{Ag}_4$  cluster, similar to the vdW-DF2 method, the lowest energy structure is parallel to the surface. Here all Ag atoms prefer to stay above hollow sites (Figure 3.10(d)) instead of top sites. This structure has an adsorption energy  $E_a = 1.01$  eV, which is slightly smaller compared to the  $\text{Ag}_3$  cluster. A parallel structure with all four silver atoms close to top sites is 50 meV higher than the ground state structure. For  $\text{Ag}_5$  also, the GPGS structure prefers a parallel structure with all Ag atoms close to hollow sites (Figure 3.10(e)). This structure has an adsorption energy  $E_a = 1.26$  eV. It also has the highest  $E_c$  among all deposited  $\text{Ag}_5$  isomers as it has a large number of Ag-C interactions. There is an increase in  $E_a$  compared to  $\text{Ag}_4$ . The cluster transfers a charge of  $0.25e$  to the graphite surface.

Similar to other methods, the high energy isomers of  $\text{Ag}_5$ ,  $\text{Ag}_7$ , and  $\text{Ag}_8$  give higher adsorption energies than their GPGS structures after deposition. In case of  $\text{Ag}_5$ , the triangular bi-pyramid structure (Fig. A.2(g)), which is 0.15 eV higher than the GPGS structure in DFT-D2, gives the highest adsorption energy after deposition. Interestingly, it transforms to a planar structure on the substrate (Fig. 3.10(e)) as in vdW-DF2. In case of  $\text{Ag}_7$ , the centered hexagon planar isomer (Fig. A.2(k)), which is 0.59 eV higher than the GPGS structure (Fig. A.2(h)), gives the highest adsorption energy (1.836 eV) after deposition (Fig. 3.10(g)). The same structure also gives the highest  $E_c$  as it has seven Ag atoms close to the surface. In this structure, the  $\text{Ag}_7$  cluster lost its magnetic moment partially and is left only with  $0.18 \mu_B$ . We also found

a charge transfer of  $0.58e$  from the cluster to the substrate. Adsorption of pentagonal bi-pyramid gives a lower adsorption energy of 0.10 eV. Similarly, for the  $\text{Ag}_8$  cluster, the highest  $E_c$  and  $E_a$  are obtained for a capped pentagonal bi-pyramid (Fig. A.2(p)). After deposition it converts to the bco2 structure (Fig. 3.10(h)), and have five Ag atoms close to the surface.

An exception to the above fact is found for  $\text{Ag}_6$  cluster, where a deposited GPGS structure gives highest  $E_c$  and  $E_a$ . In this case the GPGS structure favors a parallel orientation with all silver atoms close to hollow sites (Figure 3.10(f)) and has an  $E_a$  of 1.42 eV. The same structure also gives the highest  $E_c$  as it has six Ag atoms near to the surface. The pentagonal pyramid which is 0.15 eV higher in gas phase, gives a lower adsorption energy of 1.39 eV, 25 meV lower than the GPGS structure. This is opposite to the LSDA studies where the high energy isomer of  $\text{Ag}_6$  led to higher  $E_a$ . For the deposited GPGS structure (Figure 3.10(f)), Ag-C dispersion contributions are maximum and  $E_{\text{disp}}^{\text{Ag-C}}$  has the value of  $-1.62$  eV, whereas for pentagonal pyramid  $E_{\text{disp}}^{\text{Ag-C}} = -1.35$  eV.

In all the above structures (DFT-D2) all Ag atoms of the clusters prefer to stay above hollow sites. Similar to the LSDA results, we found a larger charge transfer from odd sized clusters and an even-odd oscillation in adsorption energy with cluster size.

Hence, both LSDA and vdW-DF2 methods give the top site to be most preferable for an Ag adatom, which is in agreement with the experimental observations [12, 14]. On the contrary, DFT-D2 method results in a hollow site to be most favorable. For a dimer, both DFT-D2 (Fig. 3.10(b)) and vdW-DF2 result in a parallel orientation in the ground state, while LSDA predicts a perpendicular structure Fig. 3.9(b). Also for the planar clusters of size 4, 5, 6, and 7, both DFT-D2 and vdW-DF2 methods give parallel orientations in the ground states. For 3D clusters (at size 8) the structure which has maximum number of Ag-C interaction, is most stable (large  $E_c$ ). Hence, in both these methods, the low energy structures are determined by the competition between the Ag-Ag and Ag-C bonding. The main difference is found in terms of adsorption sites. Within DFT-D2, the pair-wise term dominates at all cluster sizes and all Ag atoms prefer hollow sites, while in vdW-DF2 they prefer the top sites. In contrast to these, the low energy structures in LSDA are determined by the competition between the attractive electronic binding and Pauli-repulsion interactions. Hence, up to size five

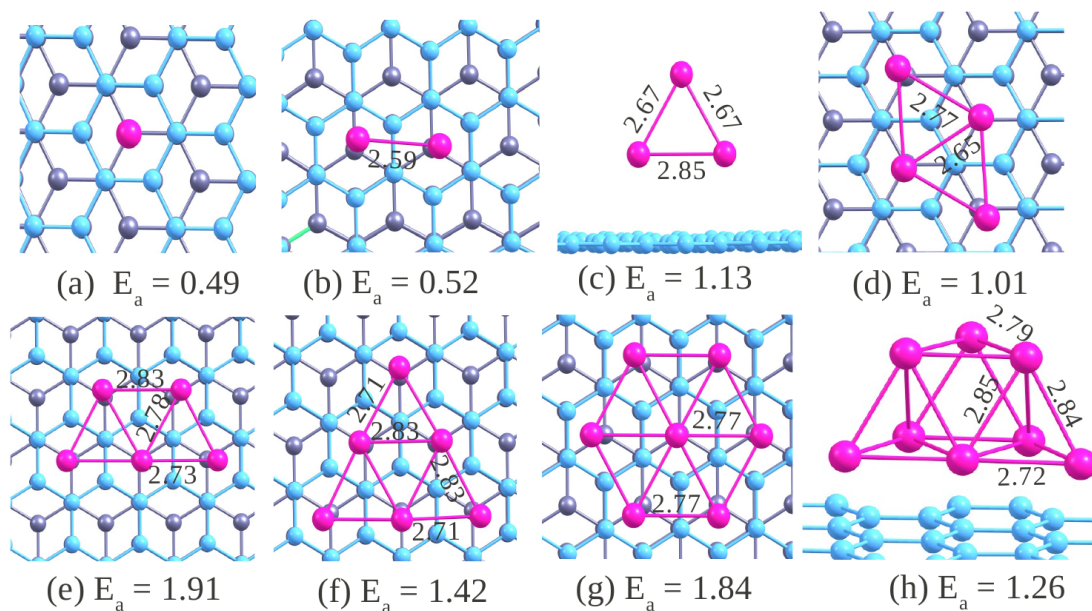


Figure 3.10: Some low-energy structures of  $\text{Ag}_n$  clusters deposited on a graphite substrate using DFT-D2.

(Fig. 3.9(a-e)), silver clusters prefer to stay perpendicular to the surface. As the cluster size increases, the number of Ag-C bonds increases. Consequently, the attractive interactions overcome the repulsive interactions and deposited clusters (for size 6, 7, and 8) prefer the those structures (orientation) which have large Ag-C interaction.

For an  $\text{Ag}_3$  cluster, all three methods give a perpendicular orientation in the ground state with different adsorption site preferences. Within vdW-DF2 and LSDA, an Ag-Ag side stays parallel to the surface with both Ag atoms above top sites, while in DFT-D2, both Ag atoms of the Ag-Ag side prefer to stay above hollow sites (Fig. 3.10(c)). Perpendicular orientation in LSDA can be explained by means of Pauli-repulsion interactions, but why DFT-D2 and vdW-DF2 give perpendicular orientations in the ground state is not clear. However, it has to be noted that the difference between the lowest energy structures and the next higher energy structures in both DFT-D2 and vdW-DF2 are quite small (11 and 4 meV respectively).

In LSDA and DFT-D2, there is an odd-even oscillation in the adsorption energies with changing cluster size. No such effect was found in vdW-DF2. This is probably related to the oscillation in the amount of charge transfer from the cluster to the substrate produced by LSDA and DFT-D2. vdW-DF2 predict no charge transfer at any size.

Table 3.8: Properties of silver clusters deposited on a graphite substrate obtained with DFT-D2 method. All notations are defined in Table 3.4 and Table 3.7.

Size	Fig. reference	$E_a$ (eV)	$E_c$ (eV)	$E_{\text{disp}}^{\text{Ag-C}}$ (eV)	$M$ ( $\mu_B$ )	$q$ (e)	$Z_r$ ( $\text{\AA}$ )	$\Delta Z_c$ ( $\text{\AA}$ )
1	3.10(a)	0.50	892.16	-0.29	0.99	0.02	0.04	0.01
2	3.10(b)	0.52	894.46	-0.55	0.00	0.02	0.05	0.04
3	3.10(c)	1.13	1676.34	-0.75	0.26	0.50	0.06	0.04
4	3.10(d)	1.01	1678.60	-1.17	0.06	0.13	0.08	0.07
5	3.10(e)	1.91	1680.89	-1.26	0.74	0.24	0.07	0.02
6	3.10(f)	1.42	2686.86	-1.62	0.00	0.05	0.29	0.07
7	3.10(g)	1.84	2688.86	-2.21	0.18	0.58	0.22	0.10
8	3.10(h)	1.26	3136.87	-1.65	0.00	0.03	0.12	0.09

As a consequence, electronic and magnetic properties of the gas phase clusters are retained within this method. This behavior is in the agreement with the experimental observations of Lopez-Salido *et. al.* [166].

### 3.7 Conclusions

In summary we have performed a systematic study of deposition of pre-formed silver clusters containing up to eight atoms on a graphite(0001) substrate using the vdW-DF2 non-local correlation method. Before deposition, ground state structures of the gas phase clusters were obtained using a global search method employing evolutionary algorithm. Top sites are found to be most favorable for an Ag adatom followed by the bridge and the hollow sites. This is in agreement with the experiments of Ganz *et al.*, [12] and Ndlovu *et al.*, [14] An  $\text{Ag}_2$  dimer prefers a parallel orientation. For larger clusters a competition between maximizing Ag-Ag and Ag-C interactions plays a major role determining the energetics after deposition. Clusters having planar structures in the gas phase prefer parallel orientations so that they can take advantage of a larger number of Ag-C neighbors. Only  $\text{Ag}_3$  turns out to be an exception. Most of the clusters retain their gas phase structures with only minor changes in bond lengths after deposition. This is in agreement with the experiments of Busolt *et al.*, [13, 73] An exception to this is the non-planar gas phase isomer of  $\text{Ag}_5$  which becomes parallel after deposition without any energy barrier. We do not find any charge transfer between

the clusters and the substrate any any size. Other exchange-correlation functionals like LSDA and DFT-D2 produce different results. There are some similarities between LSDA and DFT-D2 results (charge transfer), and some similarities between the DFT-D2 and vdW-DF2 results (preference for parallel orientations). But overall, each one of them give qualitatively different answers. Out of these, the conclusions from the vdW-DF2 calculations that small pre-formed silver clusters deposited on HOPG retain their structures (and hence electronic properties), and that there is no charge transfer are consistent with the experimental observations [73, 166]. The DFT-D2 result that an isolated Ag atom prefers a hollow site is contrary to experiments [12, 14]. Therefore, the main conclusion is that one needs to use methods based on non-local correlations functionals, vdW-DF2 for example, to account for the dispersion interactions in this system.

# Adsorption and diffusion of small silver clusters ( $n = 1 - 8$ ) on a stepped graphite surface

## 4.1 Introduction

A perfectly clean surface is an idealization and defects are inevitable in any surfaces found in nature. Atomic arrangements in real surfaces do not follow a perfect pattern, and all real surfaces have vacancies, adatoms and other point defects, steps *etc.* Adsorption of clusters on these surfaces is very different than that on clean surfaces. Some of these defects may have strong bindings with the clusters. In case of inert surfaces, which have rapid diffusion of the clusters at room temperature, sometimes defects are deliberately created [181] to fabricate ordered cluster arrays. The process of cluster deposition with high impact energy itself can produce defects on the surface.

The defect formation on graphite surface is also very natural and the deposition of clusters on these defected surfaces show very interesting properties. Particularly, deposition of silver clusters on stepped graphite surfaces has drawn special attention [12, 15-17, 19, 181--186]. A number of experimental groups have studied structure and diffusion of silver clusters on stepped graphite surface. Two different methods have been employed to put silver clusters on these surfaces: (i) deposition of atomic vapor of silver, (ii) deposition of pre-formed clusters from a cluster source, either size-selected

or otherwise. Silver atoms in an atomic vapor, after deposition on the surface, form clusters, whose diffusion and structure have been studied using STM and SEM.

In one such study Francis *et al.*, [15] have examined the morphologies and diffusion of the silver clusters, fabricated by atomic deposition, over the step edges with varying temperature using SEM. A SEM image of graphite surface after deposition of Ag atoms at 20 °C is shown in Fig. 4.1(a). The image shows seven step edges of graphite. Most of the Ag clusters are nucleated on the wide terraces and on the step edges. Almost no clusters are found on the narrow terraces between two steps (bottom-left corner of Fig. 4.1(a)). Even on wider terraces, there is a zone near the steps denuded of any cluster. This clearly indicates that steps act as effective sinks for Ag adatoms, depleting adatom density around them and so preventing the nucleation of clusters nearby. The cluster density is found to be much higher at the steps than on the terraces. Clusters at the terraces have small irregular shapes, which indicate that the adatoms diffuse across terraces until they are stabilized in a group of small clusters. The size of clusters near step-edges vary between 1 to 10 nm, which indicates that clusters have reduced mobility along the step edge. As the temperature is increased, no cluster nucleation is found on terraces above 50 °C. In SEM images at 118 °C (a different sample, Fig. 4.1(b)), they did not find any cluster even on the wider terraces. All of them were found near the step edges. This indicates that at this temperature, the clusters are able to diffuse from the terraces onto the steps. This led to the growth of quasi-one dimensional cluster chains along the steps. Some of the clusters at the step edges have dumbbell shapes. In summary, all their observations imply that Ag adatoms and clusters diffuse easily on clean terraces even at room temperature. They may get trapped at the point defects on the terraces. Once they reach the steps, they can diffuse only along the step edges. Their dumbbell shapes indicate that their mobility along the steps is lower compared to that on the terraces. At higher temperatures, they are not trapped at the terraces at all.

As for deposition of pre-formed Ag clusters on graphite substrate, most of the experiments studied clusters that are few to a few hundred, or a few thousand atoms large. Francis *et al.*, [16] deposited Ag clusters from a beam that contained clusters containing a few to a few hundred atoms. Carroll *et al.*, [17] deposited  $\text{Ag}_n^+$  clusters containing 50-400 atoms on HOPG at room temperature and explored the trapping of deposited clusters at surface steps. Goldby *et al.*, [18] deposited Ag clusters containing 50-250

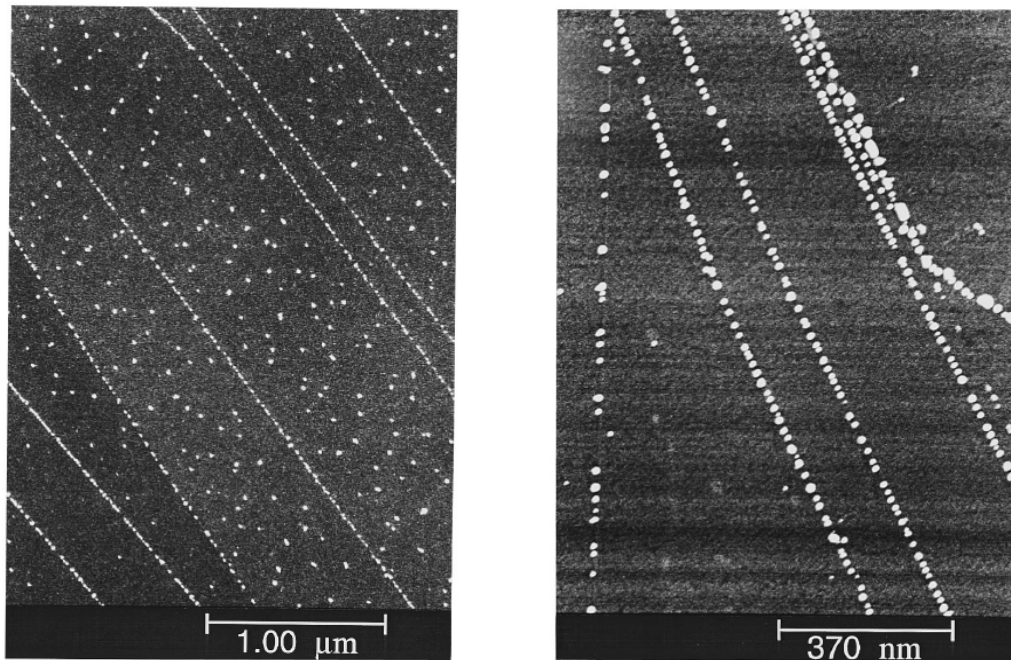


Figure 4.1: A SEM image showing Ag clusters on surface steps and terraces after deposition of Ag onto HOPG at (a) 20 °C and (b) 118 °C temperature [15].

atoms, whereas in a separate study Carroll *et al.*, [19] deposited size-selected Ag<sub>400</sub> clusters.

Francis *et al.*, [16] in their studies find that clusters (of average size of 160 atoms) deposited at low energy ( $\sim 50$  eV) are able to diffuse across the surface and tend to aggregate. Clusters deposited at higher energy ( $\sim 400$  eV) are pinned to the substrate and have limited diffusion and cluster aggregation. For low energy deposition, the deposited clusters aggregate on the terraces to form fractal islands consisting of about ten particles where average size of each particle is 9 nm. On the steps, the average size of each particle is 7 nm, smaller than those on the terraces. In the studies of Carroll *et al.*, [17] the size-selected Ag<sub>400 $\pm$ 30</sub> clusters, which were deposited with low impact energies (kinetic energy 0.125 eV/atom), found to be decorated as the cluster arrays along the step edges. No clusters were found on the terraces near step edges, revealing that clusters landing near a step had sufficient mobility to reach the step, allowing the production of organized cluster arrays. They also find that the clusters at the steps are larger( 3 – 6 nm) than the incident clusters. Goldby *et al.*, [18] and Carroll *et al.*, [19]

find that the particle size at the steps are smaller than that on the terraces. All these facts again indicate that clusters have lower mobility at the steps than on the terraces which prevents them from forming larger particles. They found that the size of the particles (particles are aggregates of clusters) on steps are smaller than those on the terraces. Also more clusters were found at the steps than on the terraces, which was explained by the presence of dangling bonds on the step edge carbon atoms. In a clean graphite surface, each carbon atom is  $sp^2$  hybridized and is covalently bonded to three neighboring carbon atoms. In case of stepped graphite surface, each edge carbon atom has only one or two neighboring carbon atoms which create dangling bonds on the step edges (discussed later). Clusters have reduced mobility along the step edge as they are strongly bonded to the dangling bonds of the step edge.

In a related work, Schmidt *et al.*, [182] deposited Ag clusters of mean diameter  $\sim 3$  nm on a graphite surface with point defects, steps, and pleats at room temperature. From their combined SEM and AFM studies, they found that the clusters can be trapped in the concavely curved borders of the pleats. However they stay mobile along direction of the pleats. The convex borders of the pleats are repulsive in nature. Step edges and defects act as a nucleation center and clusters once trapped remain immobile. Further cluster deposition lead to the formation of fractal island on point defects. Near the steps, islands with branches perpendicular to the steps are formed. This again points to reduced mobility along the step edges as compared to the defect-free terraces.

While these experiments produce an overall picture of diffusion and aggregation of silver adatoms and clusters on graphite, they cannot answer some of the details. For example, it is not clear whether, in the atomic vapor deposition, the clusters form on the terraces and then diffuse to the step edges, or the diffusing atoms reach steps, get trapped and then grow into clusters. These experiments also cannot give a detailed microscopic picture of diffusion of clusters on the terraces and at the step edges. Do step edges act as attractive sinks for adatoms and clusters? How do the atoms and clusters get trapped?

In this chapter we attempt to study adsorption and diffusion of Ag adatoms and clusters near a step on a graphite substrate. First-principles molecular dynamics calculations, as we perform here, of clusters containing a few tens or hundreds of atoms on substrates is beyond our computational capabilities. Therefore, we restrict our studies to adatoms and small clusters containing up to eight Ag atoms. Real surfaces contain

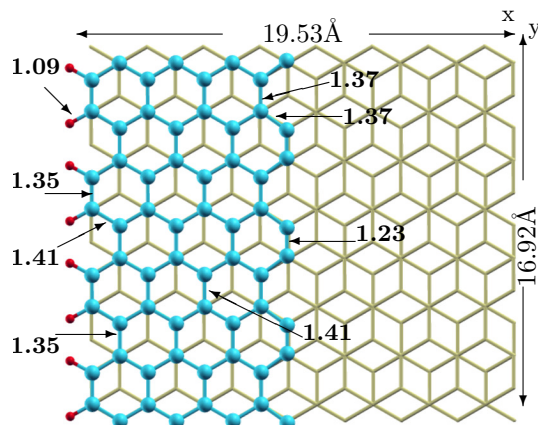


Figure 4.2: Structure of the a relaxed graphite surface with an arm-chair step edge. Bottom two layers are periodic in  $x$  and  $y$  directions. The step edge is periodic only in the  $y$  direction. Blue circle represent the carbon atoms of the top layer (step edge), while the green stick frame represent the lower graphite layers. Small red circles represent passivated hydrogen atoms.

steps that can be several atomic layers high. Again to keep the computations practical, we only considered monoatomic steps. While not exactly representing the experiments discussed above, these studies give an idea about adsorption and diffusion of small Ag clusters on the terrace and near the step edges of a graphite substrate, and give some qualitative understanding of these experiments.

The rest of the chapter is organized as follows. In section 4.2 we present the theoretical modeling used for our calculations. Later in various sections of this chapter, we present the atomic and electronic structure of the graphite step edge, the ground state structures and energetics for absorption of  $\text{Ag}_n$  ( $n = 1 - 8$ ) clusters on the step edge of graphite at 0 K, diffusion of  $\text{Ag}_5$  and  $\text{Ag}_8$  on this substrate annealed at 600 K, and the electronic structure of a stepped graphite with the step edge decorated by a self-assembled nanowire of Ag atoms. Finally we draw our conclusions in section 4.7.

## 4.2 Computational methods

The graphite substrate is represented in a repeated slab of three layers (AB stacking) with a vacuum of 15 Å. The monolayer step is created by cutting the top layer at the armchair edge as shown in Figure 4.2. This creates two armchair edges (as the system

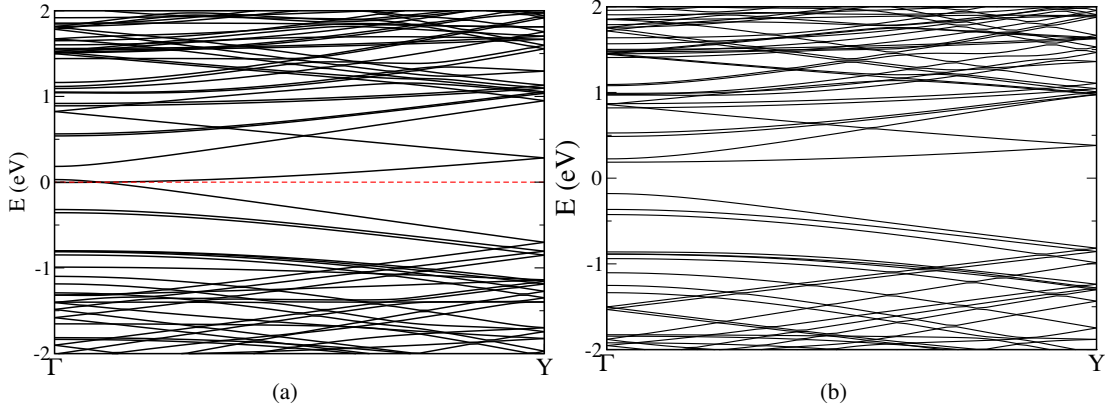


Figure 4.3: Band structures of the (a) unreconstructed and (b) reconstructed armchair step of graphite. Dotted red line represent the Fermi level.

is periodic). One of these is passivated by hydrogen atoms to mimic the semi-infinite nature of graphite terrace and other edge remains as it is. The bottom two layers extend in the  $xy$  plane and the step edge extends along the  $y$ -axis. Dimensions of the calculation supercell is  $19.53 \text{ \AA}$  in the  $x$ -direction, and  $16.92 \text{ \AA}$  along the  $y$ -direction (Figure 4.2). The distance between the step edge and its periodic image along the  $x$ -direction is  $10.12 \text{ \AA}$ , which is sufficiently large to avoid the interaction between the step and the passivating H atoms at the other edge. Only the bottom layer was kept fixed, while the middle layer and step layer were allowed to relax during the simulations.

The DFT calculations are performed using VASP [149, 150]. An energy cutoff of 400 eV is used for the plane-wave basis set to represent the wave functions. The BZ integrations are performed using only the  $\Gamma$ -point point as additional  $\mathbf{k}$ -points do not change the computed results. We have used L(S)DA for the exchange-correlation energy functional due to the following reasons. As mentioned in chapter 3, graphite is a layered material in which successive layers are held together by van der Waals forces. Both LDA and GGA functionals are unable to capture these interactions, however LDA produces a bonding between the successive layers. We also discussed that dispersion interactions have to be included for a proper description of bonding between Ag atoms and the C atoms on a clean graphite surface. But in this chapter, our main aim is to describe the adsorption of Ag clusters over a stepped graphite substrate. Step C atoms have dangling bonds that lead to formation of strong covalent Ag-C bonds. Therefore, we believe that L(S)DA would be sufficient to describe this system. We have indeed

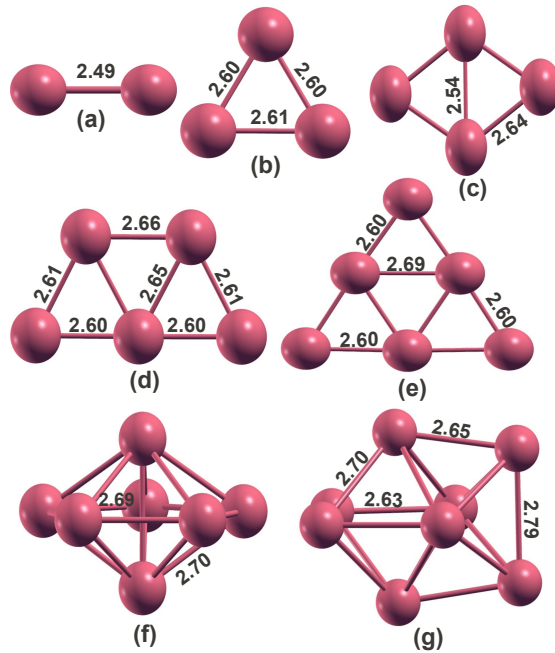


Figure 4.4: The ground state structures of gas phase  $\text{Ag}_n$  clusters ( $n = 2 - 8$ ) obtained using L(S)DA. Here large red colored circles represent Ag atoms.

found that L(S)DA and vdW-DF2 methods give qualitatively similar results for an Ag adatom and the  $\text{Ag}_2$  dimer. We will discuss these details in the later sections. Also, because of the increased computational cost of the vdW-DF2 calculations, the finite temperature MD calculations would be difficult to perform.

For adsorption of  $\text{Ag}_n$  ( $n = 1 - 8$ ) clusters, we considered several initial structures with different orientations using random rotation technique (section 2.7) near the step edge and optimized them to the nearest local minima using the CG method. Relative stability of the adsorbed structures for a given cluster size is measured by their adsorption energies  $E_a$  as defined in chapter 3.2.

As mentioned in the section 4.1, at low temperatures silver nano-structures have reduced mobility at the step edges, which indicates that there is an energy barrier for diffusion of adatoms and clusters along the steps. We try to have an estimate of the energy barrier for diffusion using the CINEB method. In MD calculations, the bath temperature is controlled by the Noé Hoover thermostat. The time step taken is 3 fs. We did not use hydrogen passivation of the dangling bonds in the MD simulations as a light element like H demands much smaller time step in the MD calculations which

made these calculations impractical. For these calculations, we increased the size of the supercell in  $x$ -direction to 24.67 Å so that the Ag atoms do not feel the presence of both the steps. This makes the size of the simulation box to 24.67 Å  $\times$  17.095 Å. These MD calculations are only performed for Ag<sub>5</sub> and Ag<sub>8</sub> clusters.

### 4.3 Band structure of a relaxed arm-chair step edge

One can have two different types of steps on the graphite (0001) surface: a zigzag step and an armchair step. A zigzag step has two dangling bonds per edge C atom (have one nearest neighbor), while an armchair edge has one dangling bond per edge C atom (have two nearest neighbors). As a consequence, the formation energy of a zigzag step is larger than that of an armchair step. To have a rough estimate, we calculated the formation energies of zigzag and armchair edges in a graphene sheet, and these are 1.43 eV/Å and 1.34 eV/Å respectively. For an unrelaxed armchair step, the edge states associated with the dangling bonds cross the Fermi level and show a metallic character (shown in Fig. 4.3(a)). However, a lower energy state is one in which pair of step-edge C atoms dimerize to open up a gap in the band structure (Fig. 4.3(b)). In the unrelaxed structure, the nearest neighbor (NN) C-C distance (the distance between an edge C atoms and its NN second-line C atom) at the armchair edge is 1.41 Å. After step-edge reconstruction, this distance becomes 1.37 Å. The structure of the stepped graphite slab after this reconstruction, and all the relevant bond lengths are shown in Fig. 4.2. The distance between two NN C atoms in the second line also becomes 1.37 Å. Alternate C atoms along the step edge form dimers with a C–C distance of 1.23 Å, which is very close to the triple bond of acetylene (1.20 Å).

### 4.4 Zero temperature adsorption of clusters

We now describe our results for deposition of Ag<sub>*n*</sub> clusters on a stepped graphite surface at zero temperature in detail. Ground state structures of the isolated clusters up to Ag<sub>8</sub> calculated with L(S)DA are shown in Fig. 4.4. Some high energy isomers along with the ground state structures of Ag<sub>*n*</sub> ( $n = 1 - 8$ ) are shown in Fig. A.1 in Appendix. In this chapter we will only deposit the ground state structures of gas phase.

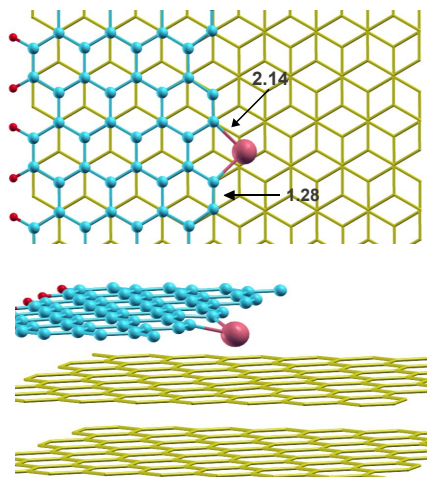


Figure 4.5: Structure of a stepped graphite surface with single Ag adatom adsorbed at an active site. Top and bottom panels show top and side views. Color coding is same as in Fig. 4.2 and Fig. 4.4

A silver adatom is very mobile on a clean graphite substrate [15, 19], which means that it can rapidly diffuse until it finds a step edge. Once it reaches the step, it binds to two carbon atoms belonging to two neighboring step dimers (Fig. 4.5) with an adsorption energy of 3.20 eV. We call this site the active site of the step. The Ag-C bond distance is found to be 2.14 Å, which is much smaller than the Ag-C distance of 2.36 Å (at the LSDA level) on a clean graphite layer. The adsorption energy is much lower ( $E_a = 0.38$  eV) on a clean surface. This contrast between a clean surface and a step edge indicates that there is a covalent bond formation between Ag and C atoms at the step edge, while on the clean graphite surface the Ag atom is physisorbed through van der Waal's forces (section 3.5). It is also worth noting here that vdW-DF2 functional [156] gives an adsorption energy of 1.33 eV for an Ag adatom at an active site. Although the vdW-DF2 adsorption energy is much lower than the LSDA value, it is much larger than that of an Ag adatom on a clean graphite, which is 0.21 eV (Table 3.3)), again indicating formation of covalent bonds, which has also been confirmed through partial charge density plot (discussed later). In its lowest energy structure, the distance between silver atom and the carbon layer below is 2.65 Å, which is larger than the sum of covalent radii of Ag and C atoms (2.35 Å). This indicates there is no direct bonding of the Ag atom with the lower layer. The C-C distance in the step dimers on either side of the Ag atom increases to 1.28 Å. Thus Ag-C bond formation weakens the

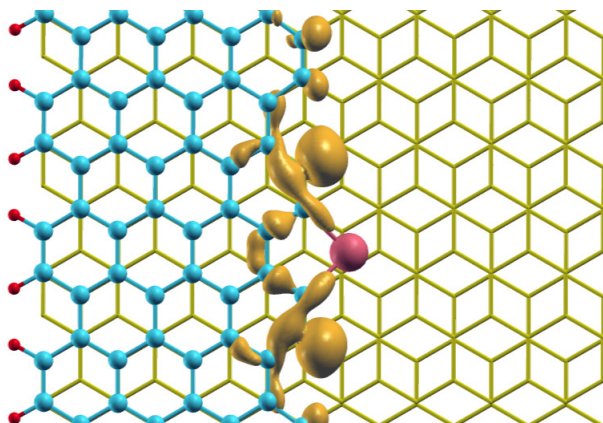


Figure 4.6: Partial (band decomposed) charge density plot for a silver adatom deposited over a stepped graphite surface. Charge density isosurface is plotted at an isovalue of  $0.1 \text{ electron}/\text{\AA}^3$ .

C-C dimer bond. Ag-C bond formation can also be confirmed from the partial charge density plot which is shown in the Fig. 4.6. A large charge density between the Ag adatom and carbon atoms can be seen clearly.

In order to understand the nature of bonding between an Ag atom and the graphite substrate, we calculated the Bader charges on all the atoms. There was a charge transfer of  $0.4 e$  from the silver adatom to the C atoms. After adsorption of an Ag adatom, there is a moment of  $0.98 \mu_B$  in the system, which is very similar to the clean graphite case. In case of the clean surface, all the moment was on the Ag adatom (chapter 3). In the present case, spin density is localized on the edge C atoms that are second neighbors of the Ag atom (Fig. 4.7). The carbon atoms which are bonded to the Ag atoms partly saturate their dangling bonds due to the Ag-C bonding. In this process the dangling bonds of second carbon atoms become unsaturated giving rise to an overall moment of  $0.98 \mu_B$ . The adsorption energies, magnetic moments, and charge transfer (from the clusters to the substrate) for all cluster sizes are given in Table 4.1.

As discussed in section 4.1, experiments indicate that steps act as attractive sinks and have a denuded zone around them on the terraces that do not have any cluster nucleation. The fact that steps act as attractive centers may be understood from the fact that the step-edge C atoms have dangling bonds, which the C atoms on the terrace do not. We tried to have a quantitative idea about the distance up to which the basin of attraction of a step extends. This would be the location of the maximum of the PES

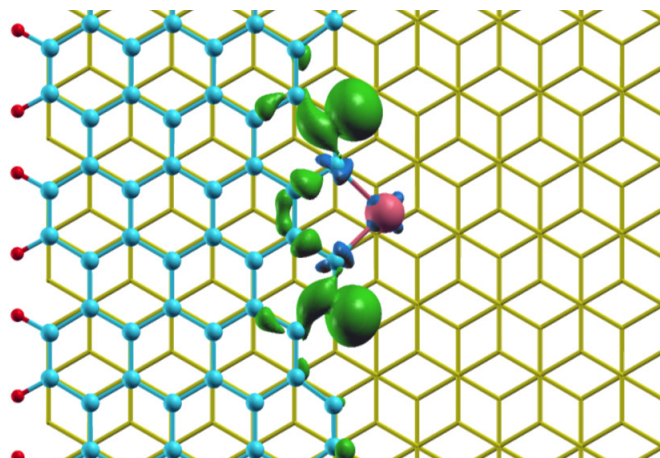


Figure 4.7: Spin density plot for a silver adatom deposited over a stepped graphite surface. Isosurface is plotted at an isovalue of  $100 \text{ e}/\text{\AA}^3$ .

of an adatom on the surface as one moves away from the step edge. We find this by identifying the maximum distance from where an Ag adatom relaxes to the step edge without any barrier. Interestingly, the basin of attraction is not symmetric on the upper and lower terraces, which is consistent with experimental observations [15, 19]. In our L(S)DA calculations, it extends up to  $6.0 \text{ \AA}$  on the lower terrace, while it is only  $3.5 \text{ \AA}$  on the upper terrace. Since interactions between a clean graphite substrate and Ag atoms are dominated by dispersion forces, we also calculated the extent of the basin of attraction on the lower terrace using the vdW-DF2 functional as well. It turns out that the basin of attraction is exactly of the same size in terms of the number of bond lengths from the step edge. However, because the graphite in-plane NN distance is slightly larger in vdW-DF2, the distance turns out to be  $6.3 \text{ \AA}$ .

Before we consider diffusion of clusters, we wanted to have a quantitative estimate of the diffusion barrier of a single adatom along the step edge. For this we considered two consecutive active sites on the step-edge and calculated the diffusion barrier between them using the CINEB method. The optimized pathway is shown in Appendix Fig. B.1. The barrier turns out to be  $0.92 \text{ eV}$ , which is quite large in comparison to the diffusion barrier of Ag atoms on a clean graphite substrate which is  $0.052 \text{ eV}$ , both calculated at the L(S)DA level. It should be emphasized that this result is on diffusion of a single Ag atom. It is most likely that diffusion of individual atoms and clusters have different paths or mechanisms which we will discuss later.

Table 4.1: Adsorption energies, magnetic moments and charge transfer from the cluster to the graphite substrate in the lowest energy structures of Ag clusters adsorbed on an armchair step edge of graphite.

Size	$E_a$ (eV)	$M$ ( $\mu_B$ )	$Q$ (e)
1	3.20	0.98	0.38
2	4.76	0.00	0.73
3	5.35	0.00	0.39
4	6.15	0.00	0.74
5	6.06	0.99	0.67
6	6.21	0.00	0.70
7	5.32	0.00	1.04
8	5.54	0.00	0.76

Next we studied adsorption of an  $\text{Ag}_2$  dimer on graphite step-edge. For initial structures, we considered many orientations of the dimer near the step at both the upper and lower terraces. From all the initial structures, the dimer always moves towards the step and dissociates into two Ag atoms. The two Ag atoms attach to two consecutive active sites of the step as shown Fig. 4.8(a). The adsorption energy turns out to be  $E_a = 4.76$  eV. The same behavior is obtained with vdW-DF2 method, except that the adsorption energy is lower in this case ( $\sim 1$  eV). An isolated  $\text{Ag}_2$  dimer has a bond length of 2.49 Å (Fig. 4.4(a)), but after deposition the distance between two Ag atoms increase to 4.20 Å. Clearly, the Ag-Ag bond breaks after deposition, which implies that gain in Ag-C bonding energy is larger than the cost of Ag-Ag bond breaking. For large sized clusters, the final structure after deposition near step edge is determined by the competition between Ag-C bond formation and Ag-Ag bond stretching or breaking. As we discuss later, in many cases the cluster is distorted or fragmented after deposition.

An  $\text{Ag}_3$  trimer has an isosceles triangular structure in the ground state in which two of the Ag-Ag bond lengths are 2.60 Å, and the third one is 2.61 Å. After deposition near the step, one of the Ag-Ag bonds is broken, and the two Ag atoms occupy two neighboring active sites at a separation of 4.01 Å. The third Ag atom remains bonded to these two Ag atoms at bond distances of 2.66 Å (Fig. 4.8(b)). In this structure the adsorption energy is 5.35 eV. We also created a structure by hand in which  $\text{Ag}_3$  is completely broken, and the three Ag atoms occupy three neighboring active sites. This structure is 1.24 eV lower in energy than the previous structure. Obviously, there

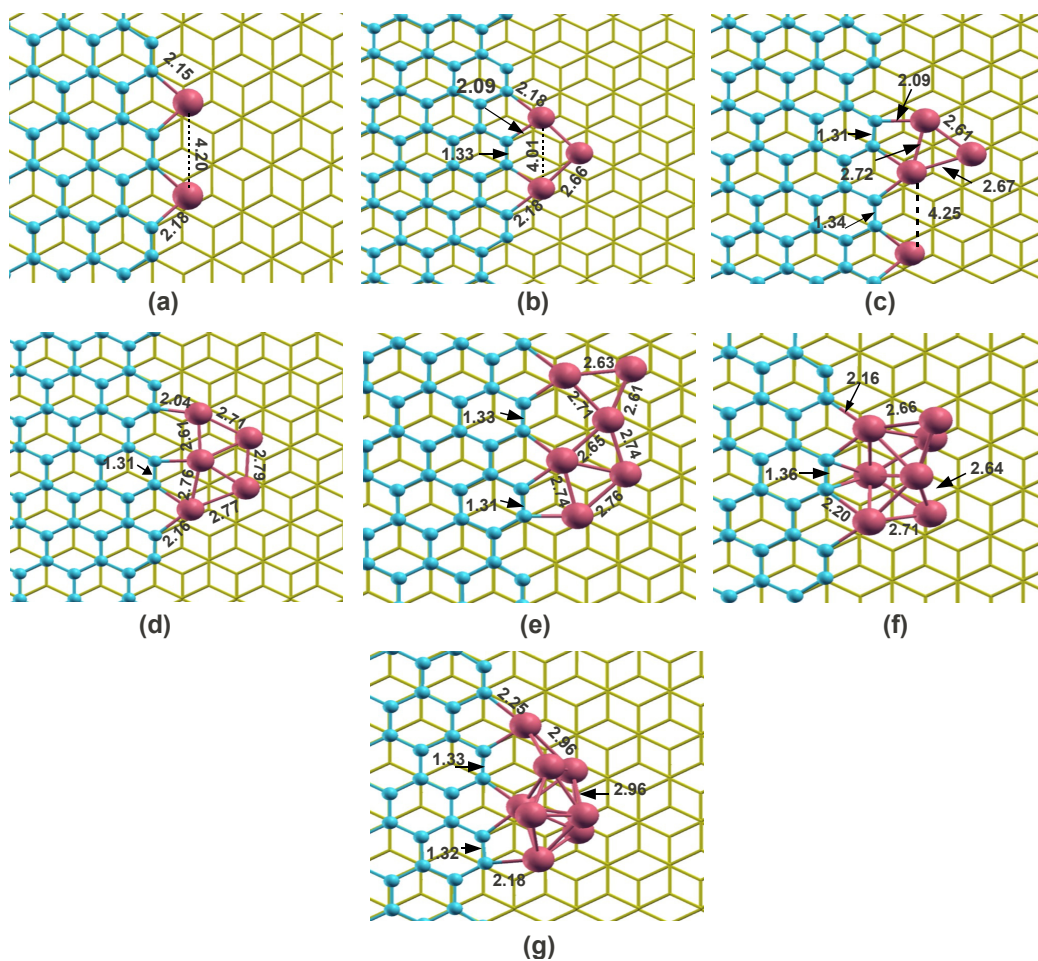


Figure 4.8: Lowest energy structures obtained after adsorption of  $\text{Ag}_n$  ( $n = 2 - 8$ ) clusters on a stepped graphite surface. Relevant bond lengths are indicated (in  $\text{\AA}$ ).

is a kinetic barrier between these two structures as otherwise all the Ag atoms would have moved to the the active sites. We performed CINEB calculations to get a rough estimate of this barrier, and it turned out to be 0.57 eV.

An  $\text{Ag}_4$  cluster has a rhombus structure in its ground state in the gas phase (Fig. 4.4(c)) with Ag-Ag bond lengths of 2.64  $\text{\AA}$ . Interestingly, after deposition it breaks into two fragments: an  $\text{Ag}_3$  cluster and an Ag atom (Fig. 4.8(c)). The minimum distance between these two is 4.25  $\text{\AA}$ , which is quite large for a chemical bond. The adsorption energy in this structure is 6.15 eV. Unlike the  $\text{Ag}_4$  cluster,  $\text{Ag}_5$  does not break into fragments after deposition. It retains its gas phase shape but with very different bond lengths. Its bond lengths increase significantly to maximize the Ag-C bonding as shown

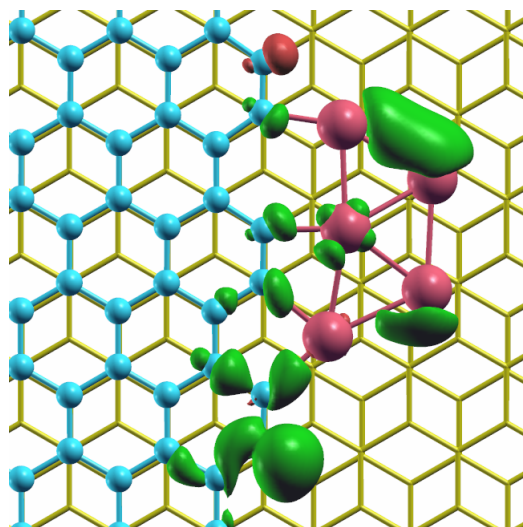


Figure 4.9: Spin density isosurface plot for the  $\text{Ag}_5$  cluster bonded at the armchair step edge of graphite.

in Fig. 4.8(d). Apart from the Ag adatom,  $\text{Ag}_5$  is the only other cluster we found which retains its spin moment in the lowest energy structure after deposition. The spin is localized mostly on the edge C atoms that are second neighbors of the Ag atoms, and the Ag atoms that are not bonded to the C atoms. The spin density iso-surface in this case is shown in Fig. 4.9.

Similarly,  $\text{Ag}_6$ ,  $\text{Ag}_7$ , and  $\text{Ag}_8$  clusters are heavily deformed after deposition from their gas phase structures (Fig. 4.8(e,f,g)).  $\text{Ag}_6$  has a planar structure in gas phase. After deposition,  $\text{Ag}_6$  is distorted in such a way that, three of its Ag atoms are trapped at the step edge, while rest are attached to the already trapped Ag atoms at the edge. It has an adsorption energy of 6.21 eV.  $\text{Ag}_7$  cluster has a pentagonal bi-pyramid structure in the gas phase (Fig. 4.4(f)). After deposition it is distorted such that three Ag atoms are attached to step edge and remaining four stay near to the bonded Ag atoms (Fig. 4.8(f)). Similarly for  $\text{Ag}_8$ , which has bicapped-octahedron structure (Fig. 4.4(g)) in gas phase, deformed such that four of its Ag atoms are bonded to the step edge while rest four Ag atoms are attach to these bonded Ag atoms. Hence, after deposition their structures are distorted in a way that they can have maximum Ag-C bonding with the minimum energy cost for stretching of Ag-Ag bonds. One point worth noting here is that unlike  $\text{Ag}_2$  or  $\text{Ag}_4$ , none of the Ag atoms at these sizes ( $n = 6 - 8$ ) gets completely dissociated from the cluster.

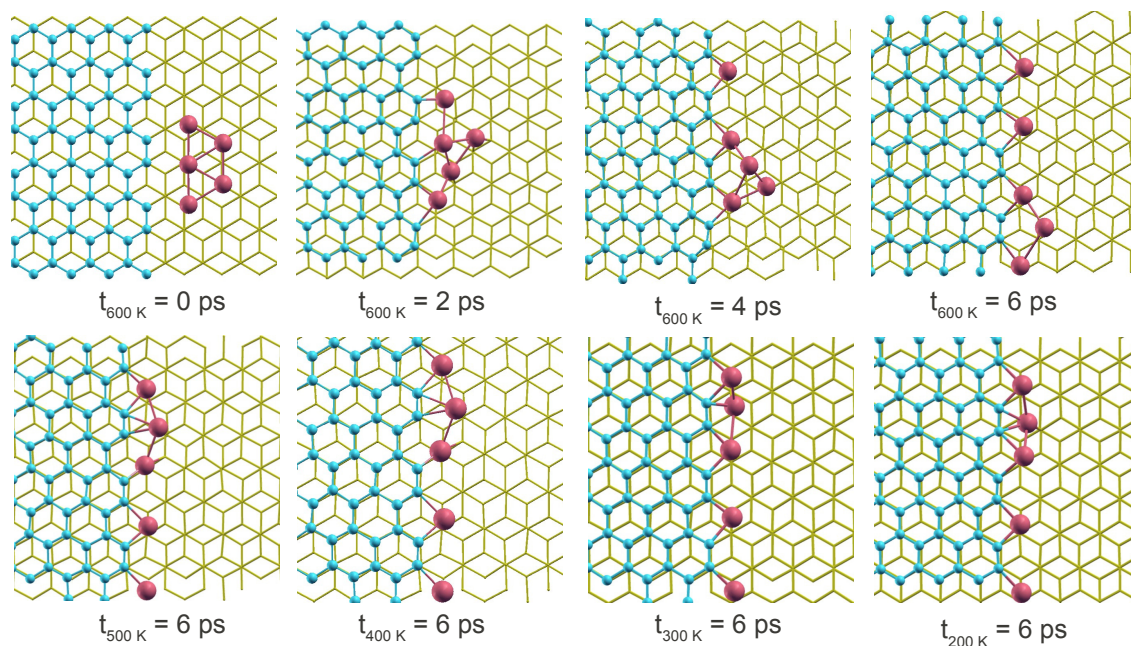


Figure 4.10: Top panels: Snapshots from the MD simulation of an Ag<sub>5</sub> cluster on a stepped graphite surface at T= 600 K at specified times. Bottom panels: Snapshots after 6 ps of MD simulation at each temperature.

## 4.5 Finite temperature results

From the above discussions it is clear that Ag clusters deposited on a stepped graphite surface try to maximize Ag-C bonds. Ag<sub>2</sub> dimer spontaneously dissociates even at zero temperature. Ag<sub>3</sub> would also break into three Ag atoms located at three active sites if it could. The process is kinetically hindered. The behavior of Ag<sub>4</sub> also points to the same trend. Even the larger clusters follow the same trend. In order to explore the behavior of larger clusters on the stepped surface at finite temperatures, we simulate the annealing of Ag<sub>5</sub> and Ag<sub>8</sub> clusters at 600 K deposited on the lower terrace of a stepped surface. In particular, we start MD calculations at 600 K with the clusters on the lower terrace in the same initial structure that gave the lowest energy structure in the zero temperature situation. We then slowly cool the temperature down to 200 K in steps of 100 K making sure that the system thermalizes at every temperature in the cooling schedule. It takes  $\sim 0.4\text{ ps}$  for the system to thermalize at a given temperature. But we let it evolve for 6 ps before lowering temperature to the next step. Ideally one should study many MD trajectories at each of the sizes to get an idea about the statistical behavior of a

number of clusters being deposited on the substrate. However, this is computationally too expensive to be practical. Moreover, since Ag clusters and adatoms tend to move towards the step edge and get adsorbed there even at zero temperature, it is expected that they will diffuse more easily at finite temperatures. Although starting from different initial structures of the clusters would lead to trajectories differing in their details, the qualitative features would remain the same. The snapshots of MD simulations for Ag<sub>5</sub> and Ag<sub>8</sub> are shown in Fig. 4.10 and Fig. 4.11 respectively. Our observations from the MD calculations are as follows.

At 600 K an Ag<sub>5</sub> cluster moves as a single entity on the terrace, and reaches the step within 0.3 ps. Once it reaches the step edge, the cluster atoms start moving independently. Atoms that are close to the active sites are immediately trapped and atoms away from the active sites move until they find vacant active sites. Finally, the Ag atoms arrange themselves into an atomically thin nanowire along the step edge. Since we have only four active sites in our simulation box, only four of the Ag atoms can be trapped at the active sites. The last remaining Ag atom is bonded to two consecutive Ag atoms which are already trapped at active sites. Once this arrangement is reached, the Ag atoms execute thermal vibrations around their respective positions. Between 600 K and 400 K we also occasionally find that an Ag atom at an active site is 'pushed' out of its position by one away from the active site. At 300 K or lower, this process stopped. All the Ag atoms finally take positions along the step edge, either trapped at active sites or bonded to two C atoms of a step-edge dimer, and the atoms only executed thermal vibrations. We do not find any moment on the Ag or edge C atoms in this low temperature structure.

Dynamics of Ag<sub>8</sub> is slightly different from that of Ag<sub>5</sub> because of its larger size, larger number of Ag-Ag bonds, and non-planar structure. Ag<sub>8</sub> takes about 0.6 ps to reach the step edge, and after that the cluster atoms start moving independently. At 2 ps, only three of the cluster atoms get attached to the step edge, while others are still within the cluster environment. At 4 ps, four of the Ag atoms are found near the step edge, three of them are at active sites and one of them is close to a step edge C<sub>2</sub> dimer. At 6 ps they assemble into a nano-wire structure. Here the number of Ag atoms is larger than the number of active sites we have in our simulation cell. Hence not all of them can find an active site individually. What happens is quite interesting. Some of them find active sites, and get trapped there. Others are found close to a step C-C dimer

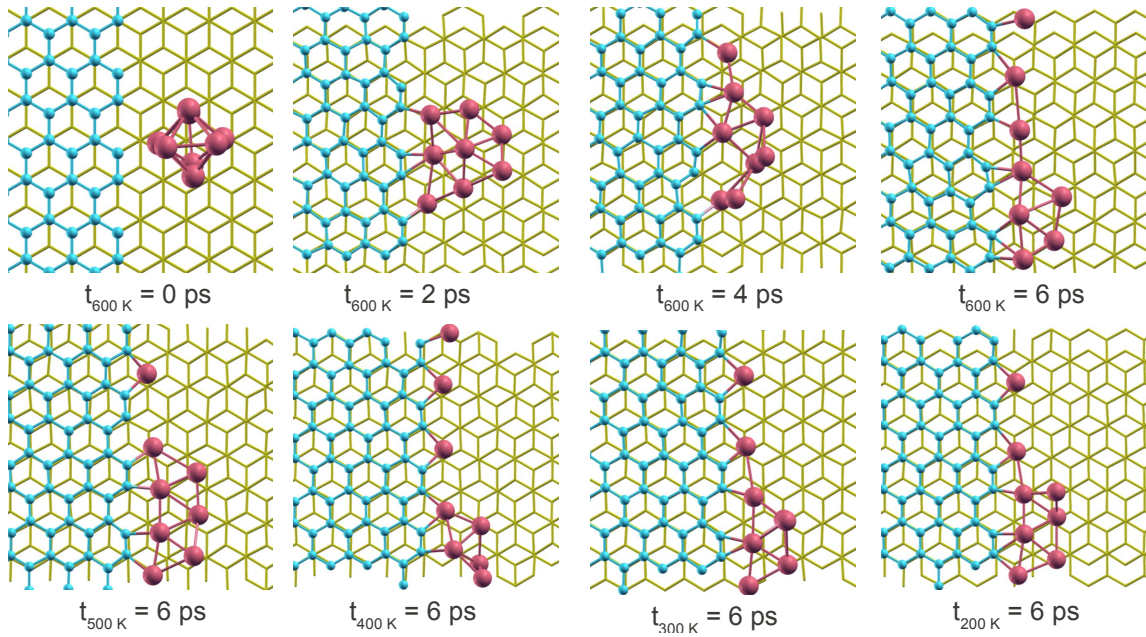


Figure 4.11: Top panels: Snapshots from the MD simulation of an  $\text{Ag}_8$  cluster on a stepped graphite surface at  $T = 600 \text{ K}$  at specified times. Bottom panels: Snapshots after 6 ps of MD simulation at each temperature.

or close to other Ag atoms that are trapped at active sites. Pushing out of Ag atoms close to the C atoms by those away from them is seen in this case also. The Ag atoms away from the step edge are seen to diffuse along the step direction between 600 K and 400 K. As the temperature is lowered, such diffusion becomes less pronounced. Finally, at 200 K five of the Ag atoms are found close to the step edge C atoms, either at active sites or close to a dimer, and the three remaining Ag atoms are found farther away from the step, bonded to the Ag atoms near the step.

The main conclusions we draw from these finite temperature MD simulations are as follows. Clusters deposited on the surface and annealed at  $\sim 600 \text{ K}$  diffuse as a single entity on the terraces but disintegrate at the step edges. The Ag atoms tend to form a nano-wire like structure along the step edges with each Ag atom ideally occupying one active site. If there are not enough active sites nearby, or, if somehow, some of the Ag atoms cannot diffuse to vacant active sites (which is more likely to happen for larger clusters and low temperatures), those atoms get attached to the Ag atoms already trapped at the edge. This may produce dumbbell-like shapes in STM images. Our simulations of the  $\text{Ag}_8$  cluster show that Ag atoms that get bonded to

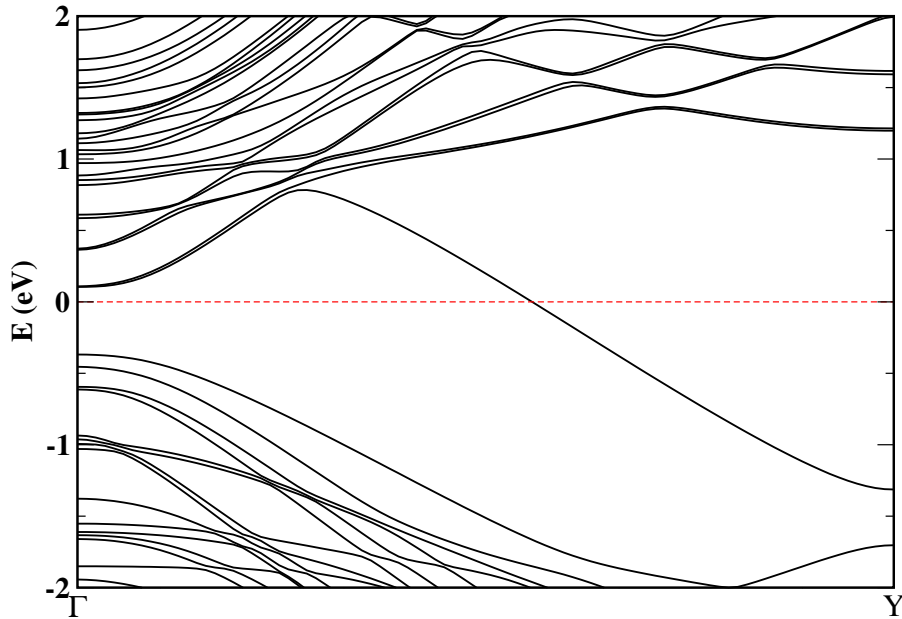


Figure 4.12: Band structures of an ordered nanowire with one silver atom at each active site.

the step edge C atoms do not diffuse even at 600 K. It is the Ag atoms away from the step, bonded to other Ag atoms, that diffuse along the step direction. Based on these observations we suggest that by depositing small size-selected Ag clusters on a stepped graphite surface at elevated temperatures ( $> 600$  K), and controlling the cluster density to match the available step-edge active sites, it may be possible to fabricate self-assembled atomically thin nano-wires.

## 4.6 Band structure of 1D monoatomic chain along step edge

With this insight into the diffusion of Ag clusters on the terraces and along the steps of a graphite surface, we now try to understand the electronic structure of the system when a nanowire-like structure has been formed along the step edge. First we calculate the band structure of an ideal system: a silver nano-wire formed at the step-edge when each of the active sites is occupied by an Ag adatom. In contrast to the band structure of the relaxed stepped graphite (Fig. 4.3), there is a band crossing the Fermi level in this

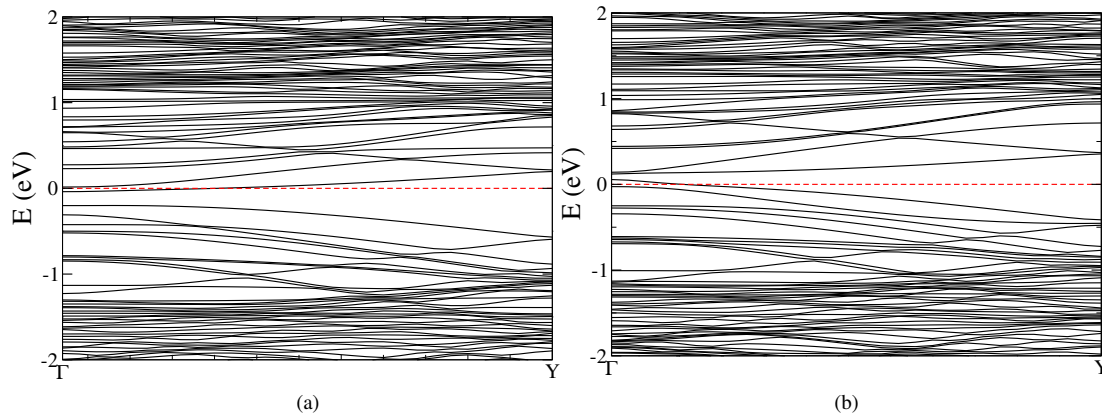


Figure 4.13: Band structures of system annealed to 200K for (a)  $\text{Ag}_5$  and (b)  $\text{Ag}_8$  cluster.

nanowire structure (Fig. 4.13). The partial DOS of the system shows a finite density of silver  $s$  states and carbon  $p$  states at the Fermi level. Thus a conducting channel is formed not by the Ag atoms alone (which are  $> 4 \text{ \AA}$  apart), but by the Ag-C-Ag-C-... chain. We also calculated the band structure for the low temperature structures of  $\text{Ag}_5$  and  $\text{Ag}_8$  clusters obtained from the MD simulations which were shown in Fig. 4.10 and Fig. 4.11. Band structures for both these clusters, also show the metallic character indicating that a conducting nano-wire can be formed by depositing Ag clusters on this surface under appropriate conditions of temperature and cluster density.

## 4.7 Conclusions

We find that step edges on a graphite surface act as attractive sinks for silver adatoms and clusters. This is the first attempt to understand the microscopic mechanism of the attractive nature of the step edges. Due to the existence of dangling bonds on the edge C atoms, the grooves at the armchair edge act as active sites of attraction for individual Ag atoms. In fact, some small clusters such as  $\text{Ag}_2$  and  $\text{Ag}_4$  dissociate to take advantage of the strong Ag-C bonds formed at these active sites. Clusters at other sizes also distort or break Ag-Ag bonds to take advantage of the Ag-C bonding. A large region extending up to  $\sim 6 \text{ \AA}$  from the step-edge on the lower terrace, and  $3.5 \text{ \AA}$  on the upper terrace acts as basin of attraction for the step-edge for an individual Ag adatom. Finite temperature MD calculations suggest that clusters deposited on graphite at  $\sim 600 \text{ K}$  diffuse rapidly

on the terrace till they reach a step-edge. Once at the step-edge they tend to break up in a way so that each Ag atom tries to occupy an active site. If that is somehow hindered, some of the Ag atoms get trapped at active sites, or get bonded to the edge dimers while the other Ag atoms bond to these Ag atoms. The Ag atoms away from the step edge diffuse significantly along the step direction at elevated temperatures. Therefore, it is clear that what diffuse along step edges are individual atoms of the cluster not directly bonded to the step-edge C atoms, and not the cluster as a whole. As the temperature is lowered, the diffusion naturally becomes less, and the Ag atoms only execute thermal vibrations. A linear chain of Ag atoms occupying active sites, and the structures of Ag<sub>5</sub> and Ag<sub>8</sub> clusters obtained after annealing at 600 K, all turn out to be metallic.

# Finding the right support for deposition and self assembly of magnetic superatoms

## 5.1 Introduction

As discussed in chapter 1 electronic orbitals in superatoms, while resembling those in real atoms in shape, do spread over multiple atoms. The filling of electronic shells generally do not follow the Hund's rule of maximizing the spin. Within shell model framework it has been proposed that magnetic superatoms with spin moments could be stabilized by inducing spin dependent splitting of supershells This can be accomplished by hybridizing the superatomic orbitals with atomic orbitals that have large exchange splitting. In order to qualify as a magnetic superatom, it is important for the stable cluster unit to retain its structural identity and magnetic properties in the assemblies. In all the theoretical works involving magnetic superatoms, the assemblies have been studied in the gas phase, *i.e.*, their free-standing dimers [5, 8] and trimers have been studied. However, for these superatoms to be useful in building cluster assembled materials, such assemblies have to be made in a form that can be made to rest. Deposition and self-assembly of magnetic superatoms will lead to production of magnetic thin films whose properties can be tuned by choosing the building blocks, *i.e.*, the superatoms. These may open new avenues in spintronic and magnetic storage materials. In fact, He *et al.*, [187] have shown that a dimer of two  $\text{VCs}_8$  units acts as an efficient spin polarizer. It would be interesting to extend such ideas to larger assemblies of these

superatoms.

In order to form useful assemblies of magnetic superatoms, proper substrates have to be identified. Some of the desirable properties of a substrate are that 1) the superatom-substrate interaction has to be weak enough so that the superatom retains its structural identity. If the superatom-substrate interaction is much stronger than the intra-cluster interactions, it would tend to wet the surface, thereby losing its structural identity. This is likely to destroy its magnetic property also. 2) Even if the superatom retains its structural identity, it is not guaranteed that its magnetic moment will be retained. The superatom-substrate interaction should be such that a substantial part of the magnetic moment of the free superatom is maintained even after deposition. 3) When two or more superatoms are deposited on the substrate they should have an interaction strength so that they each retain their structural identity. Ideally, they should retain their magnetic moments also. However, it is possible that they may not retain the entire moment of an isolated superatom while forming the assembly. This is true of elemental atoms also. For example, an isolated Fe atom has a moment of  $4 \mu_B$  because of its  $3d^6 4s^2$  configuration. An Fe<sub>2</sub> dimer [188], in its lowest energy state, has a moment of  $6 \mu_B$  rather than  $8 \mu_B$ , and bulk ferromagnetic Fe has  $2.2 \mu_B$  per atom [189].

Clearly, this is a stringent set of requirements for a substrate to be useful for assembly of a particular magnetic superatom. It is possible that different substrates may be ideal for different superatoms. To explore these issues we take FeCa<sub>8</sub> as a prototypical example and explore its properties on different types of substrates which are commonly used. Chauhan *et al.*, [6] have shown that FeCa<sub>8</sub> behaves as a magnetic superatom. Here we study alumina ( $\alpha$ -Al<sub>2</sub>O<sub>3</sub>), FCC calcium, graphene and hexagonal BN (h-BN) as possible substrates. Alumina has been chosen as a representative oxide substrate. Oxide substrates such as Al<sub>2</sub>O<sub>3</sub>, TiO<sub>2</sub>, CeO, MgO are routinely used to deposit clusters for various applications, most notably catalysis [22, 23, 190]. Calcium surface is chosen as an example where the cluster-surface interaction is expected to be of the same strength as the intra-cluster interaction since most of the clusters atoms are also Ca. Graphene and h-BN are chosen because these are 2D materials with no dangling bonds at the surface [191], and hence are expected to interact weakly with the superatom. Compared to Al<sub>2</sub>O<sub>3</sub>, the degree of ionicity is also expected to be small in h-BN. Indeed, studies [21, 169, 170, 192--194] have shown that interactions between these (as also graphite) and metal atoms are dominated by dispersion forces, and are

very weak. Metal adatoms are trapped only at defect sites and step edges on a graphite substrate.

In this chapter, we try to identify the substrate(s) on which an individual  $\text{FeCa}_8$  cluster retains its structural identity and magnetic moment. We then try to form assemblies of two  $\text{FeCa}_8$  units on such substrates. In section 5.2 we present the theoretical approach used for these calculations. Later in various sections of chapter we present results for structure and energetics and electronic structure of  $\text{FeCa}_8$  deposited on the four substrates mentioned above. We also present results of two  $\text{FeCa}_8$  units deposited on h-BN in section 5.4.5. Finally we draw our conclusions in section 5.6.

## 5.2 Method

All our calculations are performed within the framework of DFT. The wave functions are expressed in a plane wave basis set with an energy cutoff of 400 eV.  $\text{Al}_2\text{O}_3(0001)$  surface is modeled by a  $4 \times 4$  ( $18.44 \text{ \AA} \times 18.44 \text{ \AA}$ ) supercell with nine atomic layers in a slab in a repeated slab geometry. The distance between two Ca atoms in a superatom along the diagonal of a square face is  $4.5 \text{ \AA}$ . This choice of in-plane supercell size ensures that the nearest distance between cluster atoms in the simulation cell and their periodic images is  $\sim 13 \text{ \AA}$ . We believe this is enough to ensure absence of any direct electronic interaction between them. The top five atomic layers of Alumina slab are allowed to relax, while the bottom four layers are held fixed in their bulk terminated positions. Dipole corrections were included to avoid any spurious interaction between periodic images of the slab due to long-range dipole-dipole interactions [195]. The (001) surface of FCC calcium is represented by a  $5 \times 5$  supercell ( $18.81 \text{ \AA} \times 18.81 \text{ \AA}$ ) with seven layers in the slab. This also ensures that the minimum distance between cluster atoms and their periodic images is more than  $13 \text{ \AA}$ . All the atoms are allowed to relax during structure optimization. For both these surfaces, a vacuum of  $15 \text{ \AA}$  is included between a slab and its periodic image. h-BN-sheet is represented by a  $7 \times 7$  supercell in the plane for deposition of a single  $\text{FeCa}_8$  unit, and by  $11 \times 11$  and  $14 \times 14$  supercells while depositing two  $\text{FeCa}_8$  units. For graphene we used supercells of various sizes increasing from  $(4 \times 4)$  to  $(13 \times 13)$  (lateral dimensions of  $9.9 \text{ \AA}$  to  $32.2 \text{ \AA}$ ). A vacuum space of  $20 \text{ \AA}$  separating two successive sheets has been used for both h-BN and graphene. The BZ integrations were performed using the  $\Gamma$ -point only

in all cases as the unit cells are quite large and addition of more  $k$ -point does not change the adsorption energy of the cluster. For graphene we also took the cells sizes to be  $(4 \times 4)$  and  $(5 \times 5)$ . For these two sizes, we used  $5 \times 5 \times 1$  and  $3 \times 3 \times 1$   $\mathbf{k}$ -point grid respectively.

Different functionals were used to represent the exchange-correlation energy in different situations. For  $\text{FeCa}_8$  supported over alumina and calcium surfaces, we used the LSDA. For metal atoms on graphene and h-BN substrates, dispersion forces play important roles and the treatment of those are a challenge for first-principles theories. As discussed in chapter 2 and 3, the standard local and semi-local functionals are not capable of describing such interactions. Usually, two different approaches are taken to incorporate these interactions: a semi-empirical approach suggested by Grimme [146-148], and using a non-local correlation functional (vdW-DF) [152, 153]. We shown in chapter 3 that the semi-empirical approach leads to incorrect binding sites for Ag atoms on graphene/graphite. We have also showed that the behavior of Ag clusters on a graphite substrate can be described correctly only by using the non-local correlation functionals. Therefore we have used the vdW-DF2 [157] method,

Before the development of the non-local correlation functionals, a number of studies on metal-graphite or metal-graphene systems used the LSDA within DFT [20, 168, 196, 197]. For a comparison with our vdW-DF2 calculations, and to establish the fact that one may get qualitatively different results in these two methods, we also present our LSDA results on these two systems in section 5.5.

### 5.3 Isolated $\text{FeCa}_8$ superatom

Before depositing a  $\text{FeCa}_8$  superatom on substrates, one has to find its ground state structure and electronic structure. These were studied thoroughly in Ref. [6]. However, those calculations were performed using an atom-centered Gaussian basis set [198]. Here we use plane wave basis set. Therefore, we need to re-calculate the isolated cluster using this method. For calculation of an isolated cluster it was placed at the center of a periodic cubic box of dimensions 25 Å in each direction.

Fig. 5.1 shows the optimized structures of the  $\text{FeCa}_8$  cluster obtained using the LSDA and vdW-DF2 methods.  $\text{FeCa}_8$  has a square antiprism structure with an endohedral Fe atom, as found earlier using PBE [108]. In order to explain its electronic struc-

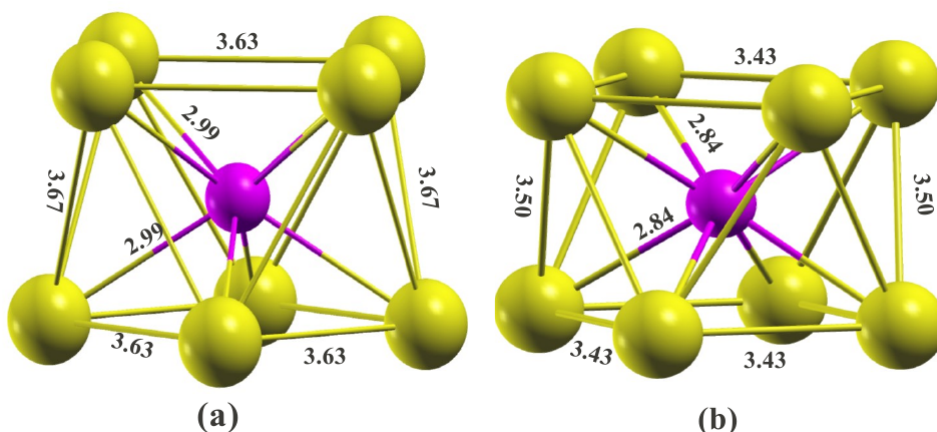


Figure 5.1: The lowest energy structure of FeCa<sub>8</sub> using (a)vdW-DF2 and (b)LSDA.

ture, we have plotted the energies of the Kohn-Sham orbitals, and the partial charge densities coming from these in Fig. 5.2. FeCa<sub>8</sub> is found to have a  $1S^21P^61D^{10}2S^22D^4_\alpha$  electronic configuration in both vdW-DF2 and LSDA in agreement with Ref. [6]. S, P, D refer to the angular momentum character of the cluster MO in conformity with the spherical shell models. They found that the Ca-Ca distance within the square planes of the anti-prism is larger than the vertical distance between the two square planes. Thus, these structures can be viewed to have oblate distortions relative to a more symmetric 'spherical' structure in the language of electronic shell models. The Ca<sub>8</sub> cage has an oblate distortion in the z-direction. As discussed in chapter 1, this oblate shape produced a crystal field that breaks the degeneracy of the 1D orbitals in  $\alpha$  channel and pushes the  $1D_{z^2}$  and  $1P_z$  orbital to a higher energy with respect to the other 1D and 1P orbitals respectively. Similarly 2D states of majority channel are split into a group of 4 ( $2D_{xy}$ ,  $2D_{x^2-y^2}$ ,  $2D_{xz}$  and  $2D_{yz}$ ) and a  $2D_{z^2}$  state. These four degenerate 2D orbitals form the HOMO of the FeCa<sub>8</sub> cluster. The LUMO of FeCa<sub>8</sub> was found to be in the  $\beta$  channel and was of 2D angular character.

Although both vdW-DF2 and LSDA give the same electronic configuration as obtained in ref [6], there are subtle differences between the vdW-DF2 and the LSDA results in terms of orderings of different molecular orbitals, and their splittings. For example, in LSDA, 1D states of  $\alpha$  channel split in groups of 2 and 3 degenerate states. In vdW-DF2 as in PBE [6] this spilling is 4 and 1. In vdW-DF2 the 1S orbital is followed by the four degenerate 1D orbitals in the  $\alpha$ -spin channel, and in LSDA it is

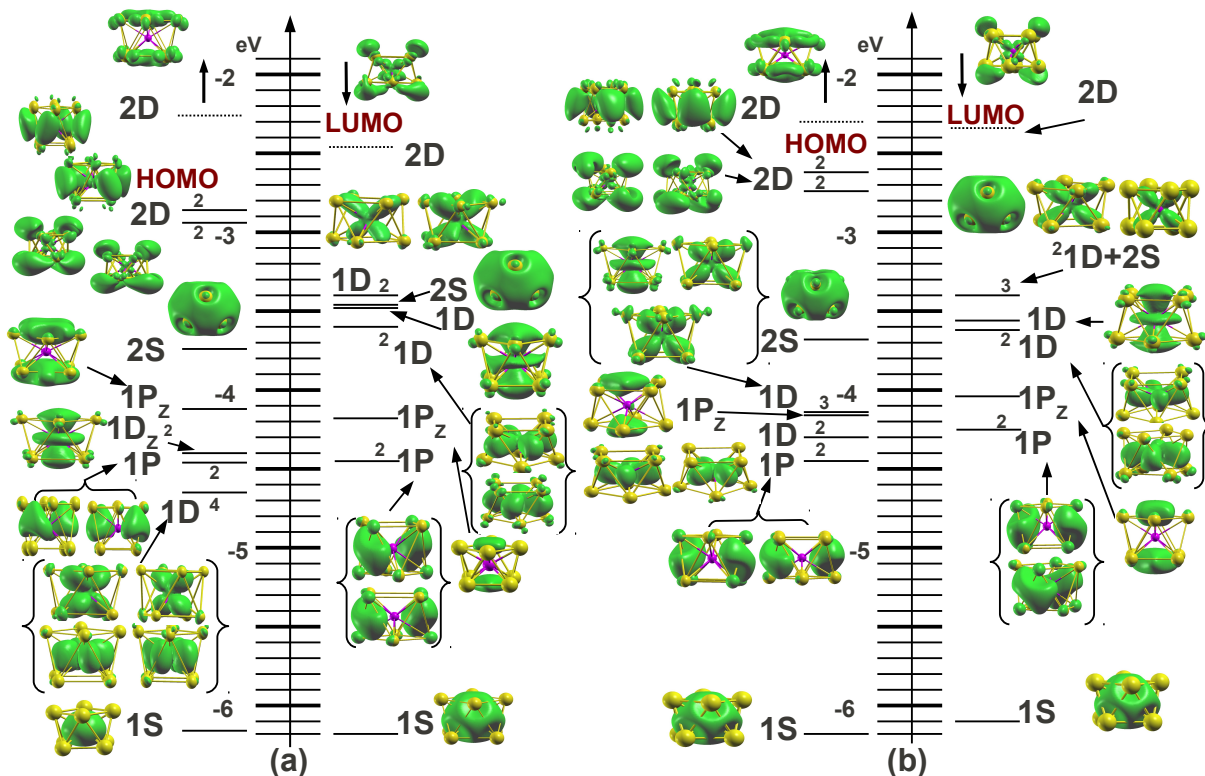


Figure 5.2: The MO's, and corresponding charge densities of FeCa<sub>8</sub> using (a) vdW-DF2 and (b) LSDA. Degeneracy of the MO's are also indicated.

followed by two degenerate 1P orbitals. Similar to the PBE results, in both cases the Ca-Ca distance within the square planes is larger than the vertical distance between the square planes. However, the ratio of the vertical distance between the planes and the in-plane Ca-Ca distance in vdW-DF2 and LSDA is 0.85 and 0.91 respectively. Ratios between the vertical distance and the in-plane diagonals and the body diagonals in the two cases are also slightly different. This difference in the amount of 'distortion' may be responsible for the slightly different electronic structures.

## 5.4 FeCa<sub>8</sub> adsorbed on substrates

To mimic the LECBD experiments, we used the random rotation technique discussed in chapter 2. For the Al<sub>2</sub>O<sub>3</sub> surface, four adsorption sites A11, O2, A13 and O5 (shown in appendix Fig. C.1(a)) are considered. For calcium surface, we choose on-top Ca-site

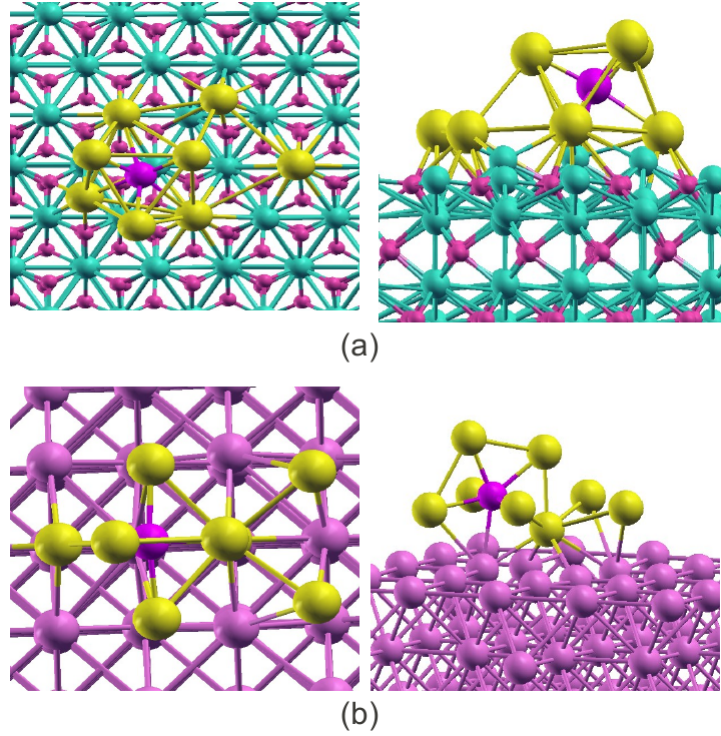


Figure 5.3: The lowest energy structure of  $\text{FeCa}_8$  supported over alumina (a) and calcium (b) substrates. In panel (b) the substrate Ca atoms are shown with a darker (blue) color to distinguish them from the Ca atoms of the superatom.

(T) and four-fold hollow site (H) (Fig. C.1(b)). For the graphene and h-BN substrates, the top site(s) (B and N atoms in case of BN), the bridge site and the hollow site are chosen.

Relative stability of different final structures on a particular substrate is measured by comparing the adsorption energies. Adsorption energy of the cluster in a particular structure is defined as.

$$E_a = E_T(\text{substrate}) + E_T(\text{FeCa}_8) - E_T(\text{FeCa}_8/\text{substrate}). \quad (5.0)$$

$E_T$ 's are the total energies of the respective systems.

### 5.4.1 Alumina substrate

Bulk  $\alpha$ -alumina has a hexagonal crystal structure, with the experimental lattice constants [199]  $a_0 = b_0 = 4.76 \text{ \AA}$  and  $c_0 = 12.99 \text{ \AA}$ . It has a direct gap of 8.8 eV [200]. Our calculated band gap is 6.68 eV, which exhibits the usual underestimation of band gaps due to LDA. We find that lattice parameters to be  $a = b_0 = 4.61 \text{ \AA}$  and  $c = 13.6 \text{ \AA}$ , which are in good agreement with the experimental values [199]. Later, we deposited  $\text{FeCa}_8$  on the alumina substrate using random rotation technique. The obtained lowest energy structure is shown in Fig. 5.3(a). It is clear that the antiprism motif of the cluster is completely destroyed and the endohedral Fe atom is exposed to the alumina surface. Such a large deformation of the  $\text{FeCa}_8$  unit is a consequence of a very strong interaction between the cluster and the substrate. This is proven by the fact that the adsorption energy of  $\text{FeCa}_8$  on  $\text{Al}_2\text{O}_3$  in this lowest energy structure is 13.46 eV. This is much larger than, for example, the adsorption energy of  $\text{Ag}_8$  on graphite (chapter 3), which is 0.71 eV. The requirement for a substrate to be a good support for superatom assembly, that the cluster-substrate interaction be weak, is clearly not met by  $\text{Al}_2\text{O}_3$ . As a consequence, the electronic structure and magnetic properties of  $\text{FeCa}_8$  also change substantially. Most importantly, the magnetic moment of the isolated superatom is lost after adsorption. The immediate reason for this is a large charge transfer to the substrate. We calculated the Bader charges on all the atoms in the final relaxed structure, and find that a charge of  $4.8 e$  is transferred from the cluster to the substrate. Most of the charge is transferred from the Ca atoms of the cluster to the neighboring Al atoms of the substrate. The DOS plot for this system is shown in Fig. 5.4. It turns out that all the energy states of the gas phase cluster lie within the band-gap region of the alumina slab. After deposition also a set of discrete states are found in the gap region which are localized on the cluster atoms and the nearby Al atoms. An equal number of such states appear in the two spin channels, and hence there is no magnetic moment. Hence an oxide substrate is not suitable for a superatom adsorption as it very reactive and can not preserve the geometric and electronic structure of the superatom.

### 5.4.2 Ca substrate

Next we explored the adsorption of the  $\text{FeCa}_8$  cluster on the  $\text{Ca}(001)$  surface. First we calculated properties of the bulk FCC calcium. Our calculated cubic lattice parameter

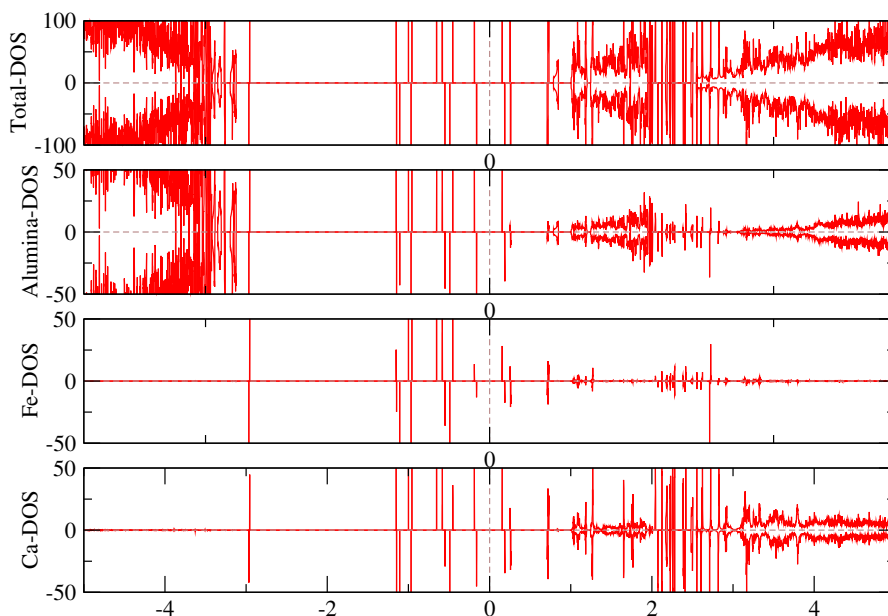


Figure 5.4: Density of states of  $\text{FeCa}_8$  deposited over alumina surface.

is  $5.32 \text{ \AA}$  within LDA. This compares well with the experimental value of  $5.582 \pm 4 \text{ \AA}$  [201]. We took several initial structures for  $\text{FeCa}_8$  over  $\text{Ca}(100)$  and relaxed them to their nearest local minima. In the lowest energy structure (Fig. 5.3(b)), the cage of the cluster is deformed and the Fe atom is exposed to the surface as on the alumina substrate. Strong interaction between the cluster and the substrate leads to a fairly large adsorption energy of  $5.75 \text{ eV}$ . Due to this strong interaction, the electronic states of the cluster are also heavily modified and the magnetic moment of the cluster is completely lost. The density of states for  $\text{FeCa}_8$  on  $\text{Ca}(100)$  is shown in Fig. 5.5. Metallic Ca has finite DOS around the Fermi energy. The cluster states are heavily mixed with the Ca states. States around  $-1.25 \text{ eV}$ , and from the Fermi energy up to  $\sim 1.9 \text{ eV}$  have significant contributions both from the substrate and the cluster. We also found a charge transfer of  $0.94 e$  from cluster to the surface.

### 5.4.3 h-BN substrate

Having found out that alumina and Ca substrates are not appropriate supports that preserve properties of the  $\text{FeCa}_8$  superatom, we now explore graphene and h-BN sheets as possible supports. For reasons discussed earlier we have used the vdW-DF2 method

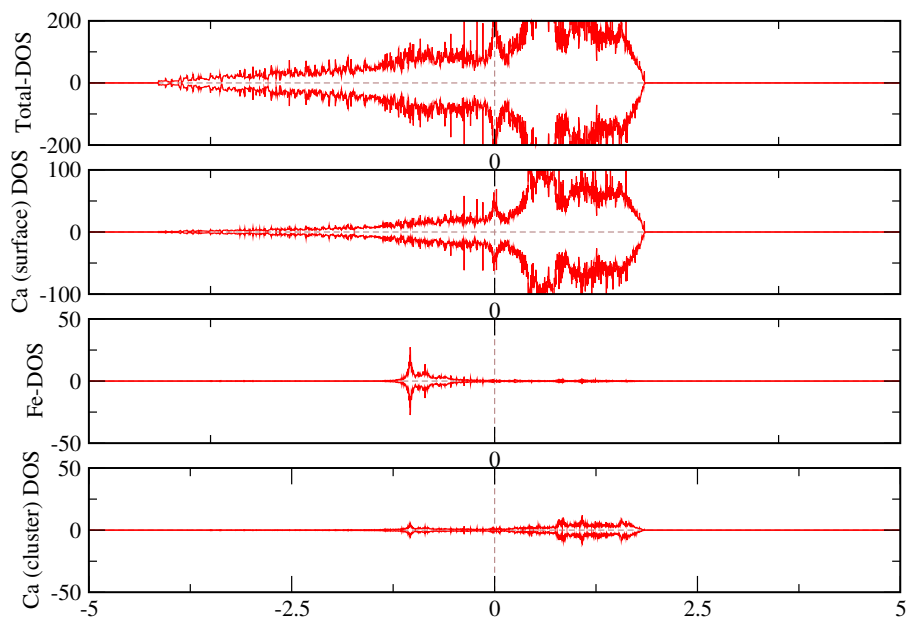


Figure 5.5: Density of states of  $\text{FeCa}_8$  deposited over calcium surface.

while studying  $\text{FeCa}_8$  on these substrates.

h-BN is an insulating material with a nearest neighbor bond length  $1.45 \text{ \AA}$  and a measured band gap of  $5.97 \text{ eV}$  [202]. Within the vdW-DF2 method, the optimized nearest neighbor B-N distance turns out to be  $1.45 \text{ \AA}$ , and the calculated band gap is  $4.52 \text{ eV}$ .

We took several initial structures for  $\text{FeCa}_8$  on the h-BN sheet using random rotation technique and relaxed these to their nearest local minima. In complete contrast to alumina and calcium substrates, the  $\text{FeCa}_8$  cluster retains its square antiprism motif in all the structures. This is the first encouraging sign that h-BN may be a good substrate for superatom assembly. In the lowest energy structure (Fig. 5.6(a,b)), one of the square planes of the antiprism structure is aligned parallel to the h-BN sheet. Three of the Ca atoms are at on-top sites, while the fourth one is near a hollow site. There is very little change in the bond lengths in the cluster. The Ca-Ca bond lengths in the square plane close to the substrate increase marginally by  $0.02 \text{ \AA}$ . The other bond lengths remain as in the isolated cluster.  $\text{FeCa}_8$  has an adsorption energy of  $0.82 \text{ eV}$  in this structure.

Another isomer having one Ca atom at a top site, two at hollow sites and the fourth one at a bridge site is only  $6 \text{ meV}$  higher in energy. Structures with smaller number

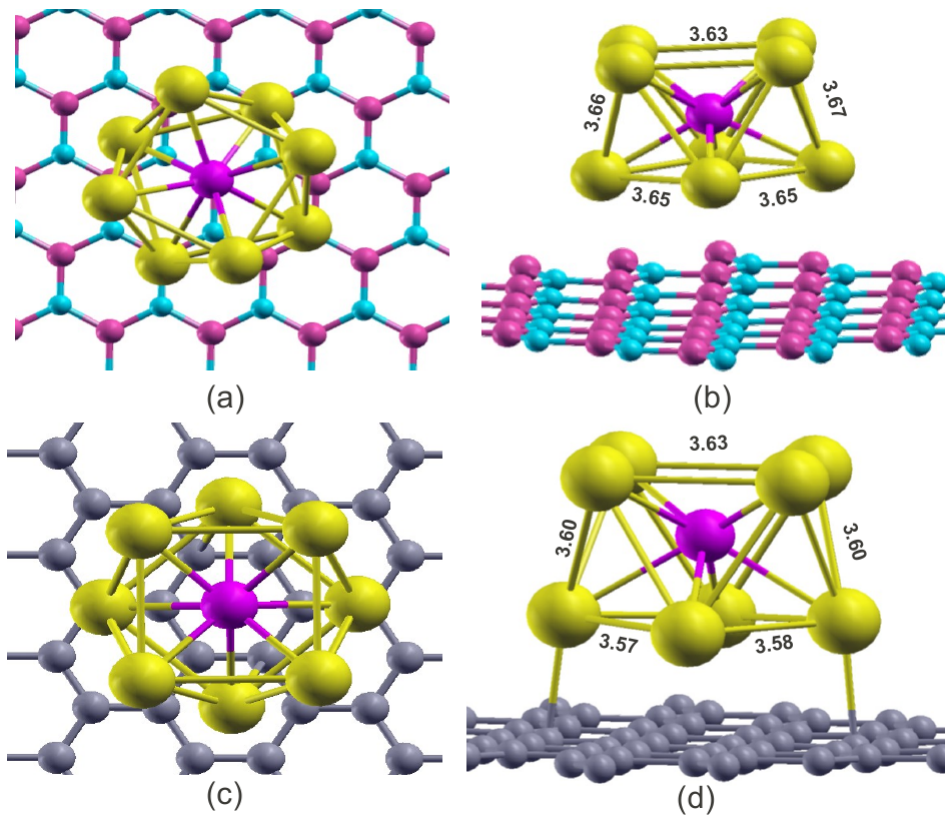


Figure 5.6: The lowest energy structure of  $\text{FeCa}_8$  supported over h-BN sheet (a) and Graphene (b) using vdW-DF2. First column: top view; second column: side view

of Ca-B/N neighbors are found to be higher in energy. To illustrate the point further we show two other structures in Fig. 5.7. In the structure in Fig. 5.7(a) only two Ca atoms are close to the surface. This structure is 21 meV higher than the lowest energy structure. The structure in Fig. 5.7(b), having only one Ca atom close to the surface, is 0.27 eV higher than the lowest energy structure.

In the lowest energy structure (Fig. 5.6(a,b)), the minimum distance between the surface and cluster atoms is 3.87 Å. This large cluster to surface distance rules out any chemical bond between them and suggests a physisorption scenario. While the superatom retains its anti-prism motif after deposition, the deformation of the surface can be given in terms of  $z_r$  and  $\Delta z_s$  (as defined in chapter 3). For the lowest energy structure, maximum  $z_r$  is 0.28 Å while the maximum  $\Delta z_s$  is 0.24 Å. These are found for the B atom directly below the Fe atom of the cluster.

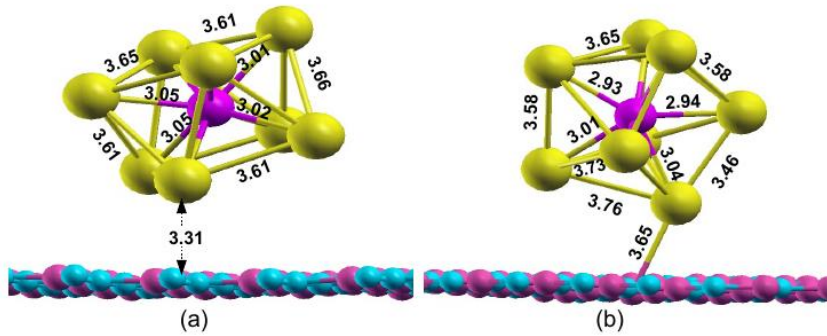


Figure 5.7: Some high energy isomers of  $\text{FeCa}_8$  deposited over BN-sheet obtained using vdW-DF2.

Now we look at the magnetic and electronic properties of the  $\text{FeCa}_8$  on h-BN. In the lowest energy adsorbed structure, the magnetic moment turns out to be  $4 \mu_B$ . Thus the magnetic moment of the isolated  $\text{FeCa}_8$  cluster is retained entirely after deposition. To understand the electronic structure of the combined cluster-substrate system, we analyze its DOS as shown in Fig. 5.8. Most of the occupied cluster states lie within the band gap region of the BN-sheet and have little mixing with the BN states. This is in clear contrast to the  $\text{FeCa}_8$ /alumina system in which the localized states had contributions both from the cluster and the surface atoms close to it. This lack of mixing preserves the MO's on the cluster nearly exactly, which we have also confirmed from the partial charge density (Fig. C.2). In particular, the four 2D states in the majority spin channel responsible for the magnetic moment in the isolated cluster appear right at the Fermi energy in the supported cluster. This preserves the moment of  $4 \mu_B$ . Indeed, most of the moment is localized on the cluster as seen in the spin density isosurface plot shown in Fig. 5.9. From this it is clear that a h-BN sheet is an ideal support for a magnetic superatom such that its structural and magnetic properties remain unaffected.

Some of the higher energy structures also preserve the magnetic moment of the isolated cluster. For example, the structure shown in Fig. 5.7(a) has a magnetic moment of  $4 \mu_B$ . Its structural motif is very similar to the gas phase cluster which preserves the MO's of the cluster. The structure in Fig. 5.7(b) on the other hand, which has only one Ca atom close to the substrate, loses part of its moment after deposition, and has a moment of  $2 \mu_B$ . This is because there is substantial distortion of the superatom

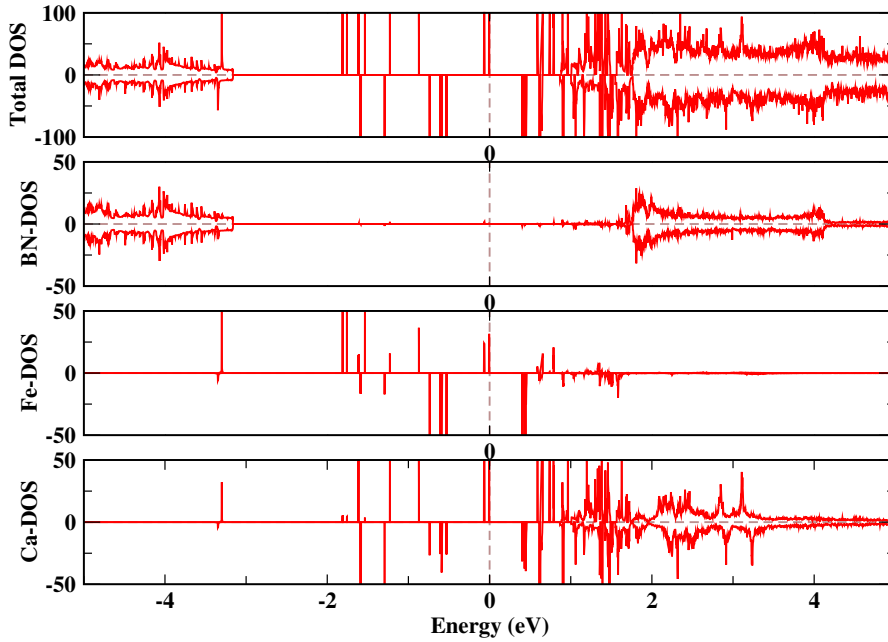


Figure 5.8: Total density of states, and atom projected partial density of states of h-BN supported  $\text{FeCa}_8$ .

geometry in this structure. As has been discussed by Chauhan *et al.*, [6] the particular anti-prism structure with an oblate distortion is crucial in obtaining a moment of  $4 \mu_B$ .

In Fig. 5.7(a), the Ca-Ca bond-lengths after deposition are very similar to the gas phase structure. Thus, there is only a minor modification in its structure after deposition. This retains its gas phase electronic states and magnetic moment. To illustrate this point further, we show a scatter plot of  $E_a$  vs magnetic moment of  $\text{FeCa}_8$  on h-BN in Fig. 5.10. In addition to the three structures discussed so far (Fig. 5.6, 5.7), an additional structure is also shown in which the superatom completely loses its moment. The superatom undergoes the maximum distortion in this structure leading to complete loss of moment.

#### 5.4.4 Graphene substrate

Next we study adsorption of  $\text{FeCa}_8$  on a graphene substrate. The calculated C-C bond length in a graphene sheet is  $1.43 \text{ \AA}$  within vdW-DF2, which is same as the intralayer lattice parameter of graphite discussed in Chapter 3. We also found two Dirac cones in the electronic structure at the  $K$  and  $K'$  points of the BZ, as expected.

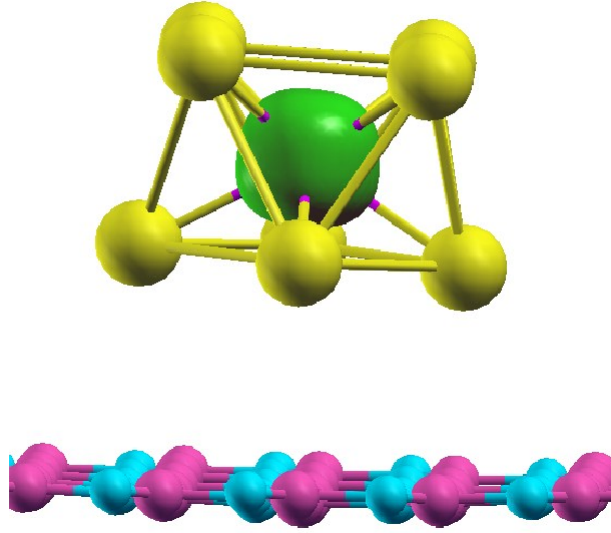


Figure 5.9: Spin density isosurface of  $\text{FeCa}_8$  deposited over h-BN using vdW-DF2 (plotted at isovalue 115 a.u.)

We took various random orientations of  $\text{FeCa}_8$  over a  $(7 \times 7)$  graphene sheet and relaxed them to their nearest local minima. Just as on h-BN, the  $\text{FeCa}_8$  cluster retained its square antiprism motif in all the structures. The lowest energy is obtained for a structure in which four Ca atoms stay close to the graphene-sheet (Fig. 5.6(c,d)), two being above hollow sites, and two above top sites. In the lowest energy structure the minimum distance between the Ca and the C atoms is 2.66 Å, which is larger than the sum of their covalent radii, indicating a weak cluster-substrate interaction. The maximum  $Z_r$  and  $\Delta Z_s$  are found to be 0.10 Å and 0.12 Å respectively. It is quite intriguing that in spite of a closer cluster-substrate distance on graphene,  $\text{FeCa}_8$  causes a larger deformation in h-BN sheet. We believe this has to do with the stiffness of the flexural phonon modes in these two materials. The flexural modes (acoustic modes with out-of-plane vibrations) exist at low energies. It has been shown [203] that flexural modes are significantly softer in BN ( $310 \text{ cm}^{-1}$  at  $K$ -point) than those in graphene ( $527 \text{ cm}^{-1}$  at  $K$ -point). This indicates that BN has greater tendency to form out of plane ripples than graphene.

Graphene is an interesting substrate because it has been shown that magnetic moments on a graphene sheet are coupled through RKKY interactions mediated by the  $\pi$  electrons [204--206]. However, unlike a usual two dimensional metal, the RKKY in-

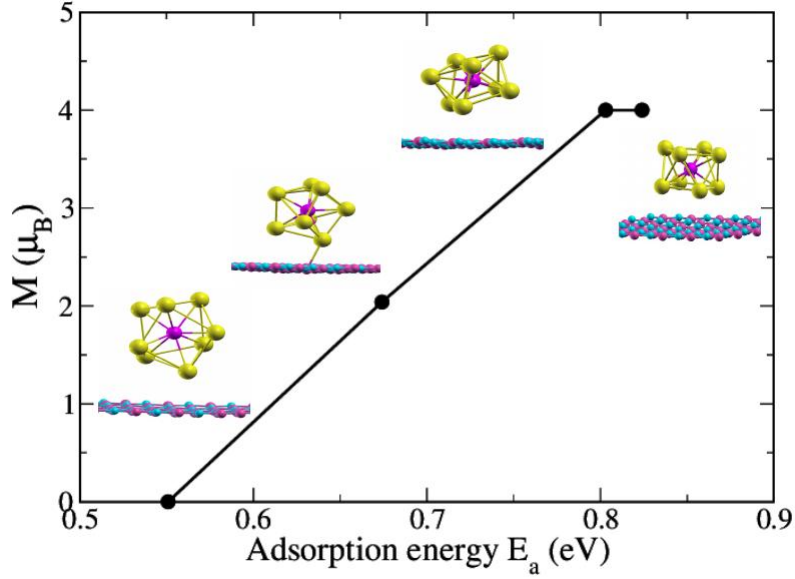


Figure 5.10: Scatter plot of adsorption energy and magnetic moment for various structures of  $\text{FeCa}_8$  on h-BN. The two structures with moment  $4 \mu_B$  are the lowest energy one and the one shown in Fig. 5.7(a). The one with a moment of  $2 \mu_B$  is the one in Fig. 5.7(b). The structure having no magnetic moment is a still higher energy one with large distortion of the anti-prism cage.

teraction on graphene has a  $1/R^3$  asymptotic behavior [204] due to its suppressed DOS at the Fermi energy. It has also been shown that the the interaction is oscillatory but is always anti-ferromagnetic for moments located on two different sublattices [205]. For moments located on the same sublattice, the oscillatory interaction remains ferromagnetic at all distances. If the moments are located at the hollow sites [205], the interaction is anti-ferromagnetic, and goes down monotonically with distance as  $1/R^3$ . It has also been argued that the RKKY interaction on graphene can be very long ranged, extending up to  $50 \text{ \AA}$  [207]. This poses a challenge for first principles calculations. In order to study adsorption of an isolated superatom the graphene sheet has to be  $\gtrsim 50 \text{ \AA}$  in each direction. This is computationally very expensive. Therefore we study adsorption of a  $\text{FeCa}_8$  cluster on graphene sheets of increasing lateral extent. It is understood from the above observations that there will be magnetic exchange interaction between the  $\text{FeCa}_8$  cluster in the simulation supercell and its periodic images in the lateral directions. Our goal is to extract an estimate of the distance dependence of the exchange

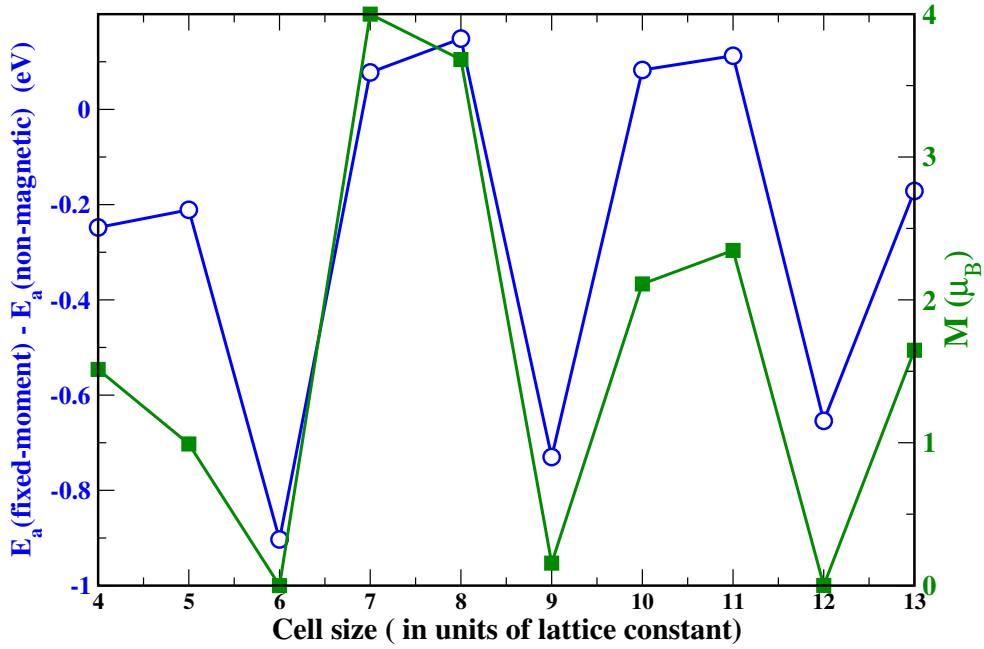


Figure 5.11: Difference in the adsorption energies (circle) of  $\text{FeCa}_8$  having magnetic moment of  $4 \mu_B$  (fixed-moment) and no magnetic moment (non-magnetic) on a graphene sheet represented by supercells of various sizes; and the moment (square) obtained through self-consistent calculations ( $M$ ).

interaction, and not necessarily to study properties of an isolated  $\text{FeCa}_8$  on graphene. Usually such estimates are made from a difference in the energies of the ferromagnetic and antiferromagnetic alignments of two fixed moments [205, 207]. However, with a single unit of  $\text{FeCa}_8$  in the supercell that is not possible. Having two units of  $\text{FeCa}_8$  is also not meaningful because of the long-range nature of the interaction.

We calculated energies of a  $\text{FeCa}_8$  cluster on a graphene sheet both in the nonmagnetic state, and with the moment fixed to that of the isolated superatom, *i.e.*,  $4 \mu_B$ . A difference in the two energies gives an estimate of the magnitude of the magnetic interaction. We plot the difference between the adsorption energies of  $\text{FeCa}_8$  in the nonmagnetic state and with a fixed moment of  $4 \mu_B$  with varying cell size in Fig. 5.11. The cell size is presented in units of lattice constant ( $a_0 = 2.476 \text{ \AA}$ ) and is the same along the two perpendicular in-plane directions. In addition we also show the moments obtained through self-consistent calculations to produce the lowest energy. It is clear that the energy difference, and hence the exchange interaction strength, has an oscillatory

behavior with distance. It is worth noting that the strength of the exchange interaction (direct plus RKKY) is  $\sim 10^2$  meV as seen in Fig. 5.11. We also made an estimate of the magnetic dipole-dipole interaction. For two spins  $\mathbf{S}_i$  and  $\mathbf{S}_j$  located at distance  $r_{ij}$ , the magnetic dipole-dipole interaction  $V(r_{ij}, \mathbf{S}_i, \mathbf{S}_j)$  can be given as

$$V(r_{ij}, \mathbf{S}_i, \mathbf{S}_j) = \left( \frac{g^2 \mu_B^2}{a_0^3} \right) \left( \frac{a_0}{r_{ij}} \right)^3 [-3(\mathbf{S}_i \cdot \hat{e}_{ij})(\mathbf{S}_j \cdot \hat{e}_{ij}) + (\mathbf{S}_i \cdot \mathbf{S}_j)], \quad (5.1)$$

where where  $a_0$  is the Bohr radius (0.529177 Å),  $\hat{e}_{ij}$  is the unit vector along the  $\mathbf{r}_{ij}$  and  $g$  is Landé g-factor and  $(g^2 \mu_B^2 / a_0^3) = 0.725$  eV [208]. For a superatom having 4 unpaired electrons,  $|\hat{\mathbf{S}}| = 2$ . On  $4 \times 4$  graphene supercell, (a distance of  $\sim 9.9$  Å the distance between a superatom and its periodic image)  $V(r_{ij}, \mathbf{S}_i, \mathbf{S}_j)$  can be calculated as  $\sim 10^{-4}$  meV, which is six orders of magnitude smaller than the strength of the exchange interactions. Dipole-dipole interaction goes down monotonically as  $1/R^3$ . Therefore, its contribution to inter-superatom interactions at still greater separations will be insignificant.

At cell sizes of 6, 9 and 12, the nonmagnetic state is favored over the magnetic state by large energies. And indeed at these sizes the self-consistent moments turn out to be nearly zero. At cell sizes 7, 8, 10 and 11, the energy difference indicates the magnetic state to be more favorable. The self-consistent magnetic moment in fact has high values at these sizes. Thus we establish a graphene mediated distance dependent oscillatory exchange interaction between FeCa<sub>8</sub> superatoms. To establish that this interaction is not present on a h-BN substrate, we calculated adsorption of FeCa<sub>8</sub> on h-BN sheets of increasing size (beyond  $7 \times 7$ ). As mentioned above, on a  $7 \times 7$  h-BN sheet, a FeCa<sub>8</sub> cluster has an adsorption energy of 0.82 eV, while on a  $8 \times 8$  sheet, FeCa<sub>8</sub> has an  $E_a = 0.86$  eV. If we compare the  $E_a$  per atom, it is only 2 meV higher for the  $8 \times 8$  unit cell, which is negligible. For both unit cells, magnetic moment of the system was equal to the gas phase magnetic moment of the FeCa<sub>8</sub> *i.e.*,  $4 \mu_B$ . Hence, no size-dependence of adsorption energy or magnetic moment was found in this large-gap insulating material.

Thus individual FeCa<sub>8</sub> superatoms retain their structures both on h-BN and graphene. On h-BN they also retain their magnetic moments in the low energy configurations. On the other hand magnetic moments on graphene interact through long range RKKY interactions and due to the periodic boundary conditions it was difficult to calculate the

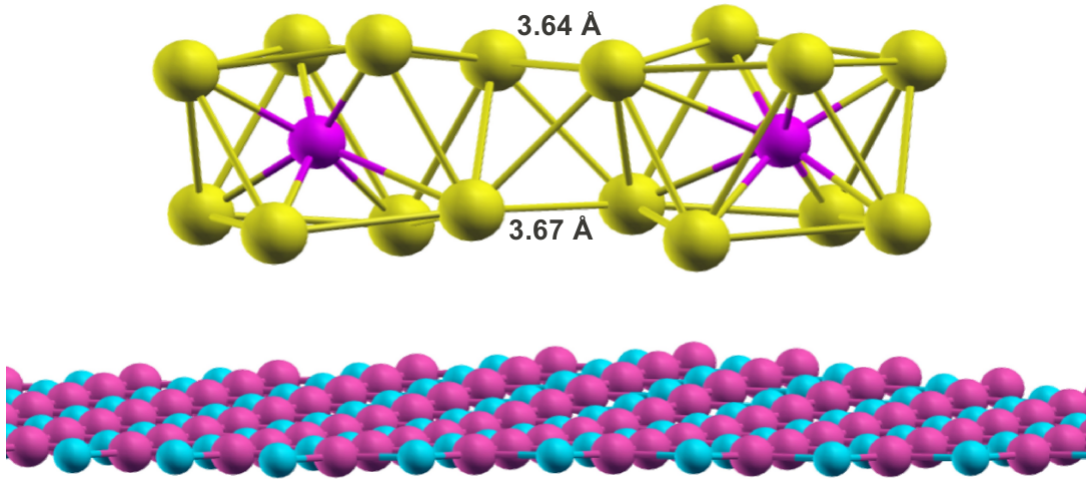


Figure 5.12: Dimer of FeCa<sub>8</sub> deposited over h-BN sheet using vdW-DF2

moment of an isolated FeCa<sub>8</sub> cluster.

#### 5.4.5 Two FeCa<sub>8</sub> units on h-BN and graphene

Having established that h-BN is an ideal support with weak enough cluster-support interaction to preserve the structure and magnetic properties of a FeCa<sub>8</sub> unit, we now address the question whether two units of FeCa<sub>8</sub> form a stable dimer on it and what magnetic states this may have. When a large number of clusters land on the substrate in LECBD experiments, their relative orientations will also be random. The magnetic interaction between two cluster units will in general depend on their relative location and orientation. It is virtually impossible to do a thorough study of all such structures on the substrate within a first-principles approach. Instead, we take a simplified view which will be relevant when the cluster flux and coverage are low. We consider a situation in which two cluster units have already landed on the substrate in their lowest energy structures, and then approach each other. While this greatly reduces the number of possible structures one has to consider, the clusters can still approach each other along arbitrary directions on the plane of the substrate. It will still be computationally prohibitive to consider all such possibilities. To make things even simpler, we consider two situations: (1) when two triangular faces of two clusters are connected directly *i.e.*, each atom of one triangular face is connected to only one atom of the other triangular

face (Fig. C.3(a)), and (2) when one of the triangular faces is twisted relative to the other and one atom of each triangular face is connected to two atoms of the other face (Fig. C.3(b)). These results should, therefore, be taken in the spirit that they give an indication of whether stable assemblies of FeCa<sub>8</sub> clusters are possible on h-BN rather than a quantitative information about possible low energy structures of such assemblies.

First we deposit the FeCa<sub>8</sub> clusters close to each other in both orientations (discussed above) so that the nearest Ca-Ca distance between them is 3 Å. Fig. 5.12 shows the relaxed structure of such a dimer. In both the orientations, the FeCa<sub>8</sub> units retain their individual identities. This structure in Fig. 5.12 has an adsorption energy of 3.72 eV. Adsorption energy of a single unit in h-BN is 0.82 eV as mentioned earlier. Thus the binding energy between the two units of FeCa<sub>8</sub> is 2.03 eV, which is slightly smaller than the binding energy of two units of FeCa<sub>8</sub> in gas phase which is 2.12 eV. Incidentally, this structure is not the lowest energy structure for the dimer in gas phase. In gas phase, the dimer of FeCa<sub>8</sub> has a moment of 8  $\mu_B$  [6]. On h-BN sheet, the magnetic moment of a dimer turned out to be 2  $\mu_B$  which is located at both Fe atoms. Although this is much smaller than the possible maximum of 8  $\mu_B$  for parallel alignment of spins on the two cluster units, the same structure in the gas phase also has a moment of 2  $\mu_B$ . Thus, there is no additional reduction in moment due to the substrate. Therefore, h-BN turns out to be an ideal support that preserves magnetic moments of individual superatoms and their assemblies. Our attempts to study anti-parallel alignment of moments on the two superatom units in this structure were not successful as at the end of the self-consistent calculations, the dimer converged to the same spin state as above with a moment of 2  $\mu_B$ .

We then wanted to understand two other aspects of assemblies of FeCa<sub>8</sub> superatoms on h-BN: (i) the distance dependence of interaction between two FeCa<sub>8</sub> units: what is the threshold distance below which they feel each other presence? (ii) What is the strength of exchange interaction between two superatom units? When we put two units far apart so that the nearest Ca-Ca distance between them is 8.5 Å, the clusters stay in their respective positions (Fig. C.4). For this calculation we use a 14 × 14 supercell (37.15 Å × 37.15 Å) of h-BN. The total moment turns out to be 8  $\mu_B$ , sum of the moments on individual clusters. The adsorption energy is found to be 1.93 eV, only slightly larger than the sum of adsorption energies of the individual clusters. All these show that the two clusters do not feel each other's presence at this distance and

indicate that interactions between two superatoms on BN are not long ranged. On the other hand, when two clusters are placed such that the nearest Ca-Ca distance between them is 5 Å, they approach each other and finally form a dimer as in Fig. 5.12 with the same magnetic moment of  $2 \mu_B$ . In this structure, two superatoms interact ferromagnetically. The anti-ferromagnetic alignment of superatoms was not stabilized. Clusters start interacting with each other between 5 – 8 Å, indicating that the magnetic interaction between two FeCa<sub>8</sub> units on h-BN is direct exchange.

We also calculated the cluster densities on the surface by assuming a circle of a given radius around a cluster. Using this assumption, we can determine the number of clusters per unit area. Hence for the average inter-cluster distances of 5 Å and 8.5 Å correspond to cluster densities of  $12.73 \times 10^{13}$  and  $4.97 \times 10^{13}$  per cm<sup>2</sup> respectively. Therefore, our results suggest that up to an areal density of  $4.97 \times 10^{13}$  per cm<sup>2</sup>, the clusters behave as isolated units on a h-BN substrate, but somewhere between  $4.97 \times 10^{13}$  per cm<sup>2</sup> and  $12.73 \times 10^{13}$  per cm<sup>2</sup>, they self-assemble to form new structures.

In order to estimate the strength of exchange interactions, we expressed the total spin exchange energy in terms of spin Heisenberg Hamiltonian.

$$H = E_0 - J \mathbf{S}_i \cdot \mathbf{S}_j,$$

where  $J$  is the exchange interaction parameter between the two superatoms. For anti-ferromagnetic interaction  $J < 0$  and for ferromagnetic interaction  $J > 0$ . The constant  $E_0$  contains all spin-independent interactions. Strength of exchange interactions can be estimated by calculating the energy difference between the ferromagnetic and antiferromagnetic orientations of the spin moments. At a distance of 8.5 Å the value of  $J$  turned out to be only  $\sim 0.75$  meV with the AFM arrangement being marginally lower in energy. At small distances, as stated earlier, we could not stabilize the antiferromagnetic alignment of the two superatoms. Hence we could not calculate the strength of the exchange interaction when superatoms are at a distance of 5 Å.

We attempted to study two FeCa<sub>8</sub> units on a graphene sheet. In this case, two superatom units in the simulation cell have a direct exchange, and also have RKKY interaction with each other, and their periodic images. All these complex magnetic interactions give rise to many possible magnetic states close in energy. In fact, for a

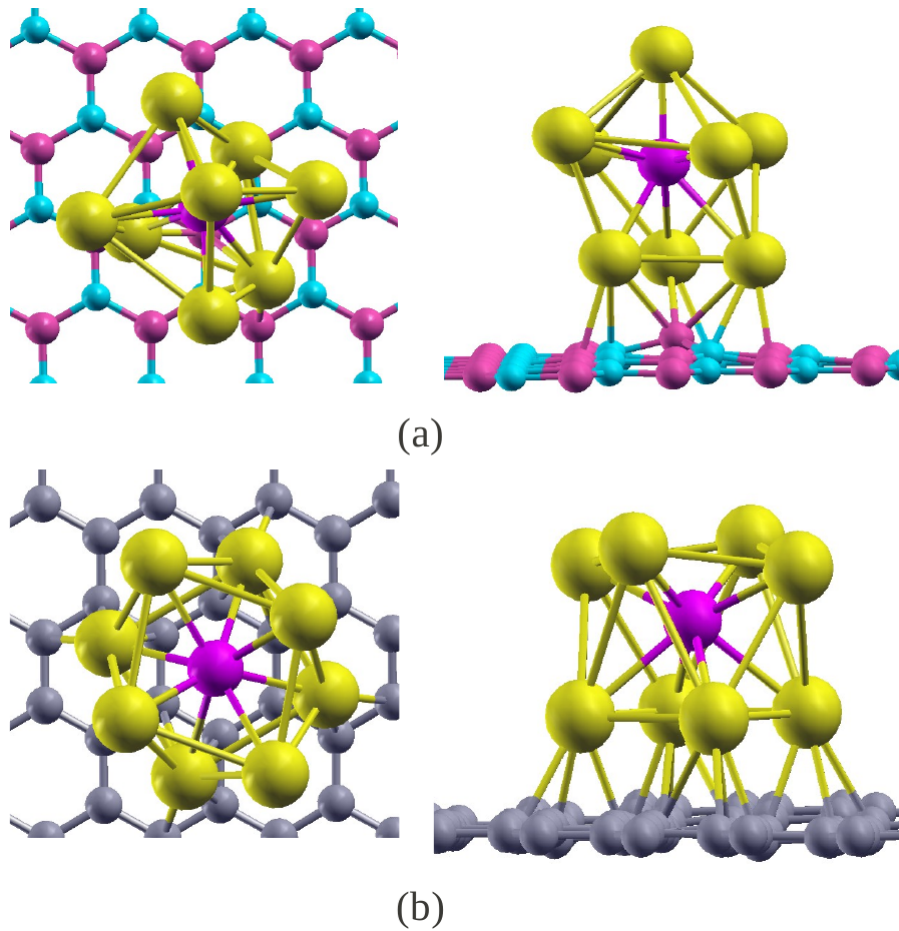


Figure 5.13: Lowest energy structure of FeCa<sub>8</sub> supported over h-BN sheet (a) and Graphene (b) using LSDA method. First column- top view; second column- side view

dimer, we failed to locate the ground state spin moment as spin states with moments 0, 2, and 4  $\mu_B$  are essentially degenerate. For a non-magnetic configuration, dimer has an  $E_a = 0.13$  eV, for magnetic state with 2  $\mu_B$  moment and for the configuration with magnetic moment of 4  $\mu_B$ ,  $E_a = 0.14$  eV.

## 5.5 LSDA results

As in chapter 3 that the L(S)DA tends to over-bind systems, while GGA usually tend to underestimate binding. This behavior is particularly acute in systems where van der Waals interactions play a major role. In case of graphene-metal interface, GGA predicts

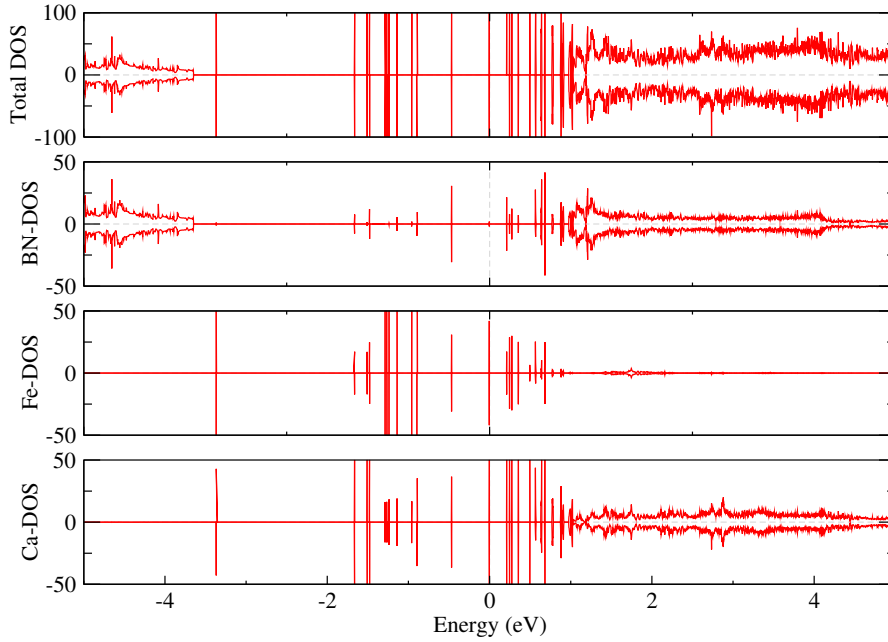


Figure 5.14: DOS of  $\text{FeCa}_8$  deposited over BN-sheet using LSDA

no binding at all [21, 169, 170], which is contrary to experiments [209]. Therefore most theoretical work on graphene-metal interfaces [210] or surface and molecular adsorption [168, 196, 197] relies on the L(S)DA. As mentioned above, a number of studies on metal-graphite or metal-graphene systems used the LSDA for the simulation. For a comparison with our vdW-DF2 calculations, we also studied the adsorption of  $\text{FeCa}_8$  over graphene and h-BN sheet using LSDA. We found that the adsorption and magnetic moment of  $\text{FeCa}_8$  on graphene or h-BN is modified when studied using LSDA.

Let us first discuss  $\text{FeCa}_8$  adsorption over h-BN. We have optimized various orientations of  $\text{FeCa}_8$  over different adsorption sites of a h-BN sheet using LSDA. The lowest energy structure is obtained for an orientation where three Ca atoms are close to the substrate, shown in Fig. 5.13(a). In this structure, h-BN is significantly damaged by superatom deposition. One of its B atoms, which is directly below the cluster, is pulled up by  $0.68 \text{ \AA}$  from the hexagonal plane. The three nearest N atoms (below the cluster) are displaced by an average of  $0.29 \text{ \AA}$  from their initial positions. The maximum  $\Delta Z_s$  for this case is  $0.723 \text{ \AA}$ . The cluster is slightly deformed from its antiprism structure, but the overall endohedral structure is preserved. Unlike oxide and metal surfaces, Fe atom is not exposed to the surface. The minimum distance between Ca and BN-sheet

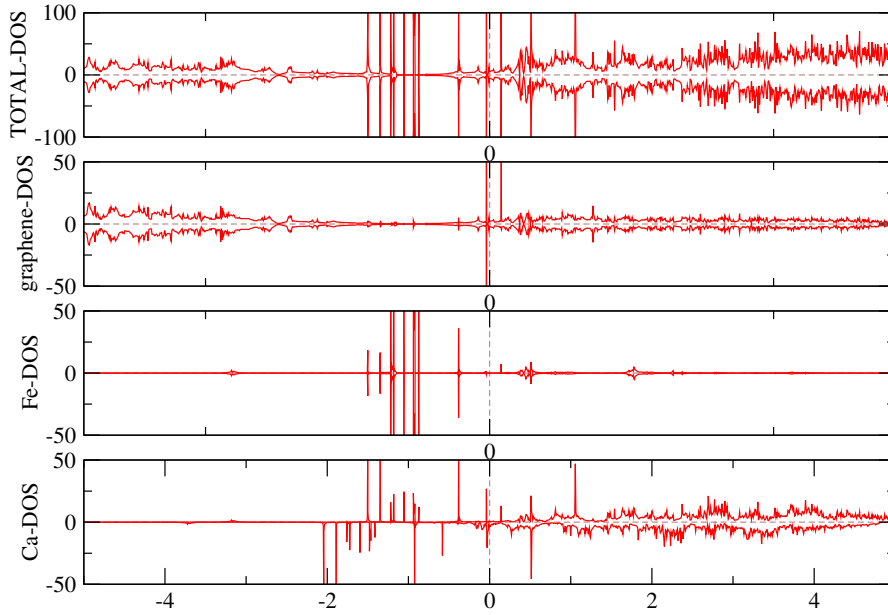


Figure 5.15: DOS of FeCa<sub>8</sub> deposited over graphene using LSDA

atoms is found to be 2.58 Å, which is much smaller than the corresponding vdW-DF2 case. This structure has an adsorption energy  $E_a = 1.49$  eV. All these facts clearly indicate that LSDA predicts a strong interaction between FeCa<sub>8</sub> cluster and h-BN than the vdW-DF2 method.

In Fig. 5.14, similar to the vdW-DF2 case, the discrete cluster states lie within the band gap of h-BN. As interaction between cluster and h-BN is quite strong, a set of discrete states appear which are localized on the cluster atom and the nearby substrate atoms. However, these states appear in equal numbers in both the spin channels and leave the system with no magnetic moment.

Similar behavior is found for the adsorption of FeCa<sub>8</sub> over graphene when studied with LSDA. In the lowest energy structure (Fig. 5.13(b)), four Ca atoms are close to the hollow and bridge sites of graphene. This structure has an adsorption energy  $E_a = 3.43$  eV. The maximum relaxation  $Z_r$  and maximum  $\Delta Z_s$  are found to be 0.18 Å and 0.22 Å respectively. Again we find few discrete states appearing due to cluster-substrate interaction (Fig. 5.15). LSDA gives a large cluster-substrate binding, which modifies the electronic states of the cluster and leads to the loss of its moment.

## 5.6 Conclusions

We have addressed the important question of finding the right support for assemblies of magnetic superatoms which can be of immense importance in spintronics and other applications. It turns out that alumina substrate, that is routinely used for supporting metal clusters for catalytic reactions, are not the ideal ones for this purpose. A calcium substrate also turns out to be interacting strongly with a  $\text{FeCa}_8$  superatom so that the structure and magnetic moment of the superatom is destroyed. On the other hand, h-BN and graphene, because of their weak interactions with metal atoms and clusters, preserve the structure of the superatom in the low energy structures. In these structures, magnetic moment of the isolated superatom is also preserved. Moreover, in a particular structure, a dimer of  $\text{FeCa}_8$  superatoms on h-BN has the same moment as in the gas phase. This suggests that assemblies of  $\text{FeCa}_8$  superatoms on h-BN will possess finite magnetic moments necessary for applications. We also estimated that  $\text{FeCa}_8$  superatoms will remain isolated on h-BN below a coverage of  $4.97 \times 10^{13}$  per  $\text{cm}^2$ . Between  $4.97 \times 10^{13}$  and  $12.73 \times 10^{13}$  per  $\text{cm}^2$  they will start forming self assemblies. This information will be useful for experimentalists. Magnetic moment of  $\text{FeCa}_8$  superatoms on graphene is complicated by long range, oscillatory RKKY interactions in addition to direct exchange. The exact magnetic structure realized in a particular assembly will depend on the exact positions of all the superatoms on the substrate. In our limited explorations we found that states with very different magnetic moments are close in energy. This may lead to magnetic frustrations and complex magnetic orders, which can be a separate topic of study. We believe that these results will motivate the experimentalists to undertake efforts to form assemblies of magnetic superatoms.

# CO oxidation on $\text{Al}_2\text{O}_3$ supported $\text{Ag}_n\text{Au}_m$ model catalysts

## 6.1 Introduction

Bulk gold is considered as a poor catalyst in heterogeneous catalysis, as it is not a reactive metal. However as one goes to the small size scale, it is found to be strongly catalytically active in several important reactions. The first breakthrough in gold chemistry came through the discovery by Haruta *et al.*, [22]. They found that when small gold particles (of diameter  $\leq 5$  nm) are deposited on various oxide surfaces such as  $\text{TiO}_2$ ,  $\text{SiO}_2$ ,  $\text{Al}_2\text{O}_3$ , and  $\text{CeO}_2$ , they show surprisingly high activities and/or selectivities for CO oxidation, direct propylene epoxidation using  $\text{H}_2$  and  $\text{O}_2$ , and water gas shift reaction. They proposed that the gold-metal oxide interface acts as an activating site for one of the reactants of the above reactions *e.g.*,  $\text{O}_2$ ,  $\text{H}_2\text{O}$  *etc.* In another study, Valden *et al.*, [190] found that nanometer-sized Au islands on  $\text{TiO}_2$  with two layers of gold are most effective catalysts for CO oxidation. They demonstrated that the pronounced structure sensitivity for CO oxidation on Au/ $\text{TiO}_2$  originates from the quantum size effects associated with the thickness of the supported clusters.

The studies by Sanchez *et al.*, [211] also supported these facts. They deposited  $\text{Au}_n$  ( $n \leq 20$ ) clusters on defect-poor and defect-rich MgO (100) surfaces using soft-landing technique and demonstrated size dependent catalytic activity for low-temperature CO-oxidation. They found that  $\text{Au}_8$  is the smallest size to catalyze the reaction. The accom-

panying theoretical calculations revealed that the charging of the cluster via (partial) electron transfer from the oxide support as well as the presence of oxygen-vacancy (F-center) in the substrate play an essential role in the activation of nanosize gold catalysts. Thus electronic interaction with the oxide support plays an important role in the oxidation reactions.

Several experimental as well as theoretical studies have also been performed on reactivity of gas phase  $\text{Au}_n$  clusters. It has been found that Au clusters can easily adsorb CO molecules. Wallace *et al.*, [212] found that adsorption of CO on small gold  $\text{Au}_n^-$  ( $n = 4 - 19$ ) clusters is highly size-dependent. They reported that cluster anions can adsorb as many as six CO molecules at the saturation. Zhai *et al.*, [213] studied the adsorption of CO molecules on small gold clusters  $\text{Au}_n(\text{CO})_m^-$  ( $n = 2 - 5; m = 0 - 7$ ) using photoelectron spectroscopy. They observed a strong chemisorption of the first few CO molecules. The adsorption of the first few CO molecules resulted in significant redshifts in the photoelectron spectra, which indicates electron-donating nature of the CO molecule. Further CO adsorption only slightly perturbed the electronic structure which indicates a relatively weak physisorption. The DFT results reported by Yuan *et al.*, [214] for CO adsorption on  $\text{Au}_n^-$  ( $n = 2 - 7$ ) agree well with these experimental findings. Another theoretical calculation by Wu *et al.*, [215] on CO adsorption on small cationic, neutral, and anionic  $\text{Au}_n$  ( $n = 1 - 6$ ) clusters reveals that atop one-fold coordinated Au site is most favorable for CO adsorption irrespective of the charge state of the cluster. In addition, they found that the adsorption energies of CO on the cationic clusters are generally greater than those on the neutral and anionic complexes, and decrease with size of the cluster. In neutral and anionic Au clusters, adsorption energies of CO show small odd-even oscillations. In combined experimental and theoretical studies, Popolan *et al.*, [216] also reported that positively charged Au clusters have strong binding with the CO molecule, which prevents the coadsorption of other ligands *e.g.*,  $\text{O}_2$ ,  $\text{H}_2\text{O}$ . Usually, CO molecule binds to the Au clusters via charge donation from the  $s\sigma^*$  orbitals of CO to the LUMO of the Au cluster and a  $\pi$  back donation from the Au cluster  $d$  orbitals in to the  $p\pi^*$  orbitals of CO. Hence CO binds more strongly to a positively charged Au clusters [217].

Several studies were also performed for the adsorption of  $\text{O}_2$  on gas phase Au clusters. Cox *et al.*, [218] found that reactivity of  $\text{O}_2$  towards gold clusters depends not only on the cluster size but also on the cluster charge state. Small gold clusters anions

were found to have a pronounced odd-even variation in their reactivity towards oxygen molecule. Several other experimental investigations also reported a marked odd-even oscillation in the reactivity of O<sub>2</sub> molecule towards the Au<sub>n</sub><sup>-</sup> ( $n \leq 20$ ) [219--221]. The even sized cluster anions can adsorb one molecule of O<sub>2</sub> per cluster, while the odd-sized cluster anions show extremely small or zero reactivity. Since O<sub>2</sub> exhibits high electron affinity, it is likely to accept appreciable electron density from Au clusters. Salisbury *et al.*, [220] explained that binding between O<sub>2</sub> and Au involves electron donation from anionic Au clusters to the  $\pi^*$  molecular orbitals of O<sub>2</sub>. An even-numbered cluster anion can easily donate one electron, forming a closed shell configuration. For odd-sized cluster anions which already have closed shell configurations, a charge transfer to O<sub>2</sub> is not energetically favorable. The theoretical studies also supported these experimental findings. In a DFT simulation, Mills *et al.*, [222] investigated the interaction of O<sub>2</sub> with neutral and anionic Au<sub>n</sub> ( $n = 2 - 5$ ) clusters and found that O<sub>2</sub> binds more strongly to the clusters with odd number of electrons than to those with an even number of electrons. The large charge transfer from Au to O<sub>2</sub> gives larger O-O bond-length. They also suggested that larger the charge transfer, easier will be the dissociation of the O-O bond.

In summary, all these studies indicate that CO adsorption is more feasible on the positively charged clusters, while O<sub>2</sub> activation is only possible on the negatively charged gas phase Au clusters. However for CO-oxidation clusters should coadsorb both the reactants. Therefore, to promote the oxidation of CO, the clusters should also adsorb and activate the oxygen molecules. The catalyst should coadsorb both CO and O<sub>2</sub> molecules near to each other. An alternative way to improve the catalytic activity of gold clusters towards CO-oxidation is to change the cluster capability to adsorb and activate oxygen molecules. This can be done by adding a second metal to the gold catalyst that has a larger affinity towards oxygen molecules than gold, for example silver metal. Silver is less electronegative (1.94) in comparison to gold (2.54). Hence silver clusters can easily donate its charge to O<sub>2</sub>, which activate the O-O bond length [223]. These ideas have recently been examined in an experimental study by Wang *et al.* [224] They studied the CO-oxidation on the nanometer-sized Au-Ag nanoparticles supported over mesoporous aluminosilicates and demonstrated the synergistic effect of combining Au and Ag. Ag was found to activate O<sub>2</sub> and Au was found to adsorb CO. The best performing Au-Ag catalyst was the one with a Au/Ag ratio of 3 : 1.

There are some theoretical initiatives in this direction. DFT calculations for the CO-oxidation on a  $\text{Au}_{25}\text{Ag}_{30}$  alloy nanoparticle showed that the electron transfer from Ag atoms to the antibonding orbital of the  $\text{O}_2$  molecule weakens the O–O bonding, which promotes oxygen activation [225]. On the same catalyst, CO molecule can coadsorb atop the Au site. Therefore, in the Au-Ag catalysts, if silver and gold atoms are in their neighborhood, the silver atoms will activate the oxygen molecules to react with the coadsorbed CO molecules on the gold atoms, and produce  $\text{CO}_2$ . In another theoretical study Koutecký *et al.*, [226] found that due to electronegativity difference, there is a charge transfer from Ag to Au atoms in the bimetallic clusters. This charge transfer promotes the formation of negatively charged gold subunits which are expected to be reactive. This is similar to that of gold clusters supported on metal oxide surfaces. In case of supported Au clusters, oxide supports promote the activation of  $\text{O}_2$  molecule on Au clusters as there is a partial charge transfer from cluster to surface which leave the supported clusters as partially negatively charged.

Most of the theoretical studies on bimetallic clusters have been performed in gas phase [26, 27, 216, 226]. The effect of oxide support for the CO-oxidation on the bimetallic clusters is still unknown. We believe that the oxide support will further increase the ionic character between the Au and Ag atoms and enhance the catalytic activity of these clusters. The alumina support donates charge to the pure Au clusters [227], while it receives an electronic charge from the pure Ag clusters [228]. The supported bimetallic Ag-Au clusters will definitely give rise to some interesting phenomena, which will strongly depend on the composition of the clusters. In addition, size dependence of the Ag-Au cluster will also affect the performance of the catalyst towards CO-oxidation. In this chapter, we will try to find the answers to these questions for the  $\text{Ag}_n\text{Au}_m$  ( $n + m = 2 - 4$ ) clusters supported over the  $\text{Al}_2\text{O}_3$  surface.

The rest of the chapter is organized as follows. In section 6.2 we present the theoretical modeling used for our calculations. Later, in various sections of this chapter, we present the ground state structure of gas phase and alumina supported  $\text{Ag}_n\text{Au}_m$  clusters and adsorption of  $\text{O}_2$  and CO molecules over gas phase and supported  $\text{Ag}_n\text{Au}_m$ . In the last section 6.5, we summarize our findings and draw our conclusions.

## 6.2 Computational method

The spin-polarized DFT calculations are performed using PAW [120, 121] method, as implemented in VASP [151]. The wave functions are expressed in a plane wave basis set with an energy cutoff of 400 eV. The exchange-correlation functional has been approximated at the GGA level. The simulation of the gas phase  $\text{Ag}_n\text{Au}_m$  ( $n + m = 2 - 4$ ) clusters are performed in a supercell of size  $15 \times 15 \times 15 \text{ \AA}^3$  and the BZ integrations are performed at the  $\Gamma$ -point only. The binding energy of the gas phase clusters has been calculated as

$$E_b = nE_T(\text{Ag}) + mE_T(\text{Au}_m) - E_T(\text{Ag}_n\text{Au}_m), \quad (6.0)$$

where  $E_T(\text{Ag})$  and  $E_T(\text{Au})$  are the total energy of the isolated Ag and Au atoms respectively,  $E_T(\text{Ag}_n\text{Au}_m)$  is the total energy of the gas phase  $\text{Ag}_n\text{Au}_m$  cluster.

The  $\alpha\text{-Al}_2\text{O}_3(0001)$  surface is modeled by a  $(3 \times 3)$  supercell cell with nine atomic layers in a repeated slab geometry. Only top five atomic layers are allowed to relax during the structure optimization, while the bottom four layers are held fixed in their bulk terminated positions. The lattice parameters for the hexagonal unit cell for bulk  $\text{Al}_2\text{O}_3$  are found to be  $a = b = 4.81 \text{ \AA}$  and  $c = 13.1 \text{ \AA}$ , which are in agreement with the experimental values [199]. A Monkhorst-Pack set of  $3 \times 3 \times 1$  of  $k$ -points are used for the BZ integration. A vacuum of  $20 \text{ \AA}$  is considered to avoid the interaction between the periodic images. Corrections are also included to avoid any spurious interaction between periodic images of the slab due to long-range dipole-dipole interactions [195].

For the deposition of  $\text{Ag}_n\text{Au}_m$  ( $n + m = 2 - 4$ ) clusters on alumina surface, we have considered several initial structures near different adsorption sites (A11, O2, A13, A14 and O5) using random rotation technique and optimized them to the nearest local minima. The relative stability of the adsorbed structures for a given cluster size is measured by their adsorption energies  $E_a$  as defined in chapter 3.3.

We also studied the adsorption as well as the coadsorption of  $\text{O}_2$  and CO molecules on the gas phase and supported  $\text{Ag}_n\text{Au}_m$  clusters. This will give us an idea about the best suitable candidate for the CO-oxidation reaction. The coadsorption energy is defined as

$$E_a^c = E_T(\text{CO}) + E_T(\text{O}_2) + E_T(\text{surface}) - E_T(\text{Ag}_n\text{Au}_m\text{O}_2\text{CO/surface}).$$

We also performed the CINEB calculations to determine the energy barriers in the CO-oxidation reaction. The calculations are performed using 5-8 images between two end points, which are connected with the springs of force constant  $-5.0 \text{ eV/\AA}^2$ . Since we have a large number of atoms in the simulation box, the barrier calculations are rather difficult to converge. We have not been able to converge all of them, unfortunately.

### 6.3 Gas phase structure of $\text{Ag}_n\text{Au}_m$ clusters

Since we are interested in studying the chemical reactivity of bimetallic clusters, it is important to determine their structures and energetics in the gas phase. We performed a thorough search for  $\text{Ag}_n\text{Au}_m$  ( $n + m = 2 - 4$ ) clusters starting from the good initial guesses and optimized them to the nearest local minima. The initial guesses were generated by taking all possible configurations for a given cluster size. We are mainly interested in the lowest energy structures, which are shown in Fig. 6.1. The high energy isomers are not discussed. An AgAu dimer has a binding energy of 2.16 eV with a bond length of 2.55 Å. This bond length is 0.028 Å smaller than the Ag-Ag dimer and 0.024 Å larger than Au-Au dimer. Similarly the binding energy of AgAu cluster is intermediate the binding energy of  $\text{Ag}_2$  (1.74 eV) and  $\text{Au}_2$  (2.28 eV) dimers. In this lowest energy structure, an Ag atom transfers a charge of 0.22  $e$  to Au atom. The three atom clusters  $\text{AgAu}_2$  and  $\text{Ag}_2\text{Au}$  have isosceles triangle structures as shown in Fig.: 6.1(b,c). For  $\text{AgAu}_2$  cluster, both Ag-Au bond lengths are equal (2.65 Å) and Au-Au bond is larger (2.75 Å). Similarly in the case of  $\text{Ag}_2\text{Au}$  cluster, the Ag-Au bond lengths are equal (2.63 Å), and the Ag-Ag bond length is larger (2.55 Å). The  $\text{AgAu}_2$  and  $\text{Ag}_2\text{Au}$  clusters have binding energies 3.56 and 3.23 eV respectively, which are intermediate to the binding energy of homoatomic  $\text{Ag}_3$  (2.54 eV) and  $\text{Au}_3$  (3.45 eV) clusters. In case of  $\text{AgAu}_2$  cluster, Ag atom transfers a charge of 0.36  $e$  to the Au atoms, while in case of  $\text{Ag}_2\text{Au}$  clusters, total charge transfer from the Ag atoms to Au atom is 0.32  $e$ . The four atom clusters,  $\text{AgAu}_3$ ,  $\text{Ag}_2\text{Au}_2$ , and  $\text{Ag}_3\text{Au}$  have rhombus geometries in their ground states as shown in Fig. 6.1(d,e,f), with binding energies 6.95, 6.10, and 5.37 eV respectively. All of these agree with the results of Zhao *et al.*, [229] which were obtained using the triple-zeta Slater-type orbital basis set. In case of  $\text{AgAu}_3$ , Ag atom transfers a charge of 0.39  $e$  to the Au atoms, for  $\text{Ag}_2\text{Au}_2$  clusters the Ag atoms transfer a charge of 0.63  $e$  to the Au atoms, and in case of  $\text{Ag}_3\text{Au}$ , there is a charge transfer of

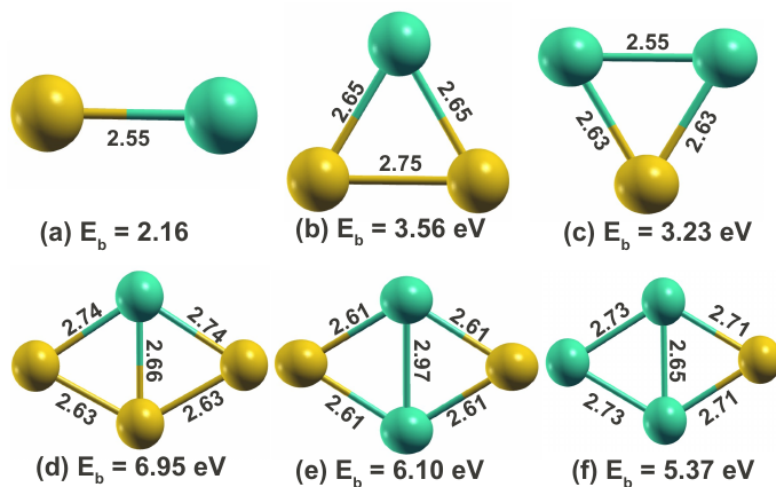


Figure 6.1: The ground state structures of gas phase  $\text{Ag}_n\text{Au}_m$  clusters. The golden colored circles represent Au atoms, while green colored circles represent Ag atoms.

0.37  $e$  from the Ag atoms to Au atom. Thus in all these clusters the Ag atoms always transfer an electronic charge to the Au atoms, which create a partial ionic character in the metallic bonding of the cluster.

The electronic structure of these clusters indicates that increasing silver content increases the energy gap between the outermost  $s$  and  $d$  orbitals in the energy spectrum of these clusters. A schematic diagram for different composition of Ag and Au for size 2 is shown in Fig. 6.2. For  $\text{Au}_2$  there is no gap between  $s$  and  $d$  states, while for  $\text{Ag}_2$  there is gap of 1.56 eV. For a mixed cluster  $\text{AgAu}$ , the gap between  $s$  and  $d$  is intermediate to the  $\text{Ag}_2$ , and  $\text{Au}_2$  case. It has a  $s$ - $d$  gap of 0.41 eV. Similar trend is followed by the clusters of size 3 (Fig. 6.3). An  $\text{Au}_3$  cluster has a  $s$ - $d$  gap of 1.6 eV, while  $\text{Ag}_3$  cluster has a  $s$ - $d$  gap of 2.58 eV. An increase in the silver content in the cluster increases the  $s$ - $d$  gap. An  $\text{AgAu}_2$  cluster has a gap of 1.74 eV, while for  $\text{Ag}_2\text{Au}$  it is 2.07 eV. Similar behavior has also been seen for size 4 clusters. The schematic diagram for size 4 is shown in Fig. D.1 in the Appendix.

### 6.3.1 Adsorption and coadsorption of $\text{O}_2$ and CO molecules

After optimizing the geometries of free  $\text{Au}_n\text{Ag}_m$  ( $n + m = 2 - 4$ ) clusters, we have investigated the adsorption behavior of  $\text{O}_2$  and CO molecules on these clusters. For all

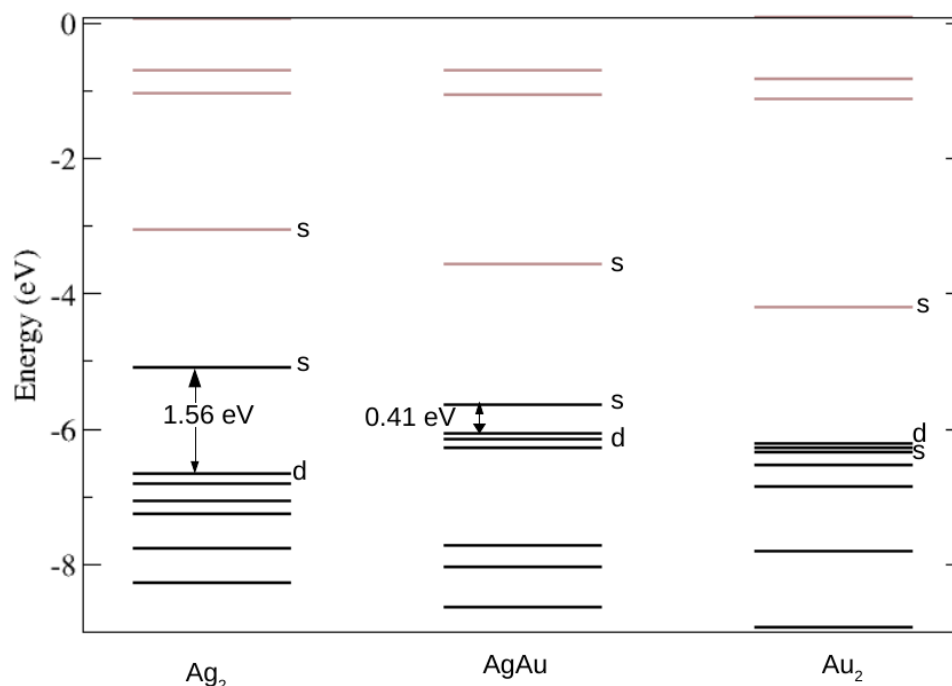


Figure 6.2: A schematic diagram for MO's for  $\text{Ag}_2$ ,  $\text{AgAu}$  and  $\text{Au}_2$  (from left) clusters respectively. The black colored lines denote the occupied MO's, while the brown colored lines denote the MO's. The labels *s* and *d* correspond to MO's which have majority contributions from the *s* and *d* states of the atoms.

these calculations, we placed  $\text{O}_2$  and/or  $\text{CO}$  at various adsorption sites with different orientations and optimized them to the nearest local minima.

Except for  $\text{AgAu}_3$ , all even sized clusters ( $\text{AgAu}$ ,  $\text{Ag}_2\text{Au}_2$ , and  $\text{Ag}_3\text{Au}$ ) have  $\text{O}_2$  adsorption energies within the range of 0.2 – 0.33 eV. All the lowest energy structures and adsorption energies for the  $\text{O}_2$  molecule are shown in Fig. 6.4.  $\text{O}_2$  molecule binds to a two atom  $\text{AgAu}$  cluster with an adsorption energy 0.29 eV. An isolated  $\text{O}_2$  has a bond length of 1.23 Å, but after adsorption on  $\text{AgAu}$  it increases marginally by 0.03 Å. Usually bond length elongation indicates the activation of  $\text{O}_2$  molecule for the oxidation reaction. In this case the minor increment in bond length suggests that the gas phase  $\text{AgAu}$  cluster is not a good catalyst for  $\text{O}_2$  activation. Similarly, in the case of four atom clusters  $\text{Ag}_2\text{Au}_2$  and  $\text{Ag}_3\text{Au}$ , the  $\text{O}_2$  molecule have adsorption energies of 0.22 eV and 0.33 eV respectively. Here the  $\text{O}_2$  bond lengths are marginally elongated by 0.02 and 0.05 Å respectively, which again indicate low activation. In all even sized

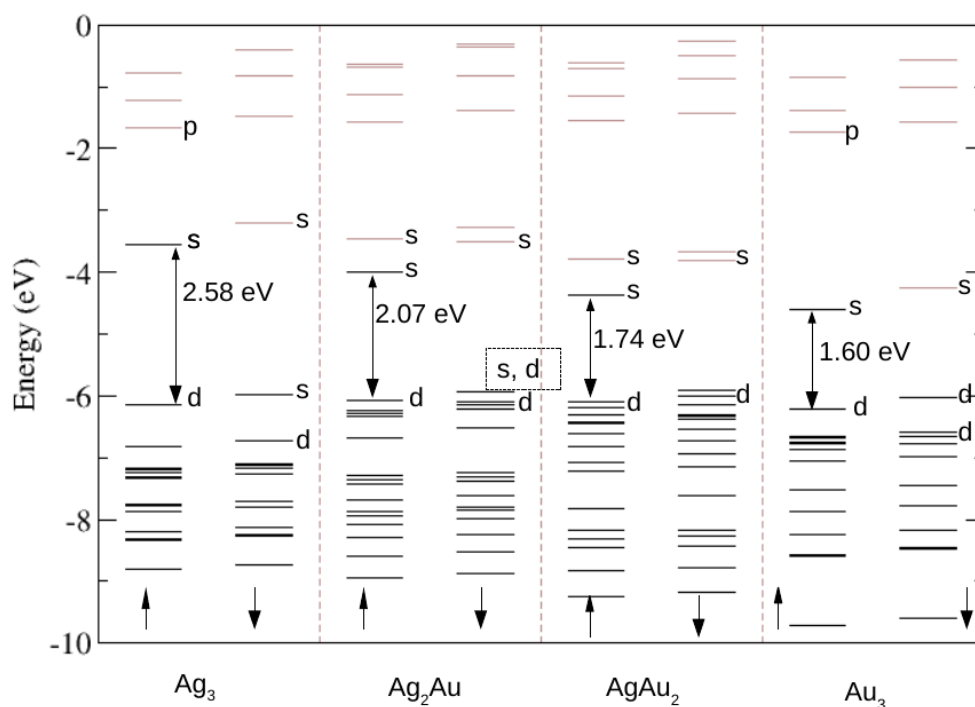


Figure 6.3: A schematic diagram for MO's for  $\text{Ag}_3$ ,  $\text{Ag}_2\text{Au}$ ,  $\text{AgAu}_2$  and  $\text{Au}_3$  (from left) clusters respectively. The color scheme and labeling is same as in Fig. 6.2. The up and down arrows represent the majority and minority spin channels.

clusters  $\text{O}_2$  molecules prefer to get adsorb atop Ag sites. An exception to this is found for  $\text{AgAu}_3$ , which does not show any binding for the  $\text{O}_2$  molecule. In all even sized clusters, there is a lack of  $\text{O}_2$  activation due to the shell closing effect.

However, the odd sized clusters  $\text{AgAu}_2$  and  $\text{Ag}_2\text{Au}$  have a strong binding with  $\text{O}_2$  molecule. For these clusters the  $\text{O}_2$  adsorption energies are 0.92 eV and 1.17 eV respectively. In case of  $\text{AgAu}_2$ , the  $\text{O}_2$  molecule is adsorbed at the Ag-Au bridge site, while in case of  $\text{Ag}_2\text{Au}$ , it prefers to bind to the Ag-Ag bridge site. In both these cases, the bond length of  $\text{O}_2$  molecule is elongated to 1.33 Å.

In all these clusters (except  $\text{AgAu}_2$ ), an  $\text{O}_2$  molecule prefers to bind to an Ag atom, which is expected as silver is less electronegative than gold. This also explains the highest adsorption energy obtained for  $\text{Ag}_2\text{Au}$ , which is an odd cluster with higher fraction of the Ag atoms. There is no binding between  $\text{O}_2$  and  $\text{AgAu}_3$  cluster as  $\text{AgAu}_3$  has a higher fraction of Au atoms and also has a pair of electron in its HOMO. These results agree with the theoretical calculations by Joshi *et al.*, [26]

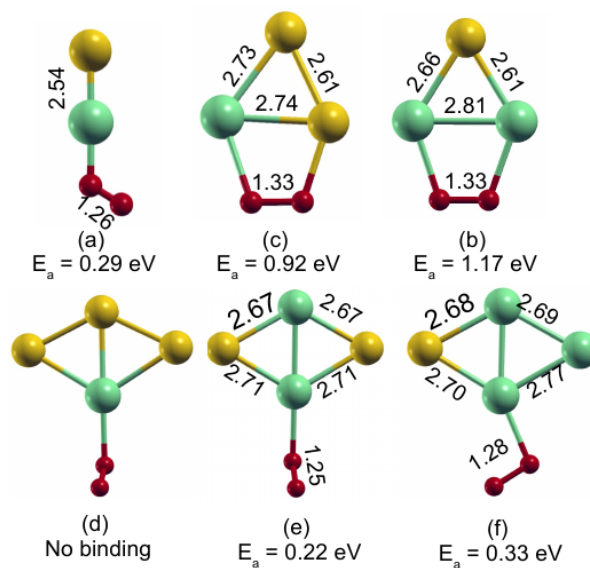


Figure 6.4: Adsorption of  $O_2$  molecule on gas phase  $Ag_nAu_m$  clusters. The red circles denote O atom. Rest of the color scheme is same as in Fig. 6.1.

Then we calculated the adsorption of CO molecule on gas phase  $Ag_nAu_m$  clusters (shown in Fig. 6.5). Except for the  $Ag_2Au_2$  and  $Ag_3Au$  clusters, a CO molecule always prefers to sit atop Au sites. For the  $AgAu$  dimer, a CO molecule prefers to adsorb atop Au site with an adsorption energy 1.04 eV. Similarly, in case of the odd sized clusters  $AgAu_2$  and  $Ag_2Au$ , the CO molecule prefers to get adsorbed atop Au sites with the adsorption energies 1.36 eV and 1.04 eV respectively. These results are in agreement with Popolan *et al.*, [216] For the four atom  $AgAu_3$ ,  $Ag_2Au_2$  and  $Ag_3Au$  clusters, the CO molecules are adsorbed with adsorption energies of 0.57, 0.81 and 0.85 eV respectively. In case of  $AgAu_3$ , CO prefers to get adsorbed at the Au site, while in case of  $Ag_2Au_2$  and  $Ag_3Au$  clusters, it prefers to get adsorbed atop Ag site.

As discussed above, the silver  $4d$  orbitals are located much deeper below the outermost  $s$  orbitals in comparison to gold  $5d$  orbitals. Thus silver  $4d$  orbitals are unfavorable for a  $\pi$  back donation necessary for the CO bonding. As a consequence, CO molecule does not bind to  $Ag_2$  dimer [27], while it has a finite adsorption energy for  $Au_2$  dimer. In line with this, the CO molecule prefers to get adsorbed atop Au sites for  $Ag_nAu_m$  clusters. In fact, the highest adsorption energy for CO molecule is obtained for the  $AgAu_2$  cluster, which is an odd sized cluster with higher number of Au atoms.

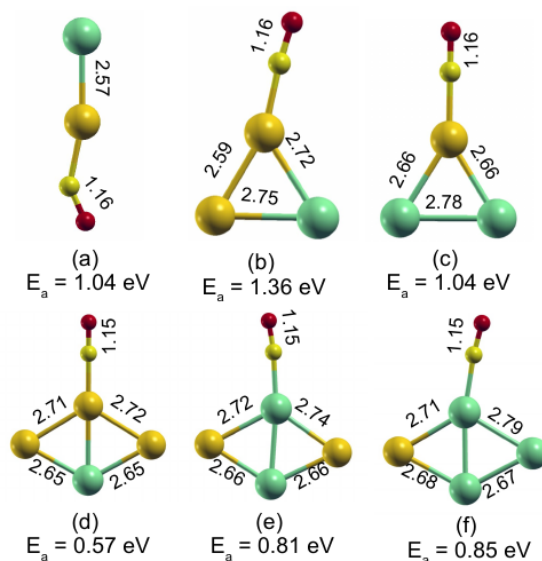


Figure 6.5: Adsorption of CO molecule on gas phase  $Ag_nAu_m$  clusters. The yellow colored circles denote C atoms. Rest of the color scheme is same as in Fig. 6.4.

As discussed above in L-H mechanism coadsorption of CO and  $O_2$  molecule is the first step towards the oxidation reaction, which is unfavorable on pure Ag or Au clusters at low temperature. In order to understand whether coadsorption is possible on bimetallic clusters and whether the presence of both these molecules at the same time will change their preference for the adsorption site(s), we have calculated simultaneous binding of the CO and  $O_2$  molecules on  $Ag_nAu_m$  clusters.

For these calculations, we attached both molecules to various sites of the cluster simultaneously, and optimized these structures to the nearest local minima. The optimized lowest energy structures and adsorption energies are shown in Fig. 6.6. In case of the AgAu dimer,  $O_2$  molecule prefers to get adsorbed atop Ag site and CO prefers to bind atop Au site. Thus the distance between CO and  $O_2$  molecule is quite large as they are at the two ends. The structure has a coadsorption energy of 1.20 eV which is 0.12 eV smaller than the sum of adsorption energies of individual  $O_2$  and CO molecule. This indicates that the coadsorption is less favorable than individual adsorptions. Similarly, for the three atom AgAu<sub>2</sub> and Ag<sub>2</sub>Au clusters, coadsorption follows the same trend of individual adsorptions. In case of AgAu<sub>2</sub>,  $O_2$  prefers to bind to the Ag-Au bridge site, while CO prefers to sit atop Au site. The structure has a coadsorption energy of

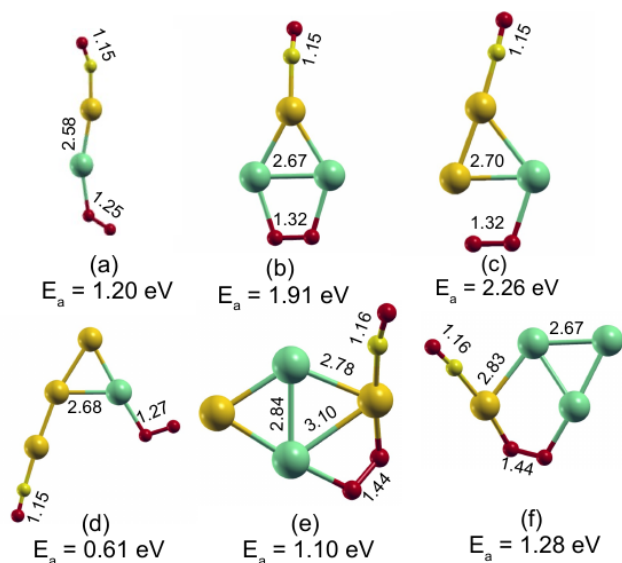


Figure 6.6: Coadsorption of CO and O<sub>2</sub> molecule on gas phase Ag<sub>n</sub>Au<sub>m</sub> clusters.

$E_a^c = 2.26$  eV, which is 0.02 eV smaller than the sum of the individual adsorption energies of O<sub>2</sub> and CO. In case of the Ag<sub>2</sub>Au cluster, O<sub>2</sub> molecule is adsorbed to the bridge site of Ag-Ag bond, while CO prefers to bind atop Au site. Their coadsorption energy  $E_a^c = 1.91$  eV, which is  $\sim 0.3$  eV smaller than the sum of the individual adsorption energies of CO and O<sub>2</sub> molecules. For both the three atom clusters, CO and O<sub>2</sub> prefer to bind at two opposite sites of the clusters (Fig. 6.6(b,c)). This results in a large distance between the molecules and makes them unsuitable for the CO-oxidation.

After adsorption of CO and O<sub>2</sub> molecules on AgAu<sub>3</sub> cluster, the structure of the gas phase cluster is deformed and the Au atoms of the cluster form a linear chain. The CO molecule prefers to sit at one of the Au atoms, while O<sub>2</sub> prefers to get adsorbed at the Ag site as shown in Fig. 6.6(d). The structure has a coadsorption energy 0.61 eV, which is 0.04 eV larger than the adsorption of the single CO molecule. As discussed above, the single O<sub>2</sub> molecule does not have any binding with this cluster. In this structure (Fig. 6.6(d)), the minimum distance between CO and O<sub>2</sub> molecule is 5.79 Å, which is quite large for the oxidation reaction to proceed.

The ground state structures for CO and O<sub>2</sub> coadsorption on Ag<sub>2</sub>Au<sub>2</sub> and Ag<sub>3</sub>Au clusters are very interesting, as shown in Fig. 6.6(e,f). For the first time we found that CO and O<sub>2</sub> molecules prefer to sit at the same site. In case of individual adsorption,

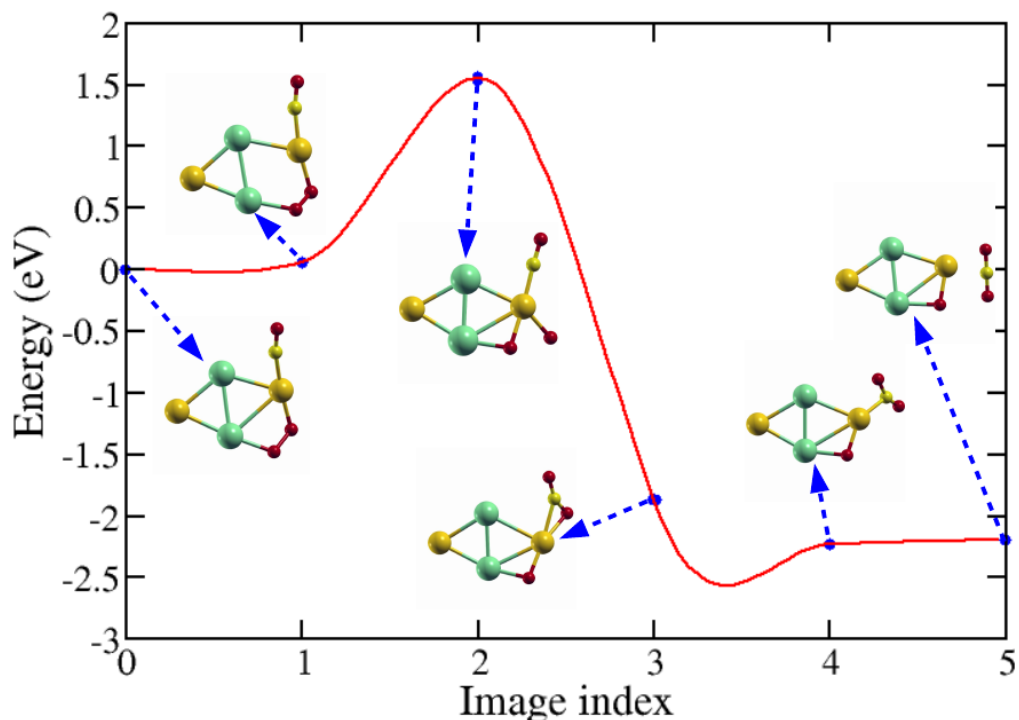


Figure 6.7: The MEP for the CO-oxidation by L-H mechanism on  $\text{Ag}_2\text{Au}_2$  cluster. The blue circles represent the energy of each image on the elastic band. The plot has been fitted by the spline interpolation.

both molecules prefer to sit atop Ag site (discussed above), while during coadsorption both CO and  $\text{O}_2$  molecules prefer to get adsorbed at the Au site. In this structure the bond elongation for  $\text{O}_2$  molecule is found to be quite large (O-O bond length=1.44 Å), which implies the activation of the O-O bond. For  $\text{Ag}_2\text{Au}_2$ , the coadsorption energy for CO and  $\text{O}_2$  molecules is 1.10 eV, which is 0.07 eV larger than the sum of the individual adsorption energies. Similarly, for  $\text{Ag}_3\text{Au}$  cluster the coadsorption energy is found to be 1.28 eV, which is 0.1 eV larger than the sum of the individual adsorption energies. From all these facts, it seems that for both these clusters the coadsorption is more favorable than the individual adsorptions and these clusters are better candidates for the CO-oxidation reaction. In order to confirm this, we performed CINEB calculations and calculated the energy barrier in the formation of  $\text{CO}_2$  molecule. The MEP for  $\text{CO}_2$  formation for  $\text{Ag}_2\text{Au}_2$  and  $\text{Ag}_3\text{Au}$  clusters is shown in Fig. 6.7 and Fig. 6.8 respectively. We found that for both these clusters, the rate determining step of the

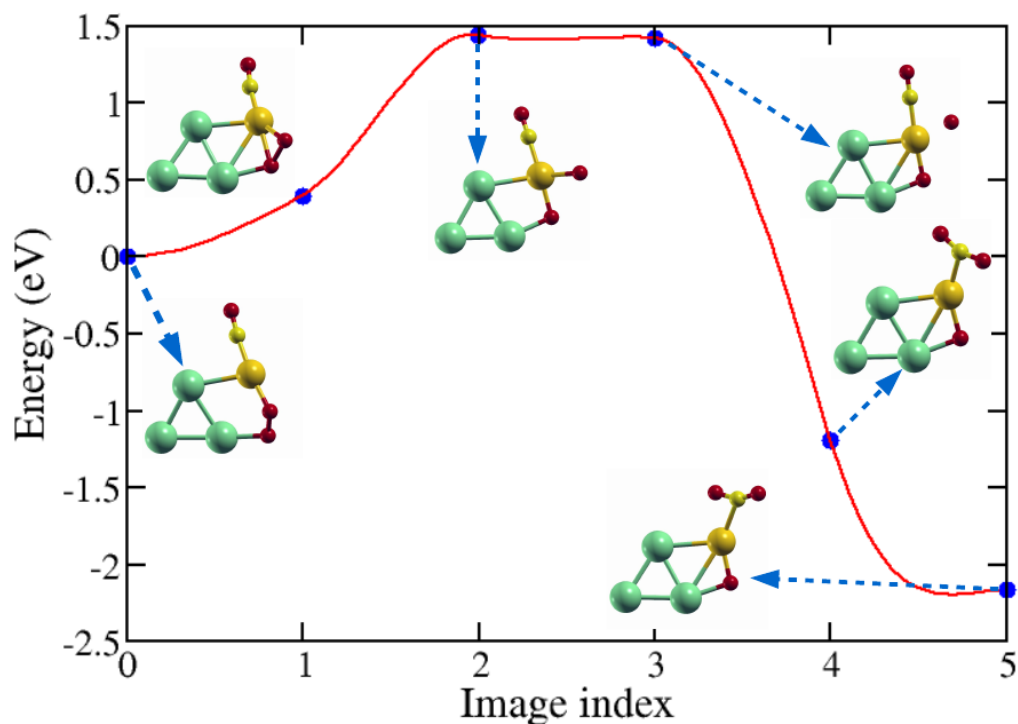


Figure 6.8: The MEP for the CO-oxidation by L-H mechanism on  $\text{Ag}_3\text{Au}$  cluster. The other descriptions of figure are same as in Fig. 6.7.

reaction is the O-O bond breaking. The energy barriers in  $\text{CO}_2$  formation for  $\text{Ag}_2\text{Au}_2$  and  $\text{Ag}_3\text{Au}$  clusters are 1.55 and 1.44 eV respectively. Such large energy barriers imply that reaction will take place at very high temperature. Hence gas phase  $\text{Ag}_2\text{Au}_2$  and  $\text{Ag}_3\text{Au}$  clusters are not very ideal candidate for the CO-oxidation reaction. In case of  $\text{Ag}_3\text{Au}$ , the last image on the MEP form a complex (Fig. 6.8) structure. The complete  $\text{CO}_2$  dissociation is further separated by an energy barrier, which we have not determined.

## 6.4 Structure of $\text{Ag}_n\text{Au}_m$ clusters supported over alumina

So far, we found that coadsorption of CO and  $\text{O}_2$  molecules is feasible on gas phase bimetallic clusters, but the barriers in the CO-oxidation reaction are rather large. As

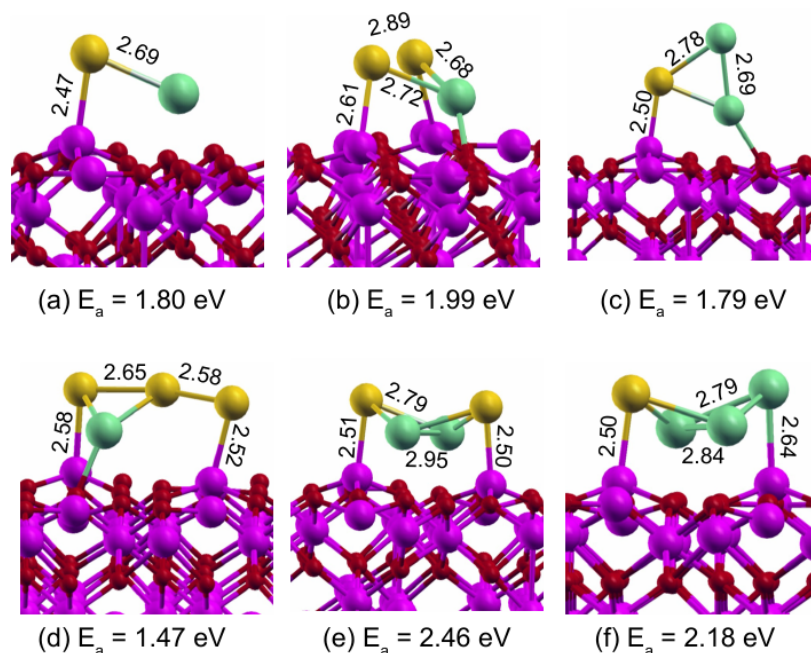


Figure 6.9: The ground state structures of  $\text{Ag}_n\text{Au}_m$  clusters supported over  $\text{Al}_2\text{O}_3$  surface.

discussed above, oxide supports play a vital role for CO-oxidation reactions performed with gold nano-catalysts [22]. We want to understand how the bimetallic clusters supported over oxide surface influence the CO-oxidation reaction. For this we considered an  $\text{Al}_2\text{O}_3$  (0001) surface, and determined the ground state structures of supported  $\text{Ag}_n\text{Au}_m$  clusters as shown in Fig. 6.9. First, we will describe the ground state structures of supported  $\text{Ag}_n\text{Au}_m$  clusters,

**AgAu cluster:** In the lowest energy structure, the AgAu cluster prefers an orientation in which the Ag atom is slightly bent towards the plane of the surface as shown in Fig. 6.9 (a). Au atom prefers to sit over the Al1 site, while Ag atom stays above the Al4 site of the surface. After deposition, the Au-Ag bond length elongates to 2.69 Å. This structure has an adsorption energy of 1.80 eV, which is 0.39 eV and 0.62 eV larger than the  $\text{Au}_2$  [227] and  $\text{Ag}_2$  [228] adsorption over alumina surface respectively. In this structure, Au atom gains a charge of 0.53  $e$ , while Ag atom lost a charge of 0.54  $e$ . A charge density difference (CDD) plot for this structure is shown in the Fig. 6.10(a). The charge gain by Au atom is much larger than the gas phase case. The CDD plot indicate that extra charge (in comparison to gas phase) on Au atom is received from the

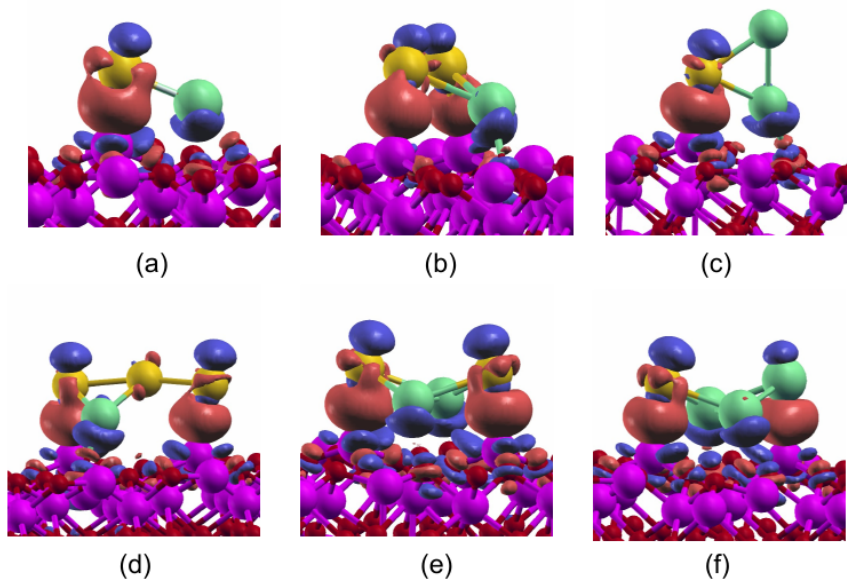


Figure 6.10: The charge density difference plot for  $\text{Ag}_n\text{Au}_m$  supported over  $\text{Al}_2\text{O}_3$  surface. The red colored isosurface represent the excess of electronic charge while the blue colored isosurfaces represent the lack of electronic charge density.

alumina substrate. Similarly Ag atom has transferred some of its charge to the substrate. The maximum distortion of the surface was found for the aluminum atom bonded to the Au atom. It was found to be  $0.59 \text{ \AA}$  away from its original position. We also found an isomer structure in which both Ag and Au atoms are attached to the same Al1 site, but the structure is  $0.97 \text{ eV}$  higher than the ground state structure.

**AgAu<sub>2</sub> cluster:** In the ground state structure of supported AgAu<sub>2</sub> cluster, it stays parallel to the surface with an Ag atom slightly bent towards the Al3 site of the surface (Fig. 6.9(b)). The AgAu<sub>2</sub> cluster is distorted in such a way that both of its Au atoms stay atop the Al1 sites of the surface. In gas phase the Au-Au distance was  $2.75 \text{ \AA}$ , but after deposition this bond length is elongated to  $2.89 \text{ \AA}$ . The structure has an adsorption energy  $E_a = 1.99 \text{ eV}$ . This is similar to the adsorption of Au<sub>3</sub> cluster on  $\text{Al}_2\text{O}_3$  surface [227], with two Au atoms adsorbed over two consecutive Al1 sites with an adsorption energy  $2.07 \text{ eV}$ . For AgAu<sub>2</sub>, the maximum distortion of the surface was found for the Al1 atom, which is bonded to one of the Au atoms of the cluster. It moved by  $0.51 \text{ \AA}$  away from its original position. In this structure, the Au atoms gained a charge of  $0.66 e$ , while Ag atom lost a charge of  $0.57 e$ . Thus overall there is a charge transfer

of  $0.09 e$  from the substrate to the cluster. The charge gained by Au atoms and lost by Ag atom in supported case is much larger than that in the gas phase. The CDD plot for this structure (shown in Fig. 6.10(b)) indicates that the extra charge is gained (transfer) from (to) the substrate. We also found an isomer in which AgAu<sub>2</sub> cluster is perpendicular to the alumina surface. This structure is 0.1 eV higher than the ground state structure.

**Ag<sub>2</sub>Au cluster:** The ground state structure of Ag<sub>2</sub>Au cluster is shown in Fig. 6.9(c). In this structure, the Ag<sub>2</sub>Au cluster prefers to stay perpendicular to the surface with the Ag-Au side nearly parallel to the surface. Again the Au atom prefers to sit over the Al1 site, while the Ag atom (which is close to the surface) stays above the Al3 site. This is in contrast to the structure of Ag<sub>3</sub> cluster over alumina [228], which is parallel to the surface with two Ag atoms atop Al1 sites and the third on the top of Al4 site. The Ag<sub>2</sub>Au cluster has an adsorption energy  $E_a = 1.79$  eV, which is 0.17 eV smaller than the adsorption of Ag<sub>3</sub> cluster over alumina [228]. The charge gain by Au atom is  $0.51 e$ , while the charge lost by the Ag atom is  $0.54 e$ . There is no charge transfer from Ag atom which is away from the surface. Again the charge gained by Au atoms and lost by Ag atom in this case is much larger than that in the gas phase case. The maximum distortion was found for the aluminum Al1 atom bonded to Au atom, which moved  $0.59 \text{ \AA}$  away from its original position. We also found a high energy structure in which Ag<sub>2</sub>Au is parallel to the surface. The isomer is only 11 meV higher than the ground state structure.

**AgAu<sub>3</sub> cluster:** The AgAu<sub>3</sub> cluster prefers to stay parallel to the surface with two of its Au atoms above the Al1 sites. After deposition cluster undergoes a structural deformation and three Au atoms become linear and form a Y shaped configuration as shown in Fig. 6.9(d). In gas phase, this linear isomer is 0.92 eV higher than the ground state structure (Fig. 6.1(d)). This is similar to the adsorption of Y shaped Au<sub>4</sub> cluster over alumina [227], which was more favorable compare to the rhombus structure. The supported AgAu<sub>3</sub> cluster has an adsorption energy  $E_a = 1.47$  eV, which is 0.77 eV smaller than the adsorption of Au<sub>4</sub> cluster over alumina surface. The total charge lost by Ag atoms is  $0.55 e$ , while the total charge gain by Au atoms is  $0.61 e$ . The largest distortion was found for an Al1 atom of the surface which is bonded to one of the Au atoms of the cluster. It moved  $0.50 \text{ \AA}$  away from its initial position.

**Ag<sub>2</sub>Au<sub>2</sub> cluster** : The ground state structure of supported Ag<sub>2</sub>Au<sub>2</sub> cluster is shown in Fig. 6.9(e). The cluster prefers to stay parallel to the surface with the Au atoms above Al1 sites and the Ag atoms above the 3-fold oxygen hollow sites. The structure has an adsorption energy of 2.46 eV. After deposition, the Au atoms gain a total charge of 1.02 *e*, while the charge lost by the Ag atoms is 1.0 *e*.

**Ag<sub>3</sub>Au cluster**: Ag<sub>3</sub>Au cluster prefers a parallel orientation to the surface with the Au atom above the Al1 site. Two of its Ag atoms prefer to stay above the 3-fold oxygen hollow sites, while the last Ag atom sits atop the Al1 site. This is similar to the adsorption of Ag<sub>4</sub> cluster where two Ag atoms sit atop Al1 site, while the rest two prefer to sit above the three fold hollow sites. For Ag<sub>3</sub>Au cluster, the Ag atom above the Al1 site gains a charge of 0.24 *e*, while the other Ag atoms lose a charge of 0.85 *e*. Au atom gains a charge of 0.54 *e*. Hence overall there is a charge transfer of 0.07 *e* from the cluster to the surface. The structure has an adsorption energy 2.18 eV, which is 0.18 eV larger than the adsorption of Ag<sub>4</sub> cluster over alumina.

Similar to the gas phase case, in all these structures we found that Au atoms have gained electronic charge and Ag atoms have lost their electronic charge. However, quantitatively this charge transfer is much more larger in the supported case. From the CDD plots, it is clear that the extra charge transfer is caused by the alumina substrate. Hence the presence of support has increased the ionic character in Ag<sub>*n*</sub>Au<sub>*m*</sub> clusters.

### 6.4.1 Absorption of O<sub>2</sub> molecule on supported Ag<sub>*n*</sub>Au<sub>*m*</sub> clusters

In this section, we will discuss adsorption of O<sub>2</sub> molecule on alumina supported Ag<sub>*n*</sub>Au<sub>*m*</sub> clusters, and compare them with the gas phase case. In case of the supported AgAu cluster, an O<sub>2</sub> molecule prefers to get adsorbed at the Ag site (Fig. 6.11(a)). This structure has an adsorption energy 0.16 eV, which is smaller than O<sub>2</sub> adsorption energy on the gas phase AgAu cluster. Deposition of AgAu cluster over alumina surface does not bring any advantage to the O<sub>2</sub> activation, as O<sub>2</sub> bond length is marginally elongated by 0.01 Å from its gas phase value.

In case of supported AgAu<sub>2</sub> cluster, an O<sub>2</sub> molecule has an adsorption energy of  $E_a = 0.52$  eV, which is 0.40 eV smaller than the O<sub>2</sub> adsorption energy on AgAu<sub>2</sub> in gas phase. In this case an O<sub>2</sub> molecule prefers to sit at Au site (Fig. 6.11(b)), which is contrary to the adsorption of O<sub>2</sub> on gas phase AgAu<sub>2</sub> cluster, where O<sub>2</sub> prefers to sit at

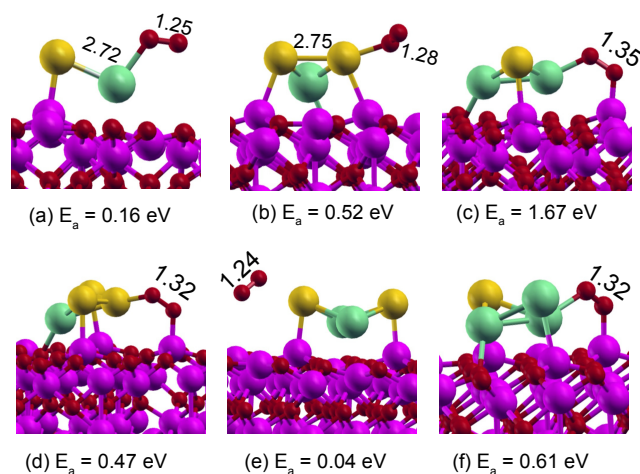


Figure 6.11: Adsorption of  $O_2$  molecule on  $Ag_nAu_m$  clusters supported over  $Al_2O_3$  surface.

Ag-Au bridge site. After deposition  $O_2$  bond length elongates marginally by  $0.05 \text{ \AA}$ , indicating no activation of the O-O bond.

In case of supported  $Ag_2Au$  cluster, the adsorption of  $O_2$  molecule gives  $E_a = 1.67 \text{ eV}$ . In its lowest energy structure one of the O atoms is bonded to the Ag atom, while other O atom is bonded to the Al1 site of the surface as shown in Fig. 6.11(c). The adsorption energy of  $O_2$  on the supported  $Ag_2Au$  is  $0.5 \text{ eV}$  larger than the gas phase  $Ag_2Au$ . Also, the O-O length is elongated to  $1.35 \text{ \AA}$  after adsorption. This is one of the example where alumina surface plays a major role in the activation of  $O_2$  molecule. In addition, adsorption of  $O_2$  distorts the perpendicular structure of  $Ag_2Au$  cluster and it becomes parallel to the alumina surface.

For supported  $AgAu_3$ ,  $O_2$  has an adsorption energy  $E_a = 0.47 \text{ eV}$ , while on gas phase  $AgAu_3$ ,  $O_2$  did not show any binding. In the lowest energy structure, one of the O atoms binds to the Au site, while other prefers to stay above the Al1 site of the surface. The  $O_2$  bond length is increased to  $1.32 \text{ \AA}$ . For supported  $Ag_2Au_2$  cluster, the adsorption energy of  $O_2$  molecule is found to be very small,  $E_a = 0.04 \text{ eV}$ . Also, we did not find any significant change in the O-O bond length. For  $O_2$  adsorption on supported  $Ag_3Au$  cluster, alumina surface plays a major role. One of the O atom sits at Ag atom of the cluster, while other stays above the Al1 site of the surface. After adsorption, the  $O_2$  bond length is elongated by  $0.09 \text{ \AA}$ . On the basis of the above results it is inferred that supported  $Ag_2Au$ ,  $AgAu_3$  and  $Ag_3Au$  clusters can be potential candidates for oxidative

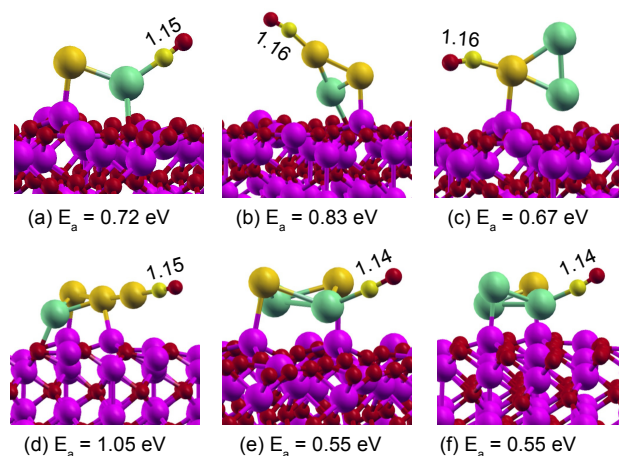


Figure 6.12: Adsorption of CO molecule on  $\text{Ag}_n\text{Au}_m$  clusters supported over  $\text{Al}_2\text{O}_3$  surface.

catalysis.

#### 6.4.2 Adsorption of CO molecule on supported $\text{Ag}_n\text{Au}_m$ clusters

In this section, we will study adsorption of CO molecule over alumina supported  $\text{Ag}_n\text{Au}_m$  clusters and compare them to the gas phase case. In case of supported AgAu cluster, a CO molecule prefers to sit at Ag site (Fig. 6.12(a)), which is contrary to the gas phase case where CO prefers to sit atop Au site. The structure has  $E_a = 0.72$  eV, which is 0.32 eV smaller than the CO adsorption on the gas phase AgAu. For supported AgAu<sub>2</sub> cluster, a CO molecule prefers to sit atop Au site near to surface (Fig. 6.12(b)). The structure has an adsorption energy  $E_a = 0.83$  eV, which is 0.53 eV smaller the  $E_a$  of CO on the gas phase AgAu<sub>2</sub>. CO adsorption deforms the structure of the supported AgAu<sub>2</sub> cluster, as one of the Au atoms (which is bonded to CO) moves away from the alumina surface and relaxes to a structure shown in Fig. 6.12(b). In case of supported Ag<sub>2</sub>Au cluster, CO molecule prefers to get adsorbed at the Au site near to the surface with an  $E_a = 0.67$  eV (Fig. 6.12(c)). This is 0.37 eV smaller than the adsorption on gas phase Ag<sub>2</sub>Au. Unlike the O<sub>2</sub> adsorption, supported Ag<sub>2</sub>Au cluster did not lose its perpendicular structure after CO deposition.

For supported AgAu<sub>3</sub> cluster, CO adsorption significantly distorts the structure of the supported bimetallic cluster and three of its Au atoms become linear on the surface

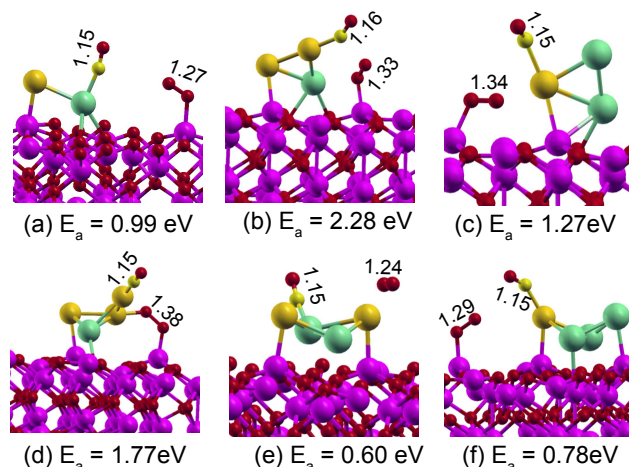


Figure 6.13: Coadsorption of CO and O<sub>2</sub> molecule on Ag<sub>n</sub>Au<sub>m</sub> clusters supported over Al<sub>2</sub>O<sub>3</sub> surface.

(Fig. 6.12(d)). A similar behavior was seen in case of gas phase AgAu<sub>3</sub> cluster. Also, this is the only case where adsorption energy of CO molecule is larger than that on the gas phase cluster. Here, the adsorption energy is 1.05 eV, which is 0.48 eV larger than the gas phase adsorption. For the supported Ag<sub>2</sub>Au<sub>2</sub> cluster, CO molecule prefers to sit on an Ag site (Fig. 6.12(e)) with an adsorption energy  $E_a = 0.55$  eV. This is 0.26 eV smaller than the gas phase case. Similarly, in the case of Ag<sub>3</sub>Au cluster, a CO molecule prefers to sit on Ag site (shown in Fig. 6.12(f)), which has also been seen in the gas phase adsorption. The CO adsorption energy is found to be  $E_a = 0.55$  eV, which is 0.30 eV smaller than the gas phase adsorption energy.

### 6.4.3 Coadsorption of CO and O<sub>2</sub> molecule over supported Ag<sub>n</sub>Au<sub>m</sub> clusters

In this section we will discuss coadsorption of CO and O<sub>2</sub> molecules on alumina supported Ag<sub>n</sub>Au<sub>m</sub> clusters and examine whether oxide support changes the preference for various adsorption sites in comparison to the gas phase case. As discussed above, in case of individual adsorption on the supported AgAu cluster, both CO and O<sub>2</sub> molecules prefer the Ag site. In coadsorption, CO molecule is adsorbed at the Ag site, while O<sub>2</sub> molecule occupies the Al1 site of the surface (Fig. 6.13(a)). This is very different than the gas phase case, where both CO and O<sub>2</sub> occupy two ends of the gas phase AgAu clus-

ter (Fig. 6.6(a)). This is a good indication that now CO and O<sub>2</sub> molecules are closer in comparison to the gas phase case. However the distance between them is still quite large (3.85 Å) and not suitable for the reaction to proceed. In addition, O<sub>2</sub> bond length is only elongated by 0.04 Å, which suggests a low activation of the O-O bond. The coadsorption energy for CO and O<sub>2</sub> molecule is 0.99 eV, which is 0.11 eV larger than the sum of individual adsorption energies of CO and O<sub>2</sub> molecules on supported AgAu cluster. This suggests that coadsorption is more favorable.

In case of gas phase AgAu<sub>2</sub> cluster, both CO and O<sub>2</sub> prefer to sit at two corners of the cluster (Fig. 6.6(b)). However, on supported AgAu<sub>2</sub> cluster, CO prefers to sit at one of the Au atoms and O<sub>2</sub> prefers to sit on the alumina surface (Al1 site) near to cluster (Fig. 6.13(b)). The structure is very interesting as O<sub>2</sub> bond is elongated to 1.33 Å. Both molecules are adsorbed such that the distance between CO and O<sub>2</sub> molecule is reasonably small (2.06 Å). The structure has an adsorption energy of 2.28 eV, which is 0.93 eV larger than the sum of individual  $E_a$  of CO and O<sub>2</sub> molecules. This indicates that coadsorption is more favorable than the individual adsorption.

Similarly, for supported Ag<sub>2</sub>Au cluster, both CO and O<sub>2</sub> prefer to sit next to each other (Fig. 6.13(c)). A CO molecule prefers to sit atop Au site, while an O<sub>2</sub> molecule prefers to sit on the surface Al1 site (the Au-O distance is 2.37 Å). The structure has a coadsorption energy  $E_a = 1.27$  eV, which is 1.07 eV smaller than the sum of individual energies of CO and O<sub>2</sub> molecules. This suggests that the coadsorption is less favorable than the individual adsorption. After adsorption, the O<sub>2</sub> bond length is elongated by 0.11 Å. The CO and O<sub>2</sub> molecules are 3 Å apart in the optimized structure, which seems to be promising for the oxidation reaction. In case of supported AgAu<sub>3</sub> cluster, the coadsorption energy is found to be 1.77 eV, which is 0.25 eV larger than the sum of the individual adsorption. This indicates that the coadsorption is more favorable. After adsorption the bond length of O<sub>2</sub> has elongated by 0.15 Å. The CO and O<sub>2</sub> molecules prefer to sit at two Au atoms of the cluster and the distance between these two is 5.22 Å. Due to the large CO...O<sub>2</sub> distance, the structure is not very promising for the CO-oxidation reaction.

For supported Ag<sub>2</sub>Au<sub>2</sub> cluster, CO and O<sub>2</sub> molecules prefer to sit at two corners of the cluster, which is not beneficial for the CO-oxidation reaction. The structure has a coadsorption energy of  $E_a = 0.60$  eV, which is comparable to the sum of the individual CO and O<sub>2</sub> adsorption energies. For the Ag<sub>3</sub>Au cluster, the CO molecule prefers to sit

atop Au site and the O<sub>2</sub> molecule prefer to sit near the Al1 site of the surface. The structure has a coadsorption energy of  $E_a = 0.78$  eV, which is 0.38 eV smaller than the sum of individual adsorption. This indicates that the coadsorption is not favorable in this case. In addition, distance between CO and O<sub>2</sub> is 3.88 Å. Hence the alumina supported Ag<sub>3</sub>Au cluster is not suitable for the CO-oxidation.

## 6.5 Conclusions

We found that only AgAu<sub>2</sub> cluster supported over alumina is a suitable candidate for the coadsorption of the CO and O<sub>2</sub> molecules and reaction can proceed through the L-H mechanism. Also, in the case of coadsorption on supported AgAu<sub>3</sub>, the O<sub>2</sub> bond length is quite large 1.38 Å. This was not found in case of single O<sub>2</sub> adsorption. However the coadsorbed CO is quite far from the activated O<sub>2</sub> molecule and clearly L-H mechanism is not possible. Since O<sub>2</sub> bond is already activated, the presence of second CO molecule may change the scenario. In the presence of second CO, the reaction can proceed through E-R mechanism.

In case of a single O<sub>2</sub> adsorption on supported Ag<sub>2</sub>Au cluster (Fig: 6.11(c)), there is significant activation of the O<sub>2</sub> molecule (bond length 1.35 Å). However coadsorption is not favorable for this clusters and hence L-H mechanism is not favorable. Other possible pathway for the reaction is E-R mechanism, where the gas phase CO molecule can react with adsorbed O<sub>2</sub> molecule. These are some of plans of our future project.

All these results indicate that there is no odd-even behavior in the reactivity of supported clusters. Each bimetallic cluster behaves in a different manner. Definitely, supported bimetallic clusters have more advantages than the gas-phase cluster. Firstly, the presence of the substrate increases the ionicity between Ag and Au atoms in the cluster. Secondly, the substrate actively participate in the oxidation reaction and increases the surface area of the catalyst. However, to have a complete picture, we need to calculate the energy barriers in CO-oxidation on the supported clusters, which require large computational resources and significant computational time. These are some of the aspects which we will look in near future.



## Future prospects

### 7.1 Introduction

In this thesis, we have studied the structural and electronic properties of various substrate supported clusters. We found that  $\text{Ag}_n$  clusters have weak binding with graphite and their bonding is mainly dominated by the van der Waals forces. We have also shown that a magnetic superatom  $\text{FeCa}_8$  can retain its structure over h-BN and graphene as they interact through the van der Waals forces. Furthermore, we studied the catalytic properties of alumina supported  $\text{Ag}_n\text{Au}_m$  ( $n + m = 2 - 4$ ) clusters. In this chapter, we present some possible future direction which can be of importance to enhance our understanding of these particular systems and substrate supported clusters in general.

### 7.2 High energy deposition of silver clusters on a clean graphite surface

So far we have focused on the low energy deposition regime, where the gas phase properties of clusters are preserved after deposition and there is not much damage to the substrate. However, at medium and high energy depositions, there will be a substantial change in the cluster properties and they will be pinned to the substrate. For example, Carroll *et al.*, [230] deposited size selected  $\text{Ag}_n^+$  ( $n = 50 - 200$ ) clusters over graphite surface at room temperature with impact energy in the range of 250 – 2500 eV. They find that clusters are pinned to the surface when the impact energy exceeds a crit-

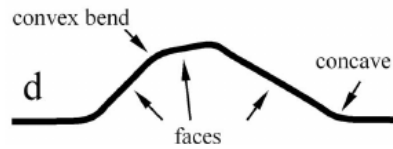


Figure 7.1: Schematic view of a three-faced pleat. The faces are terminated by sharp bends. The two outer borders of the pleat are concave and two inner borders between the faces are convex.

ical value, which is proportional to the cluster size. This prevents the lateral diffusion of the clusters even at room temperature. The MD simulations were performed classically by modeling the system through pair-potentials. However, in our experience, the pair-potentials are not sufficient to capture the van der Waals interaction between Ag clusters and graphite. Therefore, it would be of great interest to perform *ab-initio* MD simulations to understand the microscopics of the system. It would be interesting to understand the defect formation into the layers of graphite and the formation the silver thin film over the substrate. What are the parameters which determine the critical value of impact energy for pinning of a cluster other than the cluster size? How does this depends on the temperature? It would also be interesting to determine the structure of the deposited Ag thin films, grown through medium and high energy cluster deposition.

### 7.3 Silver clusters over a bent graphite substrate

In an experimental study Schmidt *et al.*, [182] deposited Ag clusters of mean diameter  $\sim 3$  nm on a graphite surface with point defects, steps and pleats (bents) at room temperature. The pleats consisting of three faces exhibit two concavely curved outer borders and two convexly curved inner borders between the three faces as shown in Fig. 7.1. From the SEM and AFM experiments, they found that the clusters can be trapped in the concavely curved borders of the pleats. However, clusters stay mobile along direction of the pleats. The outer faces of the pleats are found to be almost free of silver islands. Clusters that fall on them are soon trapped by the attractive outer borders of the pleats. The convex bends were found to be repulsive in nature and they hinder the diffusion of clusters towards the attractive outer borders from the top face of the pleat. Their observations suggested that silver clusters are attracted by the concave

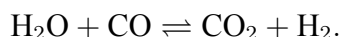
bends and repelled by convex ones. However, the microscopic understanding of why these two bends behave in this manner, was missing. Detailed theoretical calculations are required to answer these questions.

## 7.4 Real space studies of FeCa<sub>8</sub> on graphite

As discussed in chapter 5, magnetic moment of FeCa<sub>8</sub> superatoms on graphene interact through the long range oscillatory RKKY interactions, in addition to the direct exchange. The RKKY interaction on graphene can be very long ranged, extending up to 50 Å [207]. The simulation of an isolated FeCa<sub>8</sub> over graphene using plane wave basis set would require periodic boundary conditions, which need 50 Å × 50 Å graphene sheet in each direction. This is practically impossible with the current computational resources. However, one can use real space implementations of DFT, which does not require periodic boundary conditions. In this way one can study the properties of isolated FeCa<sub>8</sub> over a graphene sheet, and (FeCa<sub>8</sub>)<sub>2</sub> dimers.

## 7.5 Catalytic studies of water gas shift reaction

Hydrogen is a potential solution for the present day energy needs. Presently hydrogen supply is mainly produced via reforming of hydrocarbons (oils or natural gas). The reformed fuel contains high concentration of CO, which degrades the performance of the electrodes. Another purification is required which is achieved by the water gas shift reaction.



Usually gold or platinum are found to be good catalysts for this reaction. As discussed in chapter 6, small positively charged gold clusters are known to strongly bind carbon monoxide which prevents the coadsorption of many other ligands. In this reaction the coadsorption of CO and H<sub>2</sub>O on the catalyst is the first reaction step, which is followed by activation of the ligands and the subsequent production of the CO<sub>2</sub> and H<sub>2</sub>. It has been found that gas phase bimetallic AgAu clusters can coadsorb both H<sub>2</sub>O and CO molecule [231]. We are interested in understanding the mechanism of this reaction on the oxide (Al<sub>2</sub>O<sub>3</sub>, TiO<sub>2</sub>) supported bimetallic AgAu clusters. As discussed in chapter 6,

the oxide support increases the polarity of the Ag and Au atoms in AgAu clusters. We believe that this increased polarity will further enhance the catalytic reactivity of bimetallic AgAu cluster for water gas shift reaction.

# APPENDIX A

## Adsorption of small $Ag_n$ clusters over clean graphite substrate

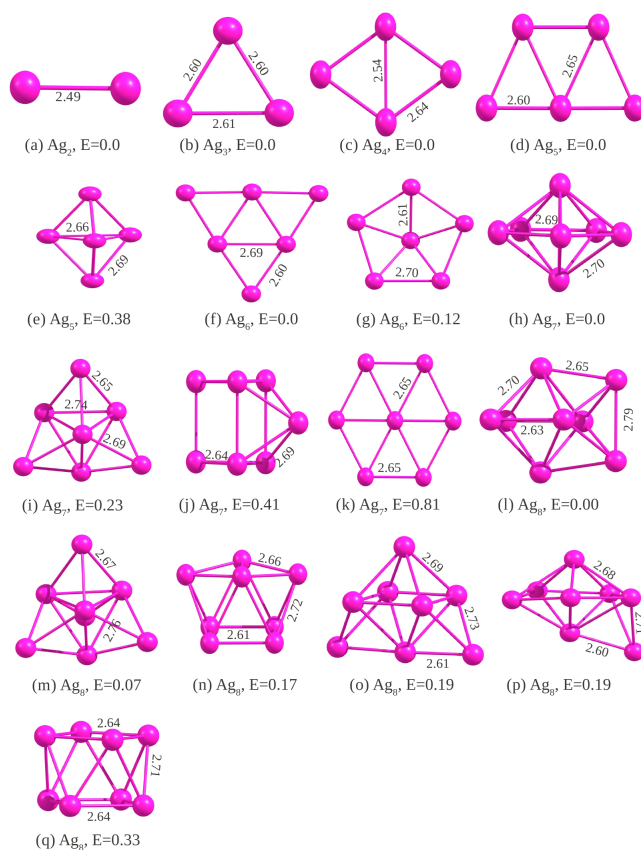


Figure A.1: Structure, bond lengths, and energies (relative to the ground state isomers) of gas phase  $Ag_n$  clusters as found in our global search methods using L(S)DA.

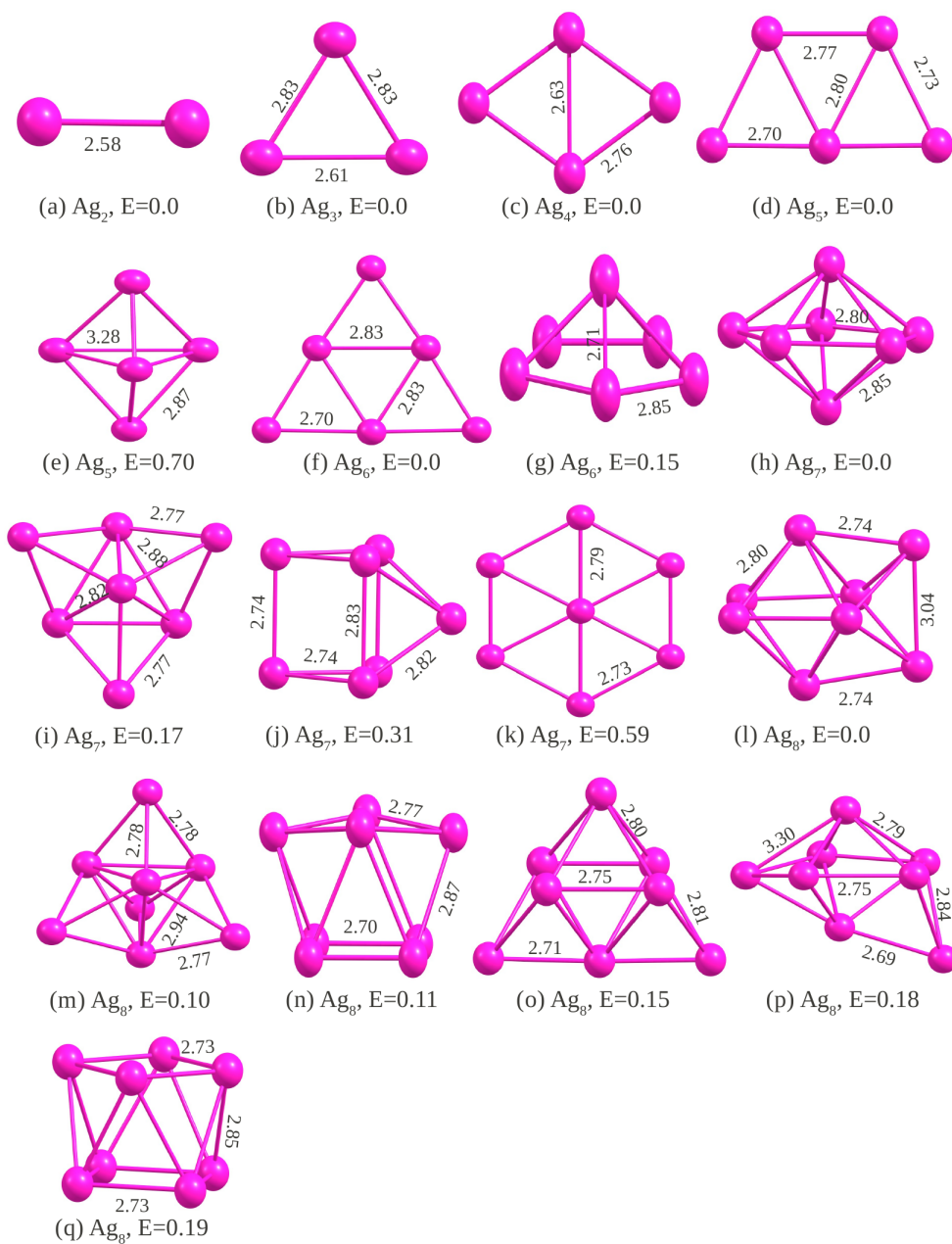


Figure A.2: Structure, bond lengths, and energies (relative to the ground state isomers) of gas phase  $\text{Ag}_n$  clusters in DFT-D2.

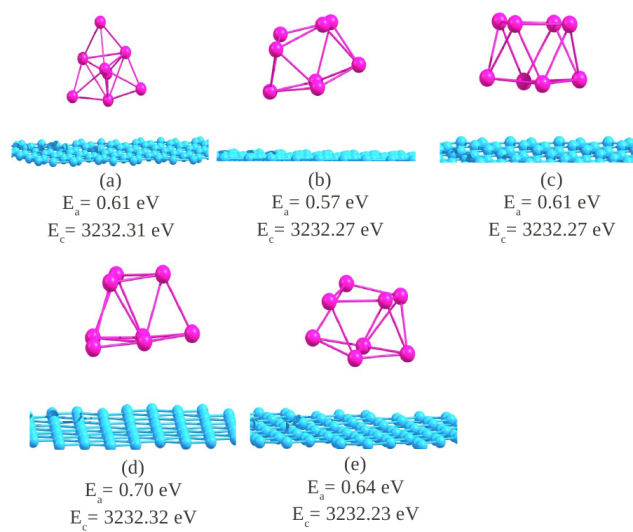


Figure A.3: Structure, bond lengths, and energies (relative to the ground state isomers) of gas phase  $Ag_n$  clusters in DFT-D2.

# APPENDIX B

## Study of small $\text{Ag}_n$ clusters on stepped graphite surface

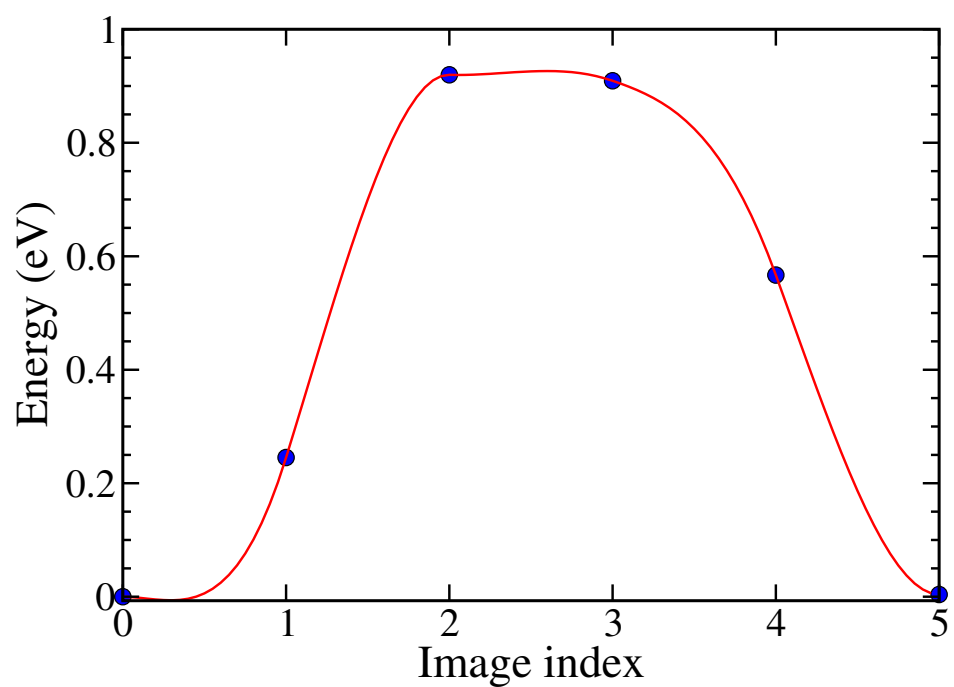


Figure B.1: Energy barrier for the diffusion of a silver adatom along the step edge of graphite.

# APPENDIX C

## Finding the right support for deposition and self assembly of magnetic superatoms

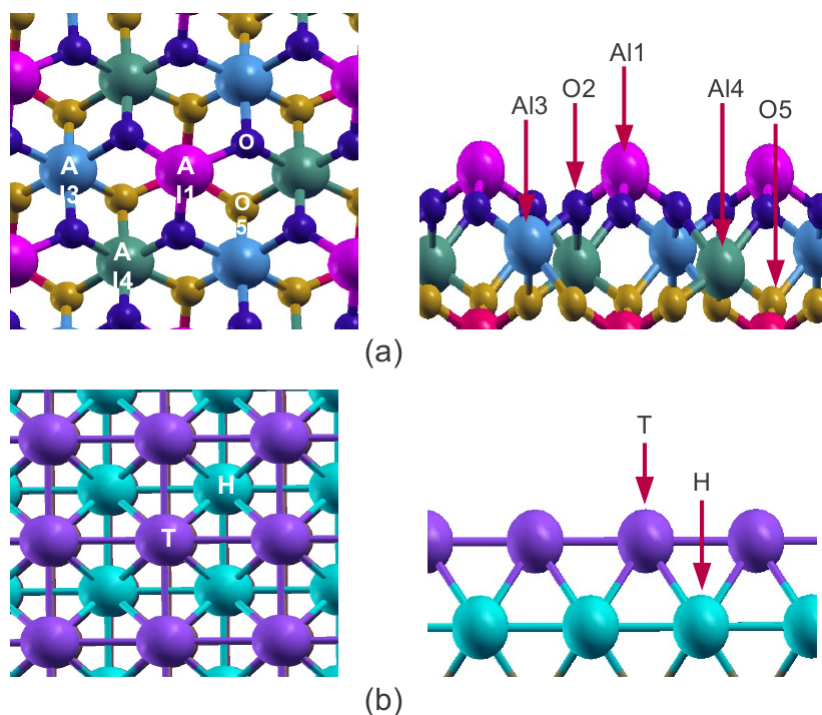


Figure C.1: Adsorption sites of Alumina and Calcium surface. Top panel: alumina surface (top and side views). Lower panel: calcium surface (top and side views). Different layers are represented with different colors.

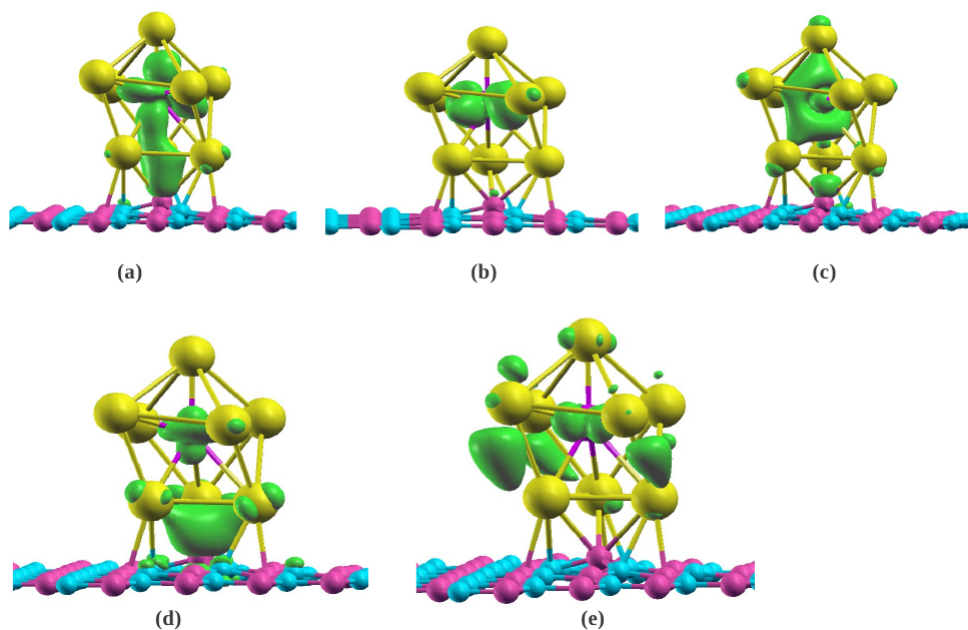


Figure C.2: Partial charge density of 2D states of h-BN supported  $\text{FeCa}_8$  cluster.

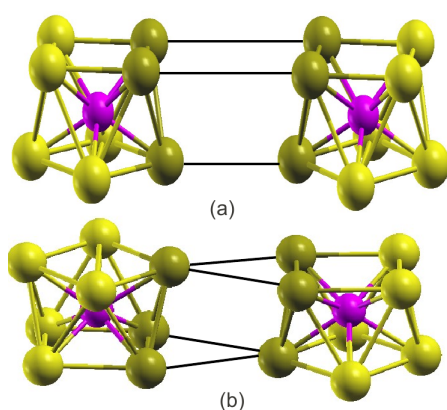


Figure C.3: Considering the two  $\text{FeCa}_8$  units are in the ground state over substrate and diffusing towards each other, we can guess two possible structures of a dimer, (a) each atom of triangular face is connected to only one atom of the other triangular face, and (b) one atom of each triangular face is connected to two atoms of the other triangular face .

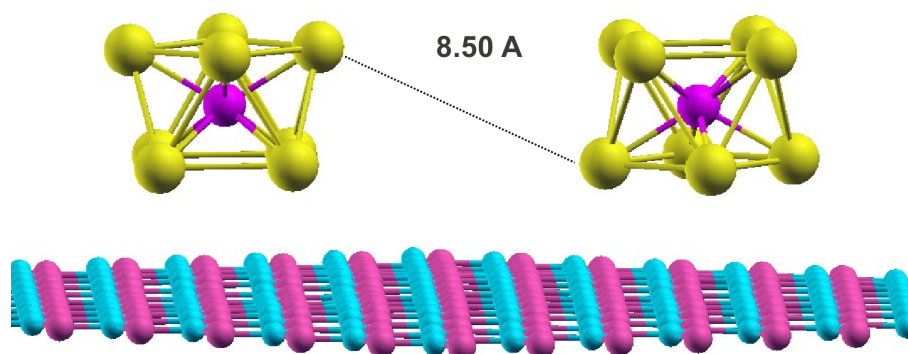


Figure C.4: Dimer of FeCa<sub>8</sub> deposited over h-BN sheet using vdW-DF2 deposited at a distance of 8.5 Å.

# APPENDIX D

## CO oxidation on $\text{Al}_2\text{O}_3$ supported $\text{Ag}_n\text{Au}_m$ model catalysts

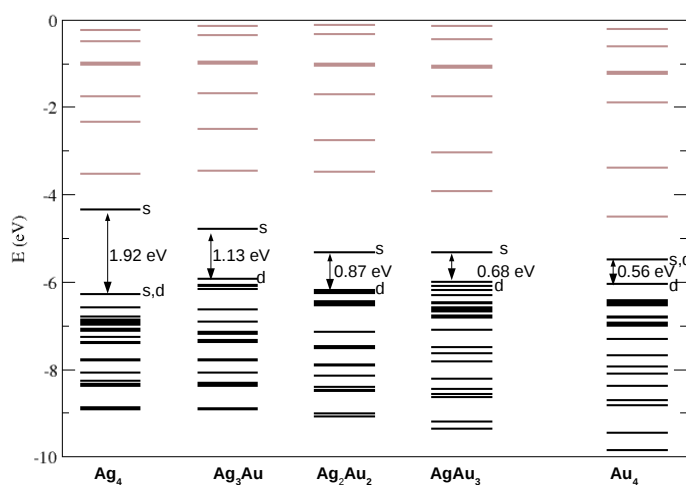


Figure D.1: A schematic diagram for the energy eigen states for  $\text{Ag}_4$ ,  $\text{Ag}_3\text{Au}$ ,  $\text{Ag}_2\text{Au}_2$ ,  $\text{AgAu}_3$ , and  $\text{Au}_4$  (from left) clusters respectively. The color scheme and labeling is same as in Fig. 6.2.

# Bibliography

- [1] S. A. Claridge, A. W. Castleman Jr., S. N. Khanna, C. B. Murray, A. Sen, and P. S. Weiss, *ACS Nano*, **3**, 244 (2009).
- [2] W. D. Knight, K. Clemenger, W. A. de Heer, W. A. Saunders, M. Y. Chou, and M. L. Cohen, *Phys. Rev. Lett.*, **52**, 2141 (1984).
- [3] W. A. de Heer, *Rev. Mod. Phys.*, **65**, 611 (1993).
- [4] A.W. Castleman Jr., and S.N. Khanna, *J. Phys. Chem. C*, **113**, 2664 (2009).
- [5] J. U. Reveles, P. A. Clayborne, A. C. Reber, S. N. Khanna, K. Pradhan, P. Sen, and M. R. Pederson, *Nat. Chem.*, **1**, 310 (2009).
- [6] V. Chauhan, V. M. Medel, J. U. Reveles, S. N. Khanna, and P. Sen, *Chem. Phys. Lett.*, **528**, 39 (2012).
- [7] V. M. Medel, J. U. Reveles, S. N. Khanna, V. Chauhan, P. Sen, and A. W. Castleman, *Proc. Natl. Acad. Sci. U.S.A.*, **108**, 10062 (2011).
- [8] V. Chauhan and P. Sen, *Chem. Phys.*, **417**, 37 (2013).
- [9] R. J. Birgeneau and P. M. Horn, *Science*, **232**, 329 (1986).
- [10] G. Barcaro and A. Fortunelli, *J. Chem. Theory Comput.*, **1**, 972 (2005).
- [11] X.-Q. Gong, A. Selloni, O. Dulub, P. Jacobson, and U. Diebold, *J. Am. Chem. Soc.*, **130**, 370 (2008).

- [12] E. Ganz, K. Sattler, and J. Clarke, *Surf. Sci.*, **219**, 33 (1989).
- [13] U. Busolt, E. Cottancin, H. Röhr, L. Socaciu, T. Leisner, and L. Wöste, *Eur. Phys. J. D*, **9**, 523 (1999).
- [14] G. F. Ndlovu, W. D. Roos, Z. M. Wang, J. K. Asante, M. G. Mashapa, C. J. Jafta, B. W. Mwakikunga, and K. T. Hillie, *Nano. Res. Lett.*, **7**, 173 (2012).
- [15] G. M. Francis, L. Kuipers, J. R. A. Cleaver, and R. E. Palmer, *J. Appl. Phys.*, **79**, 2942 (1996).
- [16] G. M. Francis, I. M. Goldby, L. Kuipers, B. V. Issendorff, and R. E. Palmer, *J. Chem. Soc. Dalton Trans.*, 665 (1996).
- [17] S. J. Carroll, P. Weibel, B. von Issendorff, L. Kuipers, and R. E. Palmer, *J. Phys.: Cond. Mat.*, **8**, L617 (1996).
- [18] I. M. Goldby, L. Kuipers, B. von Issendorff, and R. E. Palmer, *Appl. Phys. Lett.*, **69**, 2819 (1996).
- [19] S. J. Carroll and K. Seeger and R. E. Palmer, *Appl. Phys. Lett.*, **72**, 305 (1998).
- [20] D. M. Duffy and J. A. Blackman, *Surf. Sci.*, **415**, L1016 (1998).
- [21] J.-P. Jalkanen, M. Halonen, D. Fernández-Torre, L. Laasonen, and L. Halonen, *J. Phys. Chem. A*, **111**, 12317 (2007).
- [22] M. Haruta, *Catal. Today*, **36**, 153 (1997).
- [23] U. Heiz and E. L. Bullock, *J. Mater. Chem.*, **14**, 564 (2004).
- [24] A. A. Herzing, C. J. Kiely, A. F. Carley, P. Landon and G. J. Hutchings, *J. Catal.*, **321**, 1331 (2008).
- [25] A. Wang, Y.-P. Hsieh, Y.-F. Chen, and C.-Y. Mou, *J. Catal.* **237**, 197 (2006).
- [26] A. M. Joshi, W. N. Delgass, and K. T. Thomson, *J. Phys. Chem. B*, **110**, 23373 (2006).
- [27] A. M. Joshi, M. H. Tucker, W. N. Delgass, and K. T. Thomson, *J. Chem. Phys.*, **125**, 194707 (2006).

- [28] I. Katakuse, T. Ichihara, Y. Fujita, T. Matsuo, T. Sakurai, and H. Matsuda, *International Journal of Mass Spectrometry and Ion Processes*, **67**, 229 (1985).
- [29] H. Häkkinen, B. Yoon, U. Landman, X. Li, H-J. Zhai, and L.-S. Wang, *J. Phys. Chem. A*, **107**, 6168 (2003).
- [30] R. M. Olson, S. Varganov, M. S. Gordon, H. Metiu, S. Chretien, P. Piecuch, K. Kowalski, S. A. Kucharski, and M. Musial, *J. Am. Chem. Soc.*, **127**, 1049 (2005).
- [31] J. Wang, G. Wang, and J. Zhao, *Phys. Rev. B*, **66**, 035418 (2002).
- [32] G. Zanti and D. Peeters, *Theor. Chem. Acc.*, **132**, 1 (2013).
- [33] I. A. Solov'yov, A. V. Solov'yov, and W. Greiner, *Phys. Rev. A*, **65**, 053203 (2002).
- [34] A. Lyalin, I. A. Solov'yov, A. V. Solov'yov, and W. Greiner, *Phys. Rev. A*, **67**, 063203 (2003).
- [35] K. Clemenger, *Phys. Rev. B*, **32**, 1359 (1985).
- [36] W. Ekardt and Z. Penzar, *Phys. Rev. B*, **38**, 4273 (1988).
- [37] Z. Penzar and W. Ekardt, *Z. Phys. D*, **17**, 69 (1990).
- [38] S. N. Khanna and P. Jena, *Chem. Phys. Lett.*, **219**, 479 (1994).
- [39] S.N. Khanna and P.Jena, *Phys. Rev. B*, **51**, 13705 (1995).
- [40] D. E. Bergeron, A. W. Castleman Jr., T. Morisato, and S. N. Khanna, *Science*, **304**, 84 (2004).
- [41] D. E. Bergeron, P. J. Roach, A. W. Castleman Jr., N. O. Jones, and S. N. Khanna, *Science*, **307**, 231 (2005).
- [42] J. U. Reveles, S. N. Khanna, P. J. Roach, and A. W. Castleman Jr, *Proc. Nat. Acad. Sci.*, **103**, 18405 (2006).
- [43] P. D. Jadzinsky, G. Calero, C. J. Ackerson, D. A. Bushnell, and R. D. Kornberg, *Science*, **318**, 5149 (2007).

- [44] M. Walter, J. Akola, O. Lopez-Acevedo, P. D. Jadzinsky, G. Calero, C. J. Ackerson, R. L. Whetten, H. Grönbeck, and H. Häkkinen, *Proc. Natl. Acad. Sci. U.S.A.*, **105**, 9157 (2008).
- [45] X. Zhang, Y. Wang, H. Wang, A. Lim, G. Gantefoer, K. H. Bowen, J. U. Reveles, and S. N. Khanna, *J. Am. Chem. Soc.*, **135**, 4856 (2013).
- [46] K. Pradhan, J. U. Reveles, P. Sen, and S. N. Khanna, *J. Chem. Phys.*, **132**, 124302 (2010).
- [47] R. E. Leuchtner, A. C. Harms, and A. W. Castleman, Jr., *J. Chem. Phys.*, **91**, 2753 (1989).
- [48] X. Li, H. Wu, X.-B. Wang, and L.-S. Wang, *Phys. Rev. Lett.*, **81**, 1909 (1998).
- [49] V. Medel, J. U. Reveles, and S. N. Khanna, *J. App. Phys.*, **112**, 064313 (2012).
- [50] J. H. Weaver and D. M. Poirier, *Solid State Phys.*, **48**, 1 (1994).
- [51] R. C. Haddon, *Acc. Chem. Res.*, **25**, 127 (1992).
- [52] F. Liu, M. Mostoller, T. Kaplan, S. N. Khanna, and P. Jena, *Chem. Phys. Lett.*, **248**, 213 (1996).
- [53] W.-J. Zheng, O. C. Thomas, T. P. Lippa, S.-J. Xu, and K. H. Bowen Jr., *J. Chem. Phys.*, **124**, 144304 (2006).
- [54] A. C. Reber, S. N. Khanna, and A. W. Castleman, Jr., *J. Am. Chem. Soc.*, **129**, 10189 (2007).
- [55] A. W. Castleman, Jr., S. N. Khanna, A. Sen, A. C. Reber, M. Qian, K. M. Davis, S. J. Peppernick, A. Ugrinov, and M. D. Merrit, *Nano Lett.* **7**, 2734 (2007).
- [56] R. Turton, *The Quantum Dot* (Freeman, San Francisco) 1995.
- [57] K.-H. Meiwes-Broer, *Metal Clusters at Surfaces: Structure, Quantum Properties, Physical Chemistry*, Springer-Verlag Berlin Heidelberg, (2000).
- [58] Z.-P. Liu, S. J. Jenkins, and D. A. King, *Phys. Rev. Lett.*, **94**, 196102 (2005).

- [59] K. W. Kolasinski, *Surface Science: Foundations of Catalysis and Nanoscience*, John Wiley and Sons, Ltd., (2012).
- [60] G. Fuchs, P. Melinon, F. Santos Aires, M. Treilleux, B. Cabaud, and A. Hoareau, *Phys. Rev. B*, **44**, 3926 (1991).
- [61] C. Bréchnignac, Ph. Cahuzac, F. Carlier, M. de Frutos, A. Masson, C. Mory, C. Colliex, and B. Yoon, *Phys. Rev. B*, **57**, R2084(R) (1998).
- [62] V. Paillard, P. Melinon, V. Dupuis, J. P. Perez, A. Perez, and B. Champagnon, *Phys. Rev. Lett.*, **71**, 4170 (1993).
- [63] R. W. Siegel, 1991, in *Materials Science and Technology*, edited by R. W. Cahn (VCH, Weinheim, Germany), **15**, 584 (1991).
- [64] P. Jena and S. N. Khanna, *Mater. Sci. Eng., A*, **217/218**, 218 (1996).
- [65] V. M. Shalaev and M. Moskovits, 1997, Eds., *Nanostructured Materials: Clusters, Composites and Thin Films*, ACS Symposium series 679 (Am. Chem. Soc. Ed., Washington DC)
- [66] P. Jensen, *Rev. Mod. Phys.*, **71**, 1695 (1999).
- [67] H. Haberland, Z. Insepov, and M. Moseler, *Phys. Rev. B*, **51**, 11061 (1995).
- [68] V. N. Popok, I. Barke, E. E. B. Campbell, and K.-H. Meiwes-Broer, *Surf. Sci. Rep.*, **66**, 347 (2011).
- [69] P. M. I. Dinh, P. G. Reinhard, and E. Suraud, *Phys. Rep.*, **485**, 42 (2010).
- [70] B. Nacer, C. Massobrio, and C. Félix, *Phys. Rev. B*, **56**, 10590 (1997)
- [71] F. J. Palacios, M. P. Iñiguez, M. J. López, and J. A. Alonso, *Phys. Rev. B*, **60**, 2908 (1999).
- [72] E. C. Honea, A. Ogura, C. A. Murray, K. Raghavachari, W. O. Sprenger, M. F. Jarrold, and W. L. Brown, *Nature*, **366**, 42 (1993).
- [73] U. Busolt, E. Cottancin, L. Socaciu, H. Röhr, T. Leisner, and L. Wöste, *Eur. Phys. J. D*, **16**, 297 (2001).

- [74] H. P. Cheng and U. Landman, *Science*, **260**, 1304 (1993).
- [75] K. Bromann, C. Félix, H. Brune, W. Harbich, R. Monot, J. Buttet, and K. Kern, *Science*, **274**, 956 (1996).
- [76] S. Duffe, N. Grönhagen, L. Patryarcha, B. Sieben, C. Yin, B. von Issendorff, M. Moseler, and H. Hövel, *Nat. Nanotech.*, **5**, 335 (2010).
- [77] A. Perez, P. Melinon, V. Dupuis, P. Jensen, B. Prevel, J. Tuaille, L. Bardotti, C. Martet, M. Treilleux, M. Broyer, M. Pellarin, J. L. Vaille, B. Palpant, and J. Lerme, *J. Phys. D: Appl. Phys.*, **30**, 709 (1997).
- [78] C. Binns and M. J. Maher, *N. J. Phys.*, **1**, 1.1 (2002).
- [79] C. Binns, K. N. Trohidou, J. Bansmann, S. H. Baker, J. A. Blackman, J.-P. Bucher, D. Kechrakos, A. Kleibert, S. Louch, K.-H. Meiwes-Broer, G. M. Pastor, A. Perez, and Y. Xie, *J. Phys. D: Appl. Phys.*, **38**, R357 (2005).
- [80] J. Tuaille, V. Dupuis, P. Mélinon, B. Prével, M. Treilleux, A. Perez, M. Pellarin, J. L. Vialle, and M. Broyer, *Philosophical Magazine A* **76**, 493 (1997).
- [81] U. Heiz and U. Landman, *Nanocatalysis*, Springer-Verlag Berlin Heidelberg, 2007.
- [82] E. K. Parks, B. H. Weiller, P. S. Bechthold, W. F. Hoffman, G. C. Nieman, L. G. Pobo, and S. J. Riley, *J. Chem. Phys.*, **88**, 1622 (1988).
- [83] <http://www.chem.ucl.ac.uk/cosmicdust/er-lh.htm>.
- [84] A. Lyalin and T. Taketsugu, *J. Phys. Chem. Lett.*, **1**, 1752 (2010).
- [85] B. Yoon, H. Häkkinen, and U. Landman, *J. Phys. Chem. A*, **107**, 4066 (2003).
- [86] C. Bürgel, N. M. Reilly, G. E. Johnson, R. Mitrić, M. L. Kimble, A. W. Castleman, Jr., and V. Bonacić-Koutecký, *J. Am. Chem. Soc.*, **130**, 1694 (2008).
- [87] P. Frondelius, H. Häkkinen, and K. Honkala, *Phys. Rev. B*, **76**, 073406 (2007).
- [88] A. Lyalin and T. Taketsugu, *J. Phys. Chem. C*, **114**, 2484 (2010).

- [89] H. S. Benggaard, J. K. Nørskov, J. Sehested, B. S. Clausen, L. P. Nielsen, A. M. Molenbroek, and J. R. Rostrup-Nielsen, *J. Catal.*, **209**, 365 (2002).
- [90] A. M. Molenbroek, J. K. Nørskov, and B. S. Clausen, *J. Phys. Chem. B*, **105**, 5450 (2001).
- [91] <https://www.flickr.com/photos/36409365@N04/3481853691/>
- [92] V. Fock, *Zeitschrift für Physik*, **61**, 126 (1930).
- [93] J. C. Slater, *Phys. Rev.*, **81**, 385 (1951).
- [94] J. C. Slater, *Phys. Rev.*, **51**, 846 (1937).
- [95] <http://link.aps.org/doi/10.1103/PhysRev.46.618> C. Møller and M. S. Plesset, *Phys. Rev.*, **46**, 618 (1934).
- [96] Rodney J. Bartlett, *J. Phys. Chem.*, **93**, 1697 (1989).
- [97] J. Kohanoff, *Electronic Structure Calculations for Solids and Molecules Theory and Computational Methods*, Cambridge University Press, (2006).
- [98] A. Szabo and N. S. Ostlund, *Modern Quantum Chemistry: Introduction to Advanced Electronic Structure Theory*, Dover Publications Inc., (1996).
- [99] P. Hohenberg and W. Kohn, *Phys. Rev.* **136**, B864 (1964).
- [100] W. Kohn and L. J. Sham, *Phys. Rev.* **140**, A1133 (1965).
- [101] N. W. Ashcroft and N. Mermin, *Solid State Physics*, Brooks/Cole (1976).
- [102] D. M. Cepreley and B. J. Alder, *Phys. Rev. Lett.*, **45**, 566 (1980).
- [103] S. J. Vosko, L. Wilk, and M. Nusair, *Can. J. Phys.* **58**, 1200 (1980).
- [104] J. P. Perdew and A. Zunger, *Phys. Rev. B*, **23**, 5048 (1981).
- [105] A. D. Becke, *Phys. Rev. A*, **38**, 3098 (1988).
- [106] J. P. Perdew, J. A. Chevary, S. H. Vosko, K. A. Jackson, M. R. Pederson, D. J. Singh, and C. Fiolhais, *Phys. Rev. B*, **46**, 6671 (1992); Erratum *Phys. Rev. B*, **48**, 4978 (1993).

- [107] J. P. Perdew and Y. Wang, *Phys. Rev. B*, **45**, 13244 (1992).
- [108] J. P. Perdew, K. Burke, and M. Ernzerhof, *Phys. Rev. Lett.*, **77**, 3865 (1996).
- [109] by Richard M. Martin, *Electronic Structure: Basic Theory and Practical Methods*, Cambridge University Press, (2008).
- [110] J. C. Phillips and L. Kleinman, *Phys. Rev.*, **116**, 287 (1959).
- [111] M. L. Cohen and V. Heine, in *Solid State Physics*, edited by H. Ehrenreich, F. Seitz, and D. Turnbull, Academic Press, New York, **24**, 37 (1970).
- [112] M. T. Yin and Marvin L. Cohen, *Phys. Rev. B*, **26**, 5668 (1982).
- [113] N. Troullier and J. L. Martins, *Phys. Rev. B*, **43**, 1993 (1991).
- [114] N. Troullier and J. L. Martins, *Phys. Rev. B* **43**, 8861 (1991).
- [115] G. P. Kerker, *J. Phys. C: Solid State Phys.*, **13**, L189 (1980).
- [116] D. R. Hamann, M. Schlüter, and C. Chiang, *Phys. Rev. Lett.*, **43**, 1494 (1979).
- [117] D. Vanderbilt, *Phys. Rev. B*, **41**, 7892 (1990).
- [118] S. Goedecker, M. Teter, and J. Hutter, *Phys. Rev. B*, **54**, 1703 (1996).
- [119] K. Laasonen, A. Pasquarello, R. Car, C. Lee, and D. Vanderbilt, *Phys. Rev. B* **47**, 10142 (1993).
- [120] P. E. Blöchl, *Phys. Rev. B*, **50**, 17953 (1994).
- [121] G. Kresse and D. Joubert, *Phys. Rev. B*, **59**, 1758 (1999).
- [122] R. P. Feynman, *Phys. Rev.* **56**, 340 (1939).
- [123] A. R. Oganov and C. W. Glass, *J. Chem. Phys.*, **124**, 244704 (2006).
- [124] C. W. Glass, A. R. Oganov, and N. Hansen, *Comp. Phys. Comm.*, **175**, 713 (2006).
- [125] A. O. Lyakhov, A. R. Oganov, H. T. Stokes, and Q. Zhu, *Comp. Phys. Comm.*, **184**, 1172 (2013).

- [126] A.R. Oganov, A.O. Lyakhov, and M. Valle. *Acc. Chem. Res.*, **44**, 227 (2011).
- [127] H. Goldstein, C. P. Poole Jr., J. L. Safko, *Classical Mechanics*, Addison-Wesley Publications: 3<sup>rd</sup> Ed., (2001).
- [128] G. Kresse and J. Hafner, *Phys. Rev. B*, **47**, 558 (1993).
- [129] G. Kresse and J. Hafner, *Phys. Rev. B*, **49**, 14251 (1994).
- [130] D. Frenkel, B. Smit, *Understanding Molecular Simulation: From Algorithms to Applications*, Academic Press; 2 edition (2001).
- [131] D. Marx, J. Hutter, *Ab Initio Molecular Dynamics: Basic Theory and Advanced Methods*, Cambridge University Press; 1 edition (2009).
- [132] S. Nosé, *Mol. Phys.*, **52**, 255 (1984).
- [133] S. Nosé, *J. Chem. Phys.*, **81**, 511 (1984).
- [134] G. W. Hoover, *Phys. Rev. A*, **31**, 1695 (1985).
- [135] D. J. Evans and B. L. Holian, *J. Chem. Phys.*, **83**, 4069 (1985).
- [136] D. M. Bylander and L. Kleinman, *Phys. Rev. B*, **46**, 13756 (1992).
- [137] D. Sholl, J. A. Steckel, *Density Functional Theory: A Practical Introduction*, Wiley-Blackwell, (2009).
- [138] H. Jónsson, G. Mills, and K. W. Jacobsen, “Nudged elastic band method for finding minimum energy paths of transitions,” in *Classical and Quantum Dynamics in Condensed Phase Simulations*, edited by B. J. Berne, G. Ciccotti, and D. F. Coker, World Scientific, Singapore, p. 385, (1998).
- [139] G. Henkelman, B. P. Uberuaga, and H. Jónsson, *J. Chem. Phys.*, **113**, 9901 (2000).
- [140] G. Henkelman and H. Jónsson, *J. Chem. Phys.*, **113**, 9978 (2000).
- [141] R. F. W. Bader, *Atoms in Molecules: A Quantum Theory (International Series of Monographs on Chemistry)*, Clarendon Press (1994).

- [142] W. Tang, E. Sanville, and G. Henkelman, *J. Phys.: Cond. Matt.*, **21**, 084204 (2009).
- [143] E. Sanville, S. D. Kenny, R. Smith, and G. Henkelman, *J. Comp. Chem.*, **28**, 899 (2007).
- [144] G. Henkelman, A. Arnaldsson, and H. Jónsson, *Comput. Mater. Sci.*, **36**, 354 (2006).
- [145] <http://theory.cm.utexas.edu/henkelman/research/bader/>
- [146] S. J. Grimme, *J. Comp. Chem.*, **27**, 1787 (2006).
- [147] S. Grimme, *J. Comp. Chem.*, **27**, 1787 (2006).
- [148] S. Grimme, J. Antony, S. Ehrlich, and H. Krieg, *J. Chem. Phys.*, **132**, 154104 (2010).
- [149] G. Kresse and J. Furthmüller, *J. Comput. Mat. Sci.*, **6**, 15 (1996).
- [150] G. Kresse and J. Furthmüller, *Phys. Rev. B*, **54**, 11169 (1996).
- [151] G. Kresse and J. Hafner, *Phys. Rev. B*, **47**, 558 (1993); G. Kresse and J. Hafner, *Phys. Rev. B*, **49**, 14251 (1994); G. Kresse and J. Furthmüller, *J. Comput. Mat. Sci.*, **6**, 15 (1996); G. Kresse and J. Furthmüller, *Phys. Rev. B*, **54**, 11169 (1996).
- [152] M. Dion, H. Rydberg, E. Schröder, D. C. Langreth, and B. I. Lundqvist, *Phys. Rev. Lett.*, **92**, 246401 (2004).
- [153] H. Rydberg, B. I. Lundqvist, D. C. Langreth, and M. Dion, *Phys. Rev. B*, **62**, 6997 (2000).
- [154] Y. Zhang and W. Yang, *Phys. Rev. Lett.* **80**, 890 (1998).
- [155] J. Klimes, D. R. Bowler, and A. Michaelides, *J. Phys.: Cond. Matt.*, **22**, 022201 (2010).
- [156] J. Klimes, D. R. Bowler, and A. Michaelides, *Phys. Rev. B*, **83**, 195131 (2011).
- [157] K. Lee, É. D. Murray, L. Kong, B. I. Lundqvist, and D. C. Langreth, *Phys. Rev. B*, **82**, 081101(R) (2010).

- [158] É. D. Murray, K. Lee, and D. C. Langreth, *J. Chem. Theory Comput.*, **5**, 2754 (2009).
- [159] D. C. Langreth, B. I. Lundqvist, S. D. Chakarova-Käck, V. R. Cooper, M. Dion, P. Hyldgaard, A. Kelkkanen, J. Kleis, L. Kong, S. Li, P. G. Moses, E. Murray, A. Puzder, H. Rydberg, E. Schröder, and T. Thonhauser, *J. Phys.:Condens. Matt.* **21**, 084203 (2009).
- [160] R. E. Mapasha, A. M. Ukpong, and N. Chetty, *Phys. Rev. B*, **85**, 205402 (2012).
- [161] G. Román-Pérez and J. M. Soler, *Phys. Rev. Lett.*, **103**, 096102 (2009).
- [162] R. J. Gooding, B. Joos, and B. Bergersen, *Phys. Rev. B*, **27**, 7669 (1983).
- [163] C. Jackschath, I. Rabin, and W. Schulze, *Z. Phys. D*, **22**, 517 (1992).
- [164] G. Gantefor, M. Gausa, K.-H. Meiwes-Broer, and H. O. Lutz, *Faraday Dis. Chem. Soc.*, **86**, 197 (1988).
- [165] I. Lopez-Salido, D. C. Lim, and Y. D. Kim, *Surf. Sci.*, **588**, 6 (2005).
- [166] R. Dietsche, D. C. Lim, M. Bubek, I. Lopez-Salido, G. Ganteför, and Y. D. Kim, *Appl. Phys. A*, **90**, 395 (2008).
- [167] H. Rafii-Tabara, H. Kamiyama, and M. Cross, *Surf. Sci.*, **385**, 187 (1997).
- [168] G. M. Wang, J. J. BelBruno, S. D. Kenny, and R. Smith, *Surf. Sci.* **541**, 91 (2003).
- [169] M. Amft, S. Lebègue, O. Eriksson, and N. V. Skorodumova, *J. Phys.: Cond. Matt.*, **23**, 395001 (2011).
- [170] M. Vanin, J. J. Mortensen, A. K. Kelkkanen, J. M. Garcia-Lastra, K. S. Thygesen, and K. W. Jacobsen, *Phys. Rev. B*, **81**, 081408(R) (2010).
- [171] M. Elstner, P. Hobza, T. Frauenheim, S. Suhai, and E. Kaxiras, *J. Chem. Phys.*, **114**, 5149 (2001).
- [172] N. Ooi, A. Rairkar and J. B. Adams, *Carbon* **44**, 231 (2006).

- [173] Y. X. Zhao and I. L. Spain, *Phys. Rev. B*, **40**, 993 (1989).
- [174] L. Brewer, *Law. Berk. Nat. Lab. Rep.*, LBL-3720 (1977).
- [175] R. Zacharia, H. Ulbricht, and T. Hertel, *Phys. Rev. B*, **69**, 155406 (2004).
- [176] R. Fournier, *J. Chem. Phys.* **115**, 2165 (2001).
- [177] G. M. Wang, J. J. BelBruno, S. D. Kenny, and R. Smith, *Phys. Rev. B*, **69**, 195412 (2004).
- [178] M. Amft, B. Sanyal, O. Eriksson, and N. V. Skorodumova, *J. Phys.: Cond. Matt.*, **23**, 205301 (2011).
- [179] G. M. Wang, J. J. BelBruno, S. D. Kenny, and R. Smith, *Surf. Sci.*, **576**, 107 (2005).
- [180] A. M. Ferrari, C. Xiao, K. M. Neyman, G. Pacchioni, and N. Rösch, *Phys. Chem. Chem. Phys.*, **1**, 4655 (1999).
- [181] M. Couillard, S. Pratontep, and R. E. Palmer, *Appl. Phys. Lett.*, **82**, 2595 (2003).
- [182] M. Schmidt, N. Kébaïli and A. Lando, S. Benrezzak, L. Baraton, Ph. Cahuzac, A. Masson, and C. Bréchnac, *Phys. Rev. B*, **77**, 205420 (2008).
- [183] C. E. Cross, J. C. Hemminger, and R. M. Penner, *Langmuir*, **23**, 10372 (2007).
- [184] S. A. Scott, M. V. Kral, and S. A. Brown, *Phys. Rev. B*, **72**, 205423 (2005).
- [185] D. N. McCarthy, D. Robertson, P. J. Kowalczyk, and S. A. Brown, *Surf. Sci.*, **604**, 1273 (2010).
- [186] Y. Sun and H. Cui, and C. X. Wang, *Phys. Chem. Chem. Phys.*, **15**, 11808 (2013).
- [187] H. He, R. Pandey, J. U. Reveles, S. N. Khanna, and S. P. Karna, *Appl. Phys. Lett.*, **95**, 192104 (2009).
- [188] J. L. Chen, C. S. Wang, K. A. Jackson, and M. R. Pederson, *Phys. Rev. B*, **44**, 6558 (1991).

- [189] I. M. L. Billas, A. Châtelain and W. A. de Heer, *Science*, **265**, 1682 (1994).
- [190] M. Valden, X. Lai, and D. W. Goodman, *Science* **281**, 1647 (1998).
- [191] C. R. Dean, A. F. Young, I. Meric, C. Lee, L. Wang, S. Sorgenfrei, K. Watanabe, T. Taniguchi, P. Kim, K. L. Shepard, and J. Hone, *Nature Nanotech.* **5**, 722 (2010); S. Tang, H. Wang, Y. Zhang, A. Li, Hong Xie, X. Liu, L. Liu, T. Li, F. Huang, X. Xie, and M. Jiang, *Sci. Rep.* **3**, 2666 (2013).
- [192] M. Bokdam, G. Brocks, M. I. Katsnelson, and P. J. Kelly, *Phys. Rev. B*, **90**, 085415 (2014).
- [193] J. G. Díaz, Y. Ding, R. Koitz, A. P. Seitsonen, M. Iannuzzi, and J. Hutter *Theor. Chem. Acc.* **132**, 1350 (2013)
- [194] P. Gehring, B. F. Gao, M. Burghard, and K. Kern, *Nano Lett.*, **12**, 5137 (2012).
- [195] J. Neugebauer and M. Scheffler, *Phys. Rev. B*, **46**, 16067 (1992).
- [196] G. M. Wang, J. J. BelBruno, S. D. Kenny, and R. Smith, *Surf. Sci.*, **576**, 107 (2005).
- [197] R. Varns and P. Strange, *J. Phys: Cond Matt.*, **20**, 225005 (2008).
- [198] N. Godbout, D.R. Salahub, J. Andzelm, and E. Wimmer, *Can. J. Chem.* **70**, 560 (1992).
- [199] P. Thomson, D. E. Cox, and J. B. Hastings, *J. Appl. Crystallogr*, **20**, 79 (1987).
- [200] R. H. French, *J. Am. Ceram. Soc.*, **73**, 477 (1990).
- [201] W. B. Pearson, *A Handbook of Lattice Spacing and Structures of Metals and alloys*, **2**, 81 (1958).
- [202] K. Watanabe, T. Taniguchi, and H. Kanda, *Nat. Mat.* **3**, 404 (2004).
- [203] A. Nag, K. Raidongia, K. P. S. S. Hembram, R. Datta, U. V. Waghmare, and C. N. R. Rao, *ACS Nano*, **4**, 1539 (2010).
- [204] S. Saremi, *Phys. Rev. B*, **76**, 184430 (2007).

- [205] A. M. Black-Schaffer, *Phys. Rev. B* **81**, 205416 (2010).
- [206] S. R. Power and M. S. Ferreira, *Crystals*, **3**, 49 (2013).
- [207] H. Chen, Q. Niu, Z. Zhang and A. H. MacDonald, *Phys. Rev. B* **87**, 144410 (2013).
- [208] H.-J. Koo, H. Xiang, C. Lee, and M.H. Whangbo, *Inorg. Chem.*, **48**, 9051 (2009).
- [209] R. Rosei, M. De Crescenzi, F. Sette, C. Quaresima, A. Savoia, and P. Perfetti, *Phys. Rev. B*, **28**, 1161(R) (1983).
- [210] G. Giovannetti, P. A. Khomyakov, G. Brocks, V. M. Karpan, J. van den Brink, and P. J. Kelly, *Phys. Rev. Lett.* **101**, 026803 (2008).
- [211] A. Sanchez, S. Abbet, U. Heiz, W.-D. Schneider, H. Hakkinen, R. N. Barnett, and U. Landman, *J. Phys. Chem. A*, **103**, 9577 (1999).
- [212] W. T. Wallace and R. L. Whetten, *J. Phys. Chem. B*, **104**, 10964 (2000).
- [213] H. J. Zhai and L. S. Wang, *J. Chem. Phys.* **122**, 051101 (2005).
- [214] D. W. Yuan and Z. Zeng, *J. Chem. Phys.*, **120**, 6574 (2004).
- [215] X. Wu, L. Senapati, S. K. Nayak, A. Selloni, and M. Hajaligol, *J. Chem. Phys.*, **117**, 4010 (2002).
- [216] D. M. Popolan, M. Nössler, R. Mitrić, T. M. Bernhardt, and V. Bonacić-Koutecký, *J. Phys. Chem. A*, **115**, 951 (2011).
- [217] A. Prestianni, A. Martorana, F. Labat, I. Ciofini, and C. Adamo, *J. Phys. Chem. B*, **110**, 12240 (2006).
- [218] D. M. Cox, R. Brickman, K. Creegan, and A. Kaldor, *Phys. D: At., Mol. Clusters*, **19**, 353 (1991).
- [219] T. H. Lee, and K. M. Ervin, *J. Phys. Chem.*, **98**, 10023 (1994).
- [220] B. E. Salisbury, W. T. Wallace, and R. L. Whetten, *Chem. Phys.*, **262**, 131 (2000).

- [221] D. Stolcic, M. Fischer, G. Ganteför, Y. D. Kim, Q. Sun, and P. Jena, *J. Am. Chem. Soc.*, **125**, 2848 (2003).
- [222] G. Mills, M. S. Gordon, and H. Metiu, *Chem. Phys. Lett.*, **359**, 493 (2002).
- [223] H. Nakatsuji, Z.-M. Hu, H. Nakai, and K. Ikeda, *Surf. Sci.*, **387**, 328 (1997).
- [224] A.-Q. Wang, J.-H. Liu, S. D. Lin, T.-S. Lin, and C.-Y. Mou, *J. Catal.*, **233**, 186 (2005).
- [225] A.-Q. Wang, C.-M. Chang, and C.Y. Mou, *J. Phys. Chem. B*, **109**, 18860 (2005).
- [226] V. Bonacić-Koutecký, J. Burda, R. Mitrić, M. Ge, G. Zampella, and P. Fantucci, *J. Chem. Phys.*, **117**, 3120 (2002).
- [227] C. Rajesh, S. Nigam and C. Majumder, *Phys. Chem. Chem. Phys.* **16**, 26561 (2014).
- [228] S. Nigam and C. Majumder, *Langmuir*, **26(24)**, 18776 (2010).
- [229] G. F. Zhao and Z. Zeng, *J. Chem. Phys.* **125**, 014303 (2006).
- [230] S. J. Carroll, S. Pratontep, M. Streun, R. E. Palmer, S. Hobday, and R. Smith *J. Chem. Phys.*, **113**, 7723 (2000).
- [231] I. Fleischer, D. M. Popolan, M. Krstić, V. Bonacić-Koutecký, and T. M. Bernhardt, *Chem. Phys. Lett.*, **565**, 74 (2013).